

BIOPHYSICAL CHARACTERIZATION OF BIS(MONOACYLGLYCERO)PHOSPHATE
(BMP) MODEL LIPID MEMBRANES USING ANALYTICAL TOOLS

By

JANETRICKS NANJALA CHEBUKATI

A DISSERTATION PRESENTED TO THE GRADUATE SCHOOL
OF THE UNIVERSITY OF FLORIDA IN PARTIAL FULFILLMENT
OF THE REQUIREMENTS FOR THE DEGREE OF
DOCTOR OF PHILOSOPHY

UNIVERSITY OF FLORIDA

2009

© 2009 Janetricks Nanjala Chebukati

To my parents:
My mom, Ritah Nekesa Muchungi and my dad, Gerishom Muchungi Chebukati.
For your endless love and for never giving up on me.

And to the memories of:
My nephew, Rocky Wasike (1993 - 1996).
Even though you have been long gone, you are still dearly missed and fond memories
of you are always close in our hearts.

My brother, Justus Wangila Wekesa (*baba Bryo*, 1966 - 2005).
Thank you for believing in me always. We miss you so much. May you rest in peace
dear brother, until we meet again.

ACKNOWLEDGMENTS

None of this work would have been accomplished without the numerous people that the Lord Almighty graciously blessed me with, to help me along this journey. I am indeed very grateful to God for blessing me with many opportunities for second chances. First and foremost, I would like to express my sincere gratitude to my advisor and mentor, Dr. Gail E. Fanucci, who took me in at a time when I most needed someone to believe in me as an aspiring scientist. Gail gave me a chance to learn and develop a renewed appreciation for science, especially the science of biological membranes. I am very grateful for her direction, support and encouragement during my time in her research group, and for always making the time to “chat” over my many questions. Gail’s resourcefulness and stimulating ideas made everything seem very possible, even in the most difficult of situations. Most of all, I thank Gail for teaching me to not only be a better scientist, but to also be a better person, and to never stop dreaming big!

I would also like to thank my committee members, Dr Dan Talham, Dr. Nicolo Omenetto, Dr. John Eyler and Dr. Byung-Ho Kang, especially for making time out of their busy schedules to serve on my committee. I am very grateful for all their input. I would also like to express my gratitude to Dr. Joanna Long for all her input and suggestions during our lipid discussions.

I am thankful to the entire Fanucci research group, both present and past members, for all their support during my time in the group. I am especially grateful to Mandy Blackburn, who always went to great lengths to simplify a lot of stuff for me, and whose sense of humor always made for the many much-needed light moments, to Dr. Yong Ran for the many lipid discussions we had, and to Tom Frederick for all the

“interesting” BMP discussions. I am also thankful to several members of the chemistry department who in one way or another made my graduate years a lot easier. I am especially grateful to Dr. Ben Smith, Lori Clark and Vivian Thompson for all their support.

I am very grateful to all my friends, both here in the US and back home in Kenya, for supporting me every step of the way. I would like to thank my best friend and sister, Dr. Catherine Nabifwo Situma (Cate), for all her support and encouragement. Thank you Cate, for always being there, for the lots and lots of laughter, and for being both a friend *in need* and *indeed!* I would also like to thank my friends, Dr. Cecelia Njeru and her husband, Mr. Peter Njeru, for all their support, friendship and encouragement. I am especially grateful to Cecelia for all her advice and encouragement during some of my lowest moments. I also thank my dear friends, Dr. William and his wife Susan Mkanta for being our family away from home. I am greatly indebted to William and Susan for being such true friends in both good and bad times, for constantly encouraging me, and for freely opening their home to us whenever we needed to get away from Gainesville once in a while! I am also very thankful to Dr. Richard and his wife Jane Makopondo for their friendship and encouragement. I would like to remember my friends Isabella Tembura and Gladys Moige for always encouraging me throughout the years.

I would also like to remember our small group friends, especially Aaron and Keane Wilkinson, Patrick and Tarasue Maness, Steve and Jenni Williams, Natalie and Justine, for their fellowship and continued prayers. Our fellowship together made me always look forward to Friday evenings with lots of excitement and anticipation, and I wish we had started doing this much sooner than just six months ago!

Without a doubt, my family has been my stronghold and inspiration every step of this journey. I am greatly indebted to my dearest friend and husband, fellow scientist Dr. George Odhiambo Okeyo. I am very grateful to George for being there always, for providing a shoulder to lean on, and for listening when at times that was all I needed, especially after a futile day of trying unsuccessfully to capture electron microscopy images of my lipid vesicles! I also thank George for all our scientific discussions, and for helping me better understand and appreciate the science of ion channels. Above all, I am grateful to George for being a selfless, understanding husband and a great dad to our daughters, and for always dreaming big with me!

I would also like to thank my daughters, Lavender and Subi, for giving me the reason to wake up each day and push myself further, and for bringing lots of joy and laughter to my life. I especially thank Lavender for helping so much with Subi, for patiently bearing with me, and for learning independence at such an early age! Subi has been such a bright spot in all our lives, and I thank her for the happiness she has brought us all!

I am also very grateful to my siblings back in Kenya, who have endured through a lot of difficulty, and in some cases sacrificed a lot, so that I could be where I am today. I would like to remember my late brother, Justus Wangila Wekesa for always encouraging me and believing in me. I also thank my sister, Violet Lukela for being very supportive, for encouraging me throughout the years, and for her great sense of humor! I am also grateful to my brother Walter Lubisia for quietly encouraging me on, believing in me and for praying for me. I thank my younger brothers Brawel Welikhe and Caleb Muchungi, and my younger sisters Esther Naliaka, Joyce Nasimiyu, Peris Namae and

Mildred Nakhumicha, especially for being such a big help with Lavender when she was younger and for never stopping to believe in me! I thank all my nephews and nieces who always believed in me, especially Harun, Bryan, Laura and Ian.

I would like to also thank my mother-in-law, Peres Jura, my father-in-law Zephaniah Jura, my sister-in-law Jacqueline and her family, my brother-in-laws Victor, James and their families, for their love, support and prayers.

Finally, and most importantly, I cannot express enough gratitude to the two people without whom I would never have made it to graduate school in the first place. I am very grateful to my parents; my dad, Gerishom Muchungi Chebukati and my mom, Ritah Nekesa Muchungi, for their unconditional love, support, prayers, for encouraging me to reach for the sky, for believing in me and for never, ever giving up on me! My deepest gratitude to my parents, and the appreciation of my PhD journey, can be better expounded by the following paragraph, which I hope may someday be an inspiration to some girl, so that she may see life as being full of possibilities, and to never lose hope!

In the year 1995, my parents displayed the biggest love a parent can have for a child, at least in my opinion. Armed with nothing but faith and hope, they requested the Jomo Kenyatta University of Agriculture and Technology (JKUAT) administration to defer my admission to the university until the following year, after I failed to report for admission as scheduled. Admission to the few Kenyan public universities is highly competitive and one can easily lose their slot if they don't report as required. At the time, my parents had no idea where I was, or if and when they could ever see me again, but still hoped and believed for the best. My absence had been caused by unusual circumstances that, for confidential purposes, cannot be disclosed here. Little did anyone know that such a simple gesture of a parent's true love, would later define who I am today, and bear so much fruit as witnessed by this work among other things. Needless to say, I turned up almost a year later in my parents' rural home in Kenya, a frustrated and hopeless single mother at 19. You can imagine my joy and relief when I learnt that because of my parents, my chance at the university was still available and that through my education, there was still hope for me for a better future! As if that was not enough, my parents readily took care of my child while I went back to school, as if she was their own! The day I received my readmission letter to Jomo Kenyatta University was one of the happiest days of my life, and that was also the beginning of

my many blessings for second chances, and since then, I have never looked back. After all, life is full of possibilities!

I am forever indebted to my parents, for the task they took upon themselves to guide me, to sacrifice everything so I can have an education, for supporting me through thick and thin, for taking care of my daughter Lavender so I could go back to school, for believing in me always, and above all else, for loving me endlessly.

All in all, I thank the Lord God Almighty for making all things possible!

TABLE OF CONTENTS

	<u>Page</u>
ACKNOWLEDGMENTS.....	4
LIST OF TABLES.....	12
LIST OF FIGURES.....	13
LIST OF ABBREVIATIONS.....	17
ABSTRACT.....	20
CHAPTER	
1 INTRODUCTION TO LIPIDS.....	22
Biological Lipids.....	22
Description and Classification.....	22
Functional Roles of Lipids in the Cell.....	25
Glycerophospholipids.....	29
Typical Structure and Anatomy.....	29
“Unusual” Phospholipids.....	32
Ether-phospholipids.....	32
Cardiolipin (CL).....	34
Bis(monoacylglycero)phosphate (BMP).....	35
Phospholipid Polymorphism.....	37
Self-assembly, organization and phase behavior.....	38
Lipid vesicles (liposomes) as membrane models.....	43
Bis(monoacylglycero)phosphate (BMP).....	46
Role of BMP in the Late Endosome.....	49
Overview of Biophysical Studies of BMP.....	51
Scope of Dissertation.....	53
2 TECHNIQUES UTILIZED IN LIPID ANALYSIS.....	57
Dynamic Light Scattering (DLS).....	57
Theory.....	57
Fundamentals of DLS.....	59
Factors that affect the translational diffusion coefficient.....	60
Basis of intensity fluctuations in DLS.....	62
How the digital autocorrelator works.....	66
The auto correlation function (ACF).....	68
Instrumental design for DLS.....	71
DLS Applications.....	73
Transmission Electron Microscopy (TEM).....	76
Theory.....	76
The need for a vacuum system in TEM.....	81

	Sample preparation methods in TEM.....	83
	Negative staining	84
	TEM Applications	85
	Fluorescence Resonance Energy Transfer (FRET).....	87
	Theory	87
	Principles of FRET	88
	Methods for measurement of FRET	93
	Biological Applications of FRET	94
	Chromatography Separations.....	97
	Thin Layer Chromatography (TLC).....	98
	Column Chromatography	100
3	INVESTIGATION OF BMP VESICLE SIZE AND MORPHOLOGY IN MODEL MEMBRANES.....	104
	Introduction	104
	Experimental section.....	108
	Materials and Reagents Used	108
	Hydrated Dispersions and Extruded Vesicle Preparation.....	109
	Sample Preparation for Vesicle-leakage Assays.....	110
	Instrumentation Used	111
	Dynamic light scattering (DLS).....	111
	Negative staining-transmission electron microscopy	112
	Fluorescence measurements.....	112
	Results and Discussion.....	113
	Evaluation of Mixing Different Sizes of Neat POPC Vesicle Populations	113
	Comparison of Vesicle “Stability”: BMP versus POPC Vesicles	120
	BMP Vesicle Leakage Assays under Acidic and Neutral pH Conditions	122
	Characterization of BMP and POPC Hydrated Dispersions and Unilamellar Vesicles.....	126
	Effect of pH	126
	Effects of Ionic strength	131
	Characterization of Hydrated Dispersions and Extruded Vesicles of POPC Mixed With BMP and PGP	133
	Conclusions	136
4	ANALYSIS OF CHANGES IN BMP VESICLE SIZE AND MORPHOLOGY IN THE PRESENCE OF GANGLIOSIDE GM1 AT LATE ENDOSOMAL pH 5.5.....	138
	Introduction	138
	Experimental Section.....	141
	Materials Used	141
	Preparation of Hydrated Lipid Dispersions and Extruded Unilamellar Vesicles.....	141
	Instrumentation.....	142
	Dynamic light scattering (DLS).....	142
	Negative staining-transmission electron microscopy (TEM)	143

Results and Discussion.....	143
Characterization of BMP Hydrated Lipid Dispersions as a Function of pH.....	143
Characterization of BMP:GM1 Hydrated Dispersions and Extruded Vesicles at Specific Concentrations.....	146
Effect of GM1 and BMP Mixing with POPC Membranes	153
Conclusions	157
5 EFFECT OF CHOLESTEROL MIXING WITH GM1 AND BMP ON PHOSPHOLIPID MODEL MEMBRANES AT LATE ENDOSOMAL pH 5.5	159
Introduction	159
Experimental Details.....	163
Materials Used	163
Hydrated Lipid Dispersions and Extruded Vesicle Preparation	163
Instrumentation.....	164
Dynamic light scattering (DLS).....	164
Negative staining-transmission electron microscopy (TEM)	165
Results and Discussion.....	165
Characterization of BMP Vesicle Size and Morphology in the Presence of Cholesterol	165
Investigation of Vesicle Size and Morphology in POPC:CHOL:BMP Mixtures.....	168
Conclusions	175
6 SUMMARY AND FUTURE PERSPECTIVES	176
BMP Forms Small Stable Lamellar Vesicle Structures and Induces Formation of Small Vesicles when mixed with POPC.....	176
Ganglioside GM1 Leads to Formation of Small Homogenous Vesicles When Mixed with BMP	176
BMP Counteracts the Cholesterol Effect when Mixed with GM1 and POPC	177
Future Perspectives	178
APPENDIX	
STEP BY STEP ANALYSIS OF DYNAMIC LIGHT SCATTERING DATA.....	180
LIST OF REFERENCES	183
BIOGRAPHICAL SKETCH.....	204

LIST OF TABLES

<u>Table</u>	<u>page</u>
1-1 Common classes of glycerophospholipids.....	31
2-1 Types of lasers commonly used in DLS instruments.....	72
3-1 Summary of POPC vesicle diameters extruded with polycarbonate membranes of varying pore sizes.....	114
3-2 Summary of BMP, POPC and POPG average vesicle diameter as a function of extrusion membrane pore diameters.....	120
3-3 Summary of average vesicle diameters of BMP and POPC dispersions and extruded vesicles at neutral pH 7.4.....	126
3-4 Average vesicle diameters of BMP and POPC hydrated dispersions and 400-nm extruded vesicles at acidic pH 4.2.....	129
3-5 Summary of average vesicle diameters of BMP vesicles hydrated without NaCl in the buffer.....	132
3-6 Summary of the average vesicle diameters of POPC:BMP (85:15) hydrated dispersions and 400 nm-extruded vesicles at neutral pH.....	134
3-7 Summary of average vesicle diameters of POPG and POPC: POPG (80:20) vesicles.....	135
4-1 Summary of the average diameter of BMP hydrated dispersions at specific pH conditions.....	145
4-2 Summary of DLS average vesicle sizes of BMP:GM1 hydrated lipid dispersions and 400-nmextruded unilamellar vesicles at specific concentrations.....	150
5-1 Average vesicle of BMP:CHOL (7:3) hydrated dispersions and extruded Vesicles.....	167
5-2 Average vesicle diameters of POPC:CHOL (8:2) and POPC:BMP:CHOL (65:15:20) hydrated dispersions and extruded vesicles.....	170
5-3 Vesicle size distributions of POPC:GM1:CHOL (70: 10: 20) and POPC:GM1:BMP:CHOL hydrated dispersions and 400 nm-extruded Vesicles.....	173
A-1 OriginPro 8 spreadsheet of the imported DLS raw data of 100 nm-extruded BMP vesicles.....	181

LIST OF FIGURES

<u>Figure</u>	<u>page</u>
1-1 General classification of eukaryotic lipids. Modified from Ref. (3).....	22
1-2 Chemical structures of A) glycerol backbone, B) triacylglycerol and C) sphingosine backbone.....	23
1-3 Enzymatic hydrolysis of phosphatidylinositol 4, 5, bisphosphate to diacylglycerol and 1, 4, 5 triphosphate.	27
1-4 Chemical structures of A) dolichol, B) vitamin A, C) vitamin E and D) vitamin K.....	27
1-5 General structural anatomy of glycerophospholipids.....	30
1-6 Chemical structures of common classes of glycerophospholipids. A) Phosphatidic acid. B) Phosphatidylcholine. C) Phosphatidylethanolamine. D) Phosphatidylserine. E) Phosphatidylglycerol. F) Phosphatidylinositol.....	31
1-7 Chemical structures of representative ether-phospholipids. A) Platelet activating factor (PAF). B) Plasmalogen.....	32
1-8 Enzyme catalyzed biosynthesis of cardiolipin from POPG and CDP-DAG.....	34
1-9 Chemical structures of A) BMP (sn-1, sn-1' stereoconfiguration) and B) phosphatidylcholine (sn-3 glycerophosphate stereoconfiguration).....	36
1-10 Different shapes of lipid polymorphisms in water (or aqueous environment).....	39
1-11 Morphology of different sizes/types of lipid vesicles (liposomes). A) Multilamellar vesicles (MLVs). B) Large unilamellar vesicles (LUVs). C) Small unilamellar vesicles (SUVs).....	41
1-12 Structural isoforms of BMP. A) (<i>R, R</i>), B) (<i>R, S</i>) and C) (<i>S, S</i>) isomers.....	48
2-1 Schematic representation of a speckle pattern observed in DLS. Adapted from Ref. (119).	63
2-2 A) Destructive interference and B) constructive interference observed in a speckle pattern.	64
2-3 Typical intensity fluctuations for A) large particles and B) small particles.....	65
2-4 Schematic showing the fluctuation in the intensity of scattered light as a function of time. Adapted from Ref. (119).....	66

2-5	Correlation spectrum for a sample containing A) large particles with long decay time and B) small particles with rapid decay time.	68
2-6	Number, volume and intensity distributions of a bimodal mixture of 5 and 50 nm lattices present in equal numbers. A) Number distributions. B) Volume distributions. C) Intensity distributions. Modified from Ref. (119).....	71
2-7	Typical experimental set-up in a dynamic light scattering instrument.....	72
2-8	Layout of major components in a basic transmission electron microscopy (TEM) instrument.....	78
2-9	A Jablonski diagram illustrating the coupled transitions involved between the donor emission and acceptor absorbance in FRET.....	89
2-10	A) Overlap of the emission spectrum of the donor and acceptor absorption spectrum results in FRET. B) Lack of overlap of the spectra means no FRET observed.....	90
3-1	Chemical structures of A) BMP, B) POPC and C) POPG.....	105
3-2	DLS histograms of size distributions of POPC vesicles extruded with polycarbonate membranes of varying pore sizes. A) Black line, 30 nm. A) Red line, 100 nm. B) Green line, 400 nm. B) Blue line, hydrated unextruded dispersions.	113
3-3	DLS histograms of populations of manually mixed POPC vesicles extruded with 30 nm and 400 nm pore size membranes and mixed in various volume/volume ratios in 5 mM HEPES buffer.....	115
3-4	DLS histograms showing populations of manually mixed POPC vesicles extruded with 100 nm and 400 nm pore size membranes in various volume/volume ratios.....	118
3-5	Dynamic light scattering size distributions of A) 30-nm extruded BMP and B) POPC vesicles monitored over a five week period.....	121
3-6	Chemical structures of A) calcein, B) ANTS, C) DPX and D) SDS.....	123
3-7	Schematic illustration of SDS detergent solubilizing the liposome and causing leakage of the vesicle contents. Figure adapted from Tom Frederick.	123
3-8	Vesicle leakage assay for BMP vesicles. A) Neutral pH 7.4. B) Acidic pH 4.2.	124
3-9	DLS vesicle size distributions of BMP and POPC vesicles, under neutral pH 7.4. A) Hydrated dispersions. B) 400 nm-Extruded vesicles.....	126

3-10	Negative staining-TEM images of BMP and POPC under neutral pH conditions. A) BMP hydrated dispersions. B) POPC hydrated dispersions. C) BMP 400 nm-extruded vesicles. D) POPC 400 nm-extruded vesicles.	127
3-11	DLS measurements of BMP and POPC A) hydrated dispersions and B) 400-nm extruded large unilamellar vesicles at acidic pH 4.2.	129
3-12	Negative staining-TEM images of BMP and POPC hydrated dispersions and 400-nm extruded vesicles at acidic pH. A) BMP hydrated dispersions. B) BMP extruded vesicles. C) POPC hydrated dispersions. D) POPC extruded vesicles.	130
3-13	Negative staining-TEM images of BMP A) hydrated dispersions and B) 400 nm-extruded vesicles. Vesicles were hydrated in buffer lacking NaCl salt.	132
3-14	DLS histograms of BMP A) hydrated dispersions and B) 400 nm-extruded vesicles that were hydrated in the absence of NaCl.	132
3-15	DLS size distribution of POPC:BMP (85:15) A) hydrated dispersions and B) 400-nm extruded vesicles at neutral pH.	134
3-16	Negative staining-TEM images of POPC:BMP (85:15) A) hydrated dispersions and B) 400 nm-extruded vesicles at neutral pH.	134
3-17	DLS measurements of POPG and POPC:POPG (80:20) hydrated dispersions and extruded vesicles at neutral pH.	135
4-1	Chemical structure of A) Phosphatidylcholine and B) BMP.	138
4-2	Negative staining-TEM images of BMP lipid dispersions as a function of pH...	144
4-3	Dynamic light scattering size distributions of BMP hydrated dispersions as a function of pH.	145
4-4	Chemical structures of A) BMP and B) ganglioside GM1.	147
4-5	Negative staining-TEM images of hydrated BMP:GM1 dispersions at specific molar ratios at pH 5.5.	148
4-6	TEM images of 70:30 mol % BMP: GM1 lipid mixture, showing A) small, aggregated homogenous vesicles, and B) magnified images of the same vesicles.	148
4-7	DLS size distribution histograms of BMP:GM1 A) Hydrated dispersions and B) 400 nm-Extruded unilamellar vesicles at specific concentrations.	150
4-8	Dynamic light scattering average vesicle diameters of POPC A), black solid line, hydrated dispersions, A), red solid line, unilamellar vesicles extruded	

	with 400 nm polycarbonate membranes and B) TEM image of POPC hydrated dispersions.	153
4-9	Dynamic light scattering average vesicle diameters of POPC:GM1 (80:20) A) hydrated dispersions, B) 400-nm extruded vesicles and C) TEM images of POPC:GM1 hydrated dispersions at pH 5.5.	154
4-10	Average vesicle diameters of POPC:BMP:GM1 (70:15:15) A) hydrated dispersions, B) 400-nm extruded vesicles and C) TEM images of POPC: BMP:GM1 hydrated dispersions.	155
5-1	Chemical structures of A) Cholesterol, B) BMP, C) GM1 and D) POPC.	166
5-2	Dynamic light scattering histograms of BMP:CHOL (7:3) A) hydrated dispersions and B) 400-nm extruded unilamellar vesicles at pH 5.5.	167
5-3	Negative staining-TEM images of BMP: CHOL (7:3) hydrated dispersions.	168
5-4	Dynamic light scattering histograms of POPC:CHOL (8:2) A) hydrated dispersions B) 400-nm extruded vesicles, POC:BMP:CHOL (65:15:20) C) hydrated dispersions and D) 400-nm extruded vesicles. Note the different scales on the x-axes.	169
5-5	TEM images of A) POPC:CHOL (8:2) and B) POPC:BMP:CHOL (65:15:20) hydrated dispersions.	171
5-6	Dynamic light scattering histograms of A) hydrated dispersions of POPC:GM1:CHOL (70: 10: 20), B) 400 nm-extruded vesicles of POC: GM1: CHOL, C) hydrated dispersions of POPC:GM1:BMP:CHOL (50:15:15:20) and D) 400 nm-extruded vesicles of POPC:GM1:BMP:CHOL. Note the different scales on the x-axes.	172
5-7	Negative staining-TEM images of A) POPC:GM1:CHOL (70: 10: 20) and B) POPC:GM1:BMP:CHOL (50:15:15::20) hydrated dispersions.	174
A-1	DLS raw data histograms (1, 2, and 3) of a sample of 100 nm-extruded BMP vesicles in 5 mM HEPES, 100 mM NaCl and 0.1 mM EDTA, pH 7.4.	180
A-2	Average vesicle diameter for 100 nm-extruded BMP vesicles.	182

LIST OF ABBREVIATIONS

BMP	Bis(monoacylglycero)phosphate
LBPA	Lysobisphosphatidic acid
POPC	1-palmitoyl-2-oleoyl phosphatidylcholine
POPG	1-Palmitoyl-2-Oleoyl-sn-Glycero-3-Phospho-rac-1-Glycerol
D-PDMP	D-threo-1-phenyl-2- decanoylamino-3-morpholino-1propanol
DPPC	Dipalmitoylphosphatidylcholine
CHOL	Cholesterol
PtdCho	Phosphatidylcholine
PtdEtn	Phosphatidylethanolamine
PtdSer	Phosphatidylserine
PtdIns	Phosphatidylinositol
PG	Phosphatidylglycerol
PA	Phosphatidic acid
SM	Sphingomyelin
PAF	Platelet activating factor
AD	Alzheimer's disease
NPC	Niemann–Pick type C
DS	Down syndrome
CDP-DAG	Cytidinediphosphate-diacylglycerol
PAMs	Pulmonary alveolar macrophages
CMC	Critical micelle concentration
SDS	Sodium dodecyl sulfate
MLVs	Multilamellar vesicles
LUVs	Large unilamellar vesicles

SUVs	Small unilamellar vesicles
MVBs	Multivesicular bodies
MVEs	Multivesicular endosomes
DNA	Deoxyribonucleic acid
RNA	Ribonucleic acid
PCR	Polymerase chain reaction
LE	Late endosome
VBs	Vesicular bodies
BHK	Baby hamster kidney
DSC	Differential scanning calorimetry
LDL	Low-density lipoprotein
DLS	Dynamic light scattering
TEM	Transmission electron microscopy
FRET	Fluorescence resonance energy transfer
FLIM-FRET	Fluorescent lifetime imaging-FRET
TLC	Thin layer chromatography
PCS	Photon correlation spectroscopy
QELS	Quasi-elastic light scattering
SLS	Static light scattering
ACF	Auto correlation function
NNLS	Non-negative least squares
PMT	Photomultiplier tube
CCDs	Charge coupled devices
Cryo-EM	Cryo-electron microscopy
R _f	Retention factor

ANTS	8-amino-naphthalene-1, 3, 6 trisulfonic acid
DPX	p-xylene- bispyridinium bromide
HEPES	4-(2-hydroxyethyl,-)1-piperazineethanesulfonic acid
EDTA	Ethylenediamine tetraacetic acid

Abstract of Dissertation Presented to the Graduate School
of the University of Florida in Partial Fulfillment of the
Requirements for the Degree of Doctor of Philosophy

BIOPHYSICAL CHARACTERIZATION OF BIS(MONOACYLGLYCERO)PHOSPHATE
(BMP) MODEL LIPID MEMBRANES USING ANALYTICAL TOOLS

By

Janetricks Nanjala Chebukati

December 2009

Chair: Gail E. Fanucci
Major: Chemistry

Bis(monoacylglycero)phosphate (BMP) is a negatively charged phospholipid found in elevated concentrations in the late endosome. BMP has an unusual structure and stereochemistry that are thought to be responsible for important roles in the endosome, including structural integrity, endosome maturation, and lipid/protein sorting and trafficking. The main objective of the work reported in this dissertation was to characterize the morphology and size distribution of BMP model membranes as a function of pH, ionic strength, concentration and lipid composition, using dynamic light scattering (DLS) and transmission electron microscopy (TEM). Dynamic light scattering is a simple, non-invasive particle sizing technique that measures the hydrodynamic diameter of particles or macromolecules suspended in solution based on their interaction with light, whereas TEM provides valuable information on the morphology and sizes of particles.

Results presented in this dissertation demonstrate that BMP forms small, stable, lamellar vesicle structures, and that BMP induces the formation of small vesicles when mixed with typical phosphatidylcholine (POPC) membranes at specific concentrations.

Morphological and size distribution studies on the interaction between BMP and ganglioside GM1 reveal that GM1 mixes with BMP at specific concentrations to form small (~100 nm) spherical shaped vesicles with a narrow size distribution. This specific mixture of GM1 with BMP may be important for *in vivo* vesicular trafficking and lipid sorting in the endosome/lysosome pathways.

Finally, when ganglioside GM1, cholesterol (CHOL) and BMP lipids are incorporated in typical POPC dispersions at specific concentrations, they form vesicles with different morphology and size distributions. Taken together, results from these investigations give a further understanding to the role that BMP, GM1 and cholesterol may play in the late endosome, and allow for possible future studies in using BMP vesicles for drug delivery applications.

CHAPTER 1
INTRODUCTION TO LIPIDS

Biological Lipids

Description and Classification

Biological lipids are a diverse group of chemical compounds, commonly defined by their insolubility in water due to their nonpolar chemical composition (1) and their solubility in nonpolar organic solvents such as acetone, ether, chloroform and benzene (2). Eukaryotic lipids are generally classified according to their biological functions as illustrated in Figure 1-1.

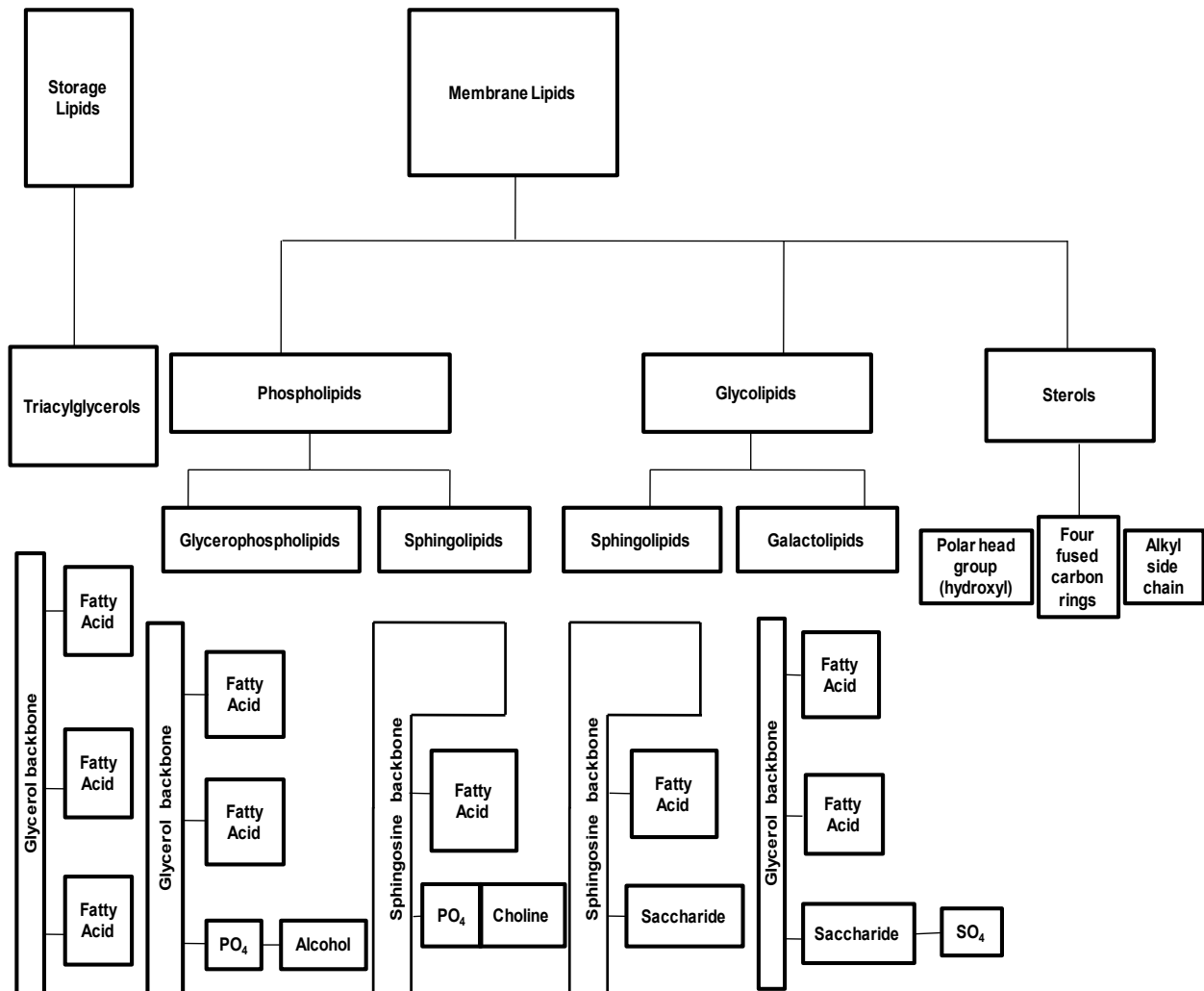


Figure 1-1. General classification of eukaryotic lipids. Modified from Ref. (3).

Storage lipids, composed of fats and oils, are the principal stored forms of energy in most organisms (3). Chemically, fats and oils are triacylglycerols that are also known as simple lipids (1). Fats are characterized by being solid at room temperature (20° C), whereas oils are liquid at room temperature (1). The structure of triacylglycerols (Figure 1-2B) consists of a glycerol backbone that has three fatty acid molecules attached to its hydroxyl groups through ester linkages (3).

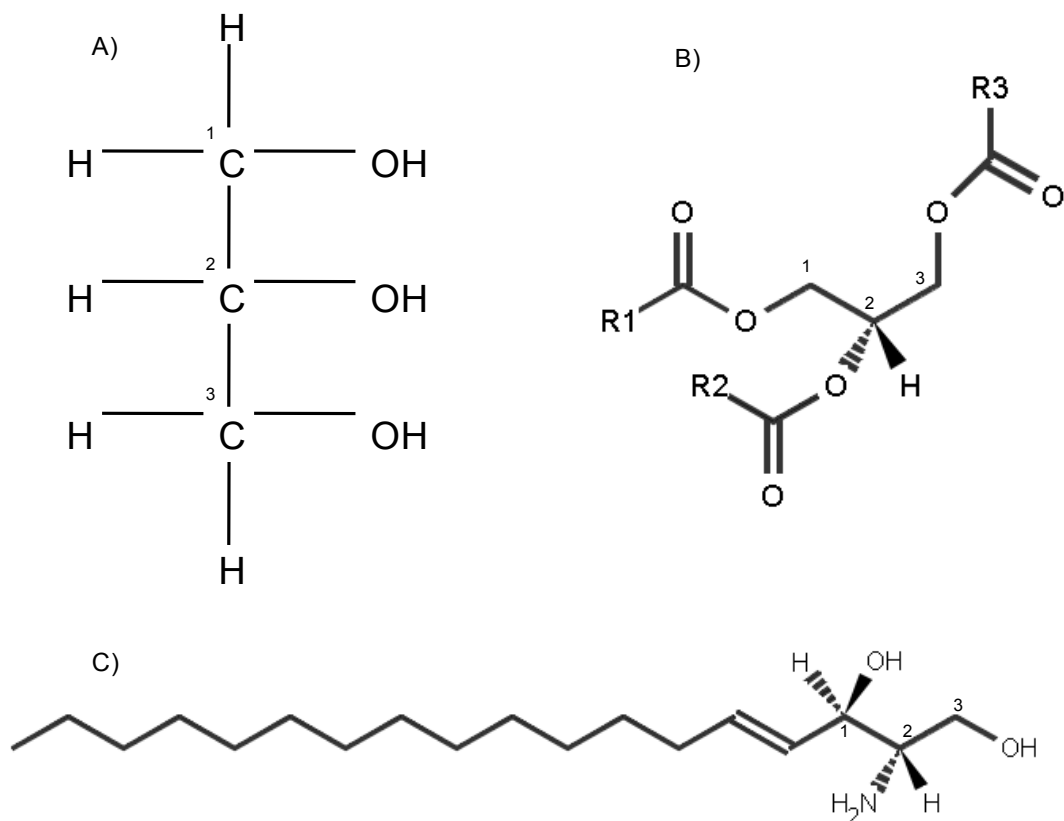


Figure 1-2. Chemical structures of A) glycerol backbone, B) triacylglycerol and C) sphingosine backbone.

Using the stereochemical numbering (sn) system, the fatty acid molecules may be designated as sn1-, sn2- and sn3- (Figure 1-2B). In most triacylglycerols, the fatty acids in the sn1 and sn3-positions are different, resulting in two possible enantiomers with similar fatty acid profiles, both with the same fatty acid located in the sn2-position (4).

Generally, variations in the saturation and hydrocarbon chain lengths of the fatty acids result in different forms of triglycerols with different physical properties such as fluidity and melting point (1).

The most fundamental structure of the biological membranes of the cell is the lipid bilayer (a double layer of lipids), which is formed from membrane lipids that act as a barrier to the passage of polar molecules and ions in and out of the cell (3), hence membrane lipids are another major class of lipids. Membrane lipids are also referred to as structural lipids and are amphipathic in nature, with one end of the molecule being hydrophobic while the other end is hydrophilic (1, 3). When membrane lipids are dispersed in water, they spontaneously self-aggregate into bilayer or micellar structures as a result of the hydrophobic effect, a phenomenon that arises due to the energetically unfavorable contact between the hydrocarbon and water molecules, hence the lipid acyl chains are directed inward towards each other and the polar lipid headgroups are exposed to water (5).

Membrane lipids obtained from eukaryotic cells can belong to one of the following general groups: glycerophospholipids, in which the hydrophobic regions are composed of two fatty acid chains bonded to a glycerol backbone, galactolipids, or sulfolipids, which also contain two fatty acids esterified to a glycerol backbone but lack the characteristic phosphate head group found in phospholipids. The other groups of eukaryotic membrane lipids are the sphingolipids, in which a fatty acid chain is joined to a sphingosine backbone and an amine or a saccharide head group and sterols, compounds that are characterized by a rigid system of four fused hydrocarbon rings (2, 3, 6, 7).

Functional Roles of Lipids in the Cell

Due to their lipid component, biological membranes are flexible self-sealing boundaries that form the permeability barrier for cells and organelles, and provide the means to compartmentalize functions in the cell (3). As a support for both integral and peripheral membrane processes, the physical properties of the lipid component directly affect these processes in a complex manner; hence each specialized membrane of a cell has a unique structure, lipid and protein composition and function (3, 6).

Additionally, within each membrane there exist microdomains such as lipid rafts, lipid domains and organizations of membrane-associated complexes with their own unique lipid composition. In essence, defining lipid function is challenging due to the diversity of chemical and physical properties of lipids and the fact that each lipid type potentially is involved at various levels of cellular function (6).

Generally, lipids serve three main purposes. First, because of their relatively reduced chemical state, lipids are used for energy storage, principally as triacylglycerol and steryl esters, in lipid droplets. The reduced state of the carbon atoms of the fatty acids allows for the enhanced oxidation of triacylglycerols, yielding more than twice as much energy as the oxidation of carbohydrates (3). Triacylglycerol and steryl esters function primarily as anhydrous reservoirs for the efficient storage of caloric reserves and as caches of fatty acid and sterol components that are needed for membrane biogenesis (8, 9).

Secondly, the matrix of cellular membranes is formed by polar lipids, which consist of a hydrophobic and a hydrophilic portion. The tendency of the hydrophobic moieties to self-associate and the ability of the hydrophilic moieties to interact with aqueous environments and with each other are the physical bases for the spontaneous formation

of membranes (9). It is thought that this unique chemical property of amphipathic lipids may have enabled the first cells to segregate their internal constituents from the external environment, and is the same principle that enables the cell to produce discrete organelles (8, 9). Cell membrane compartmentalization enables segregation of specific chemical reactions for the purposes of increased biochemical efficiency and restricted dissemination of reaction products. Lipids also provide membranes with the potential for budding, tubulation, fission and fusion, characteristics that are essential for cell division, biological reproduction and intracellular membrane trafficking (9, 10).

Although storage lipids and membrane lipids are major cellular components, with membrane lipids making up 5-10% of the dry mass of most cells, and storage lipids more than 80% of the mass of an adipocyte, a third group of lipids are in much smaller amounts but have active roles in the metabolic traffic as metabolites and messengers. Some of these lipids may serve as potent signals, such as hormones carried in the blood from one tissue to another or as intracellular messengers generated in response to an extracellular signal (1, 3). For instance, phosphatidylinositol and its phosphorylated derivatives act at several levels to regulate cell structure and metabolism (3). Phosphatidylinositol bisphosphate is hydrolyzed by phospholipase C to yield two intracellular messengers, diacylglycerol and 1, 4, 5 triphosphate (3), as illustrated in Figure 1-3.

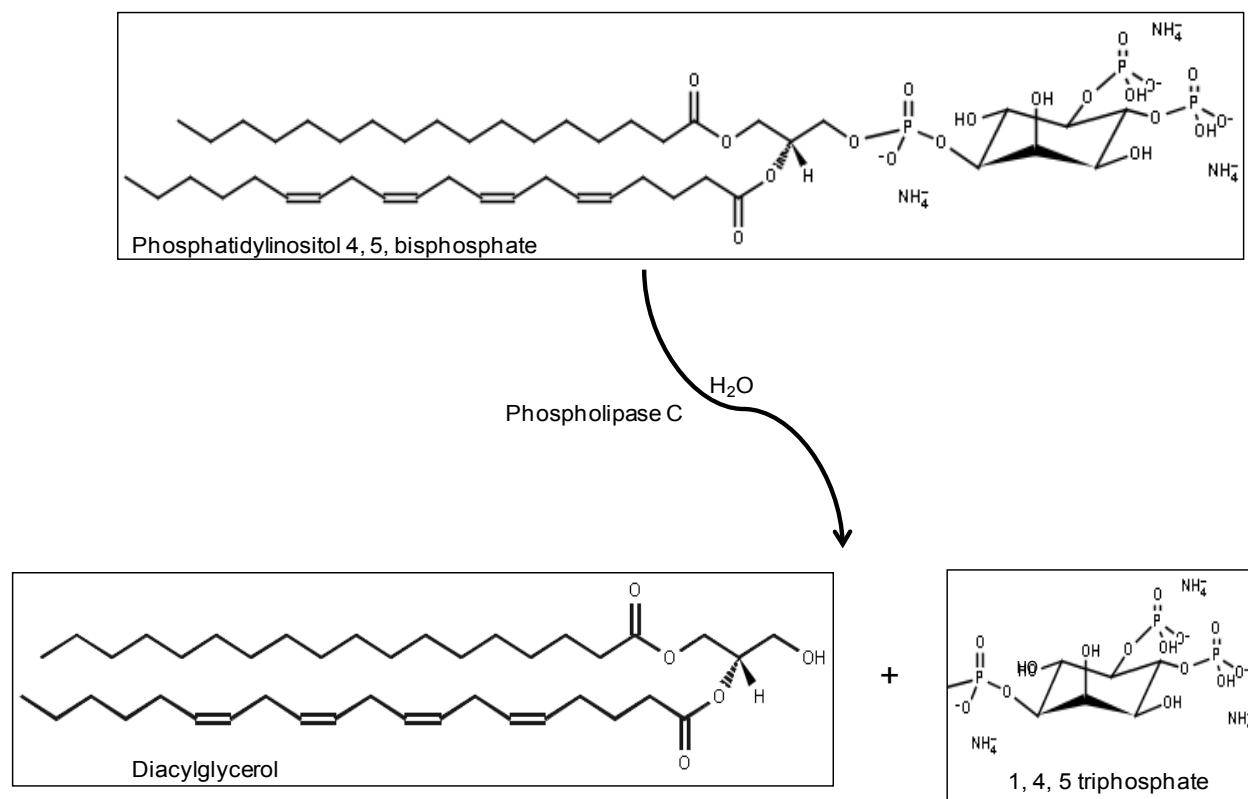


Figure 1-3. Enzymatic hydrolysis of phosphatidylinositol 4, 5, bisphosphate to diacylglycerol and 1, 4, 5 triphosphate.

Other lipids may function as enzyme cofactors in electron-transfer reactions in mitochondria or in the transfer of sugar moieties in a variety of glycosylation reactions. For instance dolichols (which are isoprenoid alcohols, Figure 1-4A), are known to activate and anchor sugars on cellular membranes for use in the synthesis of certain complex carbohydrates, glycolipids and glycoproteins (3).

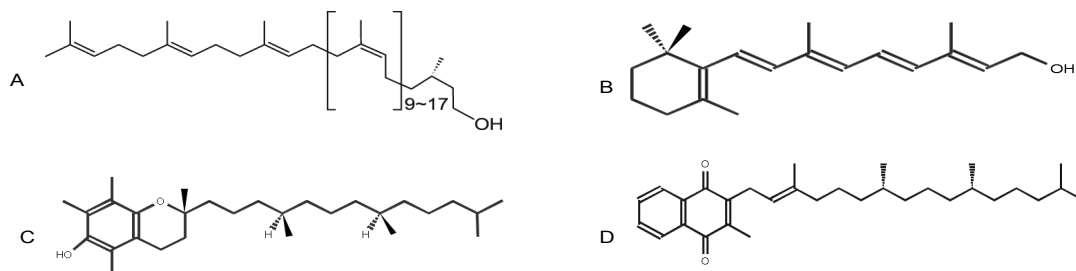


Figure 1-4. Chemical structures of A) dolichol, B) vitamin A, C) vitamin E and D) vitamin K.

Another group consists of lipids with a system of conjugated double bonds that may function as pigments that absorb visible light. For example, vitamin A (Figure 1-4B) furnishes the visual pigment of the vertebrate eye and is a regulator of gene expression during epithelial cell growth, Vitamin E (Figure 1-4C) protects membrane lipids from oxidative damage and vitamin K (Figure 1-4D) is essential in the blood-clotting process (1, 2, 6, 7).

Finally, lipids can act as first and second messengers in signal transduction and molecular recognition processes. The degradation of amphipathic lipids allows for bipartite signalling phenomena, which can be transmitted within a membrane by hydrophobic portions of the molecule and also propagated through the cytosol by soluble (polar) portions of the molecule. In addition, some lipids function to define membrane domains, which recruit proteins from the cytosol that subsequently organize secondary signalling or effector complexes (6, 9, 11). For instance, phosphoinositols (PIs) are important in cell signalling and vesicle formation, both of which are key events in neurotransmission and in the transit of vesicles from the endoplasmic reticulum to Golgi (12, 13).

All biological membranes consist of a lipid bilayer to which proteins and carbohydrates may be associated or covalently linked. Evidently, the roles of membrane lipids in cells have evolved from a simple physical barrier to a critical component in cell signaling and other cellular processes (13). It has long been established that lipids provide the physical support of organelle membranes, acting as a barrier for water-soluble molecules and as a solvent for the hydrophobic domains of membrane proteins. By contributing to the intrinsic properties of membranes, such as thickness, asymmetry

and curvature, lipids can potentially regulate protein movement and distribution among other functions (14).

The most abundant group of structural lipids in eukaryotic membranes are the glycerophospholipids, which include but are not limited to phosphatidylcholine (PtdCho), phosphatidylethanolamine (PtdEtn), phosphatidylserine (PtdSer), phosphatidylinositol (PtdIns) and phosphatidylglycerol (PG) (9). The structural differences in the headgroups of these glycerophospholipids are further illustrated in Figure 1-6 and Table 1-1. Because glycerophospholipids were the basis of the work covered in this dissertation, they are discussed in detail in the following subsection.

Glycerophospholipids

Typical Structure and Anatomy

Glycerophospholipids (also called phosphoglycerides) are the most common class of naturally occurring phospholipids; phospholipids are lipids with phosphate-containing head groups (15). These compounds are derivatives of sn-glycero-3-phosphoric acid (2). The stereospecific numbering (sn) system is used in phospholipid nomenclature. The glycerol is drawn in a Fischer projection with the β -hydroxyl on the left and the sn-1 position is then located at the top of this projection, while the sn-3 position is located at the bottom (the prefix sn- is used before the name) as illustrated in Figure 1-5.

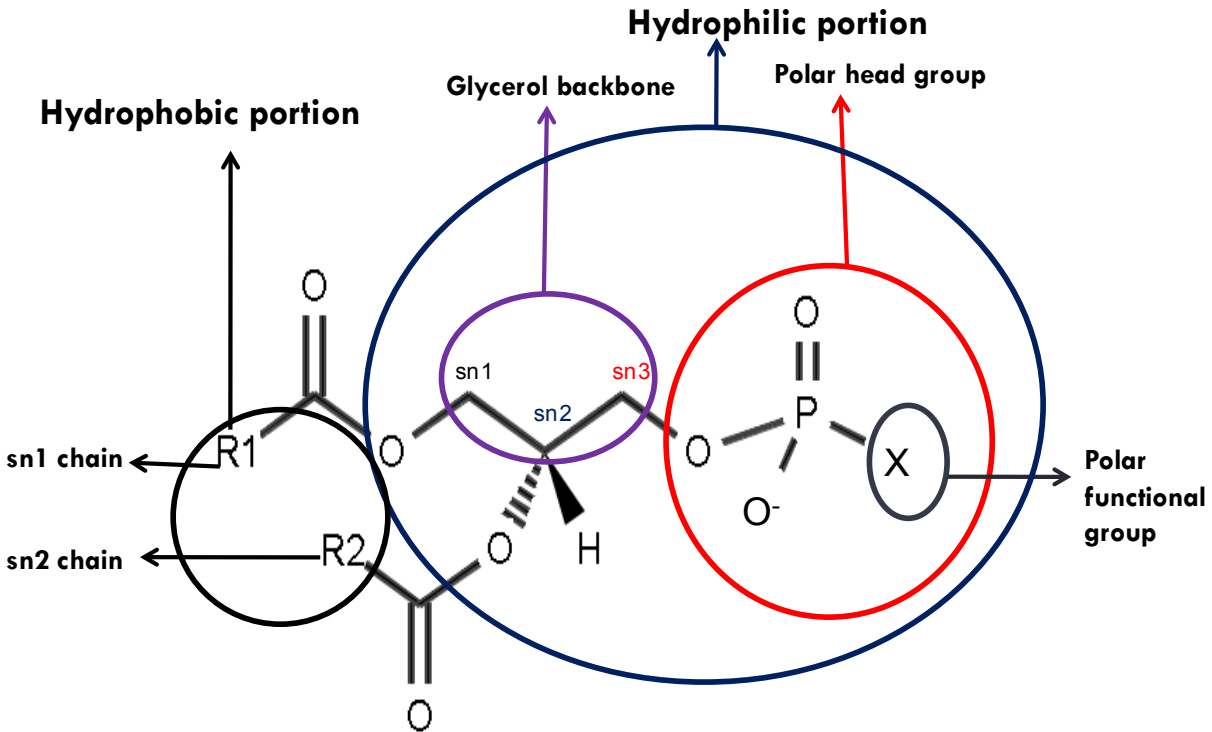


Figure 1-5. General structural anatomy of glycerophospholipids.

Figure 1-5 shows the general anatomy of glycerophospholipids. One of the glycerol hydroxyl groups (at sn-3 position) is linked to the polar phosphate-containing head group, while the other two hydroxyl groups (at sn-1 and sn-2 positions) are linked to hydrophobic acyl chains R1 and R2 (8). The hydrophobic portion contains saturated or cis-unsaturated fatty acyl chains of varying lengths (9). In all naturally occurring glycerophospholipids, the polar group is attached to the sn-3 position of the glycerol moiety except in the glycerol-based lipids of archeobacteria (2). The phosphate group is then esterified to one of several functional groups. The functional group is designated as X in Figure 1-5 and Table 1-1; replacing the X with a specific polar functional group results in different glycerophospholipids, which explains the diversity in physicochemical properties and roles of membrane lipids (7).

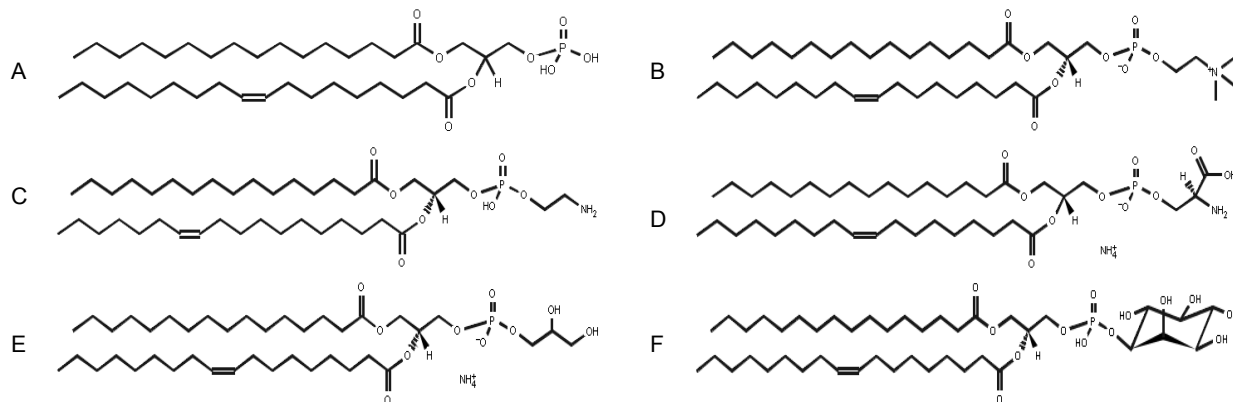


Figure 1-6. Chemical structures of common classes of glycerophospholipids. A) Phosphatidic acid. B) Phosphatidylcholine. C) Phosphatidylethanolamine. D) Phosphatidylserine. E) Phosphatidylglycerol. F) Phosphatidylinositol.

Table 1-1. Common classes of glycerophospholipids.

Name of X	Chemical Formula of X	Name of Phospholipid
Hydroxyl	-OH	Phosphatidic acid
Choline	$-\text{CH}_2 - \text{CH}_2 - \text{N}^+(\text{CH}_3)_3$	Phosphatidylcholine
Ethanolamine	$-\text{CH}_2 - \text{CH}_2 - \text{NH}_3^+$	Phosphatidylethanolamine
Serine	$-\text{CH}_2 - \text{CH}(\text{COO}^-) - \text{NH}_3^+$	Phosphatidylserine
Glycerol	$-\text{CH}_2 - \text{CHOH} - \text{CH}_2\text{OH}$	Phosphatidylglycerol
Inositol	$\text{C}_6\text{H}_6(\text{OH})_6$	Phosphatidylinositol

Figure 1-6 and Table 1-1 illustrate the common classes of glycerophospholipids. The name of the polar functional group attached to the phosphate head group lends a further distinction to the nomenclature of the phospholipids. For instance, in the absence of any alcohol or functional group, the phospholipid is called phosphatidic acid (PA, Figure 1-6A). Phosphatidate, the ionized form of PA, is not found in large quantities in cell membranes, as it is largely a biosynthetic intermediate. If the alcohol esterified to the phosphate is choline or ethanolamine, the phospholipid is called phosphatidylcholine (or lecithin) or phosphatidylethanolamine (or cephalin) respectively. Phosphatidylcholine (PC, Figure 1-6B) and phosphatidylethanolamine (PE, Figure 1-6C) are among the most common of cell membrane phospholipids, contributing prominently to the phospholipid bilayers found in most cellular membranes. PE contains a free

amino group which can be stripped of a proton at high pH (9-10) to give an uncharged, primary amine (7, 8).

Other alcohols that may be esterified to the phosphate include the L-amino acid serine, and sugars such as glycerol and inositol, resulting in the phospholipids phosphatidylserine (PS, Figure 1-6D), phosphatidylglycerol (PG, Figure 1-6E), and phosphatidylinositol (PI, Figure 1-6F), respectively. All of these phospholipids contain only one phosphate.

“Unusual” Phospholipids

A number of special glycerophospholipids vary from the rest of the diacylglycerophospholipids in terms of their chemical structure and functionality.

Ether-phospholipids

One such unusual group of glycerophospholipids are the ether-phospholipids, a special class of phospholipids that are characterized by the presence of an ether bond at the sn-1 position of the glycerol backbone instead of an ester bond like in the diacylglycerophospholipids (16). Some ether-phospholipids may be saturated as in the alkyl ether lipids exhibited by the platelet-activating factor (PAF, Figure 1-7A), or may contain a double bond between C-1 and C-2 (3), adjacent to the ether bond, forming a vinyl-ether linkage as in lipids that are referred to as plasmalogens (Figure 1-7B) (17).

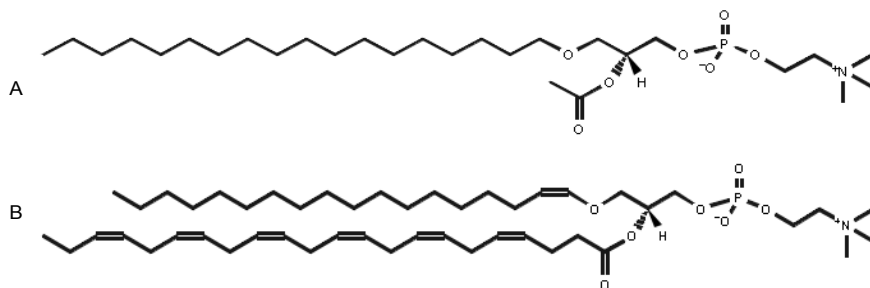


Figure 1-7. Chemical structures of representative ether-phospholipids. A) Platelet activating factor (PAF). B) Plasmalogen.

The hydrophobic acyl chain at the sn-1 position in plasmalogens consists of either C16:0 (palmitic acid), C18:0 (stearic acid) or C18:1 (oleic acid) carbon chains, whereas the sn-2 position is occupied by polyunsaturated fatty acids, and the head group is either an ethanolamine or a choline (16). Ether-phospholipids can be enriched in various tissues or even different cell types within one tissue. For instance, vertebrate heart tissue is uniquely enriched in ether lipids, where about half of the heart phospholipids are plasmalogens (3). The highest content of ethanolamine plasmalogens (PE-plasmalogen) is found in brain myelin, whereas heart muscle has a higher content of choline plasmalogens (PC-plasmalogen). Moderate amounts of plasmalogens are also found in kidney, skeletal muscle, spleen and blood cells (16).

Although the functional roles of plasmalogens are not yet fully understood, past studies have implicated plasmalogens as antioxidants, a function attributed to the presence of a vinyl–ether bond that makes plasmalogens more susceptible to oxidative attack compared to their 1-acyl analogues (18). Plasmalogens are also mediators of membrane dynamics, in which the vinyl–ether bond may affect the hydrophobic–hydrophilic interface region of phospholipid aggregates(19). Plasmalogens have been implicated in various disease forms including the Zellweger syndrome, a lethal autosomal recessive disorder in which peroxisome biogenesis is impaired, leading to a generalized loss of peroxisomal functions (20), Alzheimer’s disease (AD) (21), Niemann–Pick type C (NPC) lipid storage disorder (22, 23) and Down syndrome (DS) (24).

Additionally, the platelet-activating factor (PAF) is a potent molecular signal that is released from leukocytes called basophils and is found to stimulate platelet aggregation

and the release of serotonin, a vasoconstrictor, from platelets (3). PAF also has a variety of effects on the liver, smooth muscle, heart, uterine and lung tissues and as such plays an important role in inflammation and allergic response (25, 26).

Cardiolipin (CL)

Cardiolipin is another unique dimeric glycerophospholipid in which two phosphatidyl moieties are linked by a glycerol backbone (27, 28). Cardiolipin was first isolated from beef heart in the early 1940s (29), hence its name. This lipid is found exclusively in bacterial and mitochondrial membranes, which function in the generation of an electrochemical potential for substrate transport and ATP synthesis (27). Whereas cardiolipin is most abundant in mammalian hearts, with current commercial preparations of cardiolipin being derived from heart tissue, it is also found in all mammalian tissues throughout the eukaryotic kingdom that have mitochondria (27).

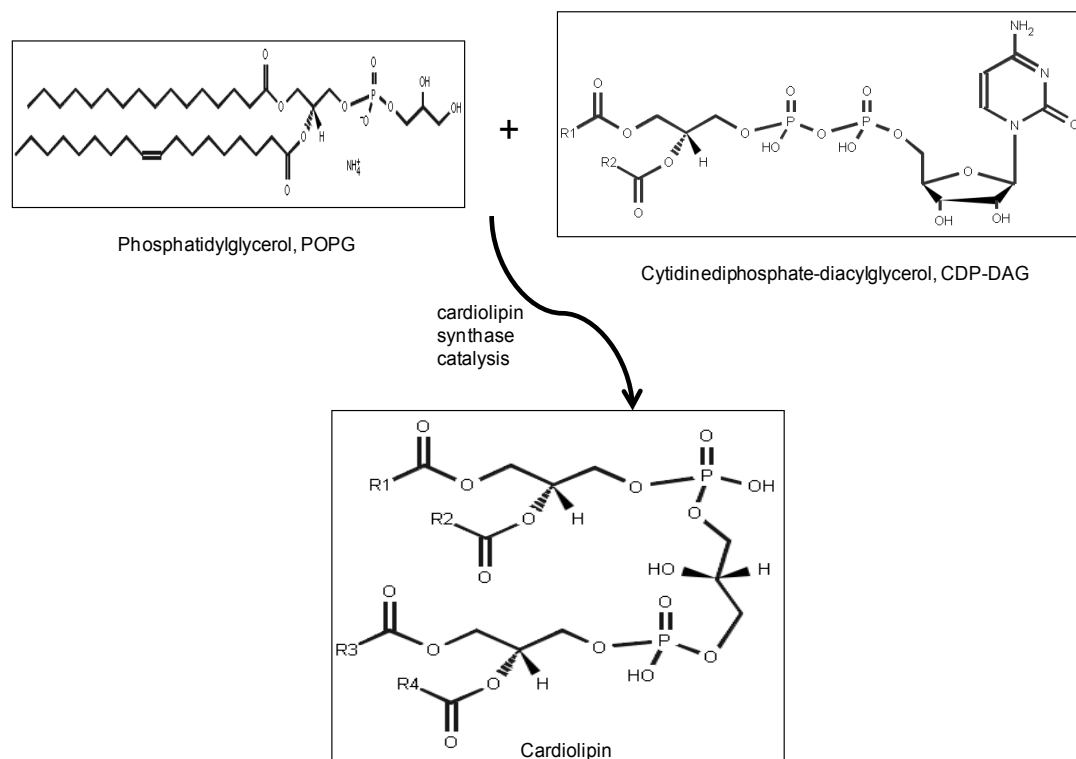


Figure 1-8. Enzyme catalyzed biosynthesis of cardiolipin from POPG and CDP-DAG.

The chemical structure of cardiolipin (Figure 1-8) differs from that of most membrane phospholipids in that it exhibits a double glycerophosphate backbone and four fatty acyl side chains (29). The biosynthesis of cardiolipin in eukaryotic cells involves phosphatidylglycerol (PG) and cytidinediphosphate-diacylglycerol (CDP-DAG)(Figure 1-8), catalyzed by cardiolipin synthase on the inner face of the inner mitochondrial membranes (30). When treated with phospholipase D, cardiolipin yields two phospholipid products; phosphatidic acid and phosphatidylglycerol (31) and conversely, cardiolipin can be chemically synthesized from phosphatidic acid and phosphatidylglycerol (32). Cardiolipin from mammalian tissues exhibits high specificity in the fatty acyl chain composition, being predominantly comprised of 18-carbon unsaturated acyl chains, the vast majority of which are linoleic acid (18:2) (33, 34).

The ability of cardiolipin to mediate the optimal function of numerous mitochondrial proteins and processes is attributed to its unique ability to interact with proteins and its role in maintaining inner membrane fluidity and osmotic stability (27, 35) . Cardiolipin is reportedly required for the proper structure and activity of several mitochondrial respiratory chain complexes involved in the oxidative generation of ATP (34, 36), and has been proposed to participate directly in proton conduction through cytochrome bc₁ (37) and prevent osmotic instability and uncoupling at higher respiration rates (38) . Other important cardiolipin roles include a regulatory role in cytochrome c release (39, 40), which triggers some of the events in apoptosis (41), essential roles in mitochondrial biogenesis (27) and the stabilization of respiratory enzyme supercomplexes (42, 43) .

Bis(monoacylglycero)phosphate (BMP)

Bis(monoacylglycero)phosphate (BMP) is a characteristic lipid of the endocytic degradative pathway that is found in the late endosome luminal membranes in

concentrations of approximately 15 mole percent (44). BMP was first isolated from pulmonary alveolar macrophages (PAMs) of lung obtained from pig and rabbit by Body and Gray (45). The chemical structure of BMP (Figure 1-9A) differs from that of other glycerophospholipids, in that BMP contains two glycerol components, each with a single acyl chain (2, 8, 46). Additionally, BMP has an sn-1-glycerophospho-sn-1'-glycerol (sn1:sn1') stereoconfiguration that differs from the typical sn-3-glycerophosphate stereoconfiguration found in other glycerophospholipids as illustrated by the red circles in Figure 1-9B (47-50).

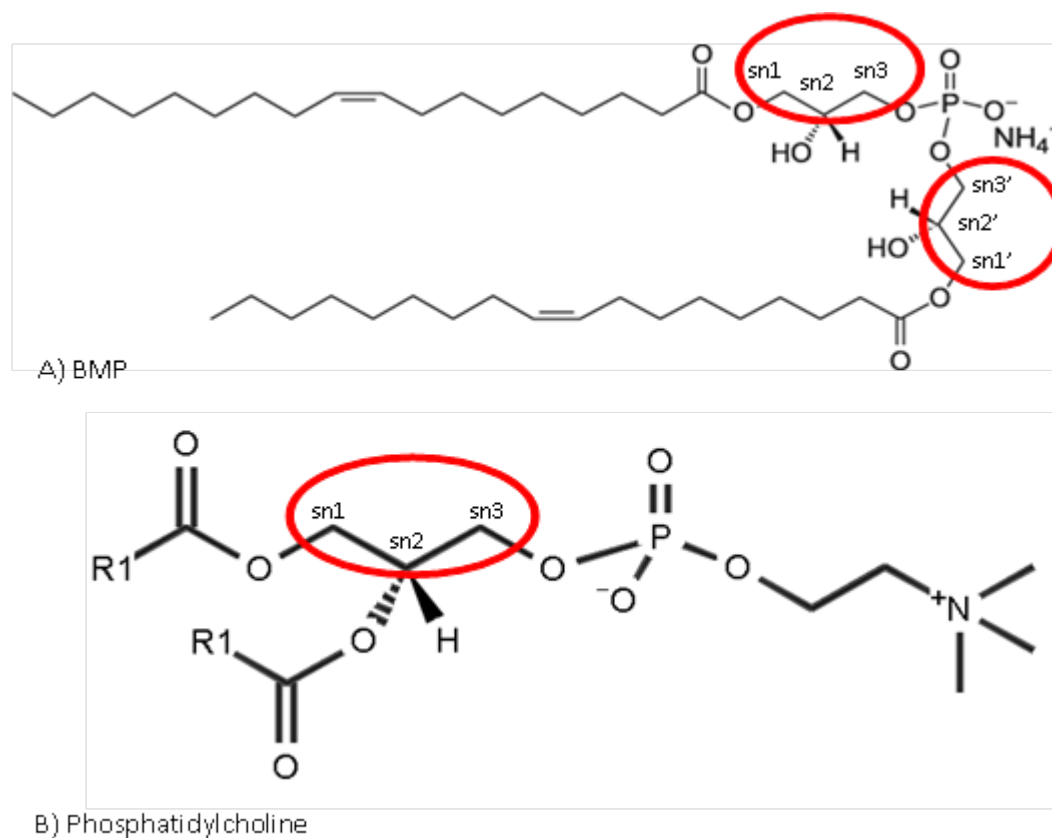


Figure 1-9. Chemical structures of A) BMP (sn-1, sn-1' stereoconfiguration) and B) phosphatidylcholine (sn-3 glycerophosphate stereoconfiguration).

Because studies of BMP form the bulk of the work presented in this dissertation, it will be discussed in more detail later on in the introduction.

Phospholipid Polymorphism

Phospholipids are amphipathic in nature, consisting of a hydrophobic portion (the hydrocarbon chains), and a hydrophilic portion (the polar head group). This property allows phospholipids to establish a hydrophobic barrier to permeability when in close proximity to an aqueous medium. To maintain the permeability barrier, lipids associate in structures that sequester the hydrocarbon portions in hydrophobic regions away from the aqueous medium so that only the polar groups then encounter the polar phase. Through this arrangement, the phospholipid molecule is able to satisfy the hydrophobic effect, which is the dominant driving force behind membrane lipid assembly (2, 7).

Membrane lipids are polymorphic, which implies that they can exist in a variety of different kinds of organized structures or phases especially when hydrated in water (2). The structural organization that a polar lipid assumes in water is determined by its concentration and the law of opposing forces; the hydrophobic forces driving self association of hydrophobic domains versus steric and ionic repulsive forces of the closely associated polar domains opposing self-association (6). At low concentrations, amphipathic molecules exist as monomers in solution, but as the concentration increases, the molecule's stability in solution as a monomer decreases until the unfavorable repulsive forces of polar domains are outweighed by the favorable self-association of the hydrophobic domains. Eventually, any further increase in concentration results in the formation of increasing amounts of self-associated monomers in equilibrium with a constant amount of free lipid monomer. This state of self-association and the remaining constant free lipid monomer is referred to as the critical micelle concentration (CMC) (6, 51).

Due to the increased hydrophobic effect, a larger hydrophobic domain results in a lower critical micelle concentration, while the larger the polar domain due to either the size of the neutral domains or charge repulsion for like-charged ionic domains, the higher the critical micelle concentration. This is attributed to the unfavorable steric hindrance or charge repulsion in bringing these domains into close proximity (6). Below the CMC, the lipid exists solely as monomers in solution, and above the CMC, the monomer concentration remains constant and is equal to the CMC (5).

Self-assembly, organization and phase behavior

Pure phospholipids are capable of undergoing transformations from one shape or morphology to another, resulting in what is termed as lipid polymorphism, which is the ability of lipids to take on structures of different shapes (52). Lipid phases can be divided into two general types: normal and inverted phases. Normal phases are those in which the polar moiety of the lipid faces outward from the lipid m, whereas the nonpolar portion of the molecule makes up the structure core. In inverted phases, the polar groups face inward and the nonpolar portion occupies the exterior of the structure (53).

Some of the factors that determine the type of phase or morphology formed by lipids include lipid structure, hydration and temperature (53). Given precise conditions and the nature of the lipids, several types of lipid aggregates or shapes can form when amphipathic lipids are hydrated in water or aqueous media (3), including micelles, inverted micelles, lipid bilayers (lamellar phase), bicelles, normal or inverse hexagonal phases and lipid vesicles or liposomes as illustrated in Figure 1-10.

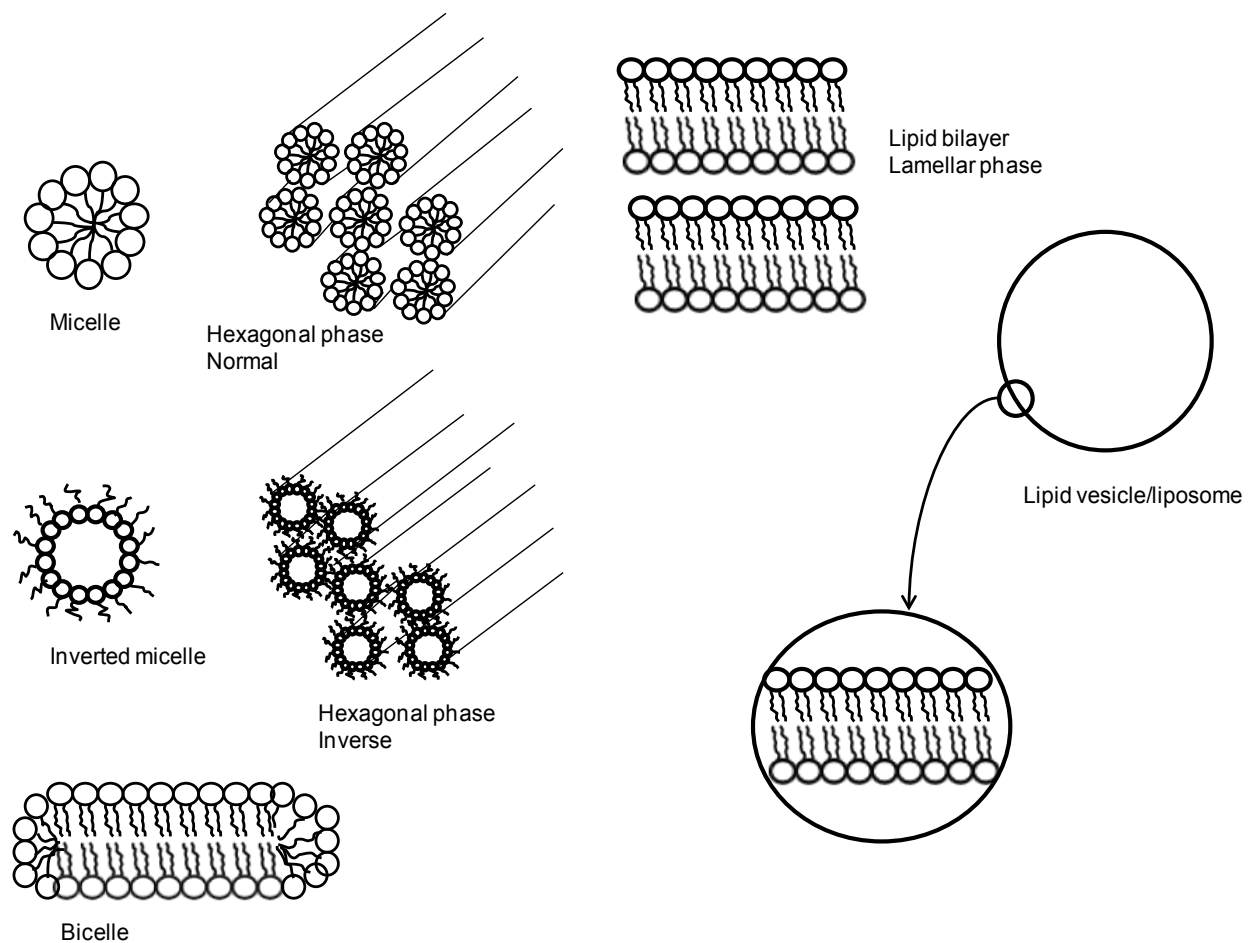


Figure 1-10. Different shapes of lipid polymorphisms in water (or aqueous environment).

Micelles, lipid bilayers and vesicles (liposomes) are the structures most commonly formed by most phospholipids in water; hence a lot of studies on the applications of these model systems have been carried out. Micelles (Figure 1-10) are spherical structures that contain about a dozen to a few thousand amphipathic molecules (3) that are arranged in water, with their hydrophobic regions aggregated in the interior, where water is excluded, and their hydrophilic head groups at the surface in contact with water. Micelle formation is generally favored when the cross-sectional area of the head group is greater than that of the acyl side chain(s). This is mostly the case in molecules such as free fatty acids, lysophospholipids (phospholipids lacking one fatty acid),

phospholipids with short alkyl chains (eight or fewer carbons) (3, 6) and detergents such as sodium dodecyl sulfate (SDS) . The overall structure of a micelle reflects the optimal packing of amphipathic molecules at an energy minimum by balancing the attractive force of the hydrophobic effect and the repulsive force of close head group association (3). The CMC for most lysophospholipids and detergents is in the micromolar to millimolar range (6).

Under physiologically relevant conditions, most membrane lipids exist as lipid bilayers (2), as illustrated in Figure 1-10, in which two lipid monolayers or leaflets form a two-dimensional sheet. Phospholipids with long alkyl chains do not form micelles but organize into bilayer structures, which allow tight packing of adjacent side chains with the maximum exclusion of water from the hydrophobic domain. Bilayer formation occurs most readily when the cross-sectional areas of the head groups and the acyl side chains are similar, which is the case in glycerophospholipids and sphingolipids (3). In living cells, phospholipids are not found free as monomers in solution but are organized into either membrane bilayers or protein complexes (6).

The bilayer sheet is relatively unstable because the hydrophobic regions at its edge are transiently in contact with water, hence it spontaneously folds back on itself to form a hollow sphere referred to as a vesicle or liposome (3), as shown in Figure 1-10. Formation of vesicles enables bilayers to lose their hydrophobic edge regions, achieving maximal stability in their aqueous environment. The lipid vesicles enclose water, creating a separate aqueous compartment (3), and this property can allow vesicles to be studied for various encapsulation applications, including use as drug-delivery vehicles.

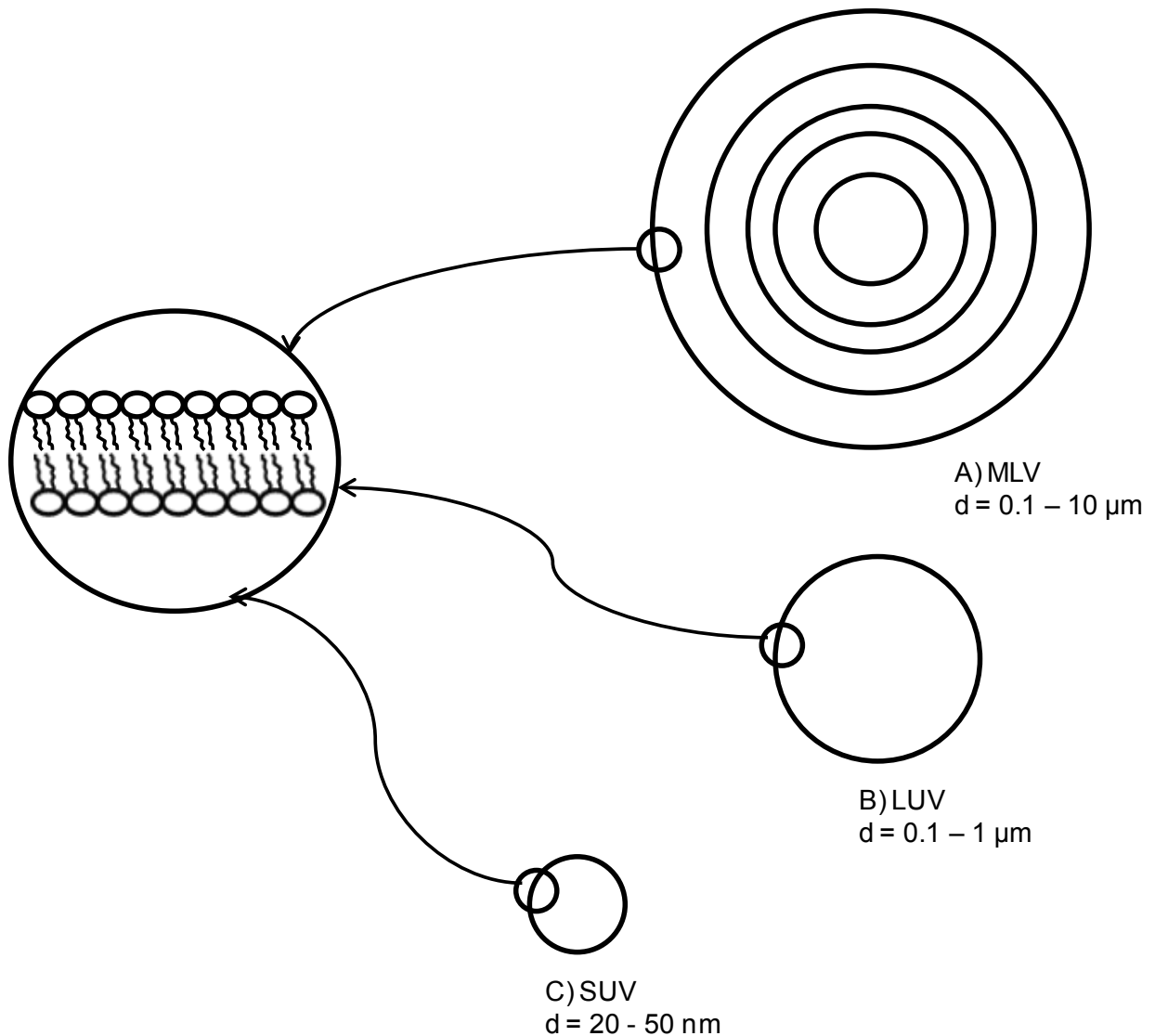


Figure 1-11. Morphology of different sizes/types of lipid vesicles (liposomes). A) Multilamellar vesicles (MLVs). B) Large unilamellar vesicles (LUVs). C) Small unilamellar vesicles (SUVs).

Liposomes are typically spherical in shape and may contain a single layer or multiple layers of amphiphilic polymolecular membranes. Liposomes that contain only a single bilayer membrane are called either small unilamellar vesicles (SUVs, which are less than 50 nm in diameter, Figure 1-11C) or large unilamellar vesicles (LUVs, 100 – 1000 nm in diameter, Figure 1-11B). When liposomes contain more than a single bilayer membrane they are referred to as multilamellar vesicles (MLVs, Figure 1-11A) if all

layers are concentric, or multivesicular bodies (MVBs), when a number of randomly sized vesicles are enclosed in the interior of another larger vesicle. MLVs can be obtained through lipid hydration in an aqueous solution of water or buffer. Lipid vesicles that are larger than 300 nm will scatter light sufficiently enough so as to be seen by the naked eye and such samples will have a cloudy white appearance (54).

Phospholipid membrane systems have complex phase behaviors (54), existing either in the lamellar liquid-crystalline or in the lamellar gel phase (2). Fully hydrated bilayers composed of single phospholipid species undergo a well-defined thermotropic phase transition in which the lipid chains change from the ordered or gel state to the fluid or liquid-crystalline state. The fluid phase is conventionally designated $L\alpha$, while the gel phase is designated $L\beta$. An intermediate phase, $L\beta'$ in which the bilayer is rippled, is found in the gel phase of certain phospholipids (5). Because most membrane lipids undergo this kind of phase transition, it is one of the most intensively studied lipid phase transitions. During this phase transition, a relatively ordered gel-state bilayer, in which the hydrocarbon chains exist predominantly in their rigid, extended, all-trans conformation, is converted to a relatively disordered liquid-crystalline bilayer, in which the hydrocarbon chains contain a number of gauche conformers and the lipid molecules exhibit greatly increased rates of intra- and intermolecular motion (2).

Thermodynamically, the gel to liquid-crystalline phase transition occurs when the entropic reduction in free energy arising from chain isomerism counterbalances the decrease in bilayer cohesive energy arising from the lateral expansion and from the energy cost of creating gauche conformers in the hydrocarbon chains (2, 8). Gel to liquid-crystalline phase transitions can be induced by changes in temperature and

hydration or changes in pressure and in the ionic strength or pH of the aqueous phase (2, 7).

Another important parameter for liposomal systems is the gel to liquid-crystalline transition temperature T_m , at which the bilayer loses much of its ordered packing structure due to a “melting” of the hydrocarbon chains. Ideally, longer hydrocarbon chain lengths translate into higher phase transition temperatures (54). Notably, most natural phospholipids contain hydrocarbon chains that are asymmetric, where the fatty acid chains may differ in length. The degree of fatty acid unsaturation in the hydrocarbon chain also influences the phase transition, and the T_m increases with increasing saturation (2).

Strong head group interactions may increase the phase transition temperature as well. Consequently, the phase transition behavior of liposomes with more than one lipid component can be quite complex. For instance, cholesterol is often added to liposomes to improve their in vivo and in vitro stability since it provides the membrane with rigidity by changing interactions between both the polar head groups and the hydrocarbon chain and a decrease in both T_m and the transition enthalpy is observed when cholesterol is added (2, 7, 54).

Lipid vesicles (liposomes) as membrane models

Liposomes, also known as lipid vesicles, are spherical, closed structures made of curved lipid bilayers that were first investigated in the early 1960s (55). Liposomes are predominantly composed of amphiphilic molecules such as phospholipids. Due to their amphipathic character, phospholipids have a strong tendency in the presence of aqueous solutions (mostly water) to aggregate spontaneously to ordered, lamellar, bilayer structures (56).

Because liposomes are highly versatile structures, they have been utilized for research involving both pharmaceutical and analytical applications. For instance, phospholipid mixtures with different polar headgroups can be functionalized for conjugation or to reduce liposome aggregation and phospholipids with hydrophobic regions of varying chain length and degrees of saturation can be used to modify the properties of the resulting liposomes (57). For example, cholesterol is often included with membrane phospholipids to reduce the membrane permeability towards encapsulated materials (57).

The structure of lipid vesicles mimics that of the cell membranes, hence vesicles can be utilized as a more easily characterized vessel for studying interactions between membrane lipids and biomolecules such as DNA and proteins; permeability of ions and drugs (57, 58); and for elucidating the mechanism of action of pesticides and antibiotics on target organisms (59). According to literature, liposomes have been used as models in several studies for estimating the partitioning of drugs into cells by surface plasmon resonance (60) and chromatography (61).

Biological molecules may be associated with liposomes in several established ways; encapsulation within the aqueous inner cavity of the liposome (62), partitioning within the lipid tails of the bilayer (63), or covalent and electrostatic interactions with the polar head-groups of the lipids. Surface modification of liposomes can be achieved through the proper choice of lipids that allow conjugation to a variety of biorecognition molecules, such as phosphatidylethanolamine (PE) (64). Other functional groups that can be used for surface modification include a carboxy-group (64-67), a maleimide

group (68), a protected disulfide group (57) and a hydroxyl group, using cholesterol or polyethylene glycol derivatives (69).

Heterobifunctional cross-linking agents have been heavily utilized in methods for the conjugation of molecular recognition elements such as receptors, enzymes, antibodies and nucleic acids (70). Generally, the reaction chemistry chosen depends on the functional groups available on the recognition site and the lipid bilayer, the desired orientation of the recognition element and the effects of the functionalized lipid and reaction conditions on liposome stability (66, 71). These modifications allow liposomes to be targeted towards specific cell types and target organs or organelles, leading to a reduction in the apparent toxicity associated with non-localized therapies (72). Some of the compounds that are frequently used to allow the targeting of liposomes to specific cell types include peptides (73, 74), lectins (75, 76), antibodies (77), and folate (78) .

Because liposomes have an inner hydrophilic cavity, a wide variety of hydrophilic molecules can be encapsulated within this cavity, including pharmaceutical compounds, enzymes, DNA molecules, vaccines, fluorescent dyes, electrochemical and chemiluminescent markers (57, 58). Previous studies have shown that the bilayer structure can potentially prolong the longevity of the encapsulated molecules by shielding them from destructive entities within the body. Chaize et al reported that the activity of the pesticide target enzyme acetylcholinesterase can be retained when encapsulated in liposomes despite the presence of proteolytic enzymes in the surrounding media (79) . In other studies, liposome-encapsulated RNA was reported to be protected from RNase present in the external solution (80) and the oxidation of heme groups present in hemoglobin was minimized when encapsulated within liposomes (81).

The application of liposomes in therapeutics stems from the fact that the encapsulation of drugs within liposomes results in their delayed release, which is beneficial for reducing toxic effects and maximizing the therapeutic index of drugs (82-84). The FDA has approved several pharmaceutical compounds that use liposomes as a drug-delivery system, including doxorubicin, daunorubicin, amphotericin B, morphine, and cytarabine, which are used for the treatment of refractory ovarian and breast cancers, Kaposi's sarcoma, fungal infections, management of post-surgical pain, and neoplastic and lymphomatous meningitis, respectively (85). Some drugs can also be associated with the lipid bilayer through electrostatic interactions (86).

Additionally, the sequestration of various molecules within liposomal cavities has been utilized for a variety of unique applications. For instance, DNA has been encapsulated into liposomes for use as an internal control for real-time PCR (87) and in similar studies, reagents have been entrapped in liposomes to allow for internal DNA transcription (80) and replication (88). Hemoglobin-based blood substitutes have also been encapsulated within liposomes to enhance their stability and clinical utility (89).

Bis(monoacylglycero)phosphate (BMP)

Bis(monoacylglycero)phosphate (BMP), also erroneously termed as lysobisphosphatidic acid (LBPA) is a unique, negatively charged phospholipid that was first detected in pulmonary alveolar macrophages (PAMs) of lung from pig and rabbit by Body and Gray (45). It has since been postulated to be synthesized from phosphatidylglycerol (PG) or lyso-phosphatidylglycerol *in vivo* (90, 91). BMP has also been found in other tissues and cell types such as the brain, liver, and kidney of a number of different species (92). It usually represents less than 1 mol% of the total phospholipid mass (45, 46), although increased BMP contents have been found in

several lipidosis and in response to some pharmaceutical agents (93). In the late endosome (LE), however, the concentration of BMP is near 15 mol % of the total lipid content of the organelle and can comprise as much as 70 mol % of the lipid composition of the intraendosomal vesicles (94-96).

Endosomes are prelysosomal organelles that serve as intracellular sites for the sorting, distribution, and processing of receptors, ligands, fluid phase components, and membrane proteins internalized by endocytosis. Endosomes are responsible for many of the critical events that regulate the trafficking, sorting, and processing of internalized macromolecules. Their acidic internal pH is also needed for the dissociation of incoming ligand-receptor complexes, allowing the receptors to return to the cell surface and the ligands to be transported to lysosomes for degradation (5). Endosomes can be identified by the presence of vesicular bodies (VBs) inside the lumen of the limiting membrane or by lipid composition (44, 97). Whereas early endosomes have a limiting membrane with a lipid composition very similar to that of the plasma membrane, late endosomes are characterized by an absence of a significant amount of cholesterol and a relatively high concentration of BMP (97). During endosome maturation, the internal pH undergoes a series of changes from that of the neutral cytosol to that of the acidic lysosome. It is within late endosome intraluminal membranes that BMP is first found in relatively higher concentrations and is believed to be partly responsible for the formation of multivesicular liposomes that resemble multivesicular endosomes (98).

BMP has an unusual structure that differs from that of other phospholipids from two aspects (Figure 1-12). First, unlike other phospholipids, it has two glycerol components, each with a single acyl chain and secondly, BMP isolated from biological

sources differs from the typical sn-3-glycerophosphate structures exhibited by most other glycerophospholipids (2, 8, 46), in that it possesses an unusual sn-1-glycerophospho- sn-1'-glycerol (sn1:sn1') stereoconfiguration (47-50, 99, 100) . However, the sn 3: sn 1' configuration has been reported for BMP isolated from baby hamster kidney (BHK) cells, although it is stipulated that this configuration is an intermediate in the synthesis of the sn1:sn1' BMP (48).

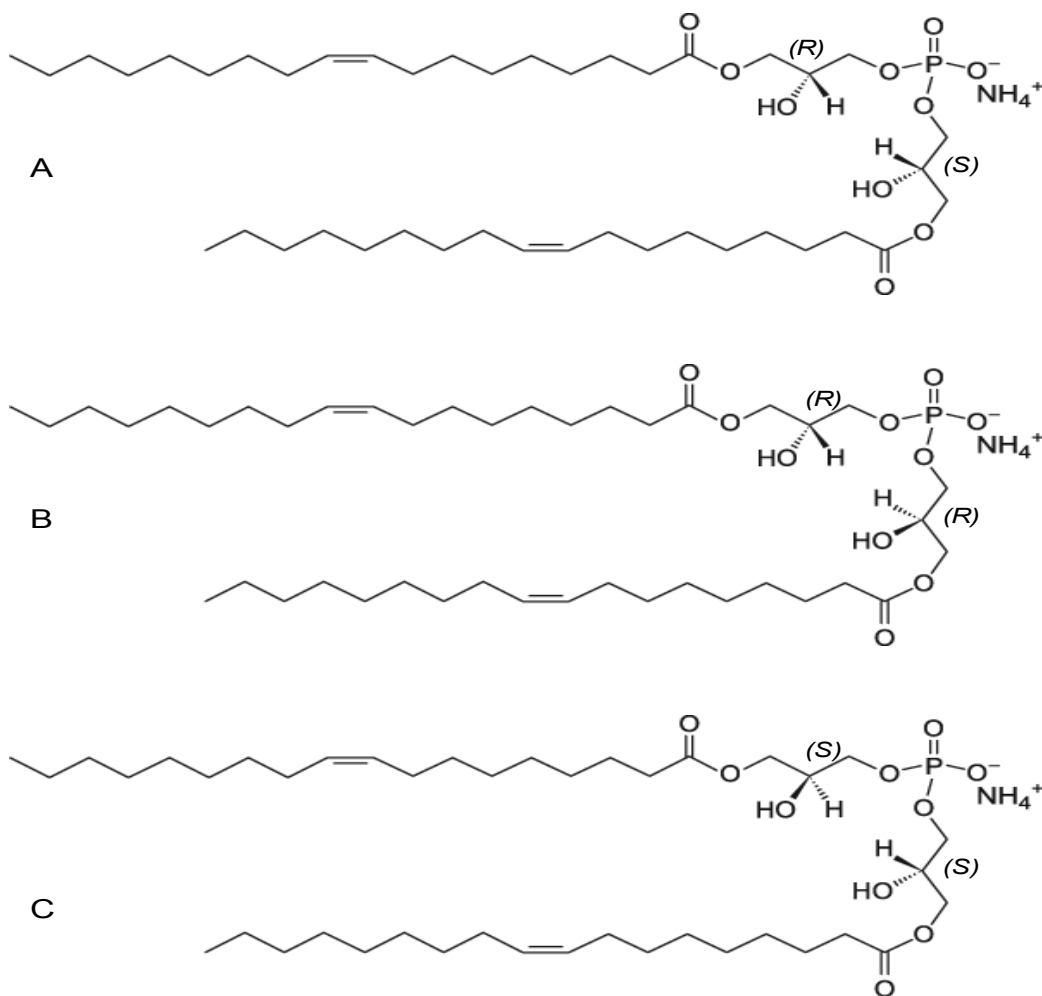


Figure 1-12. Structural isoforms of BMP. A) (R, R), B) (R, S) and C) (S, S) isomers.

Body and Gray (45) first identified BMP as a structural isomer of POPG, and since then, various structural isomers of BMP have been obtained by varying the location of the two acyl chains or by altering the sn- stereochemistry (101) . Three structural

isoforms of BMP are shown in Figure 1-12; the (*S,R*) isomer, sn-(3-oleoyl-2-hydroxy)-glycerol-1-phospho-sn-3'-(1'-oleoyl-2'-hydroxy)-glycerol (ammonium salt), (1,3' dioleoyl sn3:sn1' or BMP18:1) (Figure 1-12A); the (*R,R*) isomer, sn-(3-oleoyl-2-hydroxy)-glycerol-1-phospho-sn-3'-(1'-oleoyl-2'-hydroxy)-glycerol (ammonium salt) (1,1' dioleoyl sn3:sn3') (Figure 1-12B) and the (*S,S*) isomer, sn-(3-oleoyl-2-hydroxy)-glycerol-1-phospho-sn-3'-(1'-oleoyl-2'-hydroxy)-glycerol (ammonium salt) (3,3' dioleoyl sn1:sn1') (Figure 1-12C). The synthetic *S, R* isomer (sn3:sn1') was used in studies that were performed in this dissertation because of its commercial availability, and is designated throughout this dissertation as BMP.

Role of BMP in the Late Endosome

Late endosomes are prelysosomal endocytic organelles that are defined by the time it takes for endocytosed macromolecules to be delivered to them (102). Late endosomes are usually loaded 4-30min after endocytic uptake in mammalian cells, although the delivery time may vary between cell types and between cells in culture and in living tissue (103). Electron microscopy studies have revealed that late endosomes are more spherical than early endosomes, being concentrated near the microtubule organizing center and having the appearance of multivesicular bodies (MVBs). They can be differentiated from early endosomes by their lower luminal pH, different protein and lipid compositions and association with different small GTPases of the rab family (104).

One of the most distinct features of late endosomes is the presence of internal membranes, hence the reason that late endosomes have also been referred to as multivesicular bodies (MVBs) or multivesicular endosomes (MVEs). The accumulation of internal membranes starts at the early endosome and is thought to continue as the

endosome 'matures' to a late endosome. The lipid composition of late endosomes differs from that of earlier endocytic compartments, being enriched in triglycerides, cholesterol esters and selected phospholipids, including BMP (97) . BMP is however found to be more heavily enriched in the internal membranes of mammalian late endosomes/MVBs than in the limiting membrane (44). Because each acyl chain of BMP contains an unsaturated site, this lipid may increase the overall bilayer disorder of model and endosomal membranes due to intermolecular packing constraints (93). Although earlier studies postulated BMP to be highly hydrophobic and cone or inverted-cone shaped (93, 97, 98), our studies have shown that BMP forms stable, lamellar vesicle structures, implying a possible function in formation of MVBs (105).

Because of its high level of accumulation in late endosomes (106), its unusual structure and stereochemistry, BMP is thought to play important roles in the late endosome, including structural integrity, endosome maturation, and lipid/protein sorting and trafficking (101, 106). For instance, because of its unusual structure, BMP is inefficiently degraded by phospholipases, leading to its accumulation in intraluminal vesicles of late endosomes (44) . BMP is presumably synthesized in situ within the acidic organelles of the endocytic pathway (107). Studies have also shown that accumulation of antibodies against BMP in the late endosomes, which are observed in patients suffering from antiphospholipid syndrome, inhibit multivesicular endosome formation, suggesting that BMP does play a role in this process (108).

BMP may also be involved in cholesterol transport (44), possibly via formation of lateral microdomains. Moreover, BMP has been found to be essential for the activator-stimulated hydrolysis of ganglioside GM1 (109) and GM2 (110) and for the hydrolysis of

ceramide by acid ceramidase (111). It is unclear how BMP achieves these functions, but it is likely that the structure and biosynthesis of BMP, coupled to the change in pH during the maturation of the late endosome induces intraendosomal vesicular body formation.

Overview of Biophysical Studies of BMP

To elucidate the functional role of BMP in late endosomes, a series of studies have already been aimed at obtaining a more detailed understanding of the biophysical characteristics of this lipid. Holopainen *et al.* studied the thermotropic behavior of pure dioleoyl-BMP mono- and bilayers using Langmuir-lipid monolayers, electron microscopy, differential scanning calorimetry (DSC), and fluorescence spectroscopy. Holopainen's group reported that BMP formed metastable, liquid-expanded monolayers at an air/buffer interface, and its compression isotherms lacked any indication for structural phase transitions. Furthermore, pure BMP formed multilamellar vesicles with no structural transitions or phase transitions between 10 and 80° C at a pH range of 3.0–7.4 (93).

Holopainen's group also studied mixed BMP/dipalmitoylphosphatidylcholine (DPPC) bilayers by DSC and fluorescence spectroscopy and found that incorporating increasing amounts of BMP (up to XBMP (molar fraction) = 0.10) decreased the cooperativity of the main transition for DPPC, and a decrease in the main phase transition as well as pretransition temperature of DPPC was observed but with no effect on the enthalpy of this transition. 1-palmitoyl-2-oleoyl phosphatidylcholine (POPC)/LBPA mixed bilayers were found to be more fluid, and no evidence for lateral phase segregation was observed. These results were confirmed using fluorescence microscopy of Langmuir-lipid films composed of POPC and BMP (up to XBMP= 0.50) with no evidence for lateral

phase separation. Because late endosomes are eminently acidic, they examined the effect of lowering pH on lateral organization of mixed PC/LBPA bilayers by DSC and fluorescence spectroscopy and reported that even at pH 3.0, there was no evidence of BMP-induced microdomain formation at BMP contents found in cellular organelles (93).

Kobayashi's group reported that BMP can induce the formation of multivesicular liposomes that resemble the multivesicular endosomes where this lipid is found in vivo. They also reported that the formation of the multivesicular liposomes depends on the acyl chain composition of BMP and the position of esterification in the glycerophosphate backbone (98). Hayakawa *et al.* reported that DOBMP membranes form a closely packed multilamellar structure at low pH by adding the hydrophobic amine, D-threo-1-phenyl-2-decanoylamino-3-morpholino-1-propanol (D-PDMP) (112). They also showed that this interaction between BMP and D-PDMP is a major cause of the structural alteration of the degradative organelles found in D-PDMP-treated cells and the accumulation of cholesterol in these organelles (112, 113).

A series of studies have also demonstrated that agents that perturb BMP induce alterations in the sorting and trafficking of proteins and/or the receptor in late endosomes accompanied by structural changes of the late endosome organelle(44, 114), along with abnormal accumulation of cholesterol (108). BMP has also been shown to be an antigen in the antiphospholipid syndrome, a condition in which endosomal sorting and multivesicular endosome formation is disrupted (98). The trafficking defects observed in the cholesterol storage disorder Niemann- Pick type C can be recapitulated by disruption of LBPA function(115, 116).

Sandhoff *et al.* demonstrated that incorporation of BMP into liposomes containing glucosylceramide greatly facilitates the degradation of the glycosphingolipid by glucosylcerebrosidase and sphingolipid activator protein C (117). BMP also facilitates the degradation of GM2 by hexosaminidase A and GM2-activator protein, as well as ceramide by acid ceramidase/SAP-B and sphingomyelin by acid sphingomyelinase (46).

BMP also functions in cholesterol efflux from late endosomes and lysosomes. If antibodies against BMP are internalized by fluid-phase endocytosis, they bind to BMP and accumulate in late endosomes. Under these conditions, cholesterol released from low-density lipoprotein (LDL) remains trapped in the late endosomes and cannot be transported out from this organelle as would normally occur if the antibody were absent. The network of membrane tubules and vesicles within the lumen of late endosomes might thus have an important function in sphingolipid degradation and cholesterol distribution in the cell. Accumulation of endocytosed antibodies against BMP also results in the defective sorting/trafficking of proteins that transit via late endosomes, presumably because membrane properties are altered (118). The function and maintenance of the highly curved membrane structures are still poorly understood, but obviously BMP membrane domains do contribute to the selectivity in handling of lipid rafts in the endocytic pathway. Alterations in these processes appear to cause not only accumulation of lipid rafts but also result in disturbances in protein traffic (113).

Scope of Dissertation

Because of the unique structure and stereochemistry of BMP, our lab was interested in gaining a better understanding for the important functional roles that this lipid plays in the late endosome. In an effort to provide further insight on the morphology and sizes exhibited by BMP hydrated dispersions and extruded vesicles, dynamic light

scattering (DLS) and negative staining-transmission electron microscopy (TEM) experiments were performed at various experimental conditions, including variations in lipid composition, pH conditions, ionic strength and lipid concentrations.

Chapter 1 has introduced a detailed background on lipids, with a focus on glycerophospholipids' structure and function. Different model membrane systems were also discussed, with a special interest in lipid vesicles. A detailed discussion on the unique structure and stereochemistry of BMP was also given, followed by its role in the late endosome and an overview of previous biophysical studies that have been performed on BMP.

Chapter 2 gives a discussion of the major techniques that I utilized in analysis of the lipid dispersions and vesicles studied here, with a focus on the particle sizing technique dynamic light scattering (DLS), and negative staining-transmission electron microscopy (TEM). The chapter begins with a detailed discussion on the theory of DLS, followed by an overview of applications of DLS for particle sizing. Theory of transmission electron microscopy and its applications for biological studies is also given. A discussion on FRET, which was utilized for monitoring leakage of fluorophore-encapsulated vesicles, is also presented in detail, and lastly, a general overview of two chromatographic techniques, TLC and column chromatography are also presented. TLC was used to test for lipid integrity, whereas column chromatography was utilized for the separation of fluorophore encapsulated vesicles from free fluorophore.

Chapter 3 discusses the characterization of the morphology and size distribution observed in hydrated lipid dispersions and extruded lipid vesicles of BMP, POPC, POPG and lipid mixtures of POPC:BMP and POPC:POPG, using DLS and negative

staining-TEM. To test the analytical capability of DLS, initial control experiments were performed to test different populations of POPC vesicles extruded using 30, 100 or 400 nm pore size extrusion membranes using DLS. To assess the stability of BMP vesicles (stability defined as the ability of the vesicles to maintain the same size distribution over time), assays were performed in which BMP, POPC and POPG vesicles were mechanically passed through 30 nm pore size extrusion membranes and the size of the vesicle suspensions (stored at room temperature) were monitored by DLS measurements over a five week period. Experiments were also performed to confirm that BMP forms lamellar vesicles with an interior volume. To this end, vesicle leakage assays were performed using fluorescence resonance energy transfer (FRET), and the percent release of the encapsulated fluorophore monitored as a function of increasing concentrations of titrated sodium dodecyl sulfate (SDS) detergent.

In Chapter 4, studies on the effect of introducing ganglioside GM1 in BMP dispersions at varying concentrations, under late endosomal pH (5.5) conditions are discussed. Dynamic light scattering and negative staining-transmission electron microscopy were utilized to monitor the morphological and structural characteristics in hydrated dispersions of BMP:GM1 lipid mixtures. Other investigations in Chapter 4 included the characterization of the morphology and size distribution of BMP hydrated lipid dispersions under different pH conditions, ranging from acidic (pH 4.2) to neutral (pH 7.4) conditions, using negative staining-TEM and DLS. Studies were also performed that monitored the effect of incorporating GM1 and BMP in typical phosphatidylcholine (POPC) membranes. Because POPC is abundantly present in biological cellular membranes, it has been well characterized and studied as a typical

model system. By utilizing dynamic light scattering and transmission emission spectroscopy, the morphology and size distribution of POPC:GM1 and POPC:BMP:GM1 hydrated dispersions and extruded vesicles were investigated.

The studies presented in Chapter 5 summarize the use of dynamic light scattering and negative staining-transmission electron microscopy to characterize the vesicle size and macroscopic morphologies observed when cholesterol (CHOL) is incorporated in lipid mixtures of POPC, BMP and ganglioside GM1. These experiments were performed at pH 5.5, in efforts to mimic the late endosome environment. Finally, Chapter 6 provides a summary of the major findings from this dissertation and a brief discussion of some future perspectives, including the possibility of using BMP vesicles for pharmaceutical applications.

CHAPTER 2 TECHNIQUES UTILIZED IN LIPID ANALYSIS

Dynamic Light Scattering (DLS)

Theory

Dynamic light scattering (DLS), is a powerful non-invasive, non-destructive light scattering technique used for characterizing the properties of macromolecular particles in suspensions, solutions of colloids and polymers in solution (119). DLS is also commonly referred to as photon correlation spectroscopy (PCS), or quasi-elastic light scattering (QELS). QELS was the first name given to the technique because when photons are scattered by mobile particles, the process is quasi-elastic. QELS measurements yield information on the dynamics of the scatterer, which gave rise to the acronym DLS. The acronym DLS will be employed throughout this dissertation because its use has become more prevalent and it presents a logical juxtaposition to static light scattering (SLS) (120).

The application of DLS to particle sizing and its commercialization occurred about seven years after the first size measurements were made in 1972, to check the alignment of a multi-angle research light scattering system (121). Through the 1970s, DLS gained wide acceptance among experts in light scattering and to date it is a widely accepted technique for broad applications in particle sizing. The main focus in this section will be on the theory and application of DLS for particle sizing, which relates to the translational motion (diffusion) of particles in liquids.

By nature, all materials scatter and absorb light, and since the first light-scattering experiments by Tyndall (122), static light scattering experienced major developments in the first half of the 19th century(123). The dynamic light scattering theory is built upon

the earlier foundation of classical light-scattering theory, which is based on two light scattering theories: Rayleigh scattering and Mie scattering (120).

In Rayleigh scattering, if the particles are small compared to the wavelength of the laser used (which is typically less than $d = \lambda/10$ or ~ 60 nm for a He-Ne laser), then the scattering from a particle illuminated by a vertically polarized laser will be essentially isotropic, i.e. equal in all directions. The Rayleigh approximation is represented in Equations 2-1 and 2-2.

$$I \propto d^6 \tag{2-1}$$

$$I \propto 1/\lambda^4 \tag{2-2}$$

where I is the intensity of scattered light, d is the particle diameter and λ is the laser wavelength (119).

The d^6 term means that a 50 nm particle will scatter 10^6 or one million times as much light as a 5 nm particle; hence there is the danger that the light from the larger particles will swamp the scattered light from the smaller ones. This d^6 factor also means that it may be difficult with DLS to measure for instance a mixture of 1000 nm and 10 nm particles because the contribution to the total light scattered by the small particles will be extremely small. The inverse relationship to λ^4 means that a higher scattering intensity is obtained as the wavelength of the laser used decreases (119, 124). In Mie scattering, the size of the particles becomes roughly equivalent to the wavelength of the illuminating light, giving the complete solution for spherical particles of any size.

The use of experimental DLS is thought to have begun with the advent of the laser. In the early 1960s, Pecora (125) pioneered a new kind of light scattering: time dependent light scattering. He showed that, by analyzing the frequency distribution of

the intensity fluctuations of light scattered from suspensions of macromolecules, information can be obtained about the translational and rotational diffusion coefficients of the macromolecules(120). Initially, DLS was used to measure the diffusion coefficient of macromolecules, from which a hydrodynamic size was calculated. It is thought that a few industrial users tried this technique for submicron particle sizing in an effort to replace transmission electron microscope (TEM) measurements in quality control (QC) applications.

During the second half of the 1970s, improvement of digital correlators and the introduction of several algorithms for analyzing decay time distributions were realized. Measurements could now be done in shorter times. Bertero and group (126, 127) published a fundamental paper in 1984 that derived the limiting conditions for the resolution of the "noisy" sum of an unknown number of exponentials based on information theory. The advent of highly efficient nonlinearly spaced correlators led to an increase in the utility of DLS particle sizing in the mid-1980s, and the emerging fast computers speeded up data handling (120).

Fundamentals of DLS

Dynamic light scattering measures Brownian motion and relates it to the size of the particles. Brownian motion is the random movement of particles due to collisions with the solvent molecules that surround them. In DLS, the larger the particle, the slower the Brownian motion, hence smaller particles are "kicked" farther by collisions with the solvent molecules and move more rapidly than larger particles. Because the viscosity of a liquid is related to its temperature, it is necessary to know the temperature of the liquid. The temperature also needs to be stable in order to minimize convection

currents in the sample, which would cause non-random movements that can ruin the correct interpretation of size (119, 124).

The velocity of the Brownian motion is defined by a property known as the translational diffusion coefficient, given by the symbol D . The size of the particle is calculated from the translational diffusion coefficient using the Stokes-Einstein equation in Equation 2-3.

$$d(H) = kT/3\pi\eta D \quad (2-3)$$

where $d(H)$ is the hydrodynamic diameter, D is the translational diffusion coefficient, k is Boltzmann's constant, T is the absolute temperature and η is the liquid viscosity.

The diameter that is measured in DLS is a value that refers to how a particle diffuses within a fluid, so it is referred to as a hydrodynamic diameter. Additionally, the diameter that is obtained by this technique is assumed to be the diameter of a sphere that has the same translational diffusion coefficient as the particle.

Factors that affect the translational diffusion coefficient

The translational diffusion coefficient will depend not only on the size of the particle "core", but also on any surface structure, the concentration and type of ions in the medium and the shape of the particles.

- (i) Ionic strength of medium

The ions in the medium and the total ionic concentration can affect the particle diffusion speed by changing the thickness of the electric double layer called the Debye length (K^{-1}) (119, 128). This implies that a low conductivity medium will produce an extended double layer of ions around the particle, reducing the diffusion speed and resulting in a larger, apparent hydrodynamic diameter. Conversely, higher conductivity

media will suppress the electrical double layer and the measured hydrodynamic diameter will be reduced. Suitable polystyrene latex standards are used to verify the performance of a DLS instrument. The International Standard on DLS advises that dilution of any polystyrene standard should be made in 10 mM NaCl, so that at this concentration of salt, the electrical double layer will be suppressed enough and the hydrodynamic diameter reported will be the same as the hydrodynamic diameter on the certificate or the expected diameter (129).

(ii) Surface structure

Any changes to the surface of a particle that affects the diffusion speed will also change the apparent size of the particle. For instance, an adsorbed polymer layer projecting out into the medium will reduce the diffusion speed more than if the polymer was lying flat on the surface. The nature of the surface and the polymer, as well as the ionic concentration of the medium can affect the polymer conformation, which in turn can change the apparent size by several nanometers (130).

(iii) Non-spherical particles

An inherent problem experienced with all particle sizing techniques lies in describing the size of non-spherical particles. The sphere is the only object whose size can be unambiguously described by a single figure. Different techniques are sensitive to different properties of a particle, such as projected area, density, scattering intensity, and in general will produce different mean sizes and size distributions for any given sample. The hydrodynamic diameter of a non-spherical particle is the diameter of a sphere that has the same translational diffusion speed as the particle (119, 131). If the shape of a particle changes in a way that affects the diffusion speed, then the

hydrodynamic size will change. For example, small changes in the length of a rod-shaped particle will directly affect the size, whereas changes in the rod's diameter, which will hardly affect the diffusion speed, will be difficult to detect. The conformation of proteins and macromolecules are usually more dependent on the exact nature of the dispersing medium. As conformational changes will usually affect the diffusion speed, DLS is a very sensitive technique for detecting these changes (119, 124, 132).

Basis of intensity fluctuations in DLS

The main concept in DLS is that the diffusion of the scatterers causes the phases of the fields scattered from each of them to change with time, so that the total scattered intensity will fluctuate with time owing to constructive and destructive interference (120). Essentially, the use of DLS to determine particle size is based on the measurement of the diffusion coefficients of suspended particles undergoing Brownian motion via the autocorrelation of the time dependence of the scattered light. This is done by measuring the rate at which the intensity of the scattered light fluctuates when detected using a suitable optical arrangement. To determine how these fluctuations in the intensity of scattered light arise, imagine if a cuvette, containing particles which are stationary, is illuminated by a laser and a frosted glass screen is used to view the sample cell. A classical speckle pattern would be observed, as illustrated in Figure 2-1.

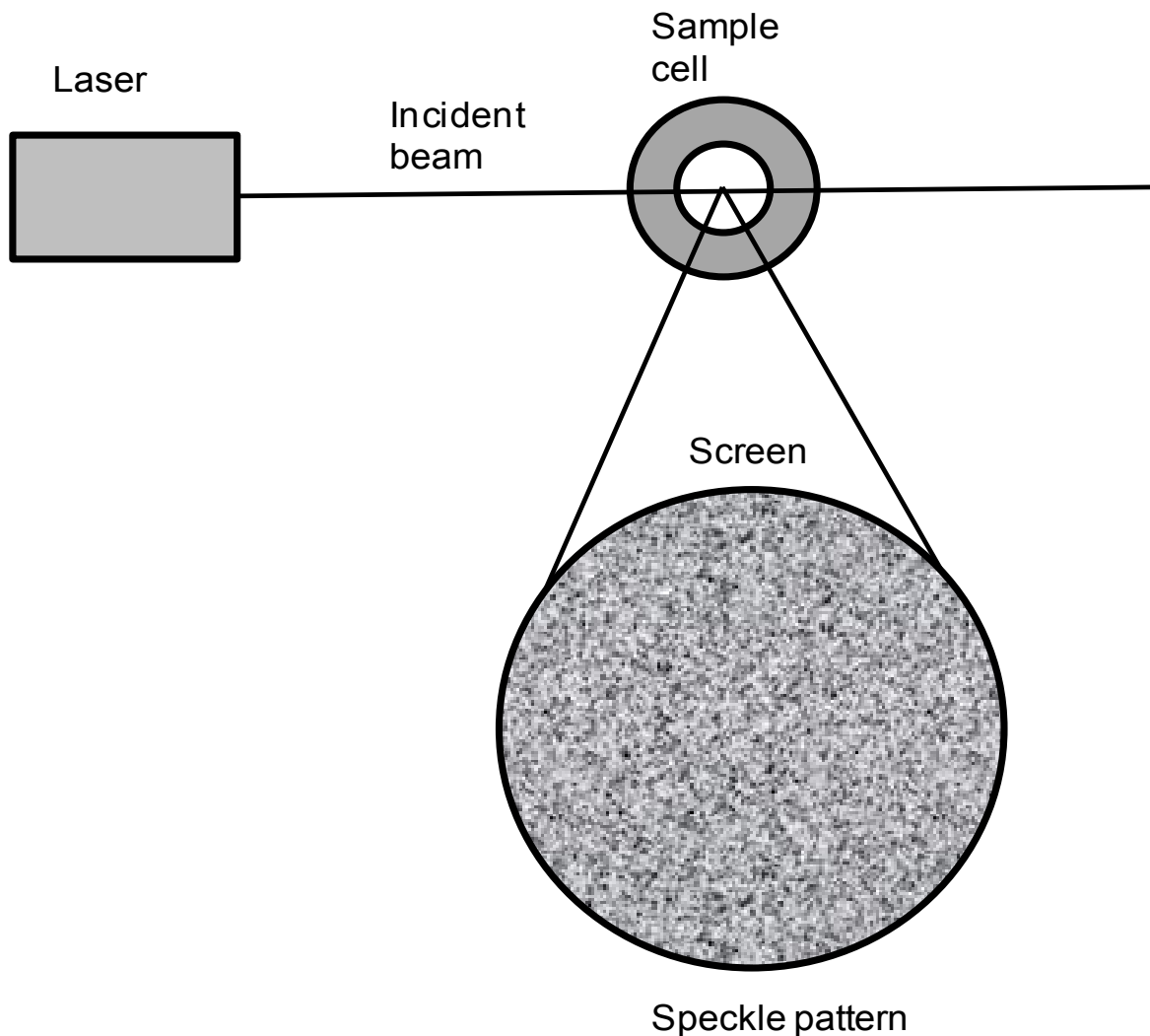


Figure 2-1. Schematic representation of a speckle pattern observed in DLS. Adapted from Ref. (119).

The speckle pattern will be stationary both in speckle size and position because the whole system is stationary. The dark spaces are where the phase additions of the scattered light are mutually destructive and cancel each other out (Figure 2-2A), while the bright blobs of light in the speckle pattern are where the light scattered from the particles arrives with the same phase and interfere constructively to form a bright patch (Figure 2-2B).

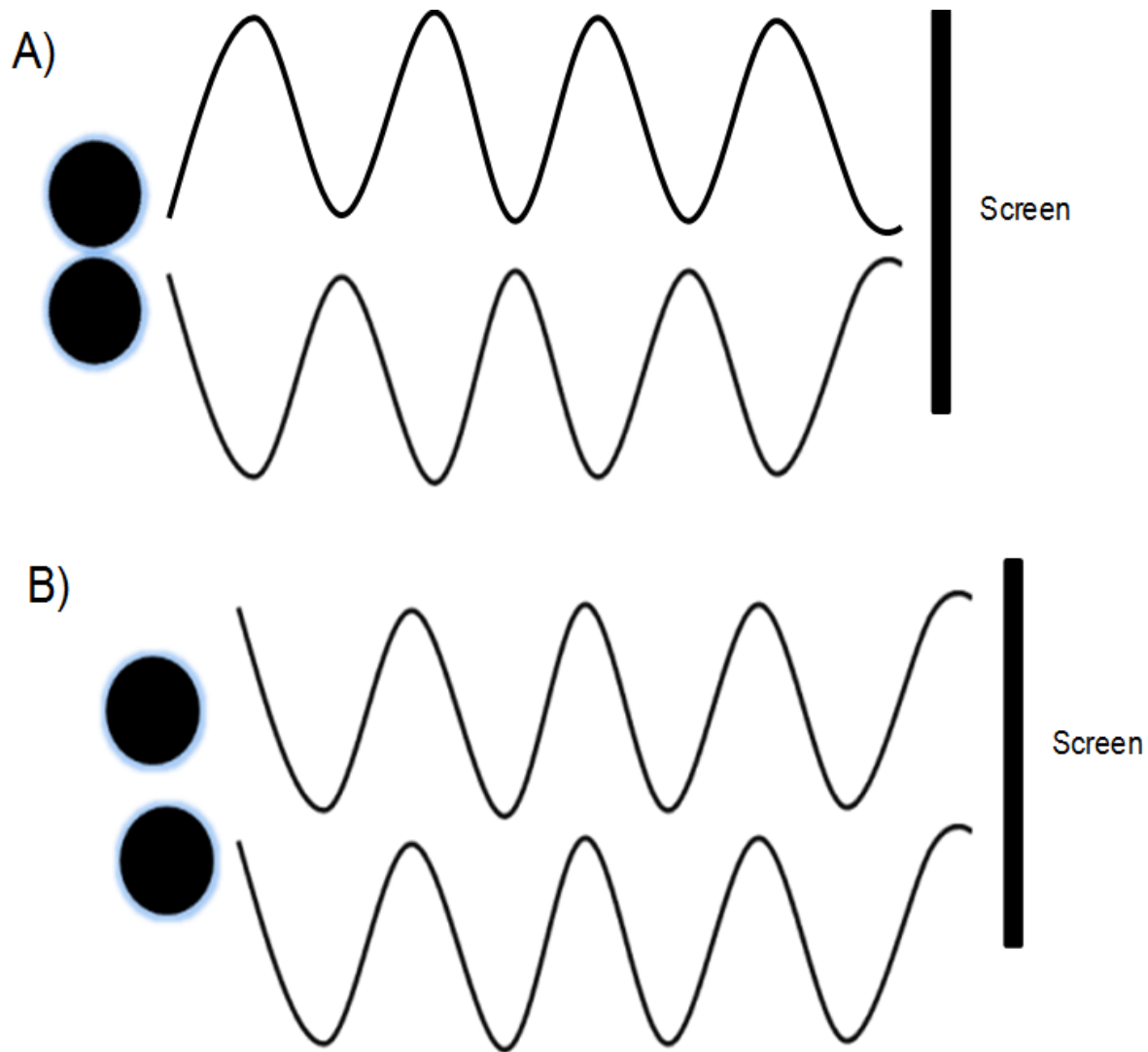


Figure 2-2. A) Destructive interference and B) constructive interference observed in a speckle pattern.

For a system of particles undergoing Brownian motion, a speckle pattern is observed where the position of each speckle is seen to be in constant motion. This is because the phase addition from the moving particles is constantly evolving and forming new patterns. The rate at which these intensity fluctuations occur will depend on the size of the particles.

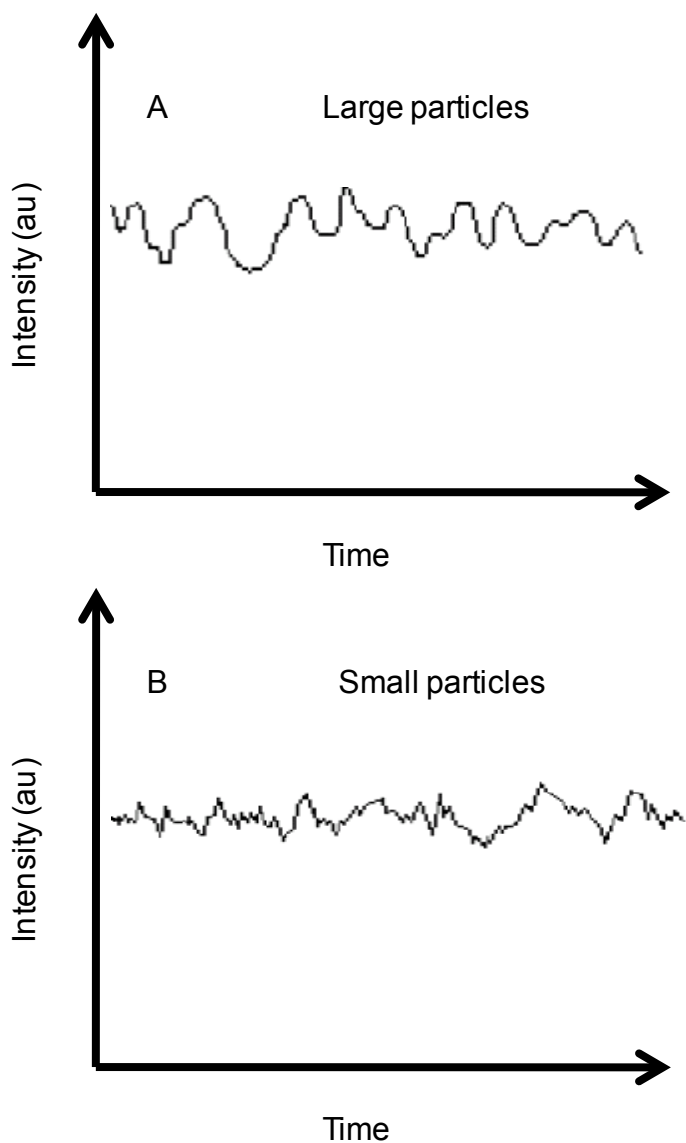


Figure 2-3. Typical intensity fluctuations for A) large particles and B) small particles.

Figure 2-3 schematically illustrates typical intensity fluctuations arising from a dispersion of large particles (A) and a dispersion of small particles (B). The small particles cause the intensity to fluctuate more rapidly than the large ones. While it may be possible to directly measure the spectrum of frequencies contained in the intensity fluctuations arising from the Brownian motion of particles, it is quite inefficient to do so, and the best way is to use a device called a digital auto correlator.

How the digital autocorrelator works

A digital correlator is basically a device that compares signals. It is designed to measure the degree of similarity between two signals, or one signal with itself at varying time intervals. If the intensity of a signal is compared with itself at a particular point in time and at another time much later, then for a randomly fluctuating signal it is obvious that the intensities and correlation between the two signals are going to vary over time, as shown in Figure 2-4.

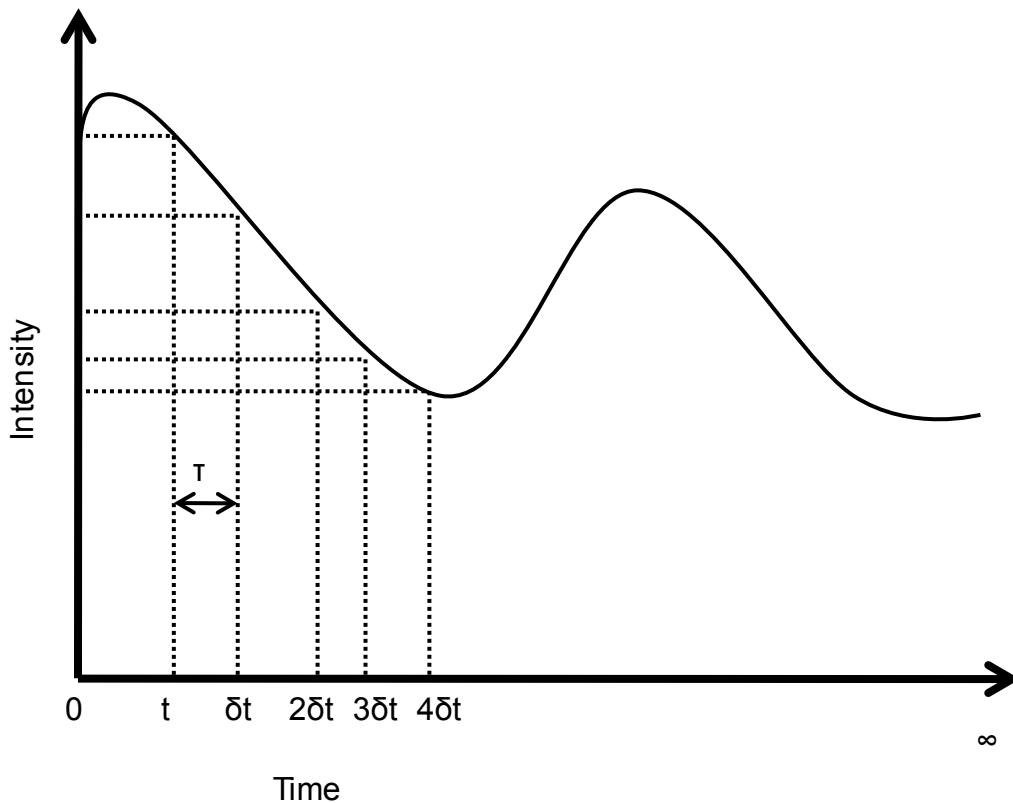


Figure 2-4. Schematic showing the fluctuation in the intensity of scattered light as a function of time. Adapted from Ref. (119).

Knowledge of the initial signal intensity will not necessarily allow the signal intensity at time $t = \infty$ to be predicted, which is true of any random process such as diffusion. However, if the intensity of the signal at time t is compared to the

intensity a very short time later (such as $t+\delta t$), there will be a strong relationship or correlation between the intensities of two signals, hence the two signals are said to be strongly or well correlated. If the signal derived from a random process such as Brownian motion at t is compared to the signal at $t+2\delta t$, there will still be a reasonable comparison or correlation between the two signals, but it will not be as good as the correlation at t and $t+\delta t$, which implies that the correlation reduces with time. The period of time δt is usually very small, on a scale of nanoseconds to microseconds, and is called the sample time of the correlator. The $t = \infty$ time maybe on the order of a millisecond or tens of milliseconds. If the signal intensity at t is compared with itself then there is perfect correlation as the signals are identical. Perfect correlation is indicated by unity (1.00) and lack of any correlation is indicated by zero (0.00). If the signals at $t+2\delta t$, $t+3\delta t$, $t+4\delta t$ and so on are compared with the signal at t , the correlation of a signal arriving from a random source will decrease with time until at some time, when $t = \infty$, there will be no correlation.

Additionally, for large particles, the signal changes slowly and the correlation remains strong for a long time (Figure 2-5A), whereas for small particles that are moving rapidly, the correlation reduces more quickly (Figure 2-5B).

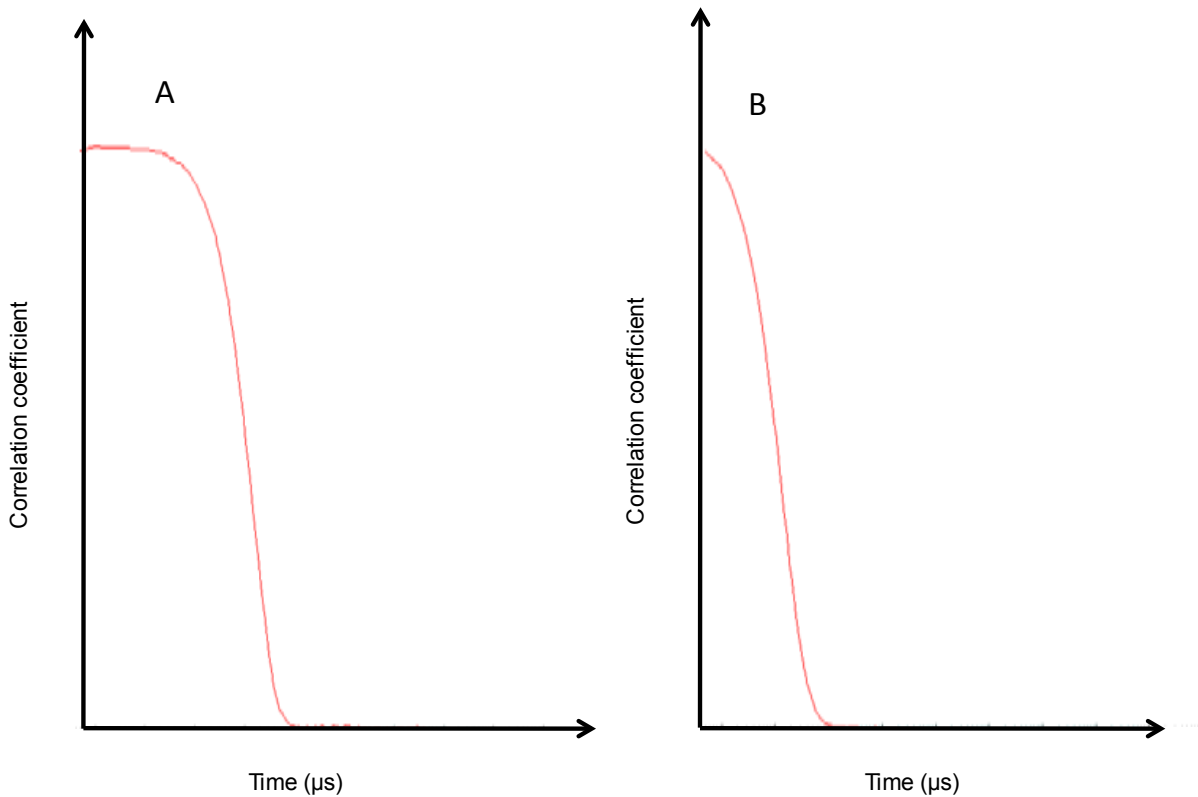


Figure 2-5. Correlation spectrum for a sample containing A) large particles with long decay time and B) small particles with rapid decay time.

Essentially, viewing the correlation spectrum from a measurement can give a lot of information about the sample. For instance, the time at which the correlation starts to significantly decay is an indication of the mean size of the sample, and the steeper the line, the more monodisperse the sample while the more extended the decay, the greater the sample polydispersity.

The auto correlation function (ACF)

We have so far established that particles in a liquid dispersion are in a constant, random Brownian motion, which causes the intensity of scattered light to fluctuate as a function of time. The digital autocorrelator utilized in a DLS instrument will then construct the correlation function $G(\tau)$ of the scattered intensity related to time as shown in Equation 2-4.

$$G(\tau) = \langle I(t) \cdot I(t+\tau) \rangle \quad (2-4)$$

where τ is the time difference (the sample time) of the correlator.

For a large number of monodisperse particles in Brownian motion, the correlation function (given the symbol $G(\tau)$) is an exponential decaying function of the correlator time delay τ as illustrated in Equation 2-5.

$$G(\tau) = A [1 + B \exp(-2\Gamma\tau)] \quad (2-5)$$

where A is the baseline of the correlation function and B is the intercept of the correlation function. The function Γ is defined in Equation 2-6.

$$\Gamma = Dq^2 \quad (2-6)$$

where D is the translational diffusion coefficient, which can be obtained using the Stokes-Einstein relationship in Equation 2-8. q is a factor defined by the relationship in Equation 2-7.

$$q = (4\pi n / \lambda_0) \sin(\theta/2) \quad (2-7)$$

where n is the refractive index of dispersant, λ_0 is the wavelength of the laser and θ is the scattering angle.

$$D = kT / 3\pi\eta d \quad (2-8)$$

where k is Boltzmann's constant, T is temperature, η is viscosity and d (H) is the hydrodynamic diameter of the particles.

For polydisperse samples, the equation for the correlation function can be described as shown in Equation 2-9.

$$G(\tau) = A [1 + B g_1(\tau)^2] \quad (2-9)$$

where $g_1(\tau)$ is the sum of all the exponential decays contained in the correlation function.

The particle size and size distribution can be obtained from the correlation function by utilizing two established algorithms:

(1) to fit a single exponential to the correlation function to obtain the mean size (z-average diameter) and an estimate of the width of the distribution (polydispersity index) (this is called the Cumulants analysis), or

(2) to fit a multiple exponential to the correlation function to obtain the distribution of particle sizes (such as Non-negative least squares (NNLS) or CONTIN program).

The size distribution obtained is a plot of the relative intensity of light scattered by particles in various size classes and is therefore known as an intensity size distribution. If the distribution by intensity is a single fairly smooth peak, then there is no point in doing the conversion to a volume distribution using the Mie theory. If the optical parameters are correct, this will only provide a slightly different shaped peak. However, if the plot shows a substantial tail, or more than one peak, then Mie theory can make use of the input parameter of sample refractive index to convert the intensity distribution to a volume distribution. This will then give a more realistic view of the importance of the tail or second peak present. In general terms it will be seen that $d(\text{intensity}) > d(\text{volume}) > d(\text{number})$ (120).

A very simple way of describing the difference between intensity, volume and number distributions is to consider two populations of spherical particles of diameter 5 nm and 50 nm present in equal numbers as illustrated in Figure 2-6.

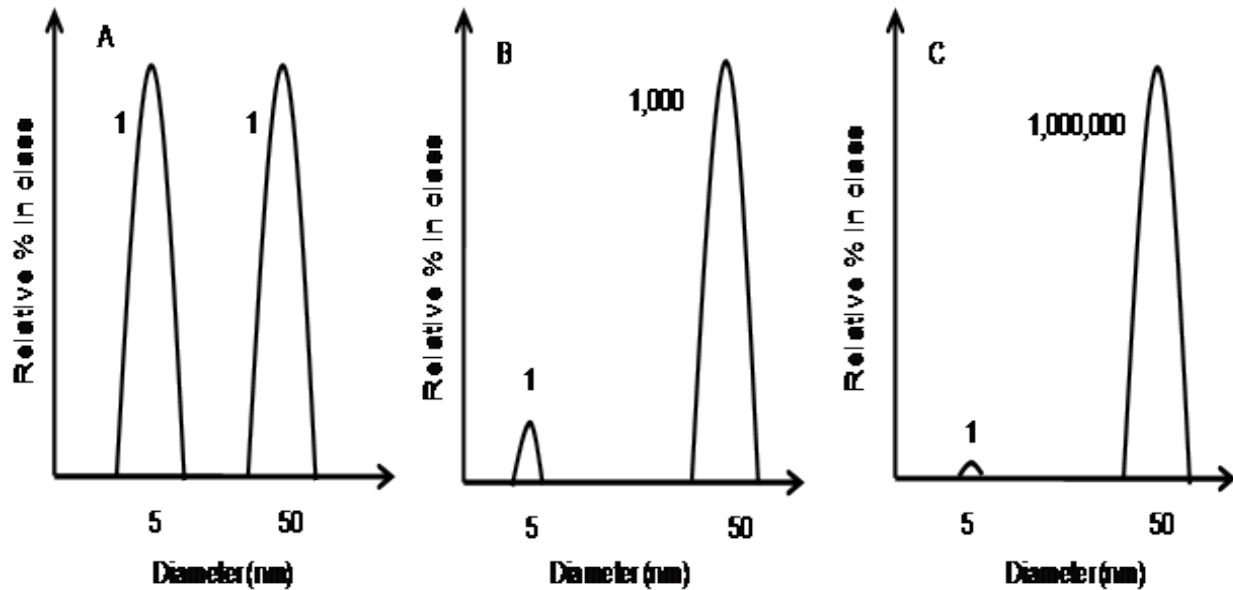


Figure 2-6. Number, volume and intensity distributions of a bimodal mixture of 5 and 50 nm lattices present in equal numbers. A) Number distributions. B) Volume distributions. C) Intensity distributions. Modified from Ref. (119).

If a number distribution of these two particle populations is plotted, a plot consisting of 2 peaks (positioned at 5 and 50 nm) of a 1 to 1 ratio would be obtained. If this number distribution was converted into volume, then the 2 peaks would change to a $1:10^3$ ratio (given that the volume of a sphere is equal to $4/3\pi (d/2)^3$). If this was further converted into an intensity distribution, a $1:10^6$ ratio between the two peaks would be obtained, given that the intensity of scattering is proportional to d^6 , from Rayleigh's approximation). Notably, in DLS, the distribution obtained from a measurement is based on intensity (119, 128).

Instrumental design for DLS

Generally, a typical DLS system should include four major functional components: a light source, an optical system, a detector system and a digital autocorrelator, as indicated in Figure 2-7.

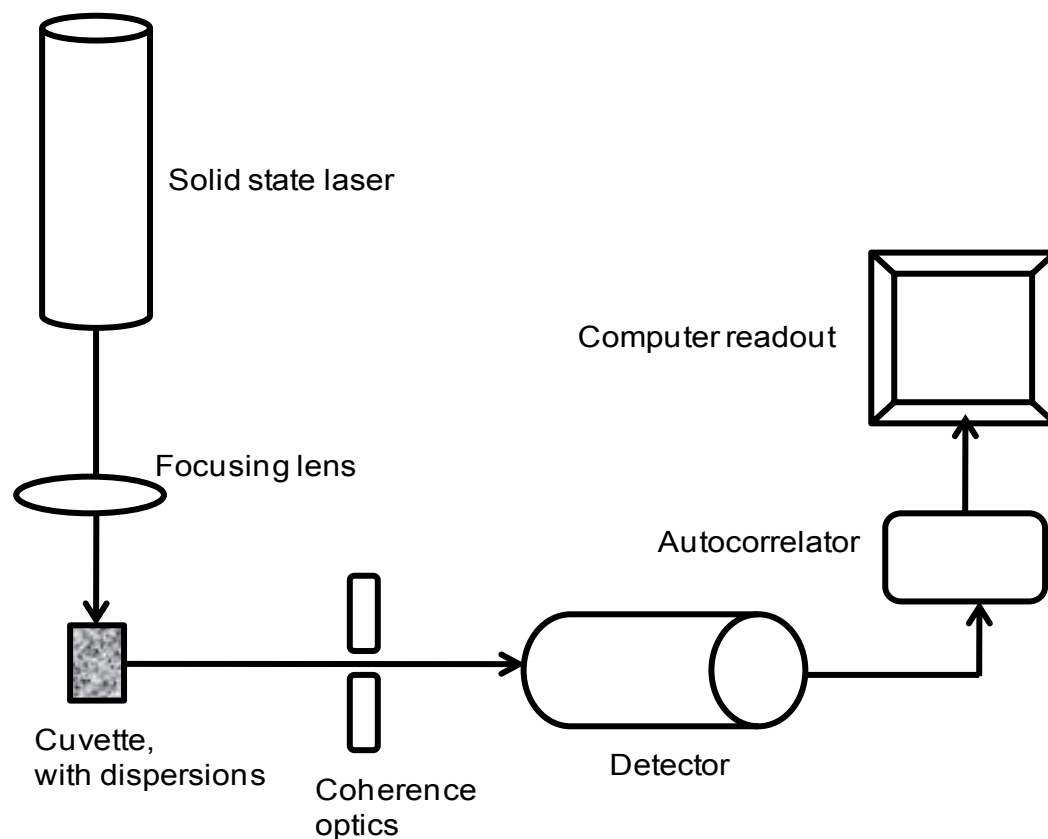


Figure 2-7. Typical experimental set-up in a dynamic light scattering instrument.

(i) The light source

Practical requirements for a sufficiently intense light source demand a narrow-band, polarized, monochromatic, continuous wave (CW) laser. Table 2-1 summarizes the popular options available for light sources (120). The DLS instrument utilized for our studies (Brookhaven 90Plus Nanoparticle Analyzer) uses a solid state laser, operated at a wavelength of 635 nm.

Table 2-1. Types of lasers commonly used in DLS instruments.

Laser Type	Wavelength	Power	Size
HeNe	632.8 nm	5-35 mW	0.4-1.5 m
Laser diodes	635-780 nm	5-100 mW	0.05-0.14 m
Ar+(air cooled)	488-514.5 nm	~100 mW	1m
Ar+(water cooled)	488-514.5 nm	~1.7 W	1.5-2 m
DPSS	532 nm	10 mW-4W	0.2-0.5 m

DPSS, diode pumped solid-state lasers. Adapted from Ref. (120).

(ii) Optical system

A lens focuses the laser beam into the sample, which is enclosed in an optional temperature-controlled scattering cell surrounded by a refractive index matching liquid. The scattered light is focused onto a photomultiplier tube (PMT) by another lens. Such systems are best constructed on a precision turntable with a stepper motor, and typically allow experiments to be conducted over a 10° - 160° angular range.

(iii) Detector system

Photomultiplier tubes (PMTs) are almost universally used as detectors in DLS instruments. The PMT should have a low dark count and a high gain since most work is done in the single photon counting regime.

(iii) The digital autocorrelator

The correlator has become the device of choice for generating raw data in a DLS experiment, although earlier experiments mostly employed "wave analyzers" or "spectrum analyzers". The autocorrelation function (ACF) is formed by recording the number of photons arriving in each sample time, maintaining a history of this signal over a large range of sample times (time series), multiplying the instantaneous and the delayed signal for a range of time delays t_d (the "channels") and accumulating these products. The BI-9000AT autocorrelator employed in our studies is an entirely digital, high speed, signal processor which can be used as an auto- or cross correlator for dynamic light scattering (DLS) measurements and as a photon counter for static light scattering measurements (SLS).

DLS Applications

The majority of applications for DLS in particle sizing include the rapid and routine measurements of mean sizes of particles in quality control and research laboratories.

Manufacturers of latexes, pigments, emulsions, micelles, liposomes, vesicles, sils and silica can track the consistency of the desired particle sizes rapidly and accurately, independent of different operators and different instruments, making DLS very versatile. Samples that tend to coagulate can also be easily tracked by DLS. Although the exact size distribution cannot be determined, the correlation will be very sensitive enough to any changes in the distribution and give a fairly accurate response. DLS-based particle sizing is also widely used for biological samples such as bacteria, viruses, proteins, DNA and so on. Many applications have also been performed in crystal growth and polymer research.

Whereas there is a currently a huge volume of studies that have employed DLS, some of the more specific earlier examples of DLS applications include the spontaneous vesicle formation in a biological surfactant (ganglioside GM3) that was investigated by Cantu and group (133), while studies of BSA and lysozyme, two very low molecular weight proteins, were conducted by Dhadwal and group in 1993 (134). Studies of protein (lysozyme) crystallization (135), submicron emulsion systems (136), and use of a fiber optic backscattering device to observe particle-particle interaction in highly concentrated latex suspension (137) have all utilized DLS. A widely used industrial process, hydro metallurgical solvent extraction, was investigated by Neuman and group (138), in which they applied the DLS technique to very small sizes of ~ 2 nm. Caldwell's group (139) investigated emulsions by employing DLS and sedimentation field flow fractionation (SFFF) methods in a complementary mode. SFFF provides for a high-resolution fractionation of the sample, whereas DLS measures the sizes without the need to know the density of the sample.

As any with other particle sizing technique, DLS has advantages and disadvantages which must be kept in mind in trying to use it for different applications.

Advantages of DLS

Some of the desirable features of the DLS technique include:-

- Fast measurements, from seconds to minutes.
- The technique is absolute, from first principles, and calibration with a known size distribution is not necessary.
- Very small sample quantities can be measured (sample volume: 50 μL to 3 mL).
- Any suitable suspending liquid can be used provided it is non-absorbing, relatively clear and not too viscous.
- The technique is applicable to a broad range of particle sizes from about 2 nm to 6 μm .
- Instrumentation is commercially available for both research and QC measurements with automation including data analysis.
- Although the interpretation of particle size is least ambiguous with a narrow distribution, an effective diameter and polydispersity index are measurable even with broad distributions.

Disadvantages of DLS

- DLS does not produce a high-resolution histogram of the size distribution.
- Like other non-imaging techniques, an equivalent sphere diameter is usually, although not always, assumed of all the particles, and as such, information on the shape of the particles cannot be easily obtained.

- Dust particles in the sample can make measurement and interpretation of data quite difficult (120).

The research presented in this dissertation utilized DLS as the main particle sizing technique, to measure the size and size distribution of liposomes/lipid vesicles suspended in different buffer solutions. The instrument used was a Brookhaven 90PLUS Nanoparticle Analyzer (Brookhaven Instruments Corporation, Holtsville, NY), which has broad range sizing capabilities of 2 nm to 6 μm .

Transmission Electron Microscopy (TEM)

Theory

Transmission electron microscopy (TEM) is an established microscopy technique in which a beam of electrons is transmitted through an ultra thin specimen, interacting with the specimen as it passes through. An image is formed from the interaction of the electrons transmitted through the specimen; the image is then magnified and focused onto an imaging device such as a fluorescent screen, a layer of photographic film, or detected by a sensor such as a CCD camera.

TEM instruments have the desirable capability of imaging at a significantly higher resolution than light microscopes, owing to the small de Broglie wavelength of electrons. This makes it possible for the user to examine fine details of the specimen, which can be as small as a single column of atoms, making it thousands of times smaller than the smallest resolvable object in a light microscope. TEM is a major analysis method in a range of scientific fields both in the physical and biological sciences, including applications in cancer research, virology, materials science as well as pollution and semiconductor research.

At smaller magnifications, TEM image contrast is due to absorption of electrons in the material, due to the thickness and composition of the material. At higher magnifications however, complex wave interactions modulate the intensity of the image, requiring expert analysis of observed images. Alternate modes of use allow for the TEM instrument to observe modulations in chemical identity, crystal orientation, electronic structure and sample induced electron phase shift as well as the regular absorption based imaging (140, 141). The first TEM instrument was developed by Max Knoll and Ernst Ruska in 1931, and the same group developed the first TEM with resolving power greater than that of light in 1933, and the first commercial TEM became available in 1939 (142).

Theoretically, the maximum resolution (d) that one can obtain with a light microscope is limited by the wavelength of the photons (λ) that are being used to probe the sample, and the numerical aperture (NA) of the system (141) as shown in Equation 2-10.

$$d = \lambda / 2n \sin \alpha \approx \lambda / 2 \text{ NA} \quad (2-10)$$

To overcome the limitations of the relatively large wavelength of visible light (λ s of 400–700 nm), early twentieth century scientists theorized the use of electrons. Like all matter, electrons have both wave and particle properties (as shown by Louis-Victor de Broglie), and the wave-like properties imply that a beam of electrons can be made to behave like a beam of electromagnetic radiation. The wavelength of electrons is found by equating the de Broglie equation to the kinetic energy of an electron. An additional correction must be made to account for relativistic effects, such as in a TEM instrument, an electron's velocity approaching the speed of light, C shown in Equation 2-11 (143).

$$\lambda \approx h / [\sqrt{2m_0 E (1+ E/2m_0C^2)}] \quad (2-11)$$

where h is Planck's constant ($6.626068 \times 10^{-34} \text{ m}^2 \text{ kg / s}$), m_0 is the rest mass of an electron and E is energy of the accelerated electron.

Electrons are usually generated in an electron microscope by a process known as thermionic emission from a filament, usually tungsten, in the same manner as a light bulb, or alternatively by field electron emission (144). The electrons are then accelerated by an electric potential that is measured in volts and focused by electrostatic and electromagnetic lenses onto the sample. The transmitted beam contains information about electron density, phase and periodicity, and this beam is used to form an image. The general experimental layout of a TEM instrument is illustrated in Figure 2-8.

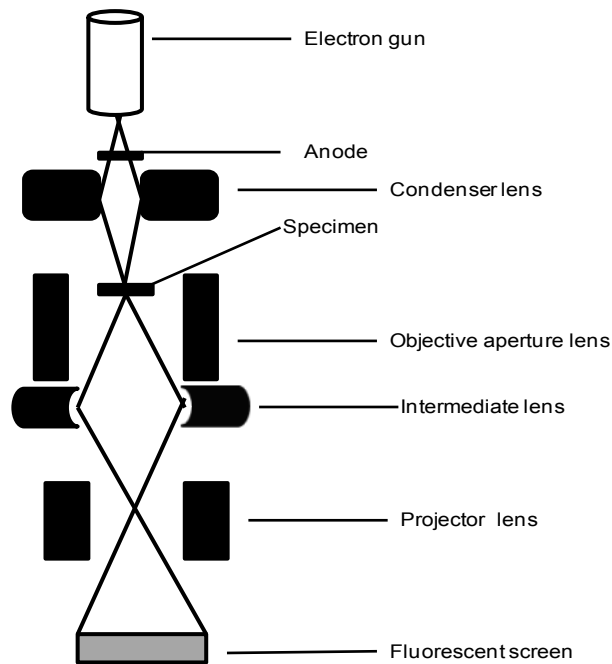


Figure 2-8. Layout of major components in a basic transmission electron microscopy (TEM) instrument.

A typical TEM instrument consists of several important components, including an electron emission source for generation of the electron stream (electron gun), a vacuum system in which the electrons travel, a series of electromagnetic lenses and

electrostatic plates that allow for guiding and manipulation of the beam as required, imaging devices to create an image from the electrons that exit the system and a specimen holder. By connecting the electron gun to a high voltage source (typically ~100-300 kV) the gun will, with sufficient current, emit electrons by thermionic emission from tungsten hairpin cathodes, or LaB₆ rods or by field emission from pointed tungsten filaments (140). Once extracted, the upper lenses of the TEM allow for the formation of the electron probe to the desired size and location for later interaction with the sample (145).

Manipulation of the electron beam can be performed using two physical effects. The interaction of electrons with a magnetic field will cause electrons to move according to the right hand rule, thus allowing for electromagnets to manipulate the electron beam. The use of magnetic fields allows for the formation of a magnetic lens of variable focusing power, in which the lens shape originates due to the distribution of magnetic flux. Alternatively, electrostatic fields can cause the electrons to be deflected through a constant angle. Coupling of two deflections in opposing directions with a small intermediate gap allows for the formation of a shift in the beam path, which is mostly used in TEM for beam shifting (140, 145).

The lenses in a TEM allow for beam convergence. The angle of convergence can be varied, which gives the TEM the ability to change magnification simply by modifying the amount of current that flows through the coil, quadrupole or hexapole lenses. The quadrupole lens is an arrangement of electromagnetic coils at the vertices of the square, enabling the generation of lensing magnetic fields, while the hexapole configuration enhances the lens symmetry by using six, rather than four coils. Typically,

the optics in a TEM consist of a three-stage lens system: the condenser lenses, the objective lenses, and the projector lenses, as shown in Figure 2-8. The condenser lenses are responsible for primary beam formation, while the objective lenses focus the beam down onto the sample itself. The projector lenses are used to expand the beam onto the phosphor screen or other imaging device, such as film. The magnifications attainable in a TEM are due to the ratio of the distances between the specimen and the objective lens' image plane (140). Additional quad or hexapole lenses allow for the correction of asymmetrical beam distortions, known as astigmatism. It is worth noting that TEM optical configurations differ significantly with implementation and different manufacturers using custom lens configurations, such as in spherical aberration corrected instruments, or TEMs utilizing energy filtering to correct electron chromatic aberration (145).

Apertures are annular metallic plates, through which electrons that are further than a fixed distance from the optical axis may be excluded. These apertures consist of a small metallic disc that is sufficiently thick to prevent electrons from passing through the disc, while permitting axial electrons. Apertures are important because they decrease the beam intensity as electrons are filtered from the beam, which is particularly desirable for beam sensitive samples. The filtering process by apertures also removes electrons that are scattered to high angles due to unwanted processes such as spherical or chromatic aberration, or due to diffraction from interaction within the sample (146). Apertures devices can either be fixed within the column, such as at the condenser lens, or are a movable aperture, which can be inserted, withdrawn from the beam path, or moved in the plane perpendicular to the beam path.

Imaging systems in a TEM consist of a phosphor screen, which may be made of fine (10-100 μm) particulate zinc sulphide, for direct observation by the operator, or an image recording system such as film based or doped Yttrium aluminum garnet (YAG, $\text{Y}_3\text{Al}_5\text{O}_{12}$) screen coupled CCDs (147). These devices can be removed or inserted into the beam path by the operator as required. Contrast formation in the TEM depends greatly on the mode of operation. Complex imaging techniques, which utilize the unique ability to change lens strength or to deactivate a lens, allow for many operating modes.

The most common mode of operation for a TEM is the bright field imaging mode, in which the contrast formation, when considered classically, is formed directly by occlusion and absorption of electrons in the sample. Thicker regions of the sample or regions with a higher atomic number will appear dark, while regions with no sample in the beam path will appear bright, hence the term "bright field". The image is effectively assumed to be a simple two dimensional projection of the sample down the optical axis, and to a first approximation may be modeled via Beer's law (144).

The need for a vacuum system in TEM

To increase the mean free path of the electron-gas interaction, a standard TEM is evacuated to low pressures, typically on the order of 10^{-4} Pascal (147), which serves two purposes. First, this allows for the voltage difference between the cathode and the ground without generating an arc, and secondly it reduces the collision frequency of electrons with gas atoms to negligible levels, an effect that is characterized by the mean free path. For these reasons, TEM specimen holders and film cartridges are routinely inserted or replaced to allow for a system that has the ability to re-evacuate on a regular basis. Consequently, TEMs are equipped with multiple pumping systems and airlocks and are not permanently vacuum sealed (148). High-voltage TEMs require ultra high

vacuums on the range of 10^{-7} to 10^{-9} Pa to prevent generation of an electrical arc, particularly at the TEM cathode (149). Poor vacuum in a TEM can result in several problems, including deposition of gas inside the TEM onto the specimen as it is being viewed through a process known as electron beam-induced deposition, or in more severe cases damage to the cathode from an electrical discharge (149).

TEM specimen stage designs include airlocks to allow for insertion of the specimen holder into the vacuum with minimal increase in pressure in other areas of the microscope. The specimen holders are adapted to hold a standard size of grid upon which the sample is placed or a standard size of self-supporting specimen. Standard TEM grids have a 3.05 mm diameter ring, with a thickness and mesh size ranging from a few to 100 μm . The sample is placed onto the inner-meshed area with a diameter of ~ 2.5 mm. Ideal grid materials are copper, molybdenum, gold or platinum. The grid is placed into the sample holder which is paired with the specimen stage (140, 147).

Once inserted into a TEM, the sample often has to be manipulated to present the region of interest to the beam, such as in single grain diffraction, in a specific orientation. To accommodate this, the TEM stage allows for the translation of the sample in the XY plane of the sample, for Z height adjustment of the sample holder, and usually for at least one rotation degree of freedom for the sample. Thus a TEM stage may provide four degrees of freedom for the motion of the specimen. Most modern TEMs provide the ability for two orthogonal rotation angles of movement (140) with specialized holder designs called double-tilt sample holders. The design criteria of TEM

stages are complex, owing to the simultaneous requirements of mechanical and electron-optical constraints and have thus generated many unique implementations.

Sample preparation methods in TEM

Sample preparation for TEM specimens can pose several challenges. Ideally, any specimen preparation techniques for TEM must avoid the collapse or loss of specimen structures during preparation and observation, since the specimens are viewed in a vacuum (150). Additionally, biological specimens are extremely sensitive to bombardment by electrons, which is a significant factor in the high noise levels of electron micrographs (151, 152). The incident electrons lose large amounts of energy by inelastic collisions, forming highly reactive ions and free radicals, which may disrupt bonds and fragment molecules in the specimen. Incident electrons can also directly transfer their momentum to atomic nuclei in the structure, resulting in atom displacement. The atoms that are present in biological molecules (such as C, H, O, N, etc.) scatter electrons weakly, producing images with low intrinsic contrast, and so in order to increase the attainable resolution, electron-beam damage to the specimen should be minimized, whereas image contrast should be maximized (140).

TEM specimens are also required to be only a few hundreds of nanometers thick. High quality samples will have a thickness that is comparable to the mean free path of the electrons that travel through the samples, which may be only a few tens of nanometers. Consequently, preparation of TEM specimens is specific to the material under analysis and the desired information needed from the specimen, hence many generic techniques have been used for the preparation of the required thin sections (141).

Materials that have dimensions small enough to be electron transparent, such as powders or nanotubes, can be quickly prepared by the deposition of a dilute sample containing the specimen onto support grids or films. For biological science applications, biological specimens can be fixated using either a negative staining material such as uranyl acetate or by plastic embedding in order to withstand the instrument vacuum and facilitate handling. Samples may also be fast-frozen and held at liquid nitrogen temperatures after embedding in vitreous ice (153). In material science and metallurgy, the specimens tend to be naturally resistant to vacuum, but still must be prepared as a thin foil, or etched so that some portion of the specimen is thin enough for the beam to penetrate. Constraints on the thickness of the material may be limited by the scattering cross-section of the atoms from which the material is comprised (150).

Negative staining

The TEM studies performed in this dissertation employed negative staining as a preparative method for lipid vesicles. Just like in light microscopy where samples can be enhanced by stains that absorb light, TEM samples of biological tissues can also utilize heavy metals with high atomic numbers as stains to enhance contrast. The stain absorbs electrons or scatters part of the electron beam which otherwise is projected onto the imaging system. Compounds of heavy metals such as osmium, lead, or uranium have been used for negative staining-TEM studies to selectively deposit electron-dense atoms in or on the sample in desired cellular or protein regions. Although negative staining is technically simple to perform, provides high contrast and has a low sensitivity to the electron beam (150, 151), it still suffers from several disadvantages. For instance, it only shows surface detail, with the distribution of the heavy metal atoms rather than the density of the specimen being revealed. (154).

Negative staining-TEM also has limited resolution of 1–2 nm because of stain movement during imaging (151, 155). To overcome some of these limitations, negative staining is sometimes complemented with electron cryo-microscopy (or cryo-electron microscopy, cryo-EM), a technique that has revolutionized the analysis of macromolecular structure by electron microscopy and 3D reconstruction studies (150, 152, 156).

In cryo-EM, samples are embedded in vitreous ice on a “holey” carbon grid and maintained at low temperatures (100 –113 K) while under the electron beam (156). Vitreous ice is a super cooled liquid that is produced when water is very rapidly cooled below 273 K (at about 10^5 Ks^{-1}) (150), which avoids damage to the specimen by ice crystal formation. Vitreous ice forms a structureless medium in which the molecules are hydrated, despite the requirement for vacuum conditions. The low temperatures result in a very slow rate of sublimation of the ice, and the specimen is therefore imaged under conditions that are a lot like those in its native environment. The low temperature and the use of low doses of electrons minimize beam damage (157).

TEM Applications

Transmission electron microscopy is a well established imaging technique for applications in both the physical and biological sciences, due to its capabilities for high magnification and resolution. In the biomedical field, TEM has proved rewarding as a diagnostic tool, especially in basic and clinical virology. Since it was first utilized in the rapid diagnosis of smallpox, TEM developed to a diagnostic routine in the early 1960s, utilizing negative staining for sample preparation (158). A routine procedure for negative staining was first developed for the examination of virus particles (159, 160), and was

subsequently applied to sub cellular fractions (161), other cell membrane preparations (162), and artificial membrane systems (163).

TEM has since been versatile in providing structural and morphological information of biomembranes such as proteins and lipids. For instance, electron microscopy is very useful as an assay for the purity and homogeneity of preparations of oligomeric proteins because it permits one to distinguish between different assembly forms and nonspecific aggregates that all may be present within the same preparation, and which may be difficult to discriminate by other means (164).

More importantly, negative staining-TEM has provided a means by which aqueous suspensions of phospholipids in a liposomal state can be characterized as unilamellar and multi-lamellar systems of varying dimensions (55). It has been demonstrated that TEM applied to negatively stained or freeze-fractured liposomes constitutes an appropriate method to study the formation and morphology of liposome structures and their interaction with biological tissue (165). These techniques have also been shown to be very convenient in the characterization of the intermediate aggregates formed during the interaction of different surfactants with liposomes (166-168).

Negative staining-TEM imaging was utilized in the studies presented in this dissertation, to characterize the structural morphology and size analysis of hydrated dispersions and extruded vesicles of phospholipid membranes. Negative staining-transmission electron microscopy (TEM) images were obtained using a Hitachi H-7000 transmission electron microscope operated at 75-100 kV, with a Soft-Imaging System MegaViewIII with AnalySIS digital camera (Lakewood, CO). Further details of the TEM

instrument and specific sample preparation procedures using negative staining are presented in the experimental section of Chapters 3, 4 and 5.

Fluorescence Resonance Energy Transfer (FRET)

Theory

Fluorescence or Förster resonance energy transfer (FRET) is a process by which a fluorophore (the donor) in an excited state transfers its energy to a neighboring molecule (the acceptor) by non-radiative dipole-dipole interactions, and although not necessary, in most cases the acceptor is also a fluorescent dye (169, 170). FRET can be an accurate measurement of molecular proximity at angstrom distances (10–100 Å), and highly efficient if the donor and acceptor are positioned within the Förster radius (the distance at which half the excitation energy of the donor is transferred to the acceptor, typically 3–6 nm). Consequently, FRET measurements can be utilized as an effective molecular ruler for determining distances between biomolecules labeled with an appropriate donor and acceptor fluorophore when they are within 10 nanometers of each other (171, 172).

The theory behind energy transfer is based on the concept of treating an excited fluorophore as an oscillating dipole that can undergo an energy exchange with a second dipole having a similar resonance frequency. Consequently, resonance energy transfer is analogous to the behavior of coupled oscillators, such as a pair of tuning forks vibrating at the same frequency. In contrast, radiative energy transfer requires emission and reabsorption of a photon and depends on the physical dimensions and optical properties of the specimen, as well as the geometry of the container and the wavefront

pathways. Unlike radiative mechanisms, resonance energy transfer can yield a significant amount of structural information concerning the donor-acceptor pair (171).

Principles of FRET

The process of resonance energy transfer (RET) can take place when a donor fluorophore in an electronically excited state transfers its excitation energy to a nearby chromophore, referred to as the acceptor. Typically, if the fluorescence emission spectrum of the donor molecule overlaps the absorption spectrum of the acceptor molecule, and the two are within a minimal spatial radius, the donor can directly transfer its excitation energy to the acceptor through long-range dipole-dipole intermolecular coupling (169, 171). A theory proposed by Theodor Förster in the late 1940s initially described the molecular interactions involved in resonance energy transfer, and Förster's equation (Equation 2-12) defines the relationship between the transfer rate, inter-chromophore distance, and spectral properties of the involved chromophores (169, 173).

Because resonance energy transfer is a non-radiative quantum mechanical process, it does not require a collision or involve production of heat. When energy transfer occurs, the acceptor molecule quenches the donor molecule fluorescence, and if the acceptor is itself a fluorophore, increased or sensitized fluorescence emission is observed, as illustrated in Figure 2-9 of the FRET Jablonski diagram. The FRET phenomenon can be observed by exciting a specimen containing both donor and acceptor molecules with light of wavelengths corresponding to the absorption maximum of the donor fluorophore, and detecting light emitted at wavelengths centered near the emission maximum of the acceptor. An alternative detection method is to measure the

fluorescence lifetime of the donor fluorophore in the presence and absence of the acceptor (171, 174).

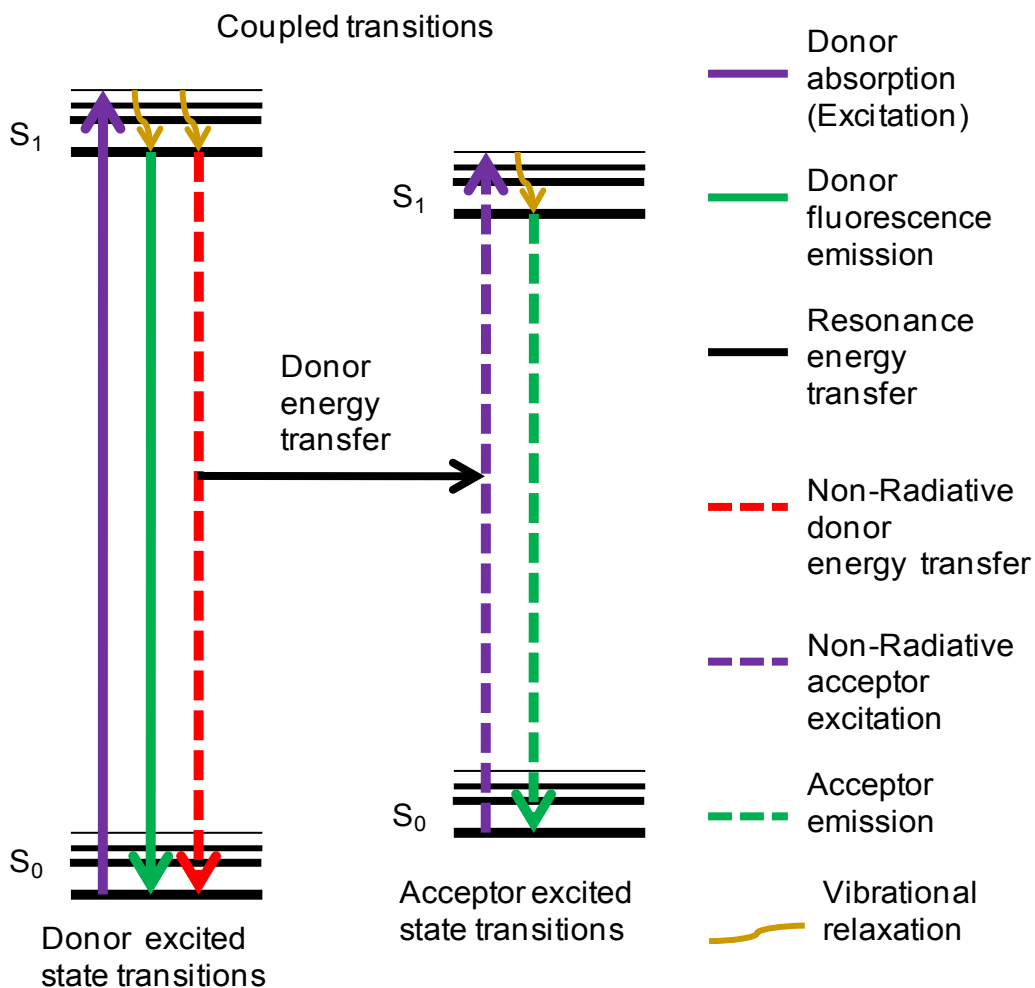


Figure 2-9. A Jablonski diagram illustrating the coupled transitions involved between the donor emission and acceptor absorbance in FRET.

In the FRET Jablonski diagram in Figure 2-9, absorption and emission of the donor molecule are represented by straight purple and green vertical arrows respectively, while vibrational relaxation is indicated by wavy yellow arrows. In the presence of a suitable acceptor, the donor fluorophore can transfer excited state energy directly to the acceptor without emitting a photon, as illustrated by a black straight arrow

in Figure 2-9. The resulting sensitized fluorescence emission has characteristics similar to the emission spectrum of the acceptor.

In summary, in order for resonance energy transfer to occur, three specific conditions must be fulfilled:

(i) The emission spectrum of the donor fluorophore must overlap the acceptor molecule's absorption spectrum as illustrated in Figure 2-10, and although the acceptor can be (and often is) a fluorophore, this is not always a requirement for FRET.

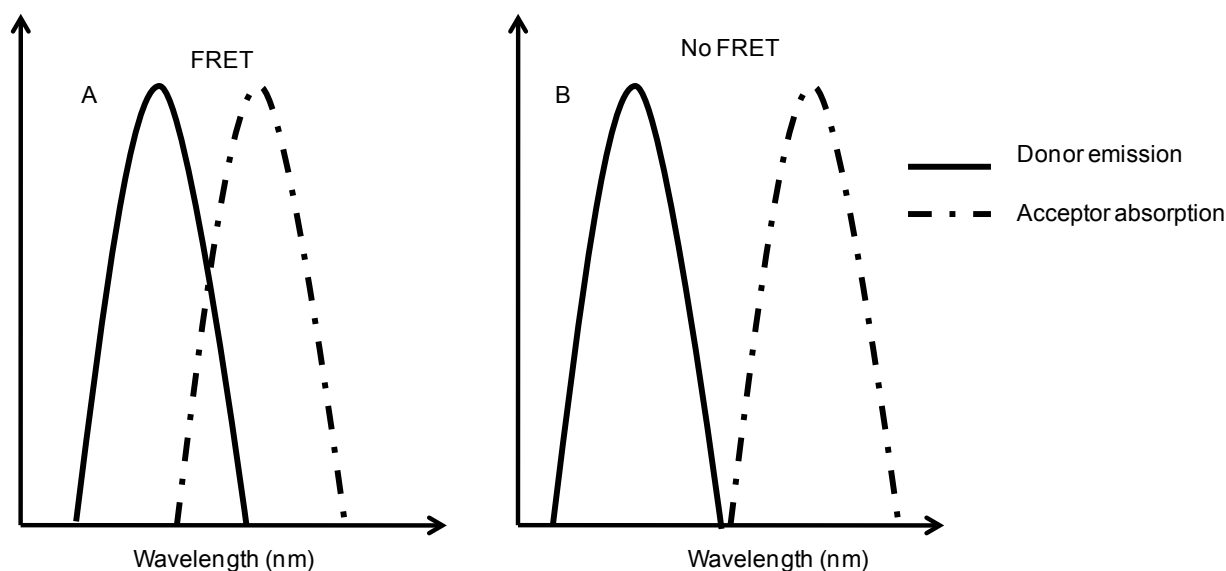


Figure 2-10. A) Overlap of the emission spectrum of the donor and acceptor absorption spectrum results in FRET. B) Lack of overlap of the spectra means no FRET observed.

(ii) The donor and acceptor molecules must be positioned within a range of 1 to 10 nanometers of each other. Equation 2-12 derived by Förster shows that the energy transfer efficiency between donor and acceptor molecules decreases as the sixth power of the distance separating the two (175). Hence, the ability of the donor fluorophore to

transfer its excitation energy to the acceptor by non-radiative interaction decreases sharply with increasing distance between the molecules, limiting the FRET phenomenon to a maximum donor-acceptor separation radius of approximately 10 nanometers. The distance dependence of the resonance energy transfer process is the primary basis for its utility in investigation of molecular interactions. In living cell studies involving molecules labeled with donor and acceptor fluorophores, resonance energy transfer will occur only between molecules that are close enough to interact biologically with one another (171, 173).

(iii) The fluorescence lifetime of the donor molecule must be of sufficient duration to permit the event to occur. Both the rate (K_T) and the efficiency (E_T) of energy transfer are directly related to the lifetime of the donor fluorophore in the presence and absence of the acceptor according to Förster's theory described by Equation 2-12.

$$K_T = (1/\tau_D) \cdot [R_0/r]^6 \quad (2-12)$$

where R_0 is the Förster critical distance, τ_D is the donor lifetime in the absence of the acceptor and r is the distance separating the donor and acceptor molecules.

The Förster critical distance R_0 is defined as the acceptor-donor separation radius for which the transfer rate equals the rate of donor decay (de-excitation) in the absence of acceptor. In essence, when the donor and acceptor radius (r) equals the Förster distance, then the transfer efficiency is 50 percent. At this separation radius, half of the donor excitation energy is transferred to the acceptor via resonance energy transfer, while the other half is dissipated through a combination of all the other available processes, including fluorescence emission (171, 173).

Ideally, the Förster critical distance is the maximal separation length between donor and acceptor molecules under which resonance energy transfer will still occur. The critical distance value typically falls within a range of 2 to 6 nanometers, which is on the order of many protein molecular dimensions. The critical distance range also corresponds to several other biologically significant dimensions, such as cell membrane thickness and the distance separating sites on proteins having multiple subunits (171). The value of R_0 (in nanometers) may be calculated as shown in Equation 2-13.

$$R_0 = 2.11 \times 10^{-2} \cdot [k^2 \cdot J(\lambda) \cdot \eta^{-4} \cdot Q_D]^{1/6} \quad (2-13)$$

where k^2 is a factor describing the relative orientation in space between the transition dipoles of the donor and acceptor, $J(\lambda)$ is the overlap integral in the region of the donor emission and acceptor absorbance spectra (the wavelength is expressed in nm), η represents the refractive index of the medium, and Q_D is the quantum yield of the donor molecule (171, 175).

The efficiency of energy transfer E_T , is a measure of the fraction of photons absorbed by the donor that are transferred to the acceptor, and is related to the donor-acceptor separation distance, r , by Equations 2-14 and 2-15.

$$r = R_0 \cdot [1/E_T - 1]^{1/6} \quad (2-14)$$

$$E_T = 1 - (\tau_{DA}/\tau_D) \quad (2-15)$$

where τ_{DA} is the donor lifetime in the presence of the acceptor and τ_D is the donor lifetime in the absence of the acceptor. So by measuring the donor fluorescence lifetime in the presence and absence of an acceptor (which is indicative of the extent of donor quenching due to the acceptor), it is possible to determine the distance separating donor and acceptor molecules (175). The rate of energy transfer therefore depends

upon the extent of spectral overlap between the donor emission and acceptor absorption spectra, the quantum yield of the donor, the relative orientation of the donor and acceptor transition dipole moments, and the distance separating the donor and acceptor molecules (171).

Methods for measurement of FRET

Methods that have been used for measuring FRET can be divided into four fundamental categories (176):

- (i) methods that monitor changes in donor fluorescence,
- (ii) methods that examine changes in acceptor fluorescence,
- (iii) methods that simultaneously measure changes in both donor and acceptor fluorescence using spectral imaging and
- (iv) methods that monitor changes in the orientation of the fluorophores

The most direct methods for measuring FRET efficiencies are based on monitoring changes in donor fluorescence (either lifetime or intensity) in the presence and absence of acceptor. The two most commonly used approaches are fluorescent lifetime imaging (FLIM-FRET) and acceptor bleaching. In FLIM-FRET, FRET is measured by monitoring changes in a donor's fluorescent lifetime, in terms of how rapidly a population of fluorophores emits light after a short excitation pulse) (177-179). Acceptor bleaching is an approach that measures the intensity of donor fluorescence before and after photobleaching of acceptor molecules (180-182). The fluorescent lifetime of a donor should reduce if FRET is occurring hence by comparing the lifetime of the donor in the presence and absence of acceptors, the FRET efficiency can be measured.

Measuring the fluorescence intensity of a donor before and after photobleaching acceptors is also equivalent to measuring the intensity of the donor in the presence and

absence of acceptors. Bleaching the acceptor should produce an increase in the donor's fluorescent emission if FRET had been occurring. An advantage of acceptor bleaching is that it can be performed on normal wide-field microscopes (176). The most popular methods used for measuring FRET involve monitoring acceptor emission as a result of donor excitation. The main advantage of this approach is that, like acceptor bleaching, it can be performed on simple wide-field fluorescent microscopes that are widely used in cell biology laboratories (183).

Microscope configurational parameters for fluorescence resonance energy transfer investigations vary with the requirements of the fluorophores, specimen, and imaging mode(s), although any upright or inverted microscope can be retrofitted for FRET microscopy. In general, the microscope should be equipped with a high-resolution (12-bit) cooled and intensified CCD camera system coupled to quality interference filters having low levels of crosstalk and band pass regions corresponding closely to the fluorophore spectra. The detector sensitivity determines how narrow the filter band pass can be and still enable data acquisition to proceed at acceptable speeds with a minimum of spectral bleed-through noise. In most cases, a single dichromatic mirror coupled to excitation and emission filter wheels or sliders should be used to acquire images in order to minimize or eliminate image shifts.

Biological Applications of FRET

In biological investigations, the most common applications of fluorescence resonance energy transfer are the measurement of distances between two sites on a macromolecule, such as a protein, nucleic acid or lipid, or the examination of in vivo interaction between biomolecular entities. Proteins can be labeled with synthetic fluorophores or immunofluorescent fluorophores to serve as the donor and acceptor,

although advances in fluorescent protein genetics now enable labeling of specific target proteins with a variety of biological fluorophores having differing spectral characteristics. In many cases, the amino acid tryptophan is used as an intrinsic donor fluorophore, which can be coupled to any number of extrinsic probes serving as an acceptor (171, 174).

Advances in fluorescent probe development have produced smaller and more stable molecules with new mechanisms of attachment to biological targets. Fluorophores have also been developed with a wide range of intrinsic excited state lifetimes, and a significant effort is being placed on development of a greater diversity in genetic variations of fluorescent proteins. Entirely new classes of fluorescent materials, many of which are smaller than previous fluorophores and allow evaluation of molecular interactions at lower separation distances, promise to improve the versatility of labeling and lead to new applications of the FRET technique (171).

The simplicity and sensitivity of fluorescence assays has also made them highly useful for membrane fusion and vesicle contents leakage applications. For instance, the NBD–Rhodamine assay has been used in monitoring the fusion of cationic liposomes or their DNA complexes with cells (184), the fusion of secretory granules with liposomes (185), and virus fusion with liposomes (186, 187). FRET has also been used to test the hypothesis that raft proteins or lipids are enriched in domains with sub-micron dimensions (173, 188-191)). For proteins and lipids in membranes, FRET can occur by chance if the concentration of donors and acceptors is high enough. However, it is possible to distinguish this type of “non-specific” FRET from FRET that occurs as the

result of clustering of proteins within lipid rafts, as well as to test various models of domain organization, with the aid of mathematical modeling (181, 192).

Based on FRET criteria, some raft proteins have shown little evidence for clustering in FRET studies (181, 193), while others appear to be clustered in sub-micron domains, as predicted by the lipid raft model (194-196). In addition to providing information about the size and area fraction of lipid rafts, FRET also holds great potential for revealing transient interactions between raft-associated molecules. This was illustrated by a recent FRET study of dynamic events that occur during B-cell signaling (197).

For FRET studies monitoring vesicle fusion or vesicle leakage, several self-quenching fluorophores or FRET pairs have been utilized. For instance, the release of aqueous contents that may accompany divalent cation-induced vesicle fusion has been monitored by using liposomes containing carboxyfluorescein (198-201). The intracellular fate of liposomes and the intracytoplasmic delivery of liposome contents were assessed with either carboxyfluorescein (202), which is permeable through liposome and endosome membranes at low pH (203, 204), or calcein, which is retained in liposomes at low pH (205-208). These fluorophores have also been used in monitoring the channel-forming properties of bacterial and other toxins (209, 210), membrane destabilization by viral proteins (211), immune complex-mediated lysis of liposomes (212), the stability of liposomes containing archaeal bolaform lipids (213), and the pH sensitivity of liposomes (207, 208).

To monitor the leakage of aqueous contents of liposomes at neutral pH, carboxyfluorescein or calcein is encapsulated at self-quenching concentrations inside liposomes. Their leakage into the external medium, and hence dilution, results in a decrease of self-quenching and in an increase in the fluorescence signal (202-204). The FRET assay for leakage of ANTS–DPX from liposomes at acidic pH results in an increase in fluorescence and was used initially to examine the destabilization of liposomes at low pH (214). The assay has also been employed to assess the interaction with liposomal membranes of surfactant-associated proteins (215) and peptides derived from viral fusion proteins (216-218).

The FRET assay was utilized in this dissertation to monitor the leakage of vesicle dye-contents encapsulated in BMP liposomes. For studies at neutral pH 7.4, calcein was used whereas the FRET pair, ANTS-DPX was used for experiments under acidic pH 4.5. Details of liposome preparation and performance of the assay are discussed in the experimental section of Chapter 3, under the FRET vesicle leakage assays subsection.

Chromatography Separations

Chromatography refers to a set of laboratory techniques utilized for the separation of mixtures. Generally, it involves passing a mixture that is dissolved in a mobile phase through a stationary phase, which separates the analyte to be measured from other molecules in the mixture based on differential partitioning between the mobile and stationary phases. Differences in the compounds' partition coefficient results in differential retention on the stationary phase, hence separation.

Chromatography may be preparative or analytical: preparative chromatography is used mainly to separate the components of a mixture for further use, so it is also a form of purification, whereas analytical chromatography is done usually with smaller amounts of material and is used for measuring the relative proportions of analytes in a mixture. Two types of chromatography were utilized in our studies; thin layer chromatography (TLC) and column chromatography. TLC was used to determine the integrity of our lipid dispersions and vesicles. Column chromatography was used to separate vesicle-encapsulated fluorophore from the free fluorophore, and the leakage of encapsulated fluorophore into the bulk solution was later monitored by FRET.

Thin Layer Chromatography (TLC)

Thin layer chromatography (TLC) was the earliest chromatographic method used to assess phospholipids, and is still frequently used today. TLC is performed on a sheet of glass, plastic, or aluminum foil that is coated with a thin layer of adsorbent material, mostly silica gel, aluminum oxide, or cellulose. The adsorbent material is known as the stationary phase (219). Once the sample is applied on the plate, a solvent or solvent mixture, known as the mobile phase, is drawn up the plate via capillary action, and because different analytes ascend the TLC plate at different rates or speeds, separation is achieved (220).

TLC plates are usually prepared by mixing the adsorbent, such as silica gel, with a small amount of inert binder like calcium sulfate (gypsum) and water. This mixture is spread as thick slurry on an unreactive carrier sheet, usually glass, thick aluminum foil, or plastic. The resultant plate is dried and activated by heating in an oven for half an hour at 110 °C. The thickness of the adsorbent layer is typically ~ around 0.1 – 0.25 mm for analytical purposes and ~0.5 – 2.0 mm for preparative TLC (220).

To perform TLC, a small spot of solution containing the sample is applied to a plate, about one centimeter from the base. The plate is then dipped in to a suitable solvent, such as hexane or ethyl acetate, and placed in a sealed container. The solvent moves up the plate by capillary action and meets the sample mixture, which is dissolved and carried up the plate by the solvent. Different compounds in the sample mixture elute at different speeds due to the differences in their interaction with the stationary phase, and differences in solubility in the solvent. By changing the solvent, or using a mixture of solvents, the separation of components (measured by the retention factor, R_f value) can be adjusted (219, 220).

Separation of compounds in TLC is based on the competition of the solute and the mobile phase for binding with the stationary phase. For instance, if normal phase silica gel is used as the stationary phase it can be considered polar. In a situation with two compounds that differ in polarity, the most polar compound would have a stronger interaction with the silica and would therefore bind more strongly with the stationary phase. Consequently, the less polar compound moves higher up the plate, resulting in a higher R_f value. On the other hand, if the mobile phase is changed to a more polar solvent or mixture of solvents, it would be more capable of displacing solutes from the silica binding places and all compounds on the TLC plate will move higher up the plate. For instance if a mixture of ethyl acetate and heptane are used as the mobile phase, adding more ethyl acetate results in higher R_f values for all compounds on the TLC plate, and changing the polarity of the mobile phase will not result in reversed order of elution of the compounds on the TLC plate (219, 221).

In most cases, the chemicals being separated are colorless; hence several methods exist to visualize the spots. A small amount of a fluorescent compound, usually manganese-activated zinc silicate, can be added to the adsorbent, allowing the visualization of spots under a blacklight (UV₂₅₄), hence the adsorbent layer will fluoresce light green by itself, but spots of analyte quench this fluorescence. Another approach is the use of iodine vapors as a general unspecific color reagent, into which the TLC plate is dipped or sprayed onto the plate. For lipid analysis, the chromatogram may be transferred to a Polyvinylidene Fluoride (PVDF) membrane and then subjected to further analysis, for example mass spectrometry. Once visible, the R_f value, or Retention factor of each spot can be determined by dividing the distance traveled by the product by the total distance traveled by the solvent (the solvent front). These values depend on the solvent used, and the type of TLC plate (222, 223).

Because of its speed, better separation efficiency than paper chromatography, and the ability to choose between different stationary phases, TLC has found versatile applications, including assaying the radiochemical purity of radiopharmaceuticals, determination of plant pigments, detection of pesticides or insecticides in food, analyzing the dye composition of fibers in forensics, or identifying compounds present in a given substance, monitoring organic reactions and for the qualitative analysis of reaction products (221, 224, 225).

Column Chromatography

In column chromatography, the stationary bed is within a tube. The particles of the solid stationary phase or the support coated with a liquid stationary phase may fill the entire inside volume of the tube (packed column) or be concentrated on or along the

inside tube wall, leaving an open, unrestricted path for the mobile phase in the middle part of the tube (open-tubular column) (226, 227).

The classical preparative chromatography column is a glass tube with a diameter from 50 mm and a height of about 50 cm to 1 m with a tap at the bottom. To prepare a column, the dry method or the wet method can be employed. In the dry method, the column is first filled with the dry stationary phase powder, followed by the addition of mobile phase, which is flushed through the column until it is completely wet, and then henceforth the column is never allowed to run dry. For the wet method, slurry is prepared of the eluent with the stationary phase powder and then carefully poured into the column, avoiding any formation of air bubbles. An organic solvent is pipetted on top of the stationary phase, and this layer is usually topped with a small layer of sand, cotton or glass wool to protect the shape of the organic layer from the velocity of newly added eluent. Eluent is slowly passed through the column to advance the organic material. Often a spherical eluent reservoir or an eluent-filled and stoppered separating funnel is put on top of the column (226).

The individual analytes are retained by the stationary phase depending on how they interact with it, and separate from each other while they are eluting at different rates through the column, arriving at the end of the column one at a time. During the elution process, the eluent is collected in a series of fractions. The composition of the eluent flow can be monitored and each fraction is analyzed for dissolved compounds using detection methods such as analytical chromatography, UV absorption, or fluorescence. Colored compounds or fluorescent compounds with the aid of an UV lamp can be easily seen through the glass wall as moving bands (228).

The stationary phase or adsorbent in column chromatography is a solid. The most common solid stationary phases for column chromatography are silica gel and alumina, although cellulose powder has also been used. The mobile phase or eluent can be either a pure organic solvent or a mixture of different solvents. The mobile phase is chosen so that the retention factor value (R_f) of the compound of interest is approximately 0.2 - 0.3, in order to minimize the time and amount of eluent used to run the chromatography. The eluent is also chosen in such a way that different compounds can be separated effectively (219).

A faster flow rate for the eluent minimizes the time required to run a column and therefore minimizes diffusion, resulting in a better separation (229), as illustrated by Van Deemter's equation in Equation 2-16.

$$H = A + B/u + C.u \quad (2-16)$$

where A is Eddy-diffusion, B is longitudinal diffusion, C is the mass transfer kinetics of the analyte between mobile and stationary phases and u is the linear velocity. A is equivalent to the multiple paths taken by the chemical compound, and in open tubular capillaries this term will be zero as there are no multiple paths. The multiple paths occur in packed columns where several routes through the column packing are possible, which results in band spreading. B/u is equal to the longitudinal diffusion of the particles of the compound, whereas C.u is equal to the equilibration point. In a column, there is an interaction between the mobile and stationary phases, C.u accounts for this (229).

A simple laboratory column runs by gravity flow, and the flow rate of such a column can be increased by extending the fresh eluent-filled column above the top of

the stationary phase or decreased by the tap controls. Better flow rates can be achieved by using a pump or by using compressed gas such as air, nitrogen, or argon, to push the solvent through the column (referred to as flash column chromatography) (219, 228).

Column chromatography has been used for both analytical and preparative separations for well over four decades. It has now largely replaced planar chromatography, which was most widely used in the 1940s–1960s, owing to the fact that column chromatography is much easier to instrumentalize than planar chromatography and that analytes are far easier to detect and quantitate in a stream of solution than in a layer of particles (226). For studies in this dissertation, Sephadex G-50 Fine column (5 cm internal diameter, 100 cm height) from GE Healthcare was used to separate fluorophore-loaded BMP vesicles from “free” or unencapsulated fluorophore, and the eluted fractions were analyzed by fluorescence resonance energy transfer (FRET).

CHAPTER 3 INVESTIGATION OF BMP VESICLE SIZE AND MORPHOLOGY IN MODEL MEMBRANES

Introduction

Bis(monoacylglycero)phosphate (BMP) is a negatively charged phospholipid found in elevated concentrations in the late endosome. BMP represents less than 1 mol % of the total phospholipid mass in most tissues and cell types (45, 46), although in the late endosome, the concentration of BMP is about 15 mol % of the total lipid content of the organelle (44, 94, 95) and can comprise as much as 70 mol % of the lipid composition of the intraendosomal vesicles (94).

Endosomes are intracellular organelles that act as a staging area for sorting endocytosed material either back to the plasma membrane for recycling or to specialized organelles such as lysosomes for degradation (46, 230). Endosomes can be identified by the presence of vesicular bodies (VBs) inside the lumen of a limiting membrane or by lipid composition (44, 97). Early endosomes have a limiting membrane with a lipid composition very similar to that of the plasma membrane, whereas late endosomes are characterized by an absence of a significant amount of cholesterol and a relatively high concentration of BMP (97). During endosome maturation, the internal pH undergoes a series of changes from that of the neutral cytosol to that of the acidic lysosome. It is within the late endosome intraluminal membranes that BMP is first found in relatively higher concentrations and is thought to be partly responsible for the formation of the intraendosomal VBs (98).

BMP has an unusual structure that differs from that of typical phospholipids such as POPC, (1-Palmitoyl-2-Oleoyl-sn-Glycero-3-Phosphocholine) and POPG, (1-Palmitoyl-2-Oleoyl-sn-Glycero-3-Phospho-rac-1-Glycerol) as shown in Figure 3-1.

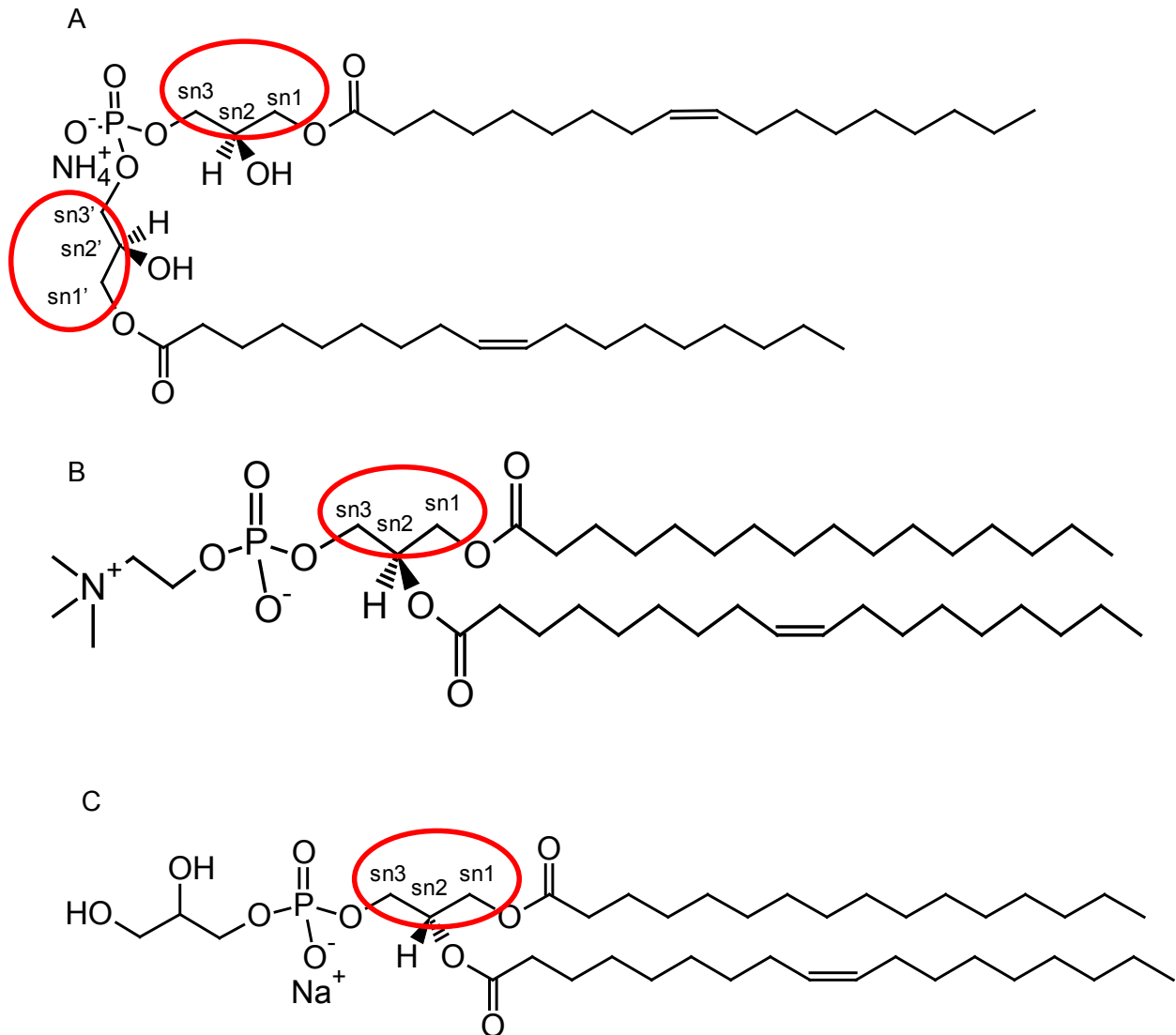


Figure 3-1. Chemical structures of A) BMP, B) POPC and C) POPG.

A comparison of the chemical structures BMP, POPC and POPG is shown in Figure 3-1. The unusual structure and stereochemistry of BMP is different from that of typical phospholipids in two aspects. Firstly, BMP has two glycerol components (Figure 3-1A), each with a single acyl chain, unlike POPC (Figure 3-1B) and POPG (Figure 3-1C), both of which have one glycerol component that is esterified to two hydrophobic acyl chains. The structures in Figure 3-1 depict the two glycerol groups in BMP and one glycerol group in POPC and POPG.

Secondly, the structure of BMP isolated from biological sources differs from the typical sn-3 glycerophosphate structures exhibited by most other glycerophospholipids (2, 8, 46), in that it possesses an unusual sn-1-glycerophospho- sn-1'-glycerol (sn1:sn1') stereoconfiguration (47, 48, 50, 99, 100, 231). The sn-3: sn-1' configuration has been reported for BMP isolated from baby hamster kidney (BHK) cells, although it is postulated that this configuration is an intermediate in the synthesis of the sn-1: sn-1' BMP (48). The unusual structure and stereochemistry of BMP are thought to be responsible for important roles in the endosome, including structural integrity, endosome maturation, and lipid/protein sorting and trafficking (101, 106). Although it is unclear how this occurs, it is possible that the structure and biosynthesis of BMP, together with the change in pH during the maturation of the endosome induces intraendosomal vesicular body formation.

This chapter presents results of the characterization of the morphology and size distribution observed in hydrated lipid dispersions and extruded lipid vesicles of BMP, POPC, POPG and lipid mixtures of POPC:BMP and POPC:POPG. Data and results were obtained by utilizing dynamic light scattering (DLS) and negative staining-transmission electron microscopy (TEM) imaging to provide information on the vesicle sizes, size distribution and macroscopic morphology of hydrated lipid dispersions and extruded vesicles. Initial DLS control experiments were performed to test different populations of POPC vesicles extruded using 30, 100 or 400 nm pore size extrusion membranes. Vesicle mixtures in various v/v ratios were then manually mixed as 30 nm- with 400 nm- and 100 nm- with 400 nm-extruded vesicles and the resulting vesicle populations measured with DLS. The aim of these experiments was to validate the

analytical capability of dynamic light scattering as a particle sizing technique in measuring and discriminating between different known vesicle populations.

To assess the stability of BMP vesicles (stability defined as the ability of the vesicles to maintain the same size distribution over time), assays were performed in which BMP, POPC and POPG vesicles were mechanically passed through 30 nm pore size extrusion membranes and the size of the vesicle suspensions (stored at room temperature) were monitored by DLS measurements over a five week period. Results from this assay clearly indicate that BMP 30 nm vesicles are smaller and more stable than either POPC or POPG. This is an interesting finding that may go a step further in elucidating the significant role of BMP in the formation of intraendosomal vesicular bodies, whose vesicle diameters (~200 nm) are in agreement with BMP vesicle sizes extruded with 400 nm membranes. The smaller, stable BMP vesicles can also be further explored for drug delivery applications.

To confirm that BMP forms lamellar vesicles with an interior volume, vesicle leakage assays were performed using fluorescence resonance energy transfer (FRET). Vesicles mechanically passed through 400 nm polycarbonate extrusion membranes were encapsulated with either calcein at neutral pH 7.4 or the FRET pair DPX/ANTS at acidic pH 4.2, and the percent release of the encapsulated fluorophore monitored as a function of increasing concentrations of titrated sodium dodecyl sulfate (SDS) detergent.

DLS and TEM results presented in this chapter also illustrate the effect of pH and ionic strength on BMP vesicle size and morphology; experiments were performed at both neutral and acidic pH, and in the presence and absence of 100 mM NaCl salt in the buffer solution used to hydrate the vesicles. Finally, DLS and negative staining-TEM

studies were performed to determine the change in vesicle sizes and shapes of lipid mixtures POPC: BMP and POP: POPG at both acidic and neutral pH and the results compared to those observed in pure BMP, POPC and POPG.

Experimental section

Materials and Reagents Used

All of the following lipids, dissolved in chloroform, were purchased from Avanti Polar Lipids (Alabaster, AL), stored at -20°C and used without further purification. BMP18:1, ((S,R Isomer) sn-(3-Oleoyl-2-Hydroxy)-Glycerol-1-Phospho-sn-(1'-Oleoyl-2'-Hydroxy)-Glycerol, ammonium Salt)); POPC, (1-Palmitoyl-2-Oleoyl-sn-Glycero-3-Phosphocholine) and POPG, (1-Palmitoyl-2-Oleoyl-sn-Glycero-3-(Phospho-rac-(1-Glycerol), sodium salt)). C₃₀H₂₆N₂O₁₃, (Calcein); ANTS, (8-amino-naphthalene-1, 3, 6 trisulfonic acid) and DPX, (p-xylene- bispyridinium bromide) were purchased from Molecular Probes (Invitrogen, Carlsbad, CA). SDS, (sodium dodecyl sulfate); HEPES, (4-(2-hydroxyethyl,-)1-piperazineethanesulfonic acid, C₈H₁₈N₂O₄S); NaOAc, (sodium Acetate); EDTA, (ethylenediamine tetraacetic acid, C₁₀H₁₆N₂O₈) and NaCl, (sodium chloride) were purchased from Fisher Biotech (Pittsburgh, PA). CH₃Cl, (chloroform); MeOH, (methanol); CH₃CH₂OH (ethanol); C₆H₁₂, (cyclohexane); NH₄OH, (ammonium hydroxide); HCl, (hydrochloric acid) and NaOH, (sodium hydroxide) were obtained from Fisher Scientific (Pittsburgh, PA). UO₂ (CH₃COO) ₂. 2H₂O, (uranyl acetate) and 400-mesh Formvar-coated copper grids were purchased from Ted Pella (Redding, CA).

Single-sealed 50- to 1000-mL disposable cuvettes (10-mm path length) were obtained from Eppendorf (Westbury, NY). 30-nm, 100-nm, and 400-nm polycarbonate extrusion membranes and filter supports were purchased from Avanti Polar Lipids

(Alabaster, AL). Silica-coated aluminum thin layer chromatography (TLC) plates were purchased from Whatman (Florham Park, New Jersey).

Hydrated Dispersions and Extruded Vesicle Preparation

All the glassware, syringes and vials used for vesicle sample preparation were cleaned and rinsed in a series of ethanol, chloroform, ethanol and copious amounts of water or buffer solutions before use. Before vesicle sample preparation, the lipid stock bottles, previously stored in the freezer at -20°C , were allowed to reach room temperature before opening.

For dynamic light scattering (DLS) and negative-staining-transmission electron microscopy (TEM) measurements, the desired amount of stock lipid (238 μL of BMP (5mg/mL), 57 μL of POPC (10mg/mL), 116 μL of POPG (10mg/mL), 49 μL POPC and 17 μL POPG for POPC:POPG (85:15) and 49 μL POPC and 36 μL BMP for POPC:BMP (85:15)) dissolved in chloroform, was dried under a gentle nitrogen stream for approximately 10 minutes or until all the solvent was evaporated, resulting in a dry, thin lipid film at the base of the test tube. Each sample was then further dried under vacuum in a desiccator for at least 12 hours to remove residual solvent. The thin lipid film was hydrated with 2 mL of either HEPES (4-(2-hydroxyethyl)-1-piperazineethanesulfonic acid) buffer, pH 7.4 (5 mM HEPES, 100 mM NaCl (sodium chloride), 0.1 mM EDTA (ethylenediamine tetraacetic acid)) or NaOAc (sodium acetate) buffer, pH 4.2 (5mM sodium acetate, 100 mM NaCl, 0.1mM EDTA) to obtain a final lipid concentration of 0.75 mM.

Additional samples were hydrated in the absence of 100 mM NaCl salt, in HEPES buffer, pH 7.4 (5 mM HEPES, 0.1 mM EDTA) and in NaOAc buffer, pH 4.2 (5 mM NaOAc, 0.1 mM EDTA). Hydrated lipid dispersions were then vortex-mixed 5–10 times,

freeze-thawed five times in liquid nitrogen and water respectively, and incubated at room temperature for at least 12 hours before extrusion or measurement by DLS and TEM. The extended incubation period of the hydrated dispersions allowed for complete lipid vesicle hydration. To form unilamellar vesicles, (either as small unilamellar vesicles (SUVs) or large unilamellar vesicles (LUVs), the multilamellar hydrated dispersions were mechanically passed 31 times through 30, 100, or 400 nm polycarbonate extrusion membranes. Unilamellar vesicles samples were then immediately used for DLS measurements.

Phospholipid integrity was verified by thin layer chromatography (TLC). Approximately 10 μ L of sample was spotted on silica-coated aluminum plates. Plates were placed in a chamber containing a $\text{CH}_3\text{Cl}:\text{MeOH}:\text{NH}_4\text{OH}$ (65:25:10) mobile phase. The TLC plates were developed in an iodine chamber and visualized by eye.

Sample Preparation for Vesicle-leakage Assays

For fluorophore-loaded vesicle assays (232), 200 μ L of stock BMP (5mg/mL), dissolved in chloroform, was placed in a medium-sized round-bottomed test tube and dried under a stream of nitrogen gas for approximately 10 minutes or until all the solvent was evaporated, forming a dry thin lipid film at the base of the test tube. The sample was subsequently placed in a vacuum desiccator overnight to remove any residual solvent. The dry lipid film was hydrated with 2 mL of either 5 mM HEPES buffer, pH 7.4 containing 70 mM calcein fluorescent dye or 5 mM NaOAc buffer (pH 4.2) containing 25 mM ANTS and 90 mM DPX fluorescent dyes. Hydrated lipid dispersions were passed through 400-nm extrusion membranes as described above to form large unilamellar vesicles.

Fluorophore-loaded unilamellar vesicles were separated from free fluorophore on a Sephadex G-50 Fine column (GE Healthcare, Piscataway, NJ). For this assay, 10 μ L of the lipid suspension was diluted to 300 μ L with either 5 mM HEPES or 5 mM NaOAc buffer in a 4-mm light path quartz cuvette (Starna, Atascadero, CA). Sodium dodecyl sulfate (SDS) detergent solubilization of calcein-loaded vesicles was monitored by fluorescence spectroscopy with excitation at 490 nm and detection of emission intensity at 520 nm. The ANTS/DPX leakage assay utilized an excitation of 360 nm and emission at 530 nm and used wider slit widths (10–20 nm). Concentrated SDS detergent (10% w/w) was titrated into the diluted lipid suspension, with a subsequent 10-min incubation period at 27° C, with stirring, before obtaining the emission intensity after each SDS titration step. Percentage fluorophore release was calculated as shown in Equation 3-1.

$$\% \text{ Fluorophore release} = (I - I_0) / (I_\infty - I_0) \cdot 100 \quad (3-1)$$

where I is the emission intensity after addition of SDS, I_0 is the emission intensity in the absence of SDS, and I_∞ is the emission intensity after the addition of a 5 mL (20% w/w) SDS. All emission intensities were corrected for dilution factor from titrations and each assay was performed in triplicate.

Instrumentation Used

Dynamic light scattering (DLS)

Dynamic light scattering size distribution and characterization measurements of lipid vesicles were performed using a Brookhaven 90Plus/BI-MAS ZetaPALS spectrometer operated at a wavelength of 659 nm and at 25° C. The instrument uses a BI-9000AT digital autocorrelator and 9KDLSW data acquisition software. A 100-mL sample volume in a disposable cuvette was used for each measurement. For each sample, 3 runs were performed with each run lasting 3 minutes. Raw Data and

histograms were further analyzed and converted into B-spline plots using OriginPro 8 software.

Negative staining-transmission electron microscopy

Negative staining-transmission electron microscopy (TEM) images were obtained using a Hitachi H-7000 transmission electron microscope operated at 75-100 kV with a Soft-Imaging System MegaViewIII with AnalySIS digital camera (Lakewood, CO). The microscope has a maximum resolution at 0.2 nm with a magnification range of 110× to 600,000×. Before TEM measurements, samples were further prepared by negative staining.

Briefly, for all samples, a drop of the lipid vesicle sample was spread on a 400-mesh Formvar-coated copper grid and incubated for 2 minutes. Excess sample was gently dabbed away with filter paper, and the grid was allowed to dry for 2 minutes. A drop of deionized water was optionally added to the grid to remove any excess salt from the buffer solution used in vesicle preparation. One drop of 2 % uranyl acetate was then added to the grid and allowed to stain for 2 minutes, after which any excess uranyl acetate was wiped away, and the sample was allowed to dry for another 2 minutes before being placed in the electron microscope specimen holder for imaging.

Fluorescence measurements

Fluorescence spectra were acquired with a FluoroMax-3 fluorometer (Jobin Yvon Horiba, Edison, NJ) with a temperature-controlled sample cell and a Haake K20 temperature controller (Thermo Electron, Waltham, MA). Measurements were made using a 4-mm light path quartz cuvette (Starna, Atascadero, CA). All spectra were collected at 27° C, with both the excitation and emission slits set to 5 nm and with excitation and emission polarizers set to 90° and 0° respectively.

Results and Discussion

Evaluation of Mixing Different Sizes of Neat POPC Vesicle Populations

To validate the analytical capability of dynamic light scattering as a particle sizing technique, control experiments were designed to measure the size distribution of POPC hydrated dispersions (unextruded), and vesicles extruded using polycarbonate membranes with varying pore sizes of 30, 100 or 400 nm. POPC vesicles of known size distributions were then manually mixed; 30 with 400-nm and 100 with 400-nm extruded vesicles in specific volume to volume ratios, with 10 μL increments to give a total of 100 μL for each sample. The resulting physical mixtures of vesicles were measured by dynamic light scattering to determine the ability of the DLS technique to distinguish between manually mixed vesicle populations. For each sample, DLS measurements were taken in triplicates, averaged and the data further analyzed and converted into B-spline plots using OriginPro 8 software.

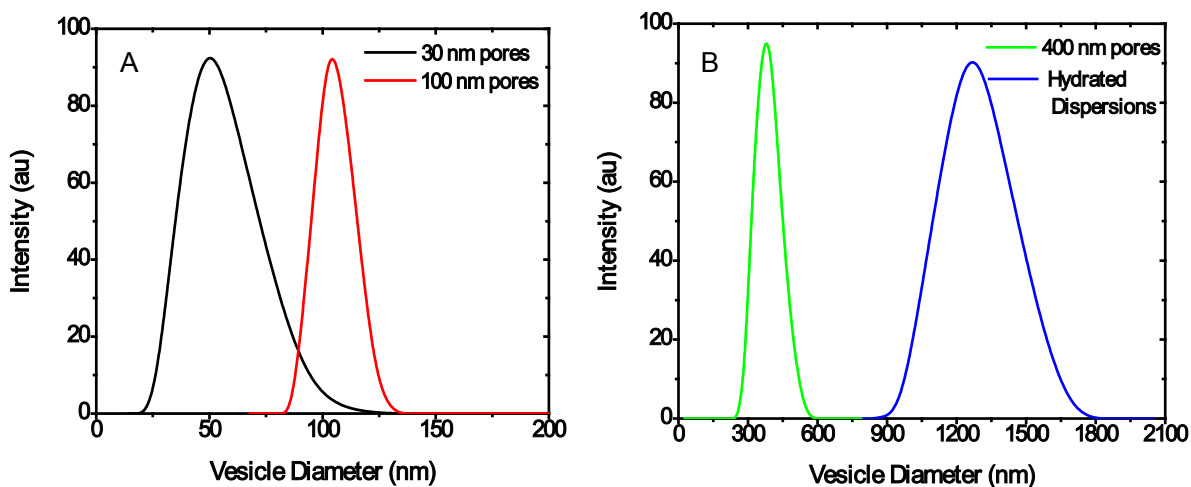


Figure 3-2. DLS histograms of size distributions of POPC vesicles extruded with polycarbonate membranes of varying pore sizes. A) Black line, 30 nm. A) Red line, 100 nm. B) Green line, 400 nm. B) Blue line, hydrated unextruded dispersions.

Table 3-1. Summary of POPC vesicle diameters extruded with polycarbonate membranes of varying pore sizes.

Membrane pore size	Average vesicle diameter (nm)
30 nm	50 ± 30
100 nm	100 ± 20
400 nm	400 ± 100
Unextruded dispersions	1300 ± 300

Figure 3-2 represents the dynamic light scattering histograms of POPC vesicles that were mechanically passed through polycarbonate extrusion membranes with pore sizes of 30 nm, 100 nm, 400 nm and hydrated, unextruded dispersions that are also referred to as multilamellar vesicles (MLVs). Table 3-1 is a summary of the POPC average vesicle diameters shown in Figure 3-2, obtained by taking an average of three independent DLS traces for each sample. The error bars were calculated as standard deviation of the average vesicle diameter in each case.

The data in Figure 3-2 and Table 3-1 show that the 30 nm-extruded vesicles (Figure 3-2A, black solid line) have the smallest diameter range, with an average vesicle size at ~ 50 nm, whereas the vesicles extruded with 100 nm polycarbonate membranes (Figure 3-2A, red solid line) have a slightly larger but narrower vesicle size distribution that is centered at ~ 100 nm. In Figure 3-2B, the green solid line represents the vesicle size distribution of vesicles extruded with 400 nm pore sizes, with the intensity centered at a vesicle diameter of ~ 400 nm. The blue solid line in Figure 3-2B is representative of the size distribution obtained for unextruded, hydrated dispersions of POPC, showing large vesicle diameters of up to ~1300 nm. Taken together, these data indicate that dynamic light scattering can accurately measure and report the vesicle size distributions of vesicles that have been mechanically extruded with polycarbonate extrusion membranes of varying pore sizes.

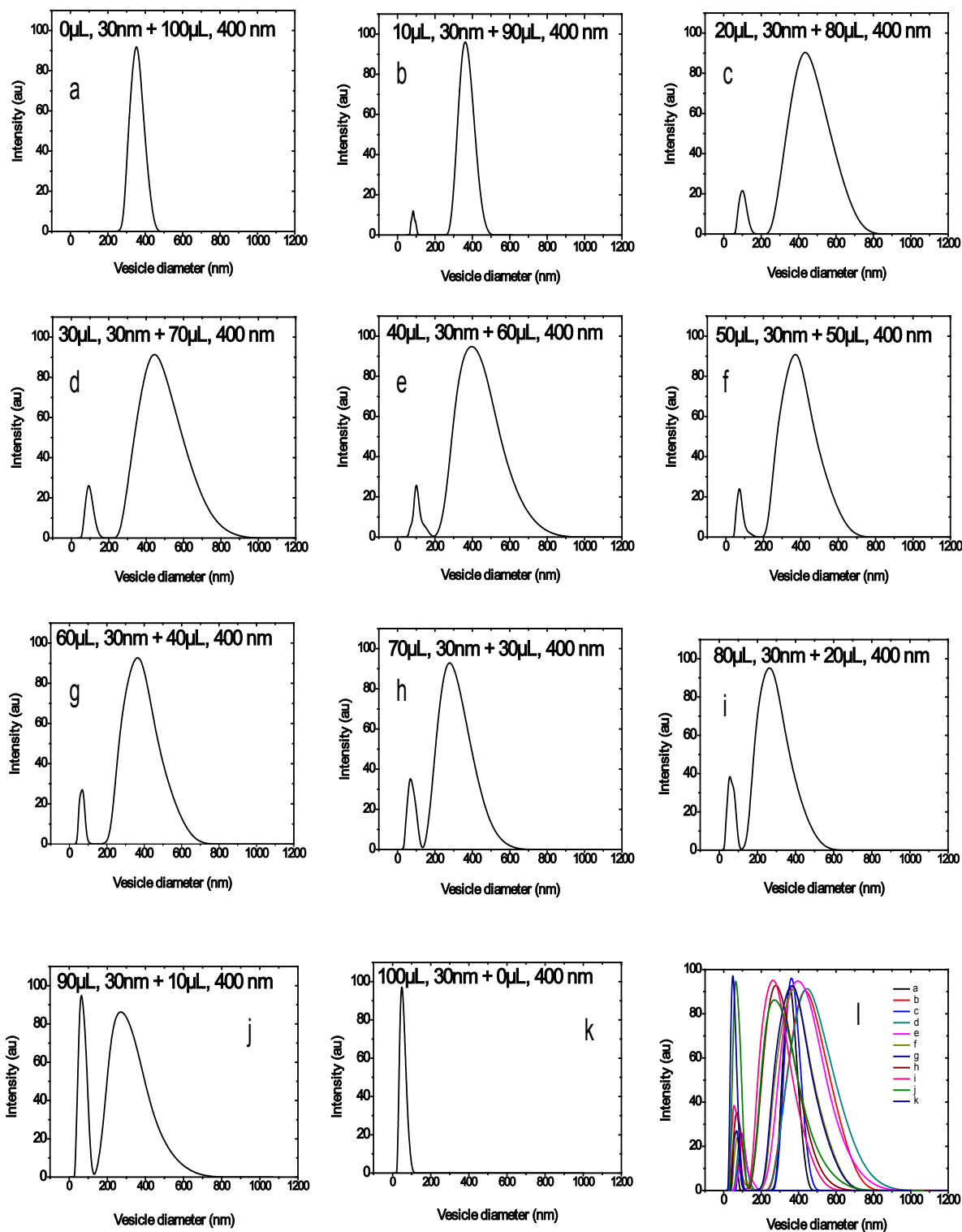


Figure 3-3. DLS histograms of populations of manually mixed POPC vesicles extruded with 30 nm and 400 nm pore size membranes and mixed in various volume/volume ratios in 5 mM HEPES buffer.

Following the accurate measurement of various populations of POPC vesicle sizes by DLS, experiments were carried out to determine the ability of DLS to differentiate between manually mixed vesicle populations of different sizes. Figure 3-3a-l is an illustration of the DLS vesicles size distributions obtained for POPC vesicles populations that were manually mixed at various v: v ratios after extrusion through 30 and 400 nm polycarbonate membranes, respectively. Each vesicle mixture consisted of 100 μ L total volume, starting at 0 μ L of 30 nm-extruded vesicles mixed with 100 μ L of 400 nm-extruded vesicles in Figure 3-3a. Therefore, the sample in Figure 3-3a was made up of only 400 nm- extruded vesicles, which is consistent with the DLS histogram obtained, with a unimodal vesicle size distribution that is centered at \sim 350 nm.

Figure 3-3b illustrates the vesicle size distribution obtained for 10 μ L of 30 nm-extruded vesicles mixed with 90 μ L of 400 nm-extruded vesicles. As would be expected, two vesicle populations can be seen; a less intense size distribution centered at 70 nm that is representative of the 30 nm- extruded vesicle population, and a more intense size distribution with an average diameter of \sim 400 nm, representing the 400 nm-extruded vesicles. This trend is observed in all of the subsequent samples represented by Figures 3-3c-j, with all samples exhibiting two distinct peaks that are representative of the two premixed vesicle populations. Figure 3-3k shows 100 μ L of 30 nm-extruded vesicles mixed with 0 μ L of 400 nm-extruded vesicles, hence this sample contained vesicles that were only extruded with a 30 nm pore size, and as expected, the DLS histogram has only one vesicle population that with an average vesicle size at \sim 70 nm. Figure 3-3l is a summary of all the DLS histograms for all the vesicle mixtures shown in

Figures 3-3a-k, showing a bimodal size distribution that represents two distinct vesicle populations in all instances.

It is noteworthy to mention that in almost all cases of the physically mixed vesicle populations, the peaks representing the smaller vesicle sizes that were extruded with 30 nm pore sizes are less intense than the larger-sized vesicle peaks, even when higher concentrations of smaller vesicles are mixed with lower concentrations of larger vesicles (for instance in Figure 3-3h, 70 μL of 30 nm-extruded vesicles were mixed with 30 μL of 400 nm-extruded vesicles, but the smaller volume of larger vesicles results in a more intense peak than the larger volume of smaller vesicles). This observation is attributed to the fact that in dynamic light scattering technique, larger particles scatter more light than smaller particles, which results in more intense peaks for observed larger particles, even when there might be a larger volume of small vesicles than large vesicles.

Similar experiments were carried out by physically mixing 100 nm-extruded vesicles with 400 nm-extruded vesicles, then measuring the resulting size distributions of the vesicle mixtures with dynamic light scattering. Results from these experiments are illustrated in Figures 3-4a-l. In Figure 3-4a, 0 μL of 100 nm-extruded vesicles were mixed with 100 μL of 400 nm-extruded vesicles, and as expected, the DLS histogram indicates one vesicle population that is centered at ~ 400 nm, since this sample contained only vesicles extruded with the 400 nm pores. Figure 3-4b for 10 μL of 100 nm-extruded vesicles mixed with 90 μL of 400 nm-extruded vesicles exhibits two vesicle populations, with a small, less intense peak at ~ 100 nm and a more intense peak at ~ 400 nm. Likewise, the subsequent samples represented by Figures 3-4c-h all show two distinct vesicle peaks representative of the two mixed vesicle populations.

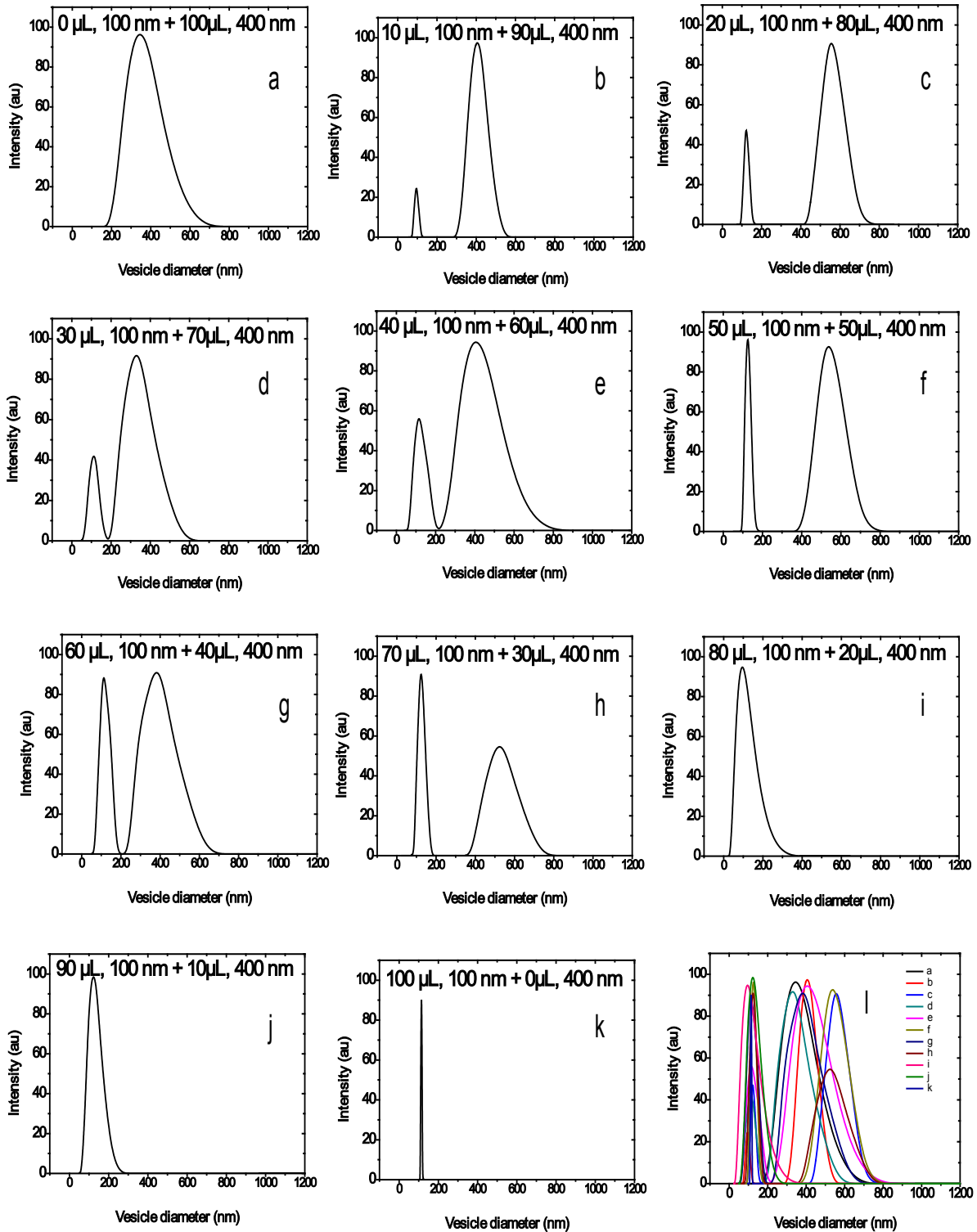


Figure 3-4. DLS histograms showing populations of manually mixed POPC vesicles extruded with 100 nm and 400 nm pore size membranes in various volume/volume ratios.

Figure 3-4i for 80 μL of 100 nm-extruded vesicles mixed with 20 μL of 400 nm-extruded vesicles has only one size distribution centered at ~ 150 nm. Likewise, Figure 3-4j also shows only one size distributions centered at ~ 180 nm although it represents 90 μL of 100 nm-extruded vesicles mixed with 10 μL of 400 nm-extruded vesicles. The unimodal size distributions observed in Figures 3-4i-j are however broader than those seen in the previous bimodal size distributions, hence it can be assumed that at a certain increased volume of ~ 80 μL of 100 nm-extruded vesicles, the vesicle populations start mixing so that DLS can no longer distinguish between them and reports them as one broad vesicle size distribution. Figure 3-4j for 100 μL of 100 nm-extruded vesicles also shows one narrow intense peak with an average vesicle diameter at ~ 120 nm, whereas Figure 3-4k summarizes the DLS histograms observed for all the vesicle mixtures, exhibiting two distinct vesicle populations in all cases.

Taken together, the data observed in Figures 3-3a-k and Figures 3-4a-k indicate that the dynamic light scattering technique has the general capability to accurately measure and differentiate between manually mixed vesicle populations, shown as two vesicle peaks in the DLS histograms.

Additional experiments were performed to determine the measured average vesicle diameters of BMP, POPC and POPG as a function of extrusion membrane pore diameter. In these experiments, samples of BMP, POPC and POPG lipid dispersions that were each hydrated in buffer containing 5 mM HEPES, 100 mM NaCl, and 0.1 mM EDTA were mechanically passed 31 times through 30, 100, and 400 nm polycarbonate extrusion membranes then measured by dynamic light scattering to determine the vesicle size distributions. Results of these experiments are summarized in Table 3-2.

Table 3-2. Summary of BMP, POPC and POPG average vesicle diameter as a function of extrusion membrane pore diameters.

Extrusion membrane pore diameter	Measured vesicle diameters (nm)		
	BMP	POPG	POPC
30 nm	50 ± 20	80 ± 10	80 ± 20
100 nm	100 ± 20	130 ± 20	120 ± 10
400 nm	230 ± 30	300 ± 100	400 ± 180

Error bars are standard deviations of the average vesicle diameters, which were obtained from the average of three independent DLS traces. Lipids were hydrated in 5 mM HEPES, 100 mM NaCl and 0.1 mM EDTA, pH 7.4.

Table 3-2 is a summary of the measured vesicle diameters obtained for BMP, POPC and POPG lipid dispersions that were extruded with 30, 100 and 400 nm polycarbonate membranes. From Table 3-2, BMP vesicles extruded with 30 nm pore membranes have an average vesicle diameter of 50 nm, while POPG and POPC both have larger average vesicle diameters of 80 nm. For the 100 nm-extrusion membrane, both POPC and POPG form vesicles with average diameters of 120 and 130 nm respectively, whereas BMP vesicles have a smaller average vesicle diameter of 100 nm. More interestingly, BMP vesicles extruded with 400 nm pores have much smaller vesicle diameters of only 230 nm, compared to the larger vesicle diameters of 300 and 400 nm for POPG and POPC respectively. The data in Table 3-2 show conclusively that perhaps because of its unique structure, BMP prefers to form smaller-sized vesicles compared to the vesicles formed by typical phospholipids POPC and POPG.

Comparison of Vesicle “Stability”: BMP versus POPC Vesicles

After demonstrating that BMP forms smaller vesicles compared to either POPC or POPG vesicles when extruded with different sizes of polycarbonate membranes, it was of interest to determine the stability of BMP vesicles compared to POPC vesicles. Stability here is defined as the ability of the vesicles to maintain the same size distribution over time, since small vesicle structures are known to generally fuse and

form larger vesicles over time. DLS experiments were performed on BMP and POPC vesicles extruded with 30 nm pore membranes in buffer containing 5 mM HEPES, 100 mM NaCl and 0.1 mM EDTA, at neutral pH 7.4. The average vesicle diameters of the 30-nm extruded vesicles of BMP and POPC under neutral were measured and monitored over a five week period to observe any changes in the vesicles size distributions. The samples were stored in 5-mL vials at room temperature. Figure 3-5 shows results from DLS measurements performed on the 30-nm extruded vesicles of BMP and POPC over a five week period.

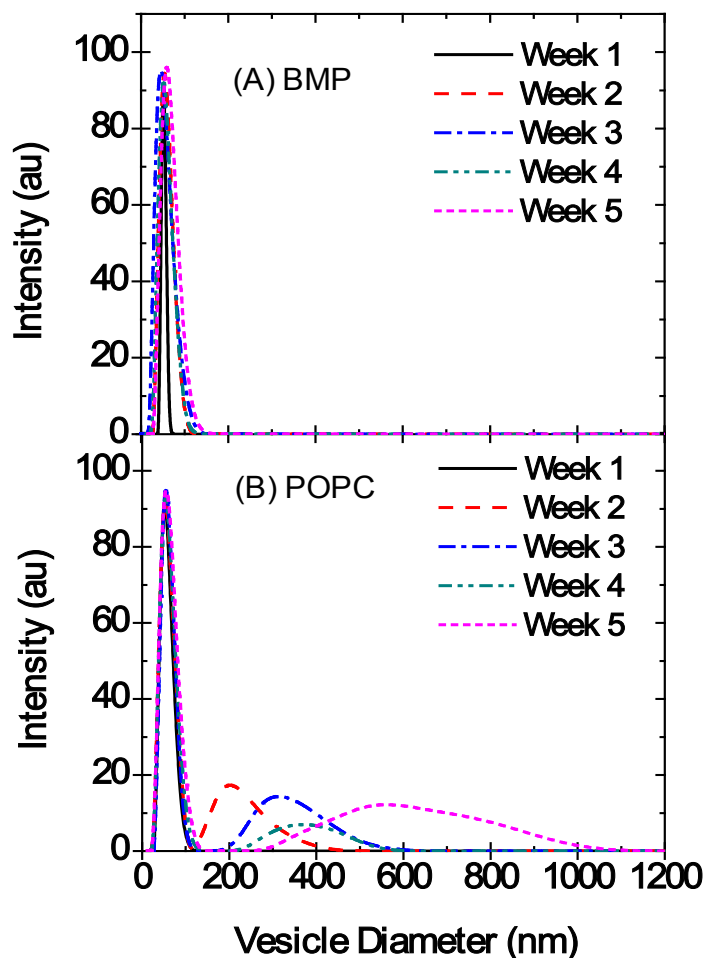


Figure 3-5. Dynamic light scattering size distributions of A) 30-nm extruded BMP and B) POPC vesicles monitored over a five week period. Lipids were hydrated in 5 mM HEPES, 100 mM NaCl and 0.1 mM EDTA, at neutral pH 7.4.

Because BMP hydrolyzes rapidly under acidic conditions, the stability data were collected only for neutral pH 7.4. From the data in Figure 3-5, it can clearly be seen that the POPC vesicles fuse to form larger structures as early as two weeks after extrusion. On the other hand, although the size distribution of the BMP 30 nm-extruded vesicles broadens, the average vesicle size is still near 50 nm, and the distribution tails off near 100 nm. Combined, the DLS results from these experiments indicate that BMP prefers to form small, stable vesicular structures.

BMP Vesicle Leakage Assays under Acidic and Neutral pH Conditions

To verify that BMP forms liposomes that contain an interior volume, fluorescence leakage assays were performed using calcein fluorescent dye for experiments at neutral pH, and the fluorescence resonance energy transfer (FRET) pair of ANTS/DPX (ANTS, 8-amino-naphthalene-1, 3, 6 trisulfonic acid and DPX, p-xylene- bispyridinium bromide) for vesicles at acidic pH. Because the quantum yield of calcein is too low at acidic pH, the ANTS/DPX pair was used instead, where DPX quenches ANTS. Lipid vesicle leakage assays were developed by loading vesicles with the appropriate fluorescent dye, and monitoring the change in fluorescence intensity as the vesicle contents leaked out into the bulk solution after solubilization with the sodium dodecyl sulfate (SDS) detergent. Dye-loaded vesicles were obtained by including the fluorophore in the lipid hydration buffer, and then once the vesicles were formed, the free dye was separated from the encapsulated dye by running the lipid dispersions down a Sephadex column.

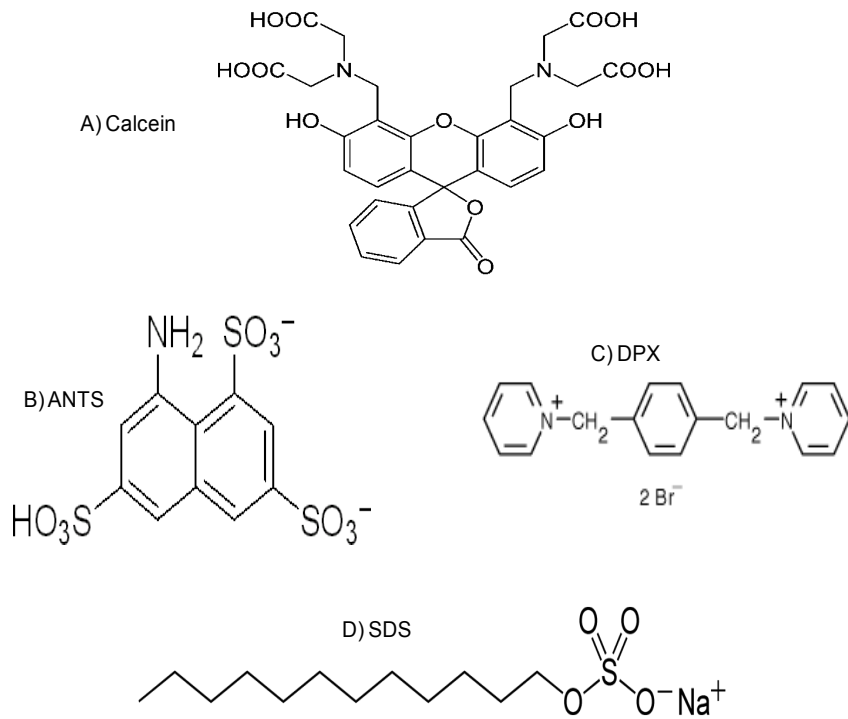


Figure 3-6. Chemical structures of A) calcein, B) ANTS, C) DPX and D) SDS.

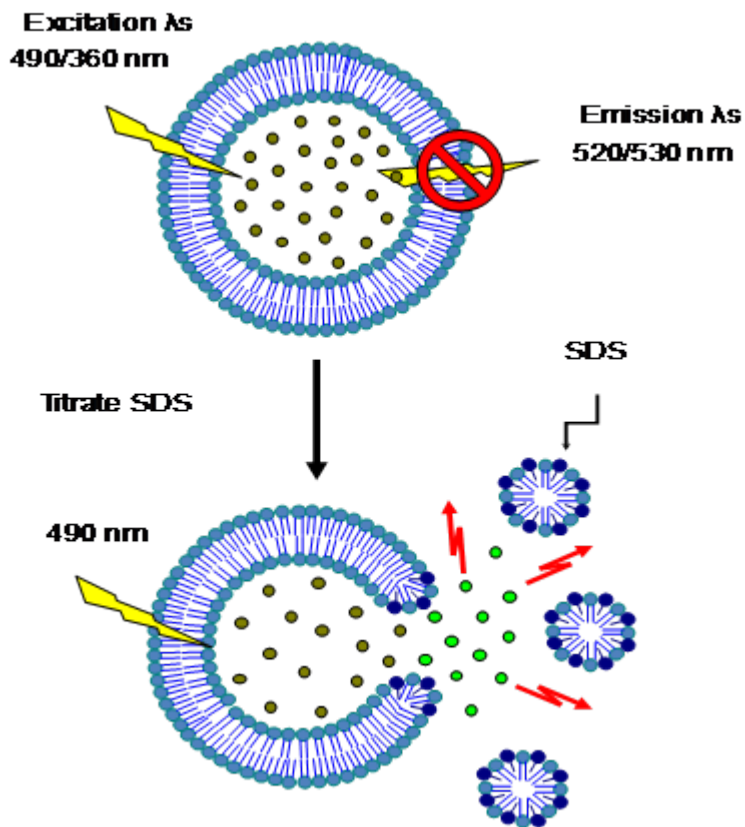


Figure 3-7. Schematic illustration of SDS detergent solubilizing the liposome and causing leakage of the vesicle contents. Figure adapted from Tom Frederick.

Figure 3-7 is a schematic illustration of vesicle contents leaking into the bulk solution after solubilization of the liposome by the sodium dodecyl sulfate (SDS) detergent. For fluorescence experiments at neutral pH, the calcein dye was excited at 490 nm, and emission was set at 520 nm, whereas for the ANTS/DPX pair at acidic pH, the excitation wavelength was at 360 nm and the emission wavelength set at 530 nm. The % fluorophore release is given by Equation 3-2.

$$\% \text{ Fluorophore Release} = 100 \times (F - F_0) / (F_t - F_0) \quad (3-2)$$

F = Fluorescence intensity with addition of SDS detergent

F_0 = Fluorescence intensity without any SDS

F_t = Fluorescence intensity after addition of a high concentration of SDS (5 μ L of 20 % w/w SDS).

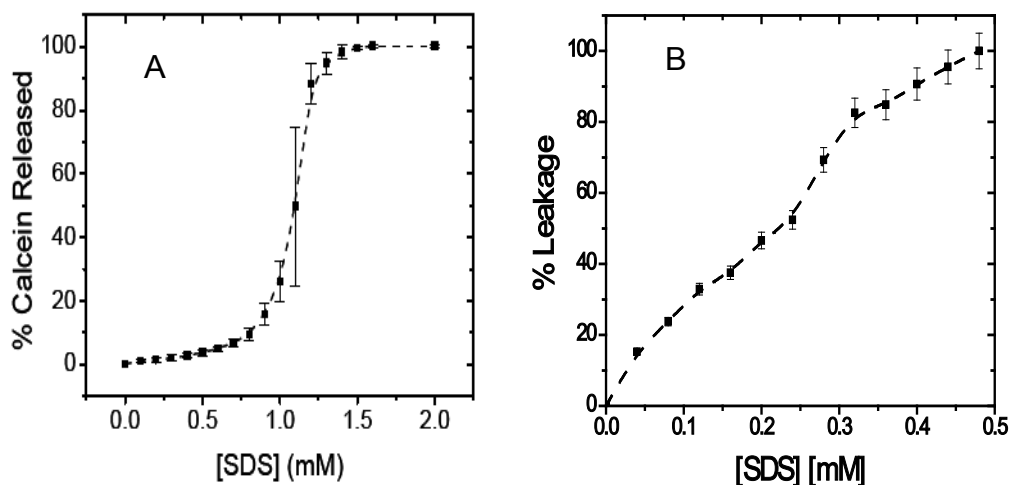


Figure 3-8. Vesicle leakage assay for BMP vesicles. A) Neutral pH 7.4. B) Acidic pH 4.2.

Figure 3-8A plots the percentage of calcein release for 400 nm-extruded BMP vesicles loaded with calcein as a function of titrated SDS concentration. Because calcein enclosed within a large unilamellar vesicle (LUV) has low fluorescence emission as a result of collisional quenching, an increase in fluorescence intensity on SDS

titration is interpreted as release of the fluorophore with SDS partitioning into the BMP LUV and eventual complete micellization. As a control (data not shown), the fluorescence intensity of calcein-loaded BMP vesicles was monitored over a two hour period and showed less than 2 % fluorescence intensity change over this time period. Hence, from these results, it is clear that extruded BMP vesicles contain an interior volume that can trap the calcein fluorophore.

The data from an analogous experiment under acidic conditions are shown in Figure 3-8B. Because the quantum yield of calcein is very low under acidic conditions, the FRET pair of ANTS/DPX was utilized, where ANTS and DPX were co-entrapped within the vesicle. Again, control experiments over two hours without addition of SDS show less than 2 % increase in fluorescence intensity, indicating that the vesicles are stable during the time course of the titration experiment. On addition of SDS, liposome contents are released into the bulk solution and diluted, producing a dequenching of ANTS fluorescence. These results demonstrate that under acidic conditions, 400 nm-extruded BMP unilamellar vesicles are stable and contain an interior volume that can entrap molecules. It is noteworthy to mention that the two graphs in Figure 3-8 differ in shape because of two main reasons; for neutral pH in A, the vesicles used had a much higher concentration (~10 mM) than that at acidic pH in B, hence more SDS was needed to solubilize the vesicles in A than in B. Additionally, the calcein experiment in A utilizes fluorescence measurements, whereas the DPX/ANTS assay utilizes FRET, hence fundamental differences between the two techniques may result in the different shapes obtained for the two graphs. Combined, the vesicle leakage assay experiments at both neutral and acidic pH demonstrate that BMP forms unilamellar vesicles that are

stable and have an interior volume that can be utilized to encapsulate aqueous molecules.

Characterization of BMP and POPC Hydrated Dispersions and Unilamellar Vesicles.

Effect of pH

Dynamic light scattering and negative staining-transmission electron microscopy imaging experiments were performed on BMP and POPC hydrated dispersions and vesicles extruded through 400 nm pore diameters, under both neutral and acidic pH conditions, to determine the vesicle diameter size distributions and vesicle morphology for the two lipids under similar conditions. The use of 400 nm pore-sized membranes for vesicle extrusion resulted in formation of large unilamellar vesicles with a large interior volume, which has the potential for studies involving encapsulation of aqueous molecules.

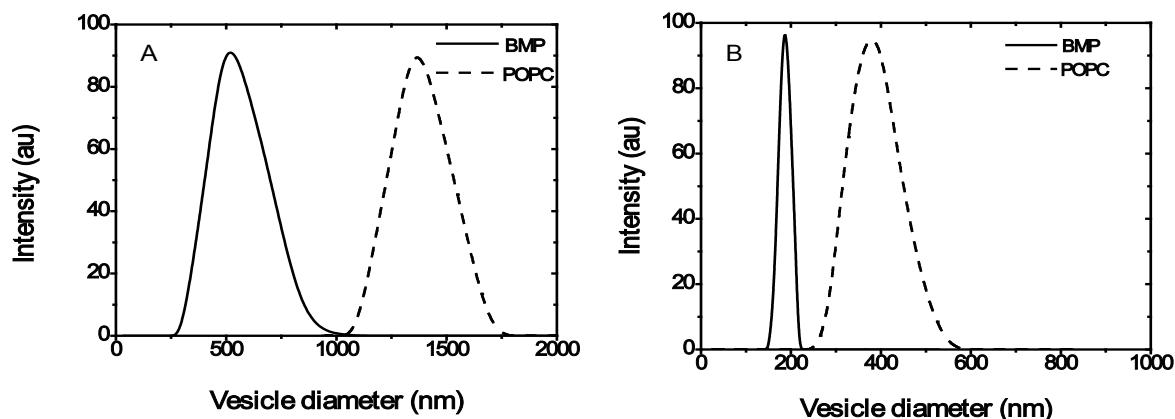


Figure 3-9. DLS vesicle size distributions of BMP and POPC vesicles, under neutral pH 7.4. A) Hydrated dispersions. B) 400 nm-Extruded vesicles.

Table 3-3. Summary of average vesicle diameters of BMP and POPC dispersions and extruded vesicles at neutral pH 7.4.

Lipid Type	Average vesicle diameter (nm)	
	Hydrated dispersions	400 nm-Extruded vesicles
BMP	500 ± 250	200 ± 30
POPC	1400 ± 200	400 ± 100

DLS is a viable technique for providing information on the size distribution of particles in solution, whereas negative staining-TEM is useful for providing information on morphological organization as well as vesicle size. Taken together, the two techniques provide valuable information on the morphology and size distribution of macromolecules. Figure 3-9 illustrates the DLS measurements of BMP and POPC hydrated dispersions and extruded unilamellar vesicles at neutral pH 7.4, while Table 3-3 provides a summary of the average vesicle diameters for BMP and POPC lipid dispersions and extruded vesicles, observed in the DLS histograms.

The hydrated dispersions data in Figure 3-9A, black solid line show that BMP forms vesicles with an average diameter of ~ 500 nm, while the POPC hydrated dispersions (Figure 3-9A, black dotted line) have their diameter centered at approximately $1.4 \mu\text{m}$. In Figure 3-9B, the black solid line represents BMP vesicles that were mechanically passed through 400 nm pore sizes membranes have a narrow size distribution, with the highest vesicle intensity observed at ~ 200 nm, while the POPC vesicles have a broader size distribution centered at ~ 400 nm. These data interestingly suggest that under neutral pH, BMP forms smaller vesicles than POPC vesicles.

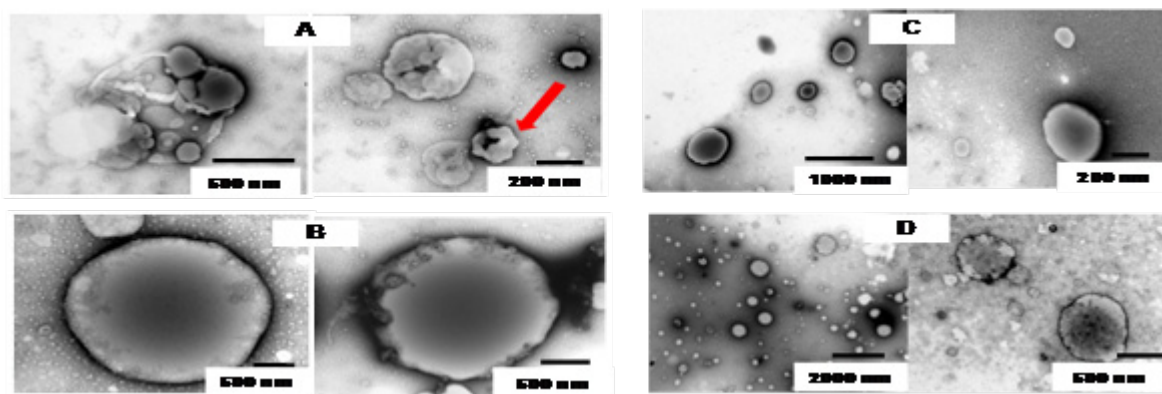


Figure 3-10. Negative staining-TEM images of BMP and POPC under neutral pH conditions. A) BMP hydrated dispersions. B) POPC hydrated dispersions. C) BMP 400 nm-extruded vesicles. D) POPC 400 nm-extruded vesicles.

TEM images of hydrated dispersions and extruded vesicles of BMP and POPC lipids under neutral pH conditions are presented in Figure 3-10A-D. Under neutral pH, BMP hydrated dispersions (Figure 3-10A) form “cauliflower-like” highly structured, non-spherical vesicular morphologies that appear aggregated in clusters of smaller vesicles, possibly containing small budlike protrusions. The red arrow in Figure 3-10A points to a possible side view of the vesicle, indicating that the clustering seen from the top-down views is likely not a vesicle-inside-a-vesicle effect but rather the fused tubular structure of smaller vesicle shapes. A size analysis of TEM images of the BMP hydrated dispersions gives a distribution between 200 and 800 nm for vesicle diameter, centered at 400 nm, which is in agreement with results obtained from DLS measurements.

It is interesting to note that when the BMP dispersions are passed through 400-nm pore size extrusion membranes to produce the unilamellar vesicles represented in Figure 3-10C, the clustered structures disappear, and well rounded, spherical structures with an average diameter of 200 nm are formed. The size is also consistent with that observed from DLS measurements. The fact that BMP “400 nm-extruded” vesicles produce 200 nm vesicles can be understood by considering that the clustered dispersions may have their smaller budlike protrusions sheared off when passed through the extrusion membranes. In comparison, we found that POPC hydrated dispersions (Figure 3-10B) form uniform, spherical structures that are much larger in size (~2000 nm) than the BMP dispersions, and analysis of the TEM images of POPC 400 nm-extruded vesicles reveals the expected spherical structures with vesicle diameter near 500 nm.

The clustered macroscopic structure of the BMP dispersions was found to vary with pH. Similar dynamic light scattering and transmission electron microscopy experiments were performed on the hydrated dispersions and extruded unilamellar vesicles of the BMP and POPC at acidic pH 4.5.

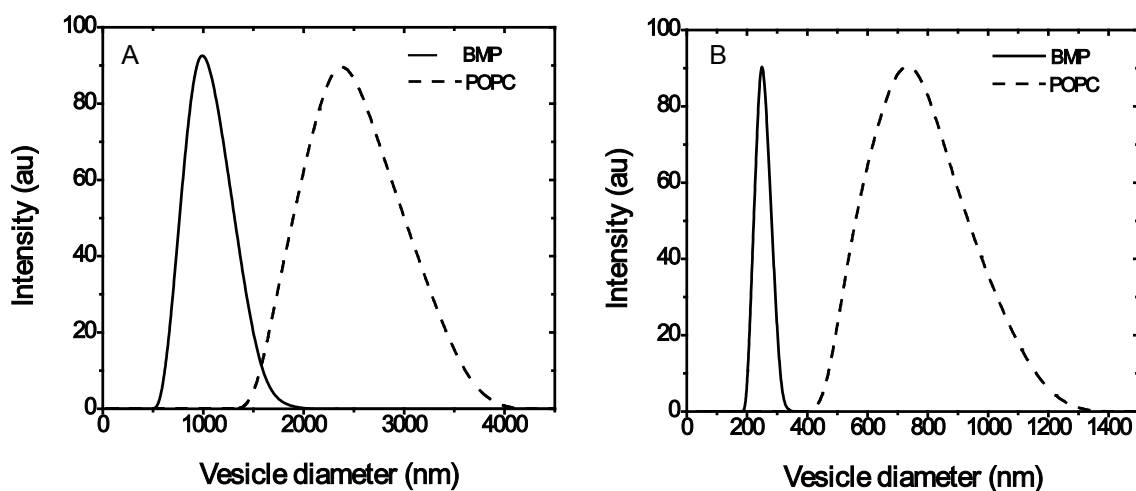


Figure 3-11. DLS measurements of BMP and POPC A) hydrated dispersions and B) 400-nm extruded large unilamellar vesicles at acidic pH 4.2.

Table 3-4. Average vesicle diameters of BMP and POPC hydrated dispersions and 400-nm extruded vesicles at acidic pH 4.2.

Lipid Type	Average vesicle diameter (nm)	
	Hydrated dispersions	400-nm Extruded vesicles
BMP	1000 ± 400	250 ± 50
POPC	2400 ± 700	750 ± 250

Figure 3-11 illustrates the vesicle diameters of hydrated dispersions of BMP (A, black solid line) and POPC (A, black dotted line), and 400 nm-extruded vesicles of BMP (B, black solid line) and POPC (B, black dotted line). The DLS average vesicle diameters data for BMP and POPC at acidic pH is also summarized in Table 3-4.

Regardless of pH, BMP dispersions have average vesicle diameters smaller than those of POPC. Dispersions obtained when samples are hydrated with sodium acetate buffer (at pH 4.5), are larger in size for both BMP (~1000 nm) and POPC (~2400 nm)

than under neutral conditions, where vesicles of BMP and POPC have average diameters near 500 nm and 1400 nm, respectively. However, the size of the BMP extruded vesicles does not change significantly when pH is altered. As shown in Figure 3-11B, (black solid line), the BMP vesicles have average diameters near 250 nm at pH 4.5 and near 230 nm for pH 7.4 (Figure 3-10B, black solid line), which are both smaller than the diameters of the 400-nm pores through which the dispersions were mechanically passed. POPC extruded vesicles at acidic pH 4.5 have average vesicle diameters at ~ 750, which is larger than that observed at pH 7.4 (~400 nm). In addition, the extruded BMP vesicles have a much narrower size distribution than that of POPC.

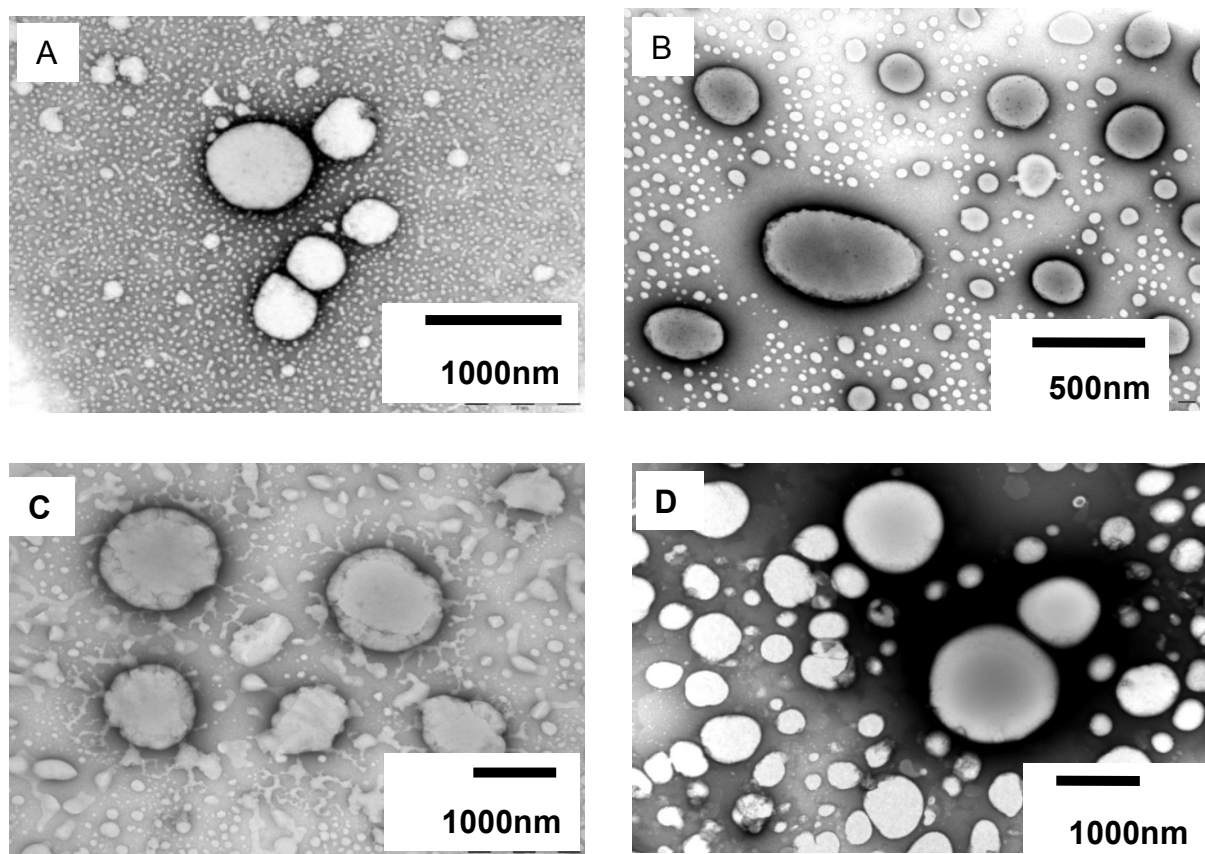


Figure 3-12. Negative staining-TEM images of BMP and POPC hydrated dispersions and 400-nm extruded vesicles at acidic pH. A) BMP hydrated dispersions. B) BMP extruded vesicles. C) POPC hydrated dispersions. D) POPC extruded vesicles.

TEM data also shows that the morphology of BMP dispersions varies with pH, forming highly structured, small vesicle clusters at neutral pH, whereas uniformly spherical vesicles are observed at acidic pH. POPC forms uniform, spherical vesicles at both acidic and neutral pH conditions. Figure 3-12 shows TEM images of BMP hydrated dispersions (A) and 400 nm-extruded vesicles (B) at pH 4.5. A clear distinction can be seen between the BMP vesicle structures formed at the two pHs, with samples at pH 7.4 exhibiting the clustered, budding structures and those at pH 4.5 forming uniformly non-structured, spherical shapes ranging from 400 to 800 nm, again much smaller in size than POPC dispersions (Figure 3-12C). BMP and POPC extruded vesicles (Figures 3-12B & D, respectively) form spherical vesicles as expected, although again BMP vesicles are relatively smaller in size (~ 250 nm), than POPC vesicles (~ 500 nm). The pH dependence of BMP vesicle morphology may have significant implications in the process of endosome maturation.

Effects of ionic strength

In addition, the clustered morphology observed in BMP dispersions is dependent on salt. A previous report in the literature provides TEM images of BMP hydrated in 5 mM HEPES buffer pH 7.4 with a spherical morphology (93, 101, 106). We obtained consistent results when using buffer lacking 100 mM NaCl, and these results are shown in Figure 3-13A. On extrusion through 400 nm membranes, spherically shaped vesicles near 200 nm in diameter are obtained for neutral pH in the absence of NaCl (Figure 3-13B).

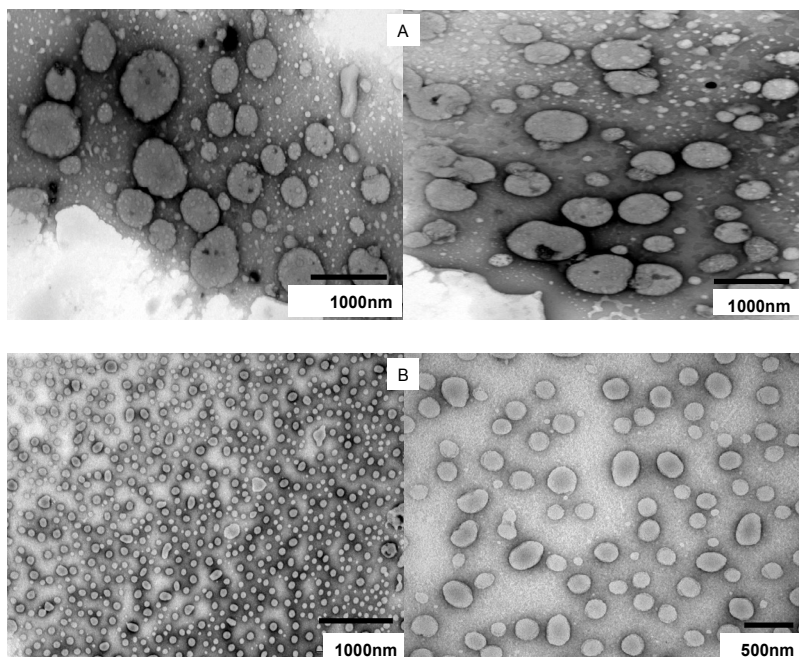


Figure 3-13. Negative staining-TEM images of BMP A) hydrated dispersions and B) 400 nm-extruded vesicles. Vesicles were hydrated in buffer lacking NaCl salt.

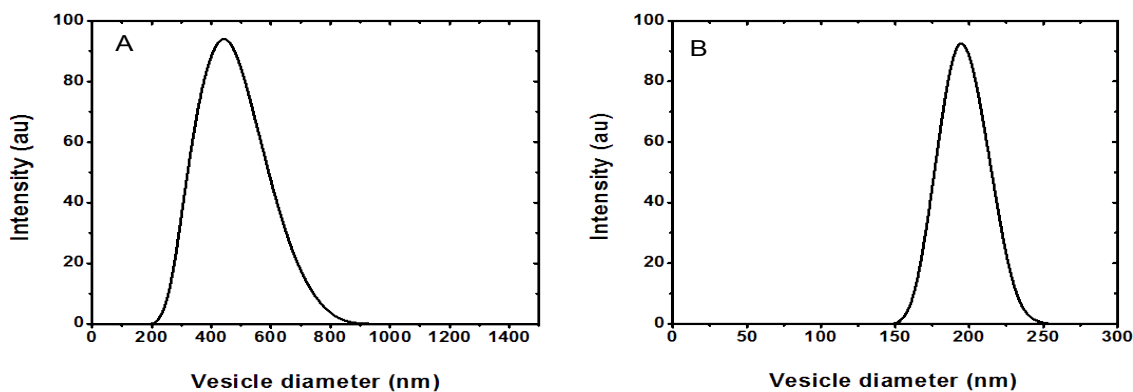


Figure 3-14. DLS histograms of BMP A) hydrated dispersions and B) 400 nm-extruded vesicles that were hydrated in the absence of NaCl.

Figure 3-14 shows DLS size distributions of BMP hydrated dispersions and extruded vesicles that were hydrated at neutral pH with buffer that lacked NaCl salt.

Table 3-5. Summary of average vesicle diameters of BMP vesicles hydrated without NaCl in the buffer.

	Average vesicle diameter (nm)
BMP vesicles	
Hydrated dispersions	500 ± 200
400 nm-Extruded vesicles	200 ± 40

Dynamic light scattering measurements were also performed on BMP dispersions and extruded vesicles in the absence of salt, at neutral pH 7.4, and the results presented in Figure 3-14 and summarized in Table 3-5 are consistent with TEM data. BMP hydrated dispersions have average diameters near 500 nm, whereas the 400 nm-extruded vesicles are ~ 200 nm in diameter.

Combined, the DLS and TEM data presented in this section demonstrate clearly that BMP forms small, stable lamellar vesicle structures that have an interior volume, and the vesicle morphology of BMP dispersions vary with pH and ionic strength.

Characterization of Hydrated Dispersions and Extruded Vesicles of POPC Mixed With BMP and POPG

Following the detailed characterization of BMP and POPC vesicle structures as a function of pH, ionic strength and polycarbonate extrusion pore diameters, we were interested in determining the effect of BMP when incorporated in typical phospholipid membranes such as POPC and POPG at certain concentrations. Because BMP is found at elevated concentrations of up to 15 mol% in the late endosome (233), DLS and negative staining-TEM experiments were performed on POPC:BMP (85:15) mixtures.

To study the effect of charge, similar DLS and negative staining-TEM experiments were performed on POPC:POPG (80:20) mixture since POPG carries a negatively charged like BMP, and is also a structural isoform of BMP. In order to mimic our previous studies on BMP and POPC lipids, experiments on the POPC:BMP and POPC:POPG lipid mixtures were performed on both their hydrated dispersions and 400 nm-extruded vesicles, and the lipids hydrated in a neutral pH 7.4 buffer containing 5 mM HEPES, 0.1 mM EDTA and 100 mM NaCl.

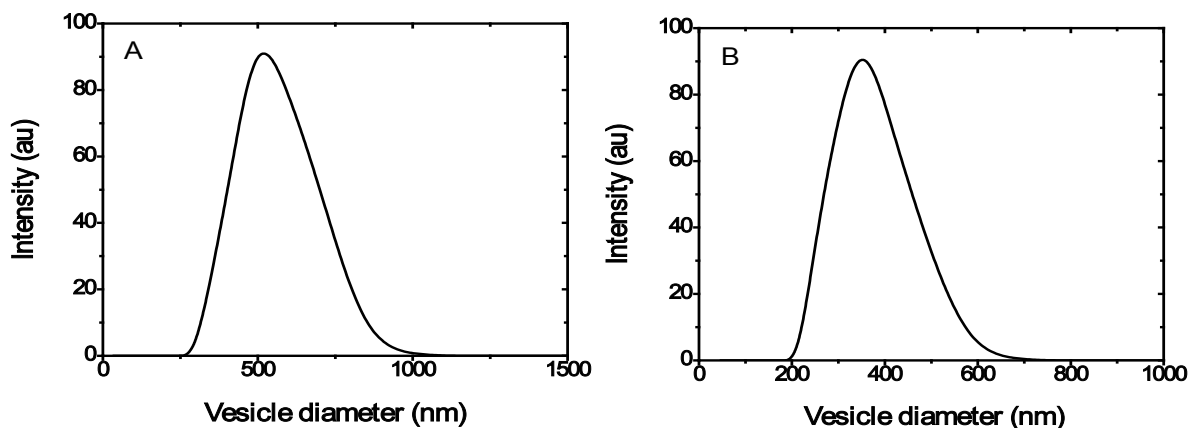


Figure 3-15. DLS size distribution of POPC:BMP (85:15) A) hydrated dispersions and B) 400-nm extruded vesicles at neutral pH.

Table 3-6. Summary of the average vesicle diameters of POPC:BMP (85:15) hydrated dispersions and 400 nm-extruded vesicles at neutral pH.

Dispersion type	Average vesicle diameters (nm)
Hydrated dispersions	900 ± 200
400 nm-Extruded vesicles	350 ± 170

The DLS average vesicle diameters for POPC:BMP hydrated dispersions and 400 nm-extruded vesicles are summarized in Figure 3-15 and Table 3-6. POPC:BMP hydrated dispersions (A) form vesicles with diameters near 900 nm, which is much smaller than that of POPC dispersions at neutral pH (~1400 nm), but slightly larger than the diameters observed in BMP dispersions (~500 nm) at the same pH. The 400 nm-extruded POPC:BMP vesicles also have relatively smaller diameters (~350 nm) than POPC (~400 nm) but still larger than BMP vesicle diameters (~230 nm).

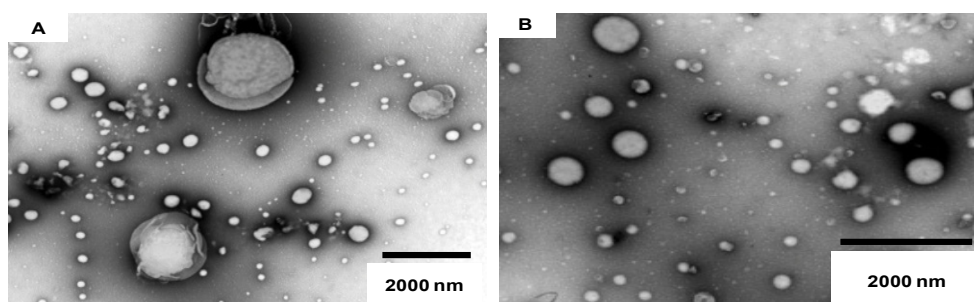


Figure 3-16. Negative staining-TEM images of POPC:BMP (85:15) A) hydrated dispersions and B) 400 nm-extruded vesicles at neutral pH.

POPC:BMP (85:15) dispersions form vesicles with morphologies that differ from those observed for both BMP and POPC dispersions at neutral pH conditions. From the TEM images in Figure 3-16A, POPC: BMP hydrated dispersions form heterogeneous vesicle structures that are composed of both spherical and nonspherical vesicles. The apparent heterogeneity can likely be attributed to some degree of immiscibility between BMP and POPC lipids, with BMP forming most of the observed nonspherical vesicle structures while POPC forms the uniformly spherical vesicles. A size analysis of the negative staining-TEM images also reveals that the POPC:BMP vesicle structures have diameters over a wide range of 200 – 1800 nm. The extruded POPC:BMP vesicles (Figure 3-16B) are uniformly spherical and non-structured as a result of being mechanically passed 31 times through 400 nm extrusion membranes.

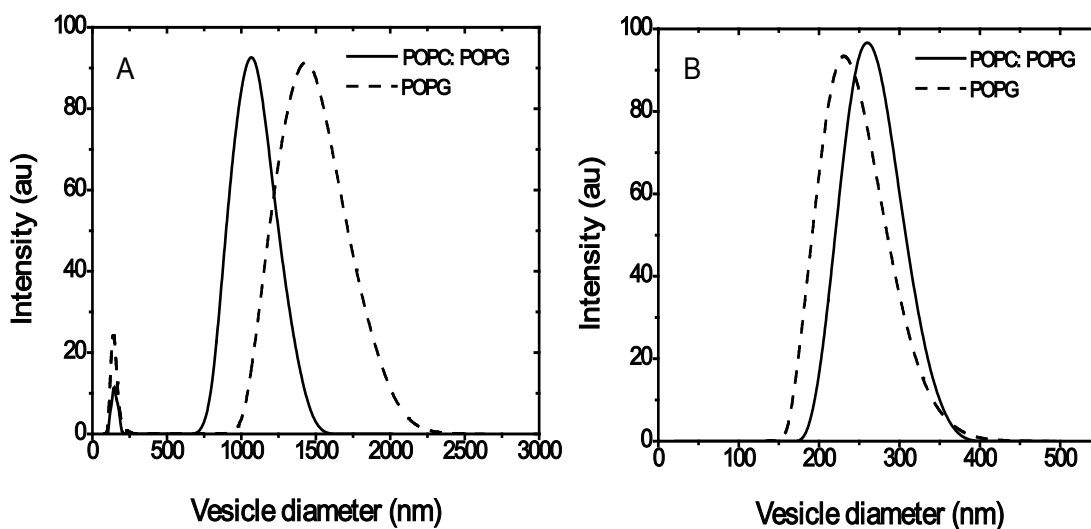


Figure 3-17. DLS measurements of POPG and POPC:POPG (80:20) hydrated dispersions and extruded vesicles at neutral pH.

Table 3-7. Summary of average vesicle diameters of POPG and POPC: POPG (80:20) vesicles.

Lipid Type	Average vesicle diameter (nm)	
	Hydrated dispersions	400 nm-Extruded vesicles
POPG	1500 ± 500	230 ± 90
POPC:POPG	1100 ± 300	250 ± 60

Results of DLS experiments performed on POPG and POPC:POPG hydrated dispersions and extruded vesicles are presented in Figure 3-17 and the average vesicle diameters are summarized in Table 3-7. Average diameters of POPG dispersions (~1500 nm) differ only slightly from POPC:POPG dispersions (~1100 nm), although both are relatively similar to the diameters previously observed for POPC dispersions (~1400 nm), but still smaller than BMP dispersions (~500 nm) under neutral pH conditions. Interestingly, POPG and POPC:POPG extruded vesicle diameters (230 and 250 nm, respectively) are close in size to BMP extruded vesicle diameters (~230 nm), although POPG and POPC:POPG extruded vesicles have more broadened size distributions.

Taken together, the characterization of POPC:BMP and POPC:POPG lipid mixtures at neutral pH reveals that BMP induces small vesicle formation when incorporated in typical POPC membranes at certain concentrations. BMP also alters the morphology of POPC hydrated dispersions, forming heterogeneous spherical and nonspherical vesicle structures. POPG does not have a significant effect on the vesicle diameter of POPC hydrated dispersions, although it results in formation of much smaller vesicles when extruded with 400 nm pore membranes, with diameters resembling those observed for BMP vesicles.

Conclusions

The analytical capability of the dynamic light scattering (DLS) technique was successfully demonstrated through the accurate measurement of manually mixed vesicle populations. DLS and negative staining-transmission electron microscopy (TEM) were utilized to characterize the size of hydrated and extruded BMP and POPC samples, revealing that when BMP is hydrated from a dry lipid film, it forms lipid

dispersions that have diameters much smaller than those of POPC dispersions, regardless of pH.

The non-spherical clustered vesicle morphology observed in the TEM images of BMP hydrated under neutral pH in the presence of 100 mM NaCl differs from what was reported earlier for this lipid. However, the data show that the absence of NaCl can account for the different morphology observed. It is interesting that spherical vesicle shapes were observed under acidic conditions. In a 2004 Science report, the Gruenberg group (98) showed that intravesicular structures will spontaneously develop for lipid mixtures containing BMP when a pH gradient was established across the liposome with the interior compartment being acidic.

The work reported here has also demonstrated, using vesicle leakage assays and vesicle “stability” assays, that BMP forms small, stable lamellar vesicles with an interior volume that can encapsulate molecules. Following the characterization of POPC:BMP and POPC:POPG lipid mixtures, it was shown that BMP can induce the formation of small vesicles when incorporated in typical POPC membranes at certain concentrations. Taken together, these data suggest that the physical-chemical properties of BMP, dictated by its unique dual glycerol structure and orientation of the phosphate group, may provide a mechanism for stabilization of small vesicle structures in the maturing endosome as the lumen acidifies, shedding further light on the potential functional role of this lipid in the late endosome.

CHAPTER 4
ANALYSIS OF CHANGES IN BMP VESICLE SIZE AND MORPHOLOGY IN THE
PRESENCE OF GANGLIOSIDE GM1 AT LATE ENDOSOMAL PH 5.5

Introduction

Bis(monoacylglycero)phosphate (BMP) is a characteristic lipid of the endocytic degradative pathway that is found in the late endosome luminal membranes in concentrations of approximately 15 mole percent (44).

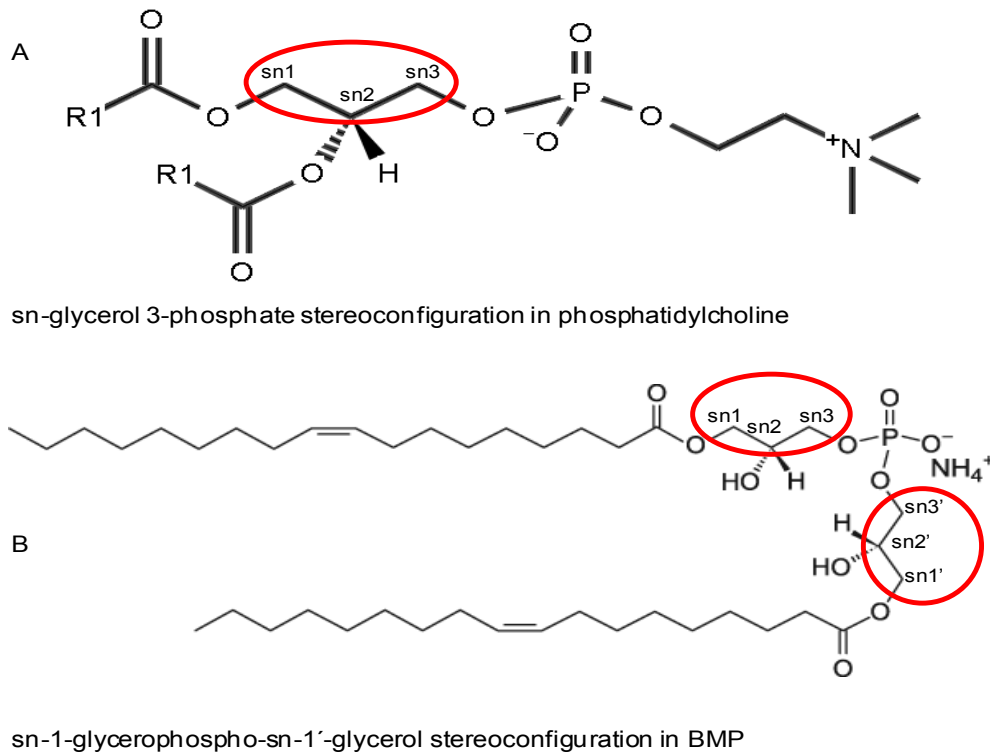


Figure 4-1. Chemical structure of A) Phosphatidylcholine and B) BMP.

The chemical structure of BMP, shown in Figure 4-1B, differs from that of other glycerophospholipids, in that BMP contains two glycerol components, each with a single acyl chain (2, 8, 46). Additionally, BMP has an sn-1-glycerophospho-sn-1'-glycerol (sn1:sn1') stereoconfiguration that differs from the typical sn-3-glycerophosphate stereoconfiguration found in other glycerophospholipids as illustrated by the red circles in Figure 4-1 (47-50).

Due to its increased concentration in the late endosomes, BMP is thought to play important structural and functional roles in this organelle (106). Several *in vivo* investigations have demonstrated that antibodies and chemicals that interact with BMP lead to changes in the sorting and trafficking of proteins and lipids in late endosomes, resulting in an altered structure of the late endosome (44, 114) and abnormal accumulation of cholesterol (108). BMP is also essential for lysosomal catabolism processes(46), such as the activator-stimulated hydrolysis of gangliosides GM1 (109) and GM2 (110), and the hydrolysis of ceramide by acid ceramidase (111).

Gangliosides are sialic acid-containing glycosphingolipids found in the cell membranes of vertebrates, and are particularly high in abundance in the plasma membrane of neuronal cells (234). Glycosphingolipid degradation proceeds via endocytosis from the plasma membrane and subsequent transportation to the endosomes, followed by intraendosomal vesicle formation, and final trafficking as intralysosomal vesicles for degradation (235). Deficiencies in the catabolism of gangliosides result in lysosomal glycosphingolipid accumulation, leading to clinical disorders known as sphingolipid storage diseases that mainly affect neuronal cells within the brain (236).

Much insight into the process of membrane digestion has been realized through the investigation of glycosphingolipid catabolism (46). The lysosomal degradation of glycosphingolipids is a sequential pathway of reactions that are catalyzed by exohydrolases with acidic pH optima. These enzymes are assisted by small glycoprotein cofactors, known as the sphingolipid activator proteins (SAPs), and lipid composition has been shown to alter the *in vitro* degradation kinetics; optimum activity

is obtained with low cholesterol content and the presence of the negatively charged lipid BMP (46).

Work presented previously in Chapter 3 discussed in detail the characterization of the morphology and molecular organization of sn-3-sn-1' dioleoyl-BMP (BMP) under both acidic and neutral pH conditions. It was showed that when hydrated, BMP forms small, stable lamellar vesicles with interior volumes and with acyl-chain dynamics and packing similar to other glycerophospholipids (105). Given the unique chemical structure of BMP, this vesicle morphology was surprising as it had been previously assumed that BMP would form either micellar structures, similar to detergent or inverted hexagonal morphologies, as is seen with phosphatidylethanolamine lipids (237).

The main objective of the work reported in this chapter was to study the effect of adding ganglioside GM1 to BMP membranes at varying concentrations, under late endosomal pH conditions. Dynamic light scattering (DLS) and negative staining-transmission electron microscopy (TEM) were utilized to monitor the size, morphological and structural changes in hydrated dispersions and extruded vesicles of BMP:GM1 mixtures. Results presented in this chapter also include the characterization of the morphology and size distribution of BMP hydrated lipid dispersions under different pH conditions, ranging from acidic (pH 4.2) to neutral (pH 7.4) conditions, using TEM and DLS. Finally, studies were performed that monitored the effect of incorporating GM1 and BMP in typical phosphatidylcholine (POPC) membranes. POPC is abundantly present in biological cellular membranes and has been well characterized as a model system; hence it made for a good lipid choice for typical model system studies. By utilizing dynamic light scattering and transmission emission spectroscopy, the

morphology and size distribution of POPC: GM1 and POPC: BMP: GM1 hydrated dispersions and extruded vesicles were investigated.

Experimental Section

Materials Used

BMP18:1, ((S, R Isomer) sn-(3-Oleoyl-2-Hydroxy)-Glycerol-1-Phospho-sn-3'-(1'-Oleoyl-2'-Hydroxy)-Glycerol, ammonium Salt)), in chloroform and ganglioside GM1 powder, were purchased from Avanti Polar Lipids (Alabaster, AL) and used without further purification. HEPES, (4-(2-hydroxyethyl)-1-piperazineethanesulfonic acid, $C_8H_{18}N_2O_4S$); NaOAc, (sodium Acetate); EDTA, (ethylenediamine tetraacetic acid, $C_{10}H_{16}N_2O_8$) and NaCl, (sodium chloride) were purchased from Fisher Biotech (Pittsburgh, PA). CH_3Cl , (chloroform); MeOH, (methanol); CH_3CH_2OH (ethanol); C_6H_{12} , (cyclohexane); NH_4OH , (ammonium hydroxide); HCl, (hydrochloric acid) and NaOH, (sodium hydroxide) were obtained from Fisher Scientific (Pittsburgh, PA). $UO_2(CH_3COO)_2 \cdot 2H_2O$, (uranyl acetate) and 400-mesh Formvar-coated copper grids were purchased from Ted Pella (Redding, CA). Single-sealed 50- to 1000-mL disposable cuvettes (10-mm path length) were obtained from Eppendorf (Westbury, NY). 400-nm polycarbonate extrusion membranes and filter supports were purchased from Avanti Polar Lipids (Alabaster, AL). Silica-coated aluminum thin layer chromatography (TLC) plates were purchased from Whatman (Florham Park, New Jersey).

Preparation of Hydrated Lipid Dispersions and Extruded Unilamellar Vesicles

The desired amount of stock lipid (5 mg/mL BMP in chloroform, or 1mg/mL GM1 in chloroform methanol mixture), was dried under a gentle nitrogen stream for about 10 minutes or until the solvent evaporated, forming a dry, thin lipid film. The sample was then further dried under vacuum in a desiccator for ≥ 12 hours to remove any residual

solvent. Dry lipid films of 100% BMP or BMP:GM1 lipid mixtures were hydrated with either 2 mL of 5 mM NaOAc buffer for pH 4.2, 5.5 and 6.1, or 2 mL 5mM HEPES buffer for pH 7.4. All buffers contained 100 mM NaCl and 0.1 mM EDTA, and the final lipid concentration was approximately 0.75 mM. Hydrated BMP:GM1 lipid mixtures were freeze-thawed in liquid N₂ five times. All hydrated dispersions were incubated at room temperature for approximately 12 hours before extrusion or measurement by dynamic light scattering (DLS) and negative staining-transmission electron microscopy (TEM).

To form large unilamellar vesicles (LUVs), hydrated lipid dispersions were extruded by passing 31 times through 400 nm polycarbonate extrusion membranes. Phospholipid integrity was verified by thin layer chromatography (TLC), where approximately 10 μ L of lipid sample was spotted on silica-coated aluminum plates. Plates were placed in a chamber containing a CH₃Cl: MeOH: NH₄OH (65:25:10) mobile phase. The TLC plates were developed in an iodine chamber and visualized by eye.

Instrumentation

Dynamic light scattering (DLS)

Size distribution measurements of hydrated dispersions and extruded unilamellar lipid vesicles were performed with a Brookhaven 90Plus/BI-MAS ZetaPALS spectrometer operated at a wavelength of 659 nm and at 25° C. The instrument uses a BI-9000AT digital autocorrelator and 9KDLSW data acquisition software. A 100- μ L sample volume in a disposable cuvette was used for each measurement. For each sample, 3 runs were performed with each run lasting 3 minutes. Data and histograms were further analyzed and converted into B-spline plots using OriginPro 8 software. DLS data were reported as an average of 3 runs for each sample, and errors calculated as a standard deviations of the mean diameter.

Negative staining-transmission electron microscopy (TEM)

TEM images were obtained using a Hitachi H-7000 transmission electron microscope operated at 75-100 kV with a Soft-Imaging System MegaViewIII with AnalySIS digital camera (Lakewood, CO). The microscope has a maximum resolution at 0.2 nm with a magnification range of 110× to 600,000×. Prior to TEM measurements, samples were further prepared by negative staining. Briefly, for all samples, using a disposable pipette, a drop of the lipid vesicle sample was spread on a 400-mesh Formvar-coated copper grid held by tweezers and incubated for 2 minutes. Excess lipid sample was gently dabbed away with filter paper, and the grid was allowed to dry for 2 minutes. In some instances a drop of deionized water was added to the grid to remove any excess salt from the buffer solution used in vesicle preparation. One drop of 2% uranyl acetate was then added to the grid and allowed to stain for 2 minutes, after which any excess uranyl acetate was wiped away, and the sample was allowed to dry for 2 minutes before being placed in the electron microscope specimen holder for image analysis and collection.

Results and Discussion

Characterization of BMP Hydrated Lipid Dispersions as a Function of pH

Because the pH varies in different sub compartments of the endocytic pathway, with acidification increasing progressively from the endocytic carrier vesicles and early endosomes to late endosomes, and eventually lysosomes (238), BMP hydrated dispersions were prepared at four different pH conditions; pHs 4.2, 5.5, 6.1 and 7.4, indicative of the *in vivo* pH in the lysosome, late endosome, early endosome and cytosol, respectively.

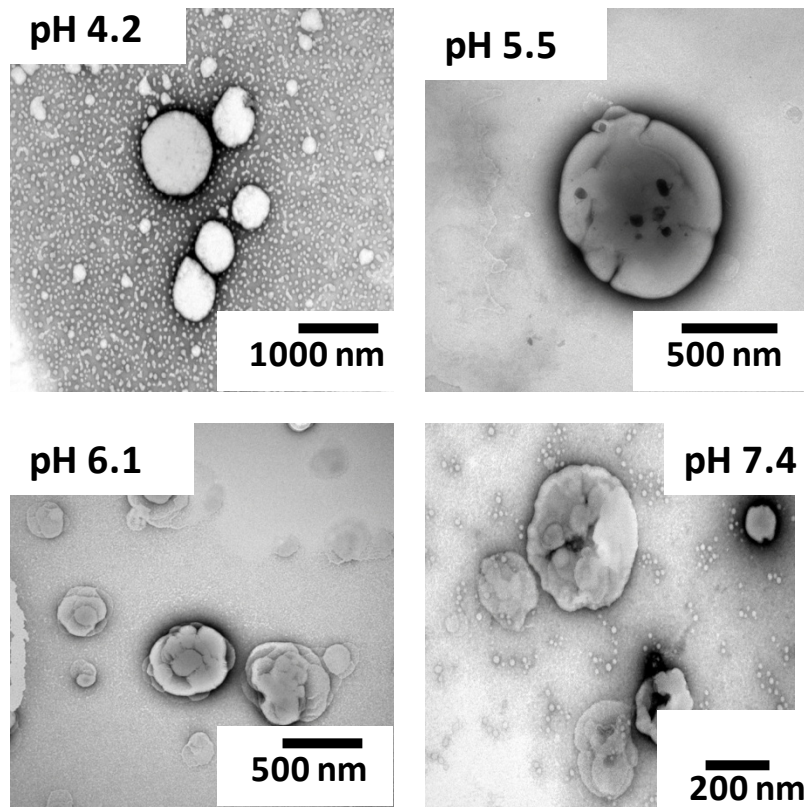


Figure 4-2. Negative staining-TEM images of BMP lipid dispersions as a function of pH.

Figure 4-2 exhibits negative staining-TEM images of BMP lipid dispersions as a function of pH. These images show that BMP dispersions exhibit different morphologies as the pH is varied; progressing from fully spherical, non-structured vesicles at acidic pH 4.2 to non-spherical, highly structured vesicle clusters at neutral pH 7.4. In addition, the sizes of the BMP dispersions are found to vary as a function of pH.

At pH 4.2, BMP lipid dispersions are homogeneously spherical, non-structured, and have an average size of $\sim 1 \mu\text{m}$. This is in contrast to the vesicle morphology of BMP dispersions seen at late endosomal pH 5.5, which though spherical, show some slight structuring and are also significantly smaller, with a size distribution of 0.5 - $1 \mu\text{m}$. BMP vesicles at pH 6.1 exhibit extensive structural deviations from a spherical shape, appearing like aggregations of a number of smaller vesicles. The vesicles at early

endosomal pH 6.1 are also smaller in size than those at both pH 4.2 and pH 5.5, with a size distribution of 0.5 – 0.8 μm . At pH 7.4, BMP dispersions have a highly budded and protruding non-spherical shape appearing highly clustered, with an average vesicle size of 500 nm.

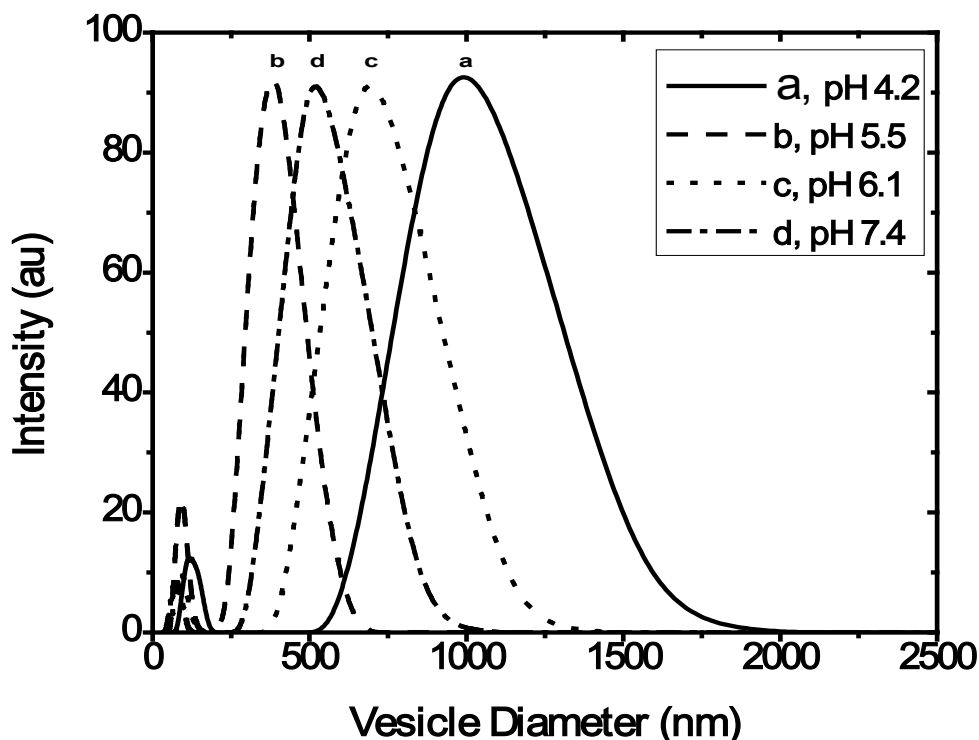


Figure 4-3. Dynamic light scattering size distributions of BMP hydrated dispersions as a function of pH.

Table 4-1. Summary of the average diameter of BMP hydrated dispersions at specific pH conditions.

pH	4.2	5.5	6.1	7.4
BMP Vesicle Diameter	950 \pm 310	390 \pm 150	670 \pm 330	500 \pm 250

The size distributions of BMP hydrated dispersions at various pH conditions were also determined by utilizing dynamic light scattering, and the results are shown in Figure 4-3, and summarized in Table 4-1. These data were obtained by averaging three independent DLS histograms and the error calculated as standard deviation from the

average size. The DLS data shows increasing vesicle diameter with increasing acidity, except endosomal pH 5.5 which exhibits the lowest vesicle diameter at ~ 400 nm. At acidic pH 4.2, the vesicles have the largest average diameter of ~ 1 μm while at pH 6.1, the vesicles exhibit diameters in the range of ~700 nm. Neutral pH 7.4 shows vesicles with diameters of ~ 500 nm and vesicles at endosomal pH 5.5 differ from this general trend by exhibiting the smallest vesicle diameter of ~ 400 nm. The variation in vesicle diameter at pH 5.5 could be attributed to the possible formation of intraendosomal vesicular bodies that are significantly smaller in size, and this finding is consistent with the TEM data discussed previously. Taken together, results from these experiments showed that the morphology of the hydrated BMP dispersions vary with pH, further suggesting a role for BMP in intraendosomal vesicular body formation, which is triggered in the late endosome by the biosynthesis of BMP and a drop in endosomal lumen pH (105).

Characterization of BMP:GM1 Hydrated Dispersions and Extruded Vesicles at Specific Concentrations

Based on their individual molecular geometries and chemical structures (Figure 4-4), BMP and GM1 independently exhibit different polymorphisms when hydrated. The ganglioside GM1 is a surfactant molecule with a bulky sugar headgroup that forms micelles rather than lamellar liposomes (239). On the other hand, BMP adopts a lamellar bilayer structure in an aqueous environment (105). We investigated the different macroscopic shapes and sizes in mixtures of BMP and GM1 under endosomal pH.

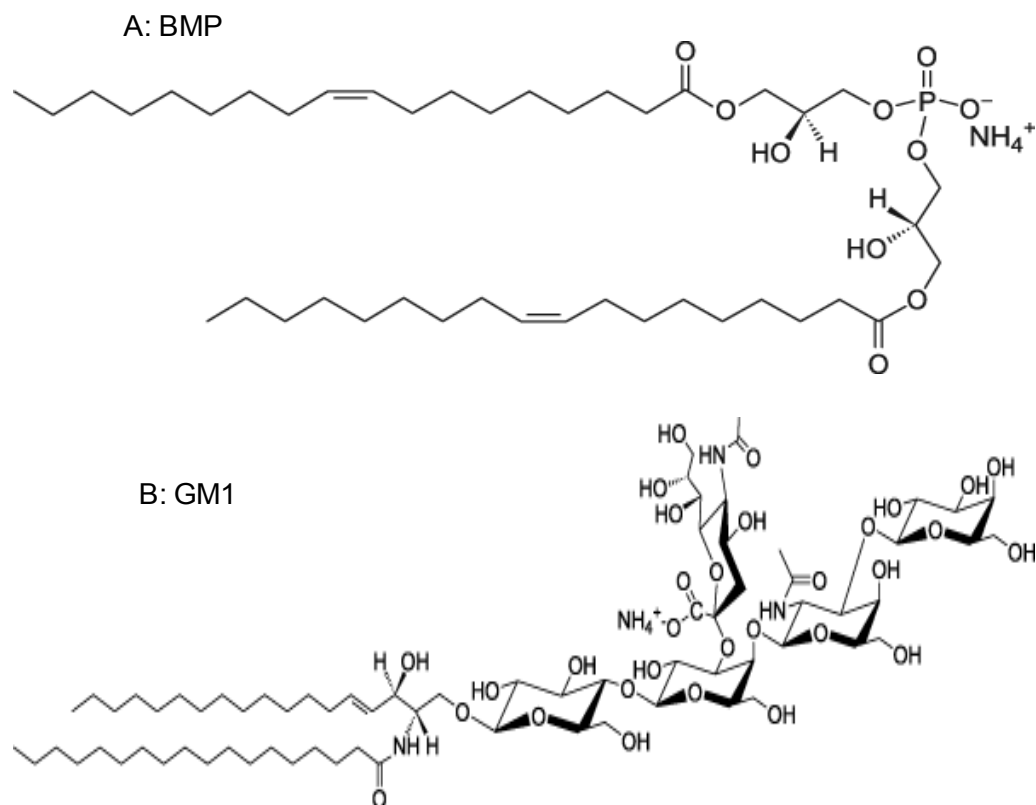


Figure 4-4. Chemical structures of A) BMP and B) ganglioside GM1.

Figure 4-4 is an illustration of the chemical structures of BMP and ganglioside GM1. By preparing samples with varying concentrations of BMP:GM1 mixtures, DLS and TEM investigations were performed to determine what lipid polymorphism would dominate as the relative mole percentages of each lipid were varied. Hydrated lipid dispersions and 400-nm extruded vesicles of 100% BMP, and BMP: GM1 lipid mixtures in 10 mole% GM1 increments at 90:10, 80:20, 70:30, 60:40 and 50:50 were prepared as discussed in the experimental section. DLS measurements were performed on both hydrated dispersions and extruded vesicles, whereas only the hydrated dispersions of BMP and BMP: GM1 were imaged by TEM, because it is expected that the extruded vesicles would form uniformly spherical morphologies as a result of being mechanically forced through 400 nm pore membranes as observed in previous investigations discussed in Chapter 3.

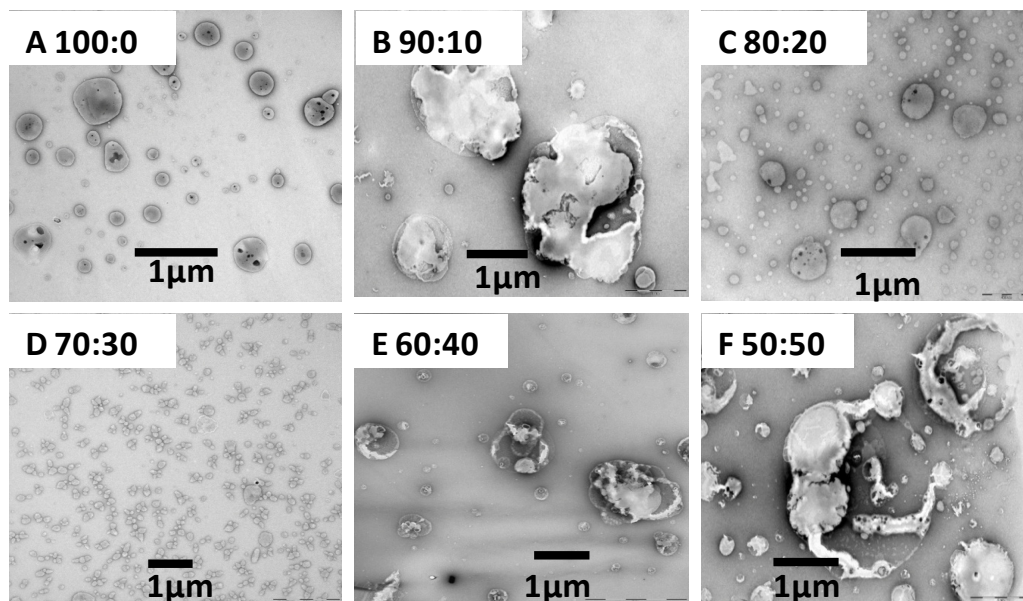


Figure 4-5. Negative staining-TEM images of hydrated BMP:GM1 dispersions at specific molar ratios at pH 5.5.

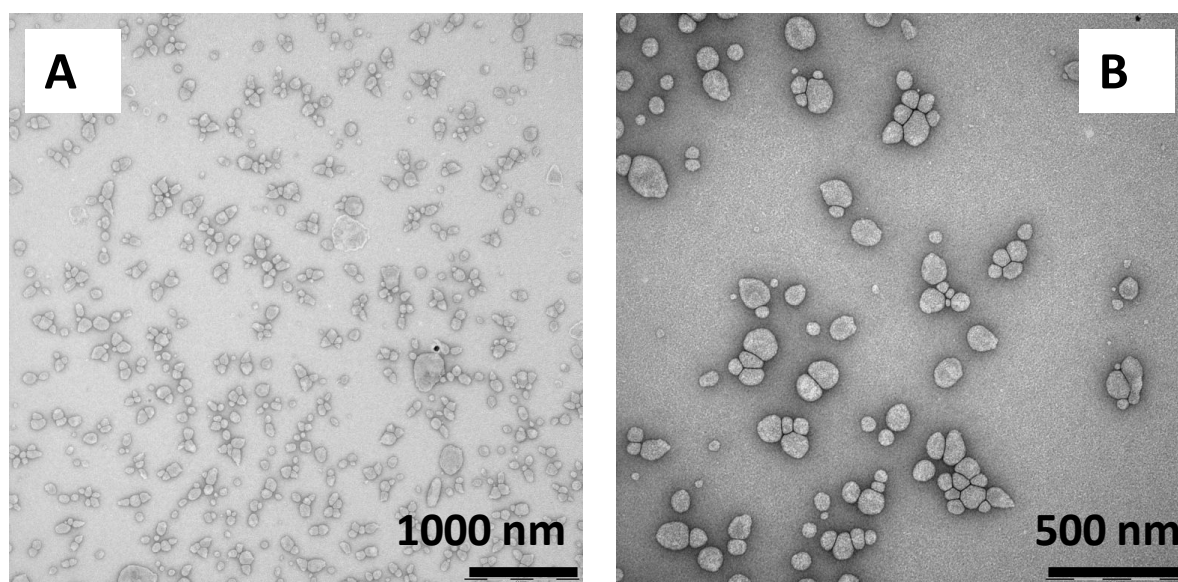


Figure 4-6. TEM images of 70:30 mol % BMP: GM1 lipid mixture, showing A) small, aggregated homogenous vesicles, and B) magnified images of the same vesicles.

Figure 4-5 show the negative staining-TEM images of BMP:GM1 hydrated dispersions where the mol % of GM1 is varied from 0 % to 50 % in 10 % increments.

Figure 4-6A shows the apparent aggregated morphology of 30% GM1 in 70% BMP

hydrated dispersions, and the magnified images of the same sample is shown in Figure 4-6B. The 100 % BMP dispersions (Figure 4-5A, 100:0) are spherical in shape with diameters ranging between ~ 200 – 500 nm. Upon mixing with 10 % GM1, (Figure 4-5B, 90:10), the vesicle morphology changes to non-spherical heterogeneous structures mixed with some small spherical vesicles observed. The average diameter for this mixture is between ~ 300 – 600 nm, with sizes larger than 1 μm detected. Note the presence of the smaller, more spherical vesicles, which may correspond to predominant BMP vesicles, suggesting immiscibility of the two lipids at this composition.

For BMP:GM1 mole ratios of 80:20 (Figure 4-5C) and 70:30 (Figure 4-5D), spherical vesicle structures are obtained. The vesicles formed from the 80:20 BMP:GM1 mixture have a spherical shape, with average diameters ranging from ~ 300-500 nm. On the other hand, BMP:GM1 (70:30) produced nearly homogeneous, spherical vesicles of diameter ~100 nm, that appeared aggregated in the TEM images.

Figure 4-7 shows dynamic light scattering size distribution histograms of BMP:GM1 hydrated dispersions (A) and extruded unilamellar vesicles (B) at specific mol %, whereas Table 4-2 displays a summary of the average vesicle diameters and error bars of the same samples in Figure 4-7, obtained from calculating the average of three independent DLS histograms. The error bars were obtained as standard deviations of the most probable vesicle diameter for each sample.

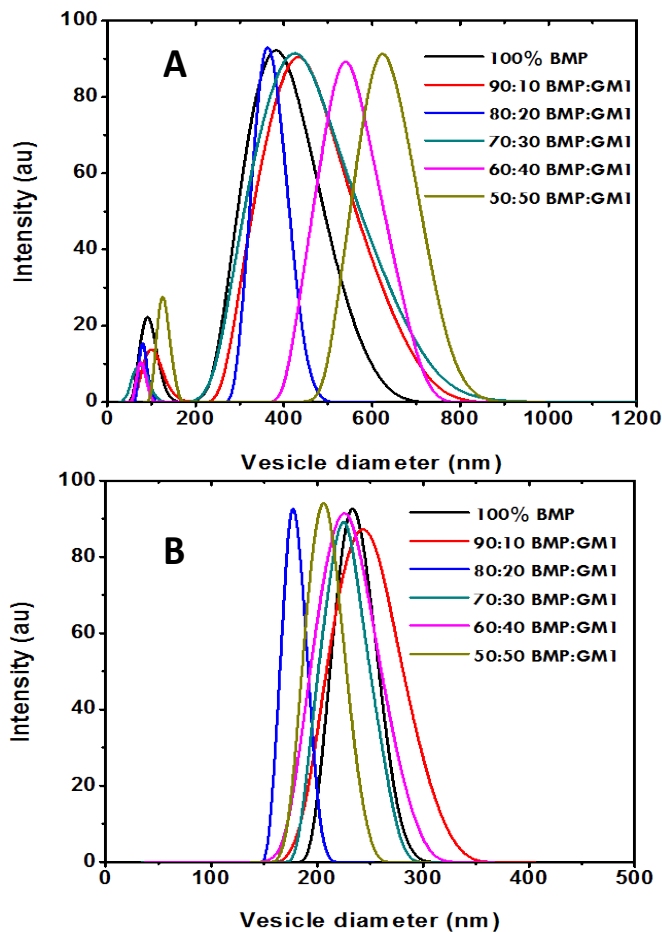


Figure 4-7. DLS size distribution histograms of BMP:GM1 A) Hydrated dispersions and B) 400 nm-Extruded unilamellar vesicles at specific concentrations.

Table 4-2. Summary of DLS average vesicle sizes of BMP:GM1 hydrated lipid dispersions and 400-nmextruded unilamellar vesicles at specific concentrations.

Lipid composition	100% BMP	90:10 BMP:GM1	80:20 BMP:GM1	70:30 BMP:GM1	60:40 BMP:GM1	50:50 BMP:GM1
Hydrated Dispersions (nm)	390±150	420 ±150	380 ± 70	430 ± 250	540 ± 110	650 ± 110
Extruded Vesicles (nm)	230 ± 40	230 ± 70	180 ± 20	230 ± 30	230 ± 50	240 ± 50

Error bars were calculated as standard deviations of the most probable average vesicle size obtained from averaging three independent DLS histograms.

Results from DLS measurements of 30 mol % GM1 sample shown in Table 4-2 reveal a size distribution of 200 – 600 nm, with the average vesicle size observed at 430 nm. The increased average vesicle size seen with DLS is likely due to the aggregation of the smaller vesicles that are discernable in the TEM images. This difference in size can be interpreted to arise from the fact that DLS reports the average spherical shape of the aggregate hydrodynamic diameter of the aggregations, and not that of the individual vesicles. Perhaps the relatively low laser power (35 mW) and detector (photo multiplier tube, PMT) of the particular DLS instrument that was used may also limit detection of the smaller-sized particles.

It is noteworthy that the formation of homogeneous vesicles with 20 - 30 mol % GM1 in BMP membranes is consistent with previous work by Lee and coworkers (239), using Langmuir-monolayer preparations of GM1 mixtures with dipalmitoylphosphatidylcholine (DPPC) to show that GM1 has a condensing effect on DPPC lipids over the concentration range of 20 - 30 mol %. Taken together, these findings indicate a biologically relevant concentration range for GM1 incorporation into lipid raft domains or being trafficked to ganglioside enriched endosomal vesicles in the lysosome.

For concentrations \geq 40 mol % GM1, heterogeneous non-spherical structures are again obtained. At this ratio (Figure 4-5E), both small spherical vesicles and irregularly shaped larger structures are observed. This heterogeneity in size and structure gives a distribution of diameters ranging from 400 – 700 nm. The presence of two distinct macroscopic morphologies may indicate immiscibility of the two lipids above the 30 mol

% ratio. Similar findings are seen for the 50:50 BMP: GM1 sample (Figure 4-5F), where the size distribution increases to 500 – 800 nm.

In general, the vesicle diameters determined from DLS measurements of the hydrated dispersions (Figure 4-7A) are consistent with results from TEM images discussed above. The DLS measurements of the unilamellar vesicles extruded with 400 nm polycarbonate membranes (Figure 4-7B) reveal vesicle diameters that are consistently centered at ~ 230 nm for all mol % ratios as would be expected, except for the 80:20 BMP:GM1 ratio, which has an average diameter at ~180 nm. However as mentioned previously, for the 70:30 BMP:GM1 ratio, the DLS measurements of the hydrated dispersions give a larger size than seen with TEM, likely because of aggregation of the smaller vesicles.

In earlier studies, Kobayashi and coworkers examined the membrane structure of various BMP: ganglioside mixtures under neutral and acidic pH conditions and found that at pH 8.5 - 6.5, the BMP:GM1 (1:1 mol/mol) mixture formed small vesicular aggregates, whereas the mixture formed closely packed lamellar structures under acidic conditions (pH 5.5- 4.6) (101). The apparent miscibility of GM1 with BMP over the 20-30 mol % ratios, as evidenced by the spontaneous formation of small homogeneously shaped vesicles with narrow diameter size distribution, suggests that optimum interactions between molecules may occur for a given molecular ratio of 3 BMP molecules for 1 GM1 molecule to form a lipid complex. This hypothesis is drawn from the analysis of Langmuir-monolayer studies, which showed that the pressure-area isotherms of GM1 and DPPC mixtures follow “ideal” mixing behavior when the two

species were considered to be a 3:1 DPPC:GM1 complex interacting with excess DPPC (239).

Effect of GM1 and BMP Mixing with POPC Membranes

Eukaryotic cellular membranes are predominantly composed of a high concentration of phospholipids (2, 8), especially phosphatidylcholine (POPC) lipid moieties, making POPC one of the most well studied and characterized phospholipids. In Chapter 3, 100 % POPC vesicle size and morphology were characterized by dynamic light scattering (DLS) and transmission electron microscopy (TEM) under neutral, physiological pH 7.4.

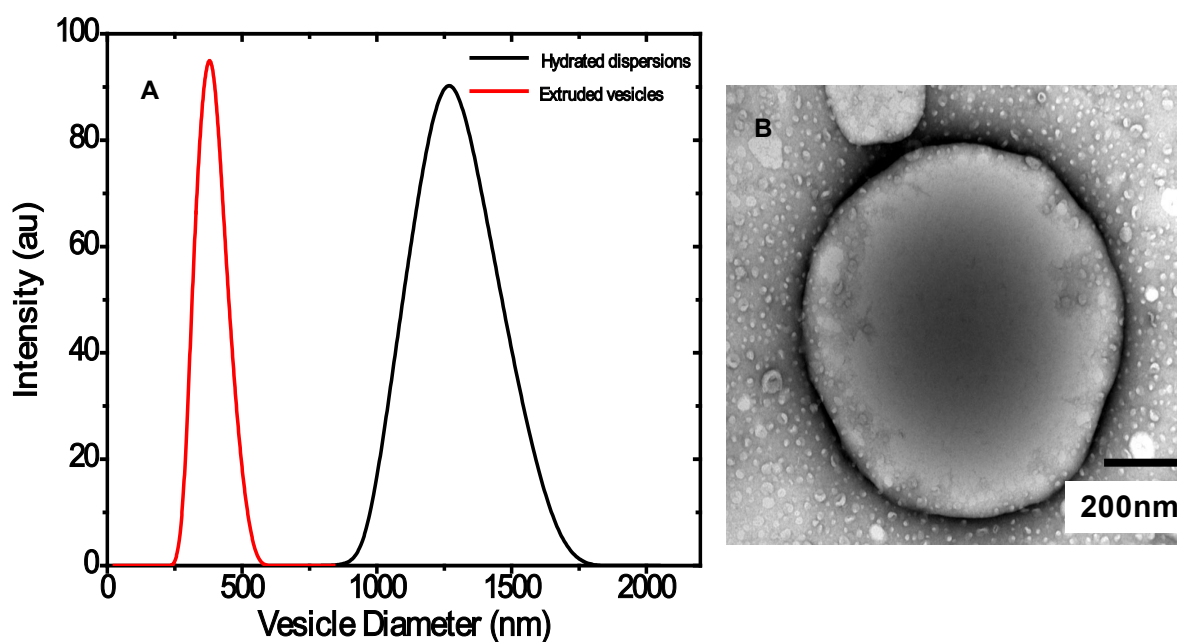


Figure 4-8. Dynamic light scattering average vesicle diameters of POPC A), black solid line, hydrated dispersions, A), red solid line, unilamellar vesicles extruded with 400 nm polycarbonate membranes and B) TEM image of POPC hydrated dispersions.

Figure 4-8 represents results of 100 % POPC characterization under neutral pH conditions, in which POPC hydrated dispersions (A, black solid line) were demonstrated

to have average vesicle diameters of $\sim 1.3 \mu\text{m}$, while unilamellar vesicles extruded with 400 nm pore membranes (A, red solid line) had $\sim 400 \text{ nm}$ vesicle diameters. TEM imaging of POPC hydrated dispersions reveals spherical vesicle structures with a size range (1-2 μm) that is consistent with DLS analysis.

In order to monitor the effect of GM1 and BMP on typical phospholipid macroscopic morphology, structure and size distribution, DLS and TEM experiments were performed that incorporated 20 mol % GM1 in 80 mol % POPC, then 15 mol % GM1 and 15 mol % BMP in 70 mol % POPC at late endosomal pH 5.5.

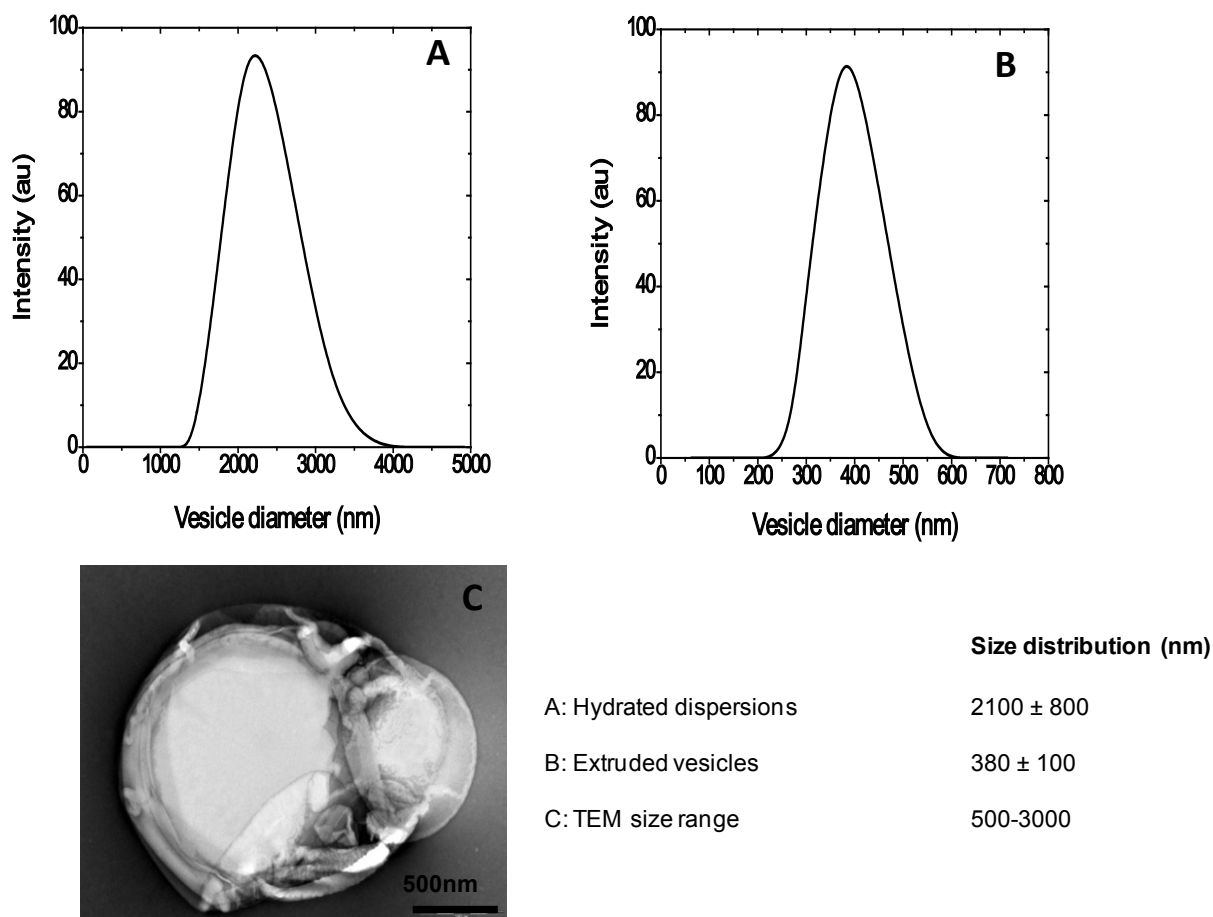


Figure 4-9. Dynamic light scattering average vesicle diameters of POPC:GM1 (80:20) A) hydrated dispersions, B) 400-nm extruded vesicles and C) TEM images of POPC:GM1 hydrated dispersions at pH 5.5.

Figure 4-9 is an illustration of the DLS average vesicle diameters obtained for POPC:GM1 hydrated dispersions (A), extruded vesicles (B) and the TEM images of POPC:GM1 hydrated dispersions (C). The DLS data reveal larger vesicle diameters for the POPC:GM1 hydrated dispersions (Figure 4-9A), with average vesicle diameters of $\sim 2.1 \mu\text{m}$ compared to the vesicle diameters observed for POPC hydrated dispersions ($\sim 1.4 \mu\text{m}$). The increased size is also supported by TEM analysis, where images of the POPC: GM1 hydrated dispersions (Figure 4-9C) have vesicle diameters of up to $3.0 \mu\text{m}$. The POPC:GM1 vesicle morphology is also different from that observed for 100 % POPC, displaying structured, budding-like vesicles. The structured morphology and increased vesicle sizes of POPC:GM1 hydrated dispersions could be as a result of the presence of ganglioside GM1, whose bulky sugar head groups contribute favorably to the formation of larger, lipid vesicles (239). POPC:GM1 unilamellar vesicles that were extruded with 400 nm polycarbonate membranes (Figure 4-9B) were also measured by dynamic light scattering, showing average vesicle diameters of $\sim 380 \text{ nm}$, as would be expected.

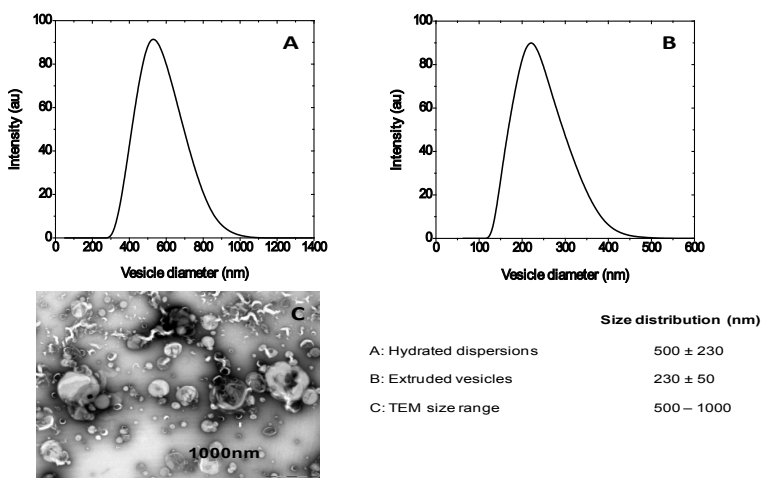


Figure 4-10. Average vesicle diameters of POPC:BMP:GM1 (70:15:15) A) hydrated dispersions, B) 400-nm extruded vesicles and C) TEM images of POPC: BMP:GM1 hydrated dispersions.

The incorporation of 15 mol % BMP in POPC and GM1 lipid membranes mimics the percent concentration of BMP in the late endosome, where it is found in concentrations of up to 15 mol %. Figure 4-10 is an illustration of the average vesicle diameters of POPC:BMP:GM1 (70:15:15) hydrated dispersions, unilamellar vesicles extruded with 400 nm polycarbonate membranes and TEM images of POPC:BMP:GM1 hydrated dispersions. The average vesicle diameters were obtained by calculating the average of three independent DLS histograms, and all experiments were performed under pH 5.5. Interestingly, the vesicle diameters of the POPC:BMP:GM1 hydrated dispersions are much smaller (~ 500 nm) than those observed for the POPC:GM1 dispersions (~ 2100 nm) discussed previously. TEM analysis also reveals highly heterogeneous vesicles formed by the POPC:BMP:GM1 dispersions (Figure 4-10C), displaying vesicles of varied sizes, ranging from 500 – 1000 nm. Some of the vesicle structures are non-spherical and clustered, while others are uniformly spherical and non-clustered, indicating possible immiscibility among the POPC, BMP and GM1 lipids. The unilamellar extruded vesicles have average diameters at ~230 nm, which is smaller than that obtained for POPC:GM1 extruded vesicles (~380 nm), but similar to the vesicle diameter obtained for 100 % BMP vesicles extruded with 400 nm polycarbonate membranes.

The significantly reduced vesicle diameters for the POPC:BMP:GM1 hydrated dispersions and extruded vesicles could be attributed to the presence of BMP in the lipid mixture, which perhaps because of unique structure and stereochemistry in its phosphate head-group allows for the energy required for the stabilization of smaller vesicle formation (105). The heterogeneous formation of vesicles with varied

morphologies could also be as a result of the ganglioside GM1 in the lipid mixture which hinders proper mixing and packing because of increased steric hindrance in the bulky sugar headgroups of the ganglioside (239). It might be interesting to perform studies that can enable tracking of the vesicles in such a lipid mixture, such as the use of secondary Au antibody labeling, to determine the preference of each individual lipid in forming either smaller or larger vesicles.

Conclusions

The results in this chapter summarize the effect of pH, concentration and lipid composition on the structural morphology and vesicle diameters of phospholipid membranes. Results show that the BMP vesicle morphology and size vary with pH, progressing from highly structured, non-spherical vesicle clusters at neutral pH 7.4 to uniformly spherical non-structured vesicles at acidic pH 4.2. BMP vesicle sizes also increase with increasing acidity, although pH 5.5 forms unusually smaller vesicles, indicative of the small intraendosomal vesicular bodies found in the late endosome. These findings might give more insight into the functions of this unique lipid in the late endosome.

The results on GM1 interactions with BMP demonstrate that GM1 mixes with BMP to form small (~100 nm) spherical shaped vesicles with a narrow size distribution at similar concentrations that were seen to condense the unsaturated DPPC lipid and form a specific complex. The apparent miscibility of GM1 with BMP over the 20-30 mol % ratios, as evidenced by the spontaneous formation of small homogeneously shaped vesicles with narrow diameter size distribution, suggests that optimum interactions between molecules may occur for a given molecular ratio of 3 BMP molecules for 1 GM1 molecule to form a lipid complex. This hypothesis is drawn from the analysis of

Langmuir-monolayer studies, which showed that the pressure-area isotherms of GM1 and dipalmitoyl phosphatidylcholine (DPPC) mixtures follow “ideal” mixing behavior when the two species were considered to be a 3:1 DPPC:GM1 complex interacting with excess DPPC (239). This specific mixture of GM1 with BMP may be important for in vivo vesicular trafficking and lipid sorting in the endosome/lysosome pathways.

Finally, when incorporated in typical POPC membranes at specific concentrations, ganglioside GM1 and BMP alter the morphology and size of the dispersions and vesicles that are formed. Larger vesicle diameters are formed in the presence of 20 mol % GM1 in 80 mol % POPC, whereas smaller, structured vesicles are obtained when 15 mol % BMP and 15 mol % GM1 lipids are mixed with 70 mol % POPC .Further studies on this model lipid system using assays such as secondary antibody labeling may shed more light on the lipid distributions in the vesicle formation, which would provide further understanding on the role of BMP and GM1 in the endocytic pathway.

CHAPTER 5
EFFECT OF CHOLESTEROL MIXING WITH GM1 AND BMP ON PHOSPHOLIPID
MODEL MEMBRANES AT LATE ENDOSOMAL PH 5.5

Introduction

Biological membranes obtained from mammalian cells are complex structures that contain a wide variety of lipids, including phospholipids and cholesterol. Cholesterol (Figure 5-1) is known to play a structural as well as a regulatory role in biomembranes, and is nonhomogeneously distributed in cell membranes, with a high concentration in the plasma membrane and a low concentration in the membranes of intracellular organelles such as the late endosomes (240).

A major characteristic feature of late endosomes is a complex system of internal membranes within the lumen (44, 97). It is thought that late endosomes are the most complex organelles of the endocytic pathway due to their ability to communicate with other organelles, such as in inter-organellar trafficking with Golgi, lysosomes, or endoplasmic reticulum (ER), and also due to the communication between the intraluminal vesicles and the limiting membrane, in intra-organellar trafficking. In essence, both proteins and lipids are responsible for generating and maintaining the compartmentalization and proper functioning of the late endosome (241).

Kobayashi's group (108) demonstrated in 1999 that the internal membrane network of late endosomes contains high amounts of the unique, poorly degradable phospholipid bis(monoacylglycero)phosphate (BMP), which is erroneously also termed as lysobisphosphatidic acid (LBPA), as shown in Figure 5-1. BMP also forms a specialized membrane domain within endosomes (44).

Studies show that BMP plays a function in cholesterol efflux from late endosomes and lysosomes. In one study, it was shown that if antibodies against BMP are internalized by fluid-phase endocytosis, they bind to BMP and accumulate in late endosomes. Under these conditions, cholesterol released from low-density lipoprotein (LDL) remains trapped in the late endosomes and cannot be transported out from this organelle as would normally occur if the antibody were absent (241, 242). Cholesterol accumulation in late endosomes is therefore caused by highly specific perturbations of internal membranes with a monoclonal antibody against BMP, or with human antibodies which recognize BMP (108).

Additionally, the network of membrane tubules and vesicles within the lumen of late endosomes might have an important function in sphingolipid degradation and cholesterol distribution in the cell. Hence, cholesterol transport depends not only on its intrinsic physical properties but also on the physicochemical and dynamic properties of BMP-rich internal membranes. The accumulation of cholesterol within BMP-rich internal membranes is thus predicted to alter membrane properties even further (243). Accumulation of endocytosed antibodies against BMP also results in the defective sorting/trafficking of proteins that transit via late endosomes, presumably because membrane properties are altered (118).

Pathological accumulation of specific lipids, especially cholesterol, in the late endosome is also associated with a special class of diseases referred to as lipid storage diseases, which are subsequently thought to trigger membrane trafficking defects (244, 245). The consequences of the accumulation of a given lipid on membrane organization, compartmentalization and function are generally still poorly understood,

although a great number of studies have been directed at better understanding the role of cholesterol in lipid storage diseases. For instance, Sobo's group (241) studied the consequences of late endosomal cholesterol accumulation as encountered in the Niemann Pick Type C disease (NPC) (245). NPC is a fatal, autosomal recessive neurodegenerative disease due to mutations in the NPC1 or NPC2 genes (246), and the main biochemical manifestation in NPC is elevated late endosomal accumulation of free cholesterol (247-249), followed by an increase in sphingolipids (250). It has been proposed that endosomal accumulation of cholesterol and sphingolipids would lead to an overload of cholesterol rich raft-like membrane domains, which means an increase in raft to non-raft membrane ratio, causing a general jam in traffic through the endosomal compartment (237).

Because of the complexity of biomembranes, and ultimately late endosomes, studies of the nature and consequences of the interaction of cholesterol with phospholipids have generally been carried out on model membranes composed of well-defined phospholipids to which cholesterol is added. In a study by Mobius and group, it was indicated by immuno-electron microscopical examination of human B-lymphocytes (251) that about 80 % of the cholesterol detected in the endocytic pathway is present in the recycling compartments and in internal membranes of early and late endosomes, whereas it is nearly completely absent in inner lysosomal membranes. Studies on the differential lipid composition of the internal endo or lysosomal membranes have also been obtained with the aid of exogenous addition of ganglioside GM1 derivatives bearing a photo affinity label and fluorescence- or biotin-labels to cultured cells and subsequent monitoring of endocytosis by fluorescence microscopy (252, 253).

A number of lipid mixtures have been used to mimic the biophysical characteristics of lipid domains in membrane model systems, and some studies have confirmed the importance of using natural raft mixtures rich in sphingomyelin (SM), CHOL and small amounts of glycosphingolipids, such as gangliosides, instead of mixtures containing “model” raft lipids such as dipalmitoyl phosphatidylcholine (DPPC) (254-256). Essentially, the experimental mixtures designed to mimic putative coexisting raft and non-raft domains are usually composed of ternary mixtures of unsaturated phospholipids (DOPC or POPC), SM (synthetic [16:0] or natural), CHOL, and in some cases small amounts of the ganglioside GM1, with all components present in the lipid mixture at specific molar fractions.

The studies reported in this chapter utilized the particle sizing technique of dynamic light scattering (DLS), and negative staining-transmission electron microscopy (TEM) to characterize vesicle size and macroscopic morphologies observed when cholesterol is incorporated in phospholipid membranes containing BMP and ganglioside GM1. In efforts to mimic the late endosome environment, all experiments were performed at pH 5.5. DLS and TEM experiments were performed on hydrated lipid dispersions and 400 nm-extruded vesicles of (1) POPC:CHOL, (2) BMP:CHOL, (3) POPC:BMP:CHOL, (4) POPC:GM1:CHOL and (5) POPC:GM1:BMP:CHOL that varied in lipid concentrations.

Extruded vesicles were produced by manually passing the hydrated dispersions of each lipid mixture through 400 nm pore membranes, for a total of 31 times, to ensure a uniform size distribution of vesicles. Findings from these studies may be helpful in

further understanding the role that cholesterol/BMP interaction may play in lipid-lipid interactions and formation of lipid rafts in the cell, specifically in the endocytic pathway.

Experimental Details

Materials Used

BMP18:1, ((S, R Isomer) sn-(3-Oleoyl-2-Hydroxy)-Glycerol-1-Phospho-sn-3'-(1'-Oleoyl-2'-Hydroxy)-Glycerol, ammonium Salt)), POPC, (1-Palmitoyl-2-Oleoyl-sn-Glycero-3-Phosphocholine) both in chloroform, and Cholesterol ($C_{27}H_{46}O$, CHOL) and ganglioside GM1 powders, were purchased from Avanti Polar Lipids (Alabaster, AL) and used without further purification. NaOAc, (sodium Acetate); EDTA, (ethylenediamine tetraacetic acid, $C_{10}H_{16}N_2O_8$) and NaCl, (sodium chloride) were purchased from Fisher Biotech (Pittsburgh, PA). CH_3Cl , (chloroform); MeOH, (methanol); CH_3CH_2OH (ethanol); C_6H_{12} , (cyclohexane); NH_4OH , (ammonium hydroxide); HCl, (hydrochloric acid) and NaOH, (sodium hydroxide) were obtained from Fisher Scientific (Pittsburgh, PA). $UO_2(CH_3COO)_2 \cdot 2H_2O$, (uranyl acetate) and 400-mesh Formvar-coated copper grids were purchased from Ted Pella (Redding, CA). Single-sealed 50- to 1000-mL disposable cuvettes (10-mm path length) were obtained from Eppendorf (Westbury, NY). 400-nm polycarbonate extrusion membranes and filter supports were purchased from Avanti Polar Lipids (Alabaster, AL). Silica-coated aluminum thin layer chromatography (TLC) plates were purchased from Whatman (Florham Park, New Jersey).

Hydrated Lipid Dispersions and Extruded Vesicle Preparation

The desired amount of stock lipid (5 mg/mL BMP and 20 mg/mL POPC in chloroform or 1 mg/mL GM1 and 5 mg/mL cholesterol in chloroform methanol mixture(2:1, v:v)), was collected and dried under a gentle nitrogen stream for about 10 minutes or until the solvent evaporated, forming a dry, thin lipid film. The sample was

further dried under in a vacuum desiccator for ≥ 12 hours to remove any residual solvent. Dry lipid films of BMP: CHOL, POPC: CHOL, POPC: GM1: CHOL, POPC: BMP: CHOL and POPC: GM1 BMP: CHOL lipid mixtures at specific mol % ratios were hydrated with 2 mL of 5 mM NaOAc buffer, containing 100 mM NaCl and 0.1 mM EDTA, at pH 5.5, forming hydrated lipid dispersions with a final lipid concentration of approximately 0.75 mM. The hydrated lipid dispersions were freeze-thawed in liquid N₂ five times, then incubated at room temperature for approximately 12 hours before extrusion or measurement by dynamic light scattering (DLS) and transmission electron microscopy (TEM). To form extruded large unilamellar vesicles (LUVs), the hydrated lipid dispersions were extruded by passing 31 times through 400 nm polycarbonate extrusion membranes. Phospholipid integrity was verified by thin layer chromatography (TLC), where approximately 10 μ L of lipid sample was spotted on silica-coated aluminum plates. Plates were placed in a chamber containing a CH₃Cl: MeOH: NH₄OH (65:25:10) mobile phase. The TLC plates were developed in an iodine chamber and visualized by eye.

Instrumentation

Dynamic light scattering (DLS)

Dynamic light scattering size distribution and characterization measurements of hydrated dispersions and extruded unilamellar lipid vesicles were performed with a Brookhaven 90Plus/BI-MAS ZetaPALS spectrometer operated at a wavelength of 659 nm and at 25° C. The instrument uses a BI-9000AT digital autocorrelator and 9KDLSW data acquisition software. A 100- μ L sample volume in a disposable cuvette was used for each measurement. For each sample, 3 runs were performed with each run lasting 3 minutes. Data and histograms were further analyzed and converted into B-spline plots

using OriginPro 8 software. DLS data were reported as an average of three independent histograms for each sample, and errors calculated as a standard deviation from the average vesicle diameter.

Negative staining-transmission electron microscopy (TEM)

Transmission electron microscopy images were obtained using a Hitachi H-7000 transmission electron microscope operated at 75-100 kV with a Soft-Imaging System MegaViewIII with AnalySIS digital camera (Lakewood, CO). The microscope has a maximum resolution at 0.2 nm with a magnification range of 110× to 600,000×. Prior to TEM measurements, samples were further prepared by negative staining. Briefly, for all samples, using a disposable pipette, a drop of the lipid vesicle sample was spread on a 400-mesh Formvar-coated copper grid held by tweezers and incubated for 2 minutes. Excess lipid sample was gently dabbed away with filter paper, and the grid was allowed to dry for 2 minutes. In some instances a drop of deionized water was added to the grid to remove any excess salt from the buffer solution used in vesicle preparation. One drop of 2 % uranyl acetate was then added to the grid and allowed to stain for 2 minutes, after which any excess uranyl acetate was wiped away, and the sample was allowed to dry for 2 minutes before being placed in the electron microscope specimen holder for image analysis and collection.

Results and Discussion

Characterization of BMP Vesicle Size and Morphology in the Presence of Cholesterol

Whereas numerous studies have focused on the phase behavior of cholesterol-incorporated phospholipid membranes, few studies address the morphological and size distribution of vesicle structures observed when CHOL is added to different

phospholipid mixtures at specific molar fractions. To study the effect of CHOL on BMP vesicle size and morphological structure, dynamic light scattering measurements and transmission electron microscopy imaging experiments were performed on hydrated dispersions and extruded vesicles of BMP:CHOL in 70: 30 mol % fractions, considering that in the late endosome, BMP is found in higher concentrations than cholesterol. Chemical structures of BMP and cholesterol are shown in Figure 5-1.

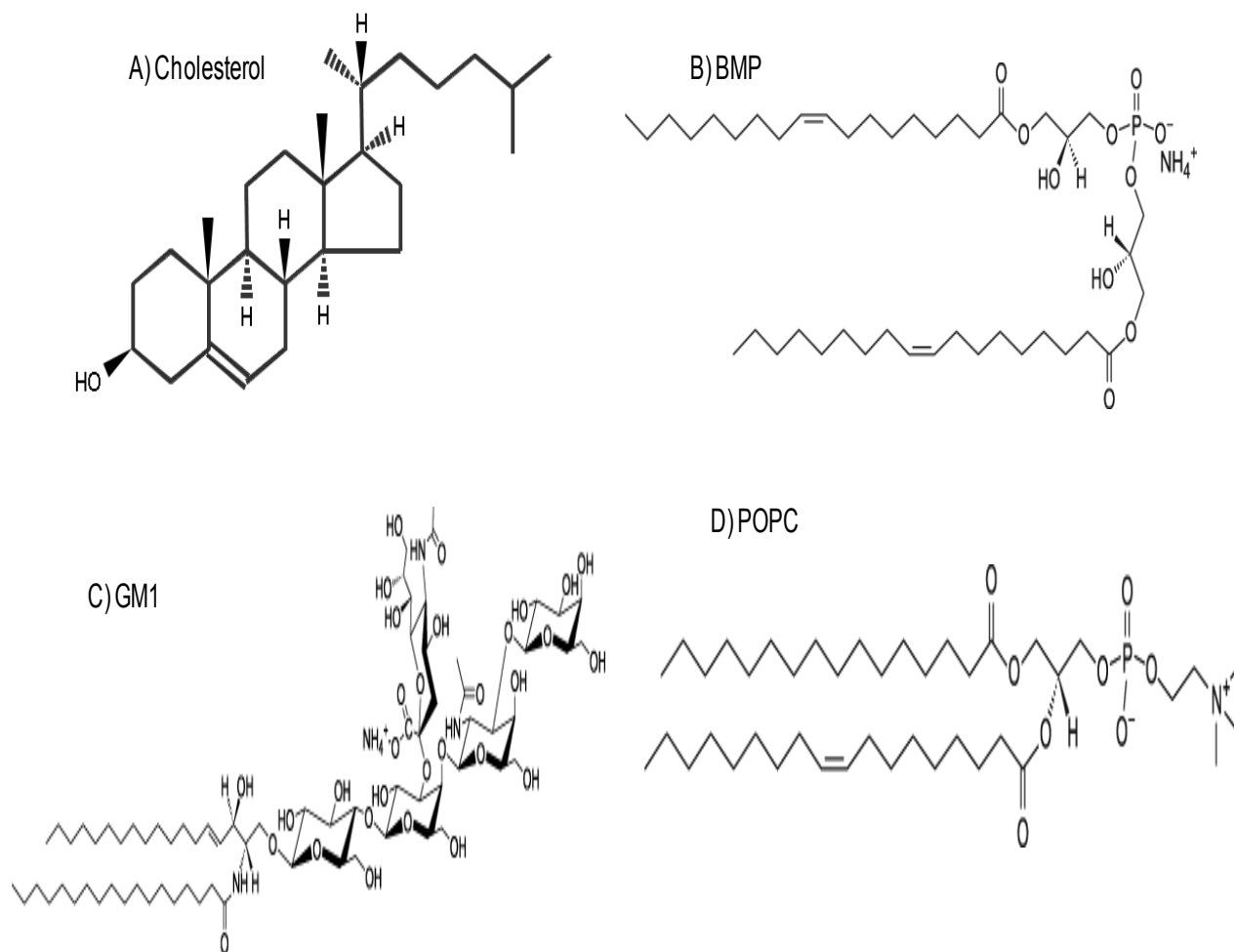


Figure 5-1. Chemical structures of A) Cholesterol, B) BMP, C) GM1 and D) POPC.

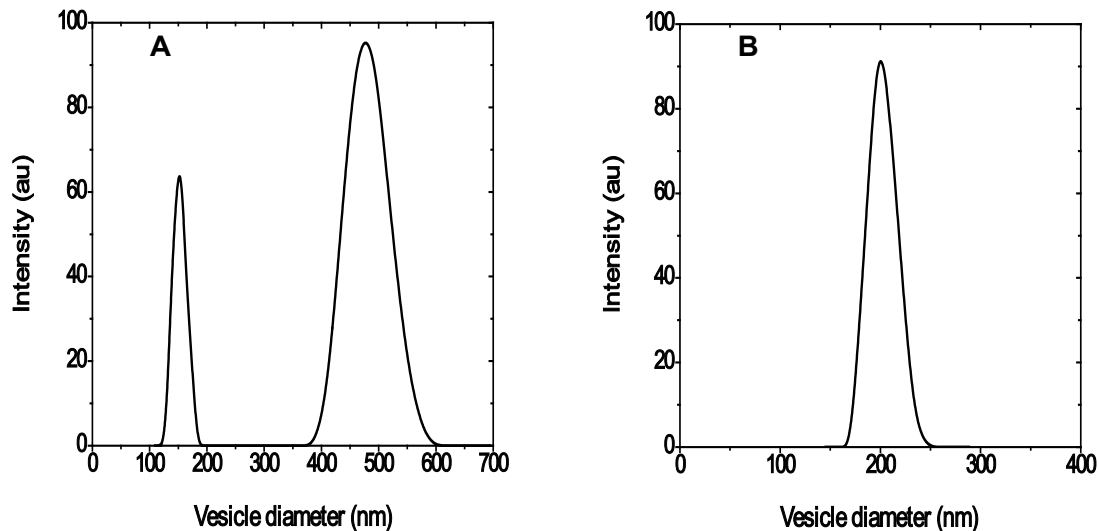


Figure 5-2. Dynamic light scattering histograms of BMP:CHOL (7:3) A) hydrated dispersions and B) 400-nm extruded unilamellar vesicles at pH 5.5.

Table 5-1. Average vesicle of BMP:CHOL (7:3) hydrated dispersions and extruded Vesicles.

Lipid composition	Vesicle size distributions (nm)
BMP: CHOL	
A: Hydrated Dispersions	130 – 170 460 ± 70
B: 400-nm Extruded Vesicles	200 ± 30

In the previous studies discussed in Chapters 3 and 4, we have demonstrated that BMP hydrated dispersions form vesicles with diameters of ~ 500 nm, and extruded BMP vesicle diameters are near 230 nm, much smaller than the 400 nm pore membranes used for their extrusion. Here, Figure 5-2 and Table -1 summarize the dynamic light scattering vesicle diameters observed for the BMP:CHOL (7:3) hydrated dispersions (A) and extruded vesicles (B). These data show that the hydrated dispersions formed by the BMP: CHOL (7:3) lipid mixture have diameters that are similar (~ 500 nm) to those observed for BMP, although instead of a single size distribution like that observed from neat BMP, the BMP:CHOL (7:3) mixture forms with sizes in a bimodal distribution, with a less intense population of vesicles with a size range of 130 -170 nm, likely as an effect

of cholesterol. The extruded vesicle diameters are also relatively the same (200 nm) as those observed for BMP.

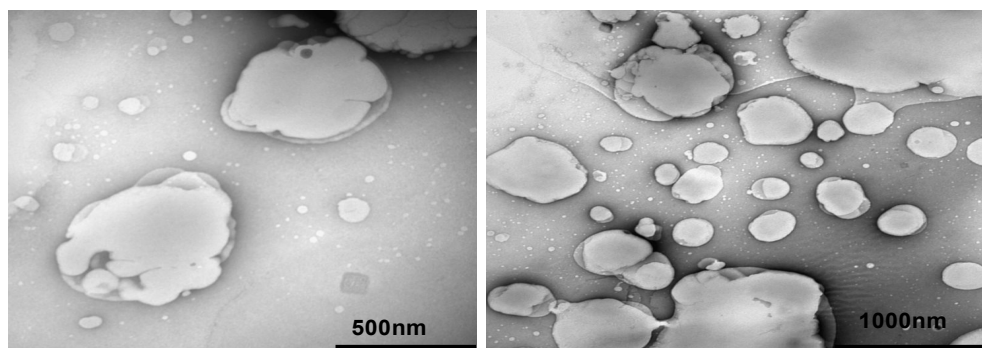


Figure 5-3. Negative staining-TEM images of BMP: CHOL (7:3) hydrated dispersions.

Figure 5-3 shows representative negative staining-TEM images observed for the hydrated dispersions of BMP:CHOL (7:3). Compared to neat BMP, the BMP:CHOL (7:3) dispersions have a different morphology, forming both large and small structures that appear more spherical than those observed in neat BMP. These vesicles also vary in size, although most are ~ 450 nm in diameter, which is consistent with the sizes obtained using DLS. Clearly, the presence of cholesterol alters the morphology of BMP:CHOL (7:3) dispersions from that observed in neat BMP. Studies reported in Chapter 4 showed that BMP and ganglioside GM1 interact in a concentration-dependent manner, hence it might also be interesting to find out the size and morphology of vesicles formed when cholesterol is mixed with BMP membranes at varying molar concentrations.

Investigation of Vesicle Size and Morphology in POPC:CHOL:BMP Mixtures

After characterization of the BMP: CHOL membranes, it was also of interest to determine the effect of cholesterol on both BMP and POPC membranes. DLS and TEM experiments were utilized to measure the vesicle diameters and observed morphologies

of hydrated dispersions and extruded vesicles of POPC: CHOL (80: 20) and POPC: BMP: CHOL (65: 15: 20) in 5 mM NaOAc, 100 mM NaCl, 0.1 mM EDTA at pH 5.5. When cholesterol is added to phosphatidylcholine mixtures, it typically aids in larger vesicle formation and stabilization (241, 257), hence it was expected that these samples would show larger vesicle structures than either neat POPC or BMP vesicles.

Figure 5-4 and Table 5-2 give a summary of the vesicle diameters obtained for hydrated dispersions and extruded vesicles of POPC:CHOL and POPC:BMP:CHOL samples. In previous characterization of POPC, it was demonstrated that POPC dispersions have large vesicles diameters (~1400 nm), and when BMP was introduced in the POPC membranes at 15 mol %, the vesicle diameters of the POPC:BMP dispersions were significantly reduced to ~ 900 nm. Here, it is found that POPC:CHOL (8:2) membranes form dispersions (Figure 5-4A) with a broad size distribution, with an average vesicle diameters of ~ 2100 nm, significantly larger than that observed for neat POPC dispersions (1400 nm), which can be attributed to the presence of cholesterol.

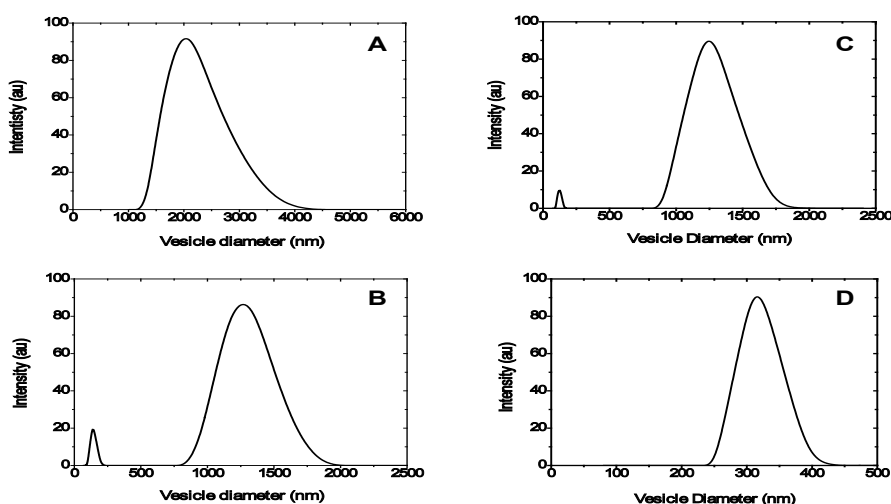


Figure 5-4. Dynamic light scattering histograms of POPC:CHOL (8:2) A) hydrated dispersions B) 400-nm extruded vesicles, POC:BMP:CHOL (65:15:20) C) hydrated dispersions and D) 400-nm extruded vesicles. Note the different scales on the x-axes.

Table 5-2. Average vesicle diameters of POPC:CHOL (8:2) and POPC:BMP:CHOL (65:15:20) hydrated dispersions and extruded vesicles.

Lipid Composition	Vesicle Size Distributions (nm)
POPC:CHOL	
A: Hydrated Dispersions	2100 ± 840
B: 400-nm Extruded Vesicles	1200 ± 410
POPC:BMP:CHOL	
C: Hydrated Dispersions	1250 ± 360
D: 400-nm Extruded Vesicles	310 ± 60

Interestingly, the average vesicle diameters of POPC:CHOL extruded vesicles (Figure 5-4B) are much larger (~ 1200 nm) than those seen for neat POPC extruded vesicles (~400 nm), and triple the size of the 400 nm pore membranes used for the extrusion of these vesicles. This is a clear indication that adding cholesterol at specific concentrations increases the cross sectional diameter of certain phospholipid bilayers, such as POPC.

In comparison, POPC:BMP:CHOL hydrated dispersions (Figure 5-4C) have average diameters of 1250 nm, much smaller than those seen in POPC:CHOL dispersions (2100 nm), and nearly the size of neat POPC dispersions (1400 nm). The POPC:BMP:CHOL extruded vesicles (Figure 5-4D) are also found to have smaller average diameters (~ 310 nm) than POPC:CHOL (1250 nm), but comparable to POPC extruded vesicles (~400 nm). Again, a consistent trend is seen: BMP incorporated into other lipid vesicles results in a drastic decrease in the average vesicle diameters as observed in the vesicles formed by the POPC:BMP:CHOL mixture. It is possible that BMP, which has been found to prefer formation of small, stable lamellar vesicles as an attribute to its unique structure and stereoconfiguration, counteracts the cholesterol effect.

TEM images obtained for POPC:CHOL dispersions (Figure 5-5A) and POPC:BMP:CHOL dispersions (Figure 5-5B) show sizes and shapes that are consistent with the DLS results obtained for these lipid mixtures. POPC: CHOL dispersions form highly structured, multilamellar onion-like vesicles with diameters of ~ 1500 nm, whereas in the POPC: BMP: CHOL sample, clustered, vesicle structures that appear like budding events are observed, with diameters of ~ 1000 nm. It can be recalled that in Chapter 3, BMP dispersions at neutral pH were observed to form highly structured non-spherical vesicle clusters.

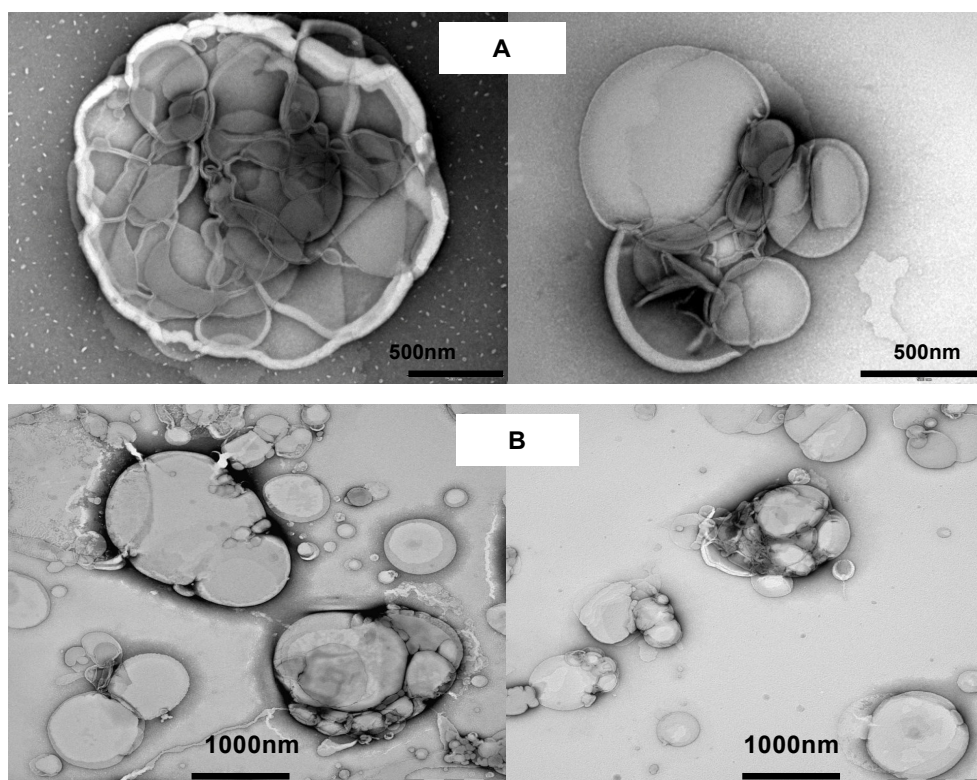


Figure 5-5. TEM images of A) POPC:CHOL (8:2) and B) POPC:BMP:CHOL (65:15:20) hydrated dispersions.

TEM analysis shows different vesicle morphologies for POPC:CHOL and POPC:BMP:CHOL dispersions as shown in Figure 5-5. The vesicle morphology observed in these phospholipid mixtures is a direct effect of the incorporation of both

cholesterol and BMP, which seem to have opposing effects on phospholipid membranes. Addition of 15 mol % BMP and 20 mol % CHOL in the POPC:BMP:CHOL mixture results in formation of spherical vesicles of various sizes and an overall decrease in vesicle diameter (compared to POPC:CHOL), while addition of 20 mol % CHOL in POPC membranes leads to formation of multilamellar vesicle structures with increased diameters.

DLS and TEM experiments were also carried out on POPC lipid mixtures incorporating ganglioside GM1, cholesterol and BMP. Experiments were performed to measure the average vesicle diameter and macroscopic morphology of POPC:GM1:CHOL (70: 10: 20), and POPC:GM1:BMP: CHOL (50:15:15:20) hydrated dispersions and vesicles extruded with 400 nm pore membranes. All samples were hydrated in 5 mM NaOAc, 100 mM NaCl, 0.1 mM EDTA at pH 5.5.

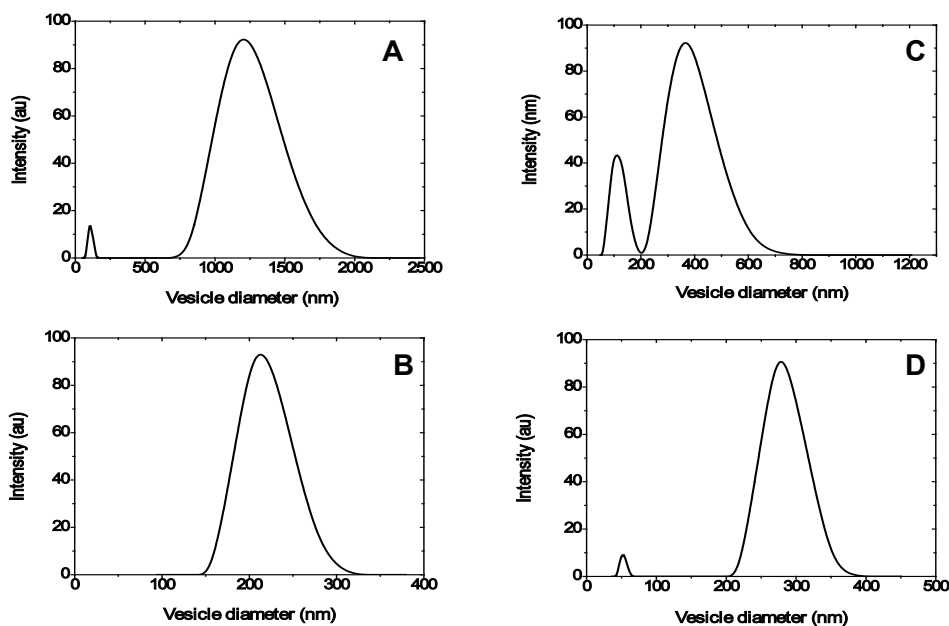


Figure 5-6. Dynamic light scattering histograms of A) hydrated dispersions of POPC:GM1:CHOL (70: 10: 20), B) 400 nm-extruded vesicles of POC: GM1: CHOL, C) hydrated dispersions of POPC:GM1:BMP:CHOL (50:15:15:20) and D) 400 nm-extruded vesicles of POPC:GM1:BMP:CHOL. Note the different scales on the x-axes.

Table 5-3. Vesicle size distributions of POPC:GM1:CHOL (70: 10: 20) and POPC:GM1:BMP:CHOL hydrated dispersions and 400 nm-extruded Vesicles.

Lipid Composition	Vesicle Size Distributions (nm)
POPC:GM1:CHOL	
A: Hydrated Dispersions	1200 ± 300
B: 400nm-Extruded Vesicles	220 ± 50
POPC:GM1:BMP:CHOL	
C: Hydrated Dispersions	80 – 160 430 ± 150
D: 400nm-Extruded Vesicles	280 ± 130

The data presented in Figure 5-5 and Table 5-3 summarizes the average vesicle diameters obtained for POPC:GM1:CHOL and POPC:GM1: BMP:CHOL hydrated dispersions and extruded vesicles at the late endosomal pH 5.5. Interestingly, the hydrated dispersions of POPC:GM1:CHOL (A) have diameters of ~ 1200 nm, but when 15 mol % BMP is introduced in the lipid mixture, the average diameters of POPC:GM1:BMP:CHOL hydrated dispersions (C) are drastically reduced to ~430 nm in diameter, and a second, less intense vesicle population with small diameters between 80 – 160 nm is also observed. Again, the formation of small vesicles in the presence of BMP might be attributed to the ability of BMP to contribute favorably to smaller vesicle formation. In both lipid mixtures, the vesicles that were extruded with 400 nm pore membranes had small average diameters of 220 nm for POPC:GM1:CHOL and 280 nm for POPC:GM1: BMP:CHOL.

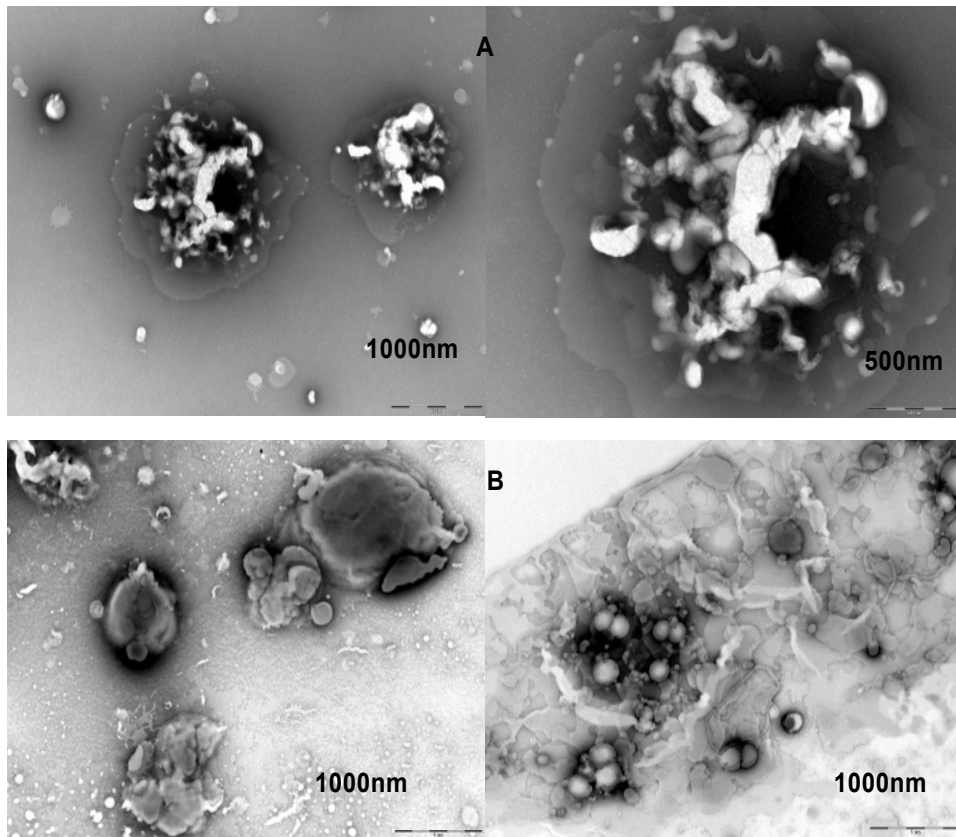


Figure 5-7. Negative staining-TEM images of A) POPC:GM1:CHOL (70: 10: 20) and B) POPC:GM1:BMP:CHOL (50:15:15::20) hydrated dispersions.

When the hydrated dispersions of both of these lipid mixtures were imaged by TEM, they both displayed highly heterogeneous nonspherical structures with diameters in the range of 500 – 1000 nm as observed in Figure 4-6A-B. The POPC:GM1:BMP:CHOL dispersions also featured some dispersions that appeared like clusters of small vesicle structures. It may be interesting to study these lipid mixtures further as ideal model systems for tracking individual lipid components in vesicles of lipid mixtures using assays such as secondary antibody Au labeling and negative staining-transmission electron microscopy. It might also be interesting to investigate whether the small clusters of vesicles in the POPC:GM1:BMP:CHOL dispersions are

actual phase-separated lipid vesicles due to the cholesterol effect or if they are related to incomplete lipid mixing during the vesicle preparation procedure.

Conclusions

The studies reported in this chapter have yielded interesting, and potentially significant findings on the effects of incorporating cholesterol, ganglioside GM1 and BMP in typical POPC membranes. It has been demonstrated clearly that in almost all instances, the addition of 20 mol % cholesterol to POPC mixtures results in increased vesicle diameters. Cholesterol also alters the vesicle morphology of the lipid dispersions, leading to formation of structured, non-spherical vesicles. This chapter also reiterates the findings in chapters 3 and 4, namely that the addition of small amounts of BMP (15 mol %) in all POPC mixtures consistently induces the formation of smaller vesicle structures, as demonstrated by the dynamic light scattering and TEM data. Together, these findings can be explored further for a better understanding of the occurrence and interaction of different lipids in the late endosome, and how the physico-chemical properties of cholesterol and ganglioside GM1 may affect the functional role of BMP in the endocytic pathway.

CHAPTER 6 SUMMARY AND FUTURE PERSPECTIVES

BMP Forms Small Stable Lamellar Vesicle Structures and Induces Formation of Small Vesicles when mixed with POPC

The analytical capability of the dynamic light scattering (DLS) technique was successfully demonstrated through the accurate measurement of manually mixed vesicle populations. DLS and transmission electron microscopy (TEM) were utilized to characterize the size of hydrated and extruded BMP and POPC samples, revealing that when BMP is hydrated from a dry lipid film, it forms lipid dispersions that have diameters much smaller than those of POPC dispersions, regardless of pH.

I also demonstrated using vesicle leakage assays and vesicle “stability” assays, that BMP forms small “stable” lamellar vesicles with an interior volume that can encapsulate molecules. Following the characterization of POPC:BMP (85:15) and POPC:POPG (80:20) lipid mixtures, this work showed that BMP can induce the formation of small vesicles when incorporated in typical phospholipid membranes at certain concentrations. Taken together, these data suggest that the physical properties of BMP, dictated by its unique diglycerol structure and stereoconfiguration, provide a mechanism for stabilization of small vesicle structures in the maturing endosome as the lumen acidifies, shedding further light on the potential functional role of this lipid in the late endosome.

Ganglioside GM1 Leads to Formation of Small Homogenous Vesicles When Mixed with BMP

The results on GM1 interactions with BMP provided morphological and size distribution information that demonstrated that GM1 mixes with BMP to form small (~100 nm) spherical shaped vesicles with a narrow size distribution at similar

concentrations to those seen to condense DPPC and form a specific complex. The apparent miscibility of GM1 with BMP over the 20-30 mol % ratios, as evidenced by the spontaneous formation of small homogeneously shaped vesicles with narrow diameter size distribution, suggests that optimum interactions between molecules may occur for a given molecular ratio of 3 BMP molecules for 1 GM1 molecule to form a lipid complex. This hypothesis is drawn from the analysis of Langmuir-monolayer studies, which showed that the pressure-area isotherms of GM1 and DPPC mixtures follow “ideal” mixing behavior when the two species were considered to be a 3:1 DPPC:GM1 complex interacting with excess DPPC (239). This specific mixture of GM1 with BMP may be important for in vivo vesicular trafficking and lipid sorting in the endosome/lysosome pathways.

Finally, when incorporated in typical POPC membranes at specific concentrations, ganglioside GM1 and BMP alter the morphology and size of the dispersions and vesicles that are formed. Larger vesicle diameters are formed in the presence of 20 mol % GM1 in 80 mol % POPC, whereas smaller, heterogeneous and structured vesicles are obtained when 15 mol % BMP and 15 mol % GM1 lipids are mixed with 70 mol % POPC .

BMP Counteracts the Cholesterol Effect when Mixed with GM1 and POPC

The studies presented in Chapter 5 have shown interesting and potentially significant findings on the effects of incorporating cholesterol, ganglioside GM1 and BMP in POPC membranes. This work has demonstrated clearly that in almost all instances, the addition of 20 mol % cholesterol to POPC mixtures results in increased vesicle diameters. Cholesterol also changes the vesicle morphology of the lipid dispersions, leading to formation of structured, non-spherical vesicles. The work in

Chapter 5 also reiterates our previous findings in Chapters 3 and 4, namely that the addition of small amounts of BMP (15 mol %) in POPC and GM1 mixtures consistently induces the formation of smaller vesicles structures, even in the presence of cholesterol, as demonstrated by the dynamic light scattering and negative staining-TEM data. Together, these findings can be explored further for a better understanding of the occurrence and interaction of different lipids in the late endosome, and how the physico-chemical properties of cholesterol and ganglioside GM1 may affect the functional role of BMP in the endocytic pathway.

Future Perspectives

One way in which the applicability of BMP vesicles can be explored is through investigation of their potential as drug-delivery vehicles. Because liposomes or lipid vesicles resemble biological cell membranes in their structure and composition, they can be engineered from natural, biodegradable and nontoxic lipid molecules and can encapsulate or bind a variety of drug molecules into or onto their membranes. As a consequence, all these properties make vesicles attractive candidates for use as drug-delivery vehicles (258).

Additionally, liposome applications in drug delivery depend on their physicochemical and colloidal characteristics such as composition, size, loading efficiency and the stability of the carrier, as well as their biological interactions with the cells (258). An added advantage of the use of encapsulated drug molecules for drug delivery is the decreased toxicity of liposomal formulations, because liposome-associated drug molecules cannot normally spill to organs such as the heart, brain and kidneys. This work has characterized the size and morphology of BMP vesicles, and

found that BMP forms small, lamellar vesicle structures with an interior volume. These properties of BMP can be utilized further for the possibility of encapsulating hydrophilic drug molecules in the aqueous core of BMP vesicles, and studied for their potential drug-delivery applications.

Following TEM and DLS studies on BMP mixed with CHOL, POPC and GM1 lipids, further studies can be carried out on the POPC/BMP/GM1/CHOL model lipid system using assays such as secondary antibody labeling. Such experiments may shed more light on the lipid distributions in the heterogeneous vesicle formations observed for lipid mixtures, which would provide further understanding of the role of each of these lipids in the endocytic pathway and in lipid raft formation.

APPENDIX A

STEP BY STEP ANALYSIS OF DYNAMIC LIGHT SCATTERING DATA

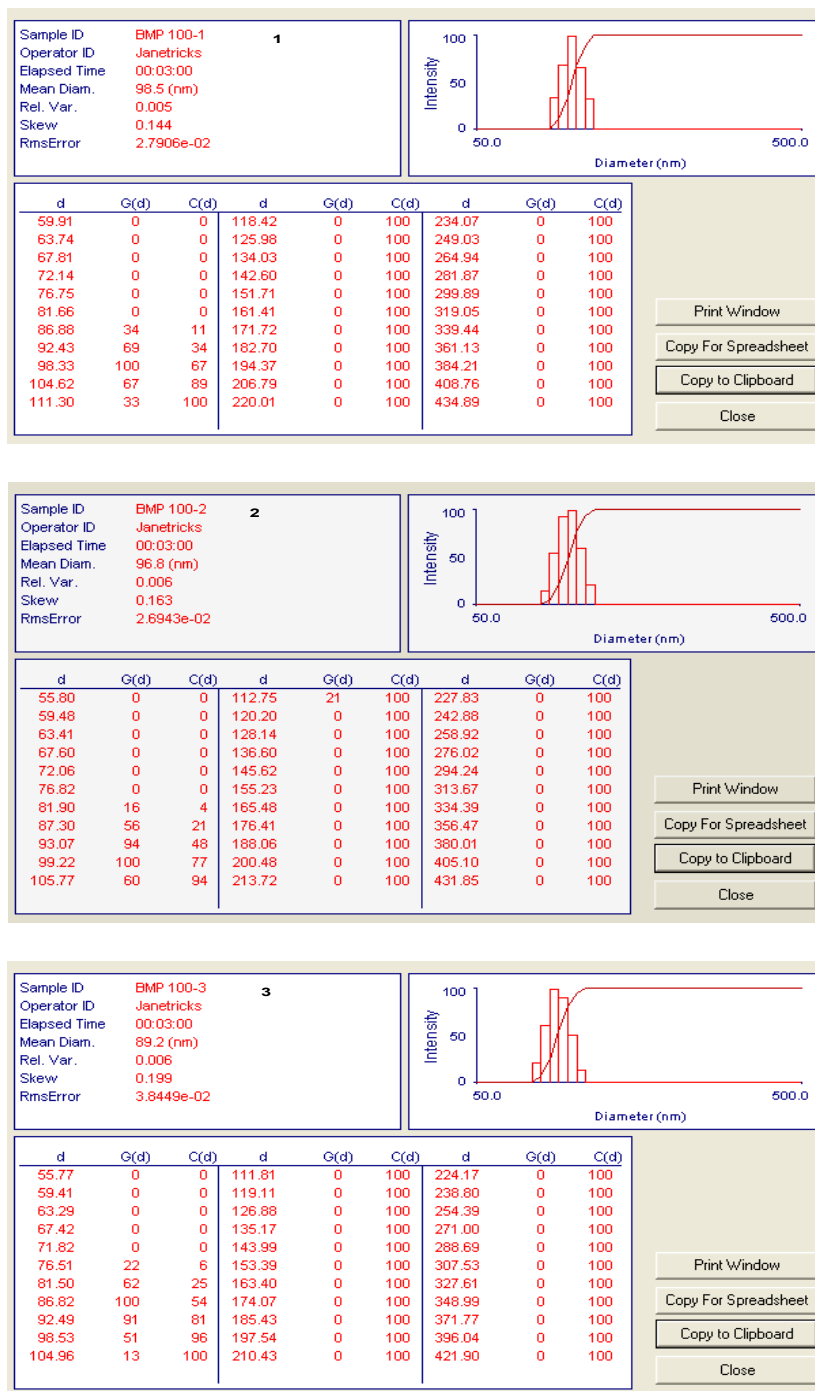


Figure A-1. DLS raw data histograms (1, 2, and 3) of a sample of 100 nm-extruded BMP vesicles in 5 mM HEPES, 100 mM NaCl and 0.1 mM EDTA, pH 7.4.

Each of the three traces/histograms were collected for 3 minutes.

The data in Figure A-1 were saved as spreadsheets and later imported into OriginPro 8 or Microsoft Excel software for further analysis.

Table A-1. OriginPro 8 spreadsheet of the imported DLS raw data of 100 nm-extruded BMP vesicles.

D-1	I-1	D-2	I-2	D-3	I-3	Mean Diameter	Mean Intensity
59.90698	0	59.48459	0	55.76741	0	58.38633	0
63.73537	0	63.41274	0	59.40784	0	62.18532	0
67.80842	0	67.60029	0	63.28592	0	66.23154	0
72.14175	0	72.06436	0	67.41715	0	70.54109	0
76.75201	0	76.82323	0	71.81806	0	75.1311	0
81.65689	0	81.89636	15.52	76.50626	0	80.01984	5.17
86.87522	34.29	87.3045	55.73	81.50050	21.87	85.22674	37.30
92.42702	68.89	93.06978	94.33	86.82000	61.75	90.77252	75.00
98.33363	100.00	99.21577	100.00	92.48831	100.00	96.67924	100.00
104.6177	67.23	105.7676	59.97	98.52584	91.01	102.97038	72.74
111.3033	32.61	112.7521	21.34	104.9575	51.33	109.67097	35.10
118.4163	0	120.1979	0	111.809	13.08	116.80773	4.36
125.9837	0	128.1353	0	119.1078	0	124.40893	0
134.0348	0	136.5969	0	126.883	0	132.5049	0
142.6003	0	145.6173	0	135.1657	0	141.12777	0
151.7133	0	155.2333	0	143.9892	0	150.31193	0
161.4086	0	165.4844	0	153.3886	0	160.09387	0
171.7235	0	176.4124	0	163.4017	0	170.51253	0
182.6976	0	188.062	0	174.0683	0	181.6093	0
194.373	0	200.4809	0	185.4313	0	193.4284	0
206.7945	0	213.72	0	197.5361	0	206.01687	0
220.0098	0	227.8333	0	210.431	0	219.4247	0
234.0697	0	242.8785	0	224.1677	0	233.7053	0
249.0281	0	258.9174	0	238.8011	0	248.91553	0
264.9424	0	276.0154	0	254.3897	0	265.11583	0
281.8737	0	294.2424	0	270.996	0	282.3707	0
299.8869	0	313.6731	0	288.6863	0	300.74877	0
319.0514	0	334.3869	0	307.5314	0	320.32323	0
339.4405	0	356.4687	0	327.6067	0	341.17197	0
361.1327	0	380.0086	0	348.9925	0	363.37793	0
384.2111	0	405.1029	0	371.7743	0	387.02943	0
408.7643	0	431.8545	0	396.0433	0	412.2207	0

The spreadsheet shows the individual diameters (D-1, D-2, and D-3 in nm) and their corresponding intensities (I-1, I-2, and I-3), the Mean Diameter (nm), and Mean Intensity of the three traces.

Once imported into OriginPro 8, the Diameter (d) and Intensity ($G(d)$) values were utilized for calculation of mean diameter and mean intensity values of the three histograms, as illustrated in Table A-2. The average vesicle diameter was obtained from the mean diameter that had the maximum (peak) mean intensity. For this particular example, the average vesicle diameter for the 100-nm extruded BMP vesicles is

96.67924 nm (in bold red), which can be approximated to 100 nm. The standard deviation (δ) can also be calculated from all the mean diameter values that have non-zero intensities, and in this case δ was found to be ± 20 . The mean diameter and mean intensity values in Table A-1 were plotted in OriginPro 8 as a B-Spline line to obtain a Gaussian distribution as illustrated in Figure A-2.

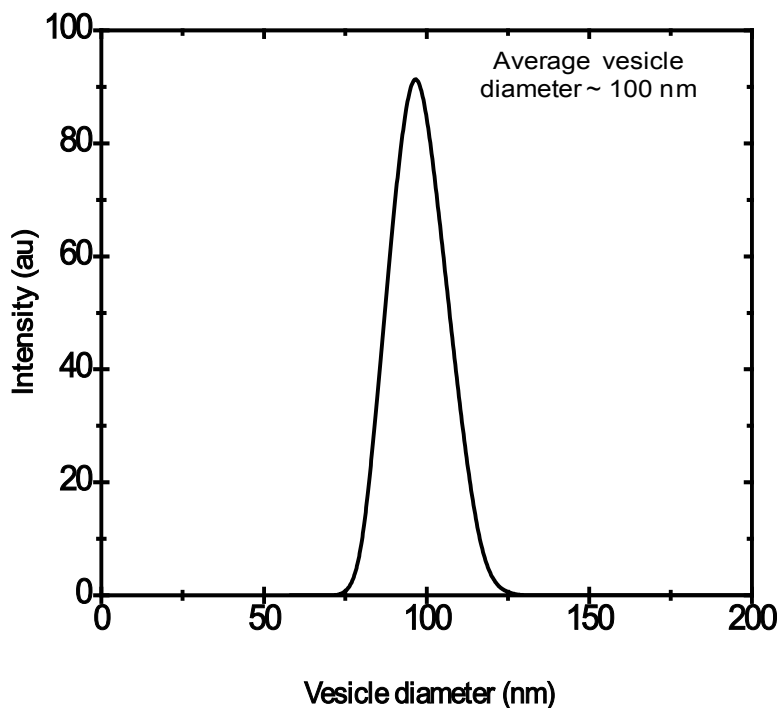


Figure A-2. Average vesicle diameter for 100 nm-extruded BMP vesicles.

LIST OF REFERENCES

1. Purves, W. K., D. Sadava, G.H. Orians and H.C. Heller. 2004. *Life: The Science of Biology*, 7th Edition, Gordonsville, VA.
2. Yeagle, P. L. 2005. *The Structure of Biological Membranes*. CRC Press, New York, NY.
3. Nelson, D. L., and M. M. Cox. 2005. *Lehninger Principles of Biochemistry*. W.H Freeman and Company, New York, NY.
4. Mu, H., and C. E. Hoy. 2004. The digestion of dietary triacylglycerols. *Prog Lipid Res.* 43:105-133.
5. Cevc, G., and D. Marsh. 1987. *Phospholipid Bilayers: Physical Principles and Models*. John Wiley and Sons, Indianapolis, IN.
6. Vance, D. E., and J. E Vance. 2008. *Biochemistry of Lipids, Lipoproteins and Membranes*. Elsevier, Maryland Heights, MO.
7. Yeagle, P. L. 1993. *The Membranes of Cells*. Academic Press, Burlington, MA.
8. Gennis, R. B. 1989. *Biomembranes: Molecular Structure and Function*. Springer-Verlag, New York, NY.
9. van Meer, G., D. R. Voelker, and G. W. Feigenson. 2008. Membrane lipids: where they are and how they behave. *Nat. Rev. Mol. Cell. Biol.* 9:112-124.
10. Roelofsen, B., G. van Meer, and J. A. Op den Kamp. 1981. The lipids of red cell membranes. Compositional, structural and functional aspects. *Scand. J. Clin. Lab. Invest. Suppl.* 156:111-115.
11. Chan, Y. H., and S. G. Boxer. 2007. Model membrane systems and their applications. *Curr. Opin. Chem. Biol.* 11:581-587.
12. Escriba, P. V., J. M. Sanchez-Dominguez, R. Alemany, J. S. Perona, and V. Ruiz-Gutierrez. 2003. Alteration of lipids, G proteins, and PKC in cell membranes of elderly hypertensives. *Hypertension.* 41:176-182.
13. Escriba, P. V., J. M. Gonzalez-Ros, F. M. Goni, P. K. Kinnunen, L. Vigh, L. Sanchez-Magraner, A. M. Fernandez, X. Busquets, I. Horvath, and G. Barcelo-Coblijn. 2008. Membranes: a meeting point for lipids, proteins and therapies. *J. Cell. Mol. Med.* 12:829-875.
14. Gruenberg, J. 2003. Lipids in endocytic membrane transport and sorting. *Curr. Opin. Cell. Biol.* 15:382-388.

15. Mathews, C. K., K.E, van Holde. 1990. *Biochemistry*. The Benjamin/Cummings Publishing Company, Lebanon, IN.
16. Brites, P., H. R. Waterham, and R. J. Wanders. 2004. Functions and biosynthesis of plasmalogens in health and disease. *Biochim. Biophys. Acta*. 1636:219-231.
17. Nagan, N., and R. A. Zoeller. 2001. Plasmalogens: biosynthesis and functions. *Prog. Lipid. Res.* 40:199-229.
18. Mangold, H. K., and N. Weber. 1987. Biosynthesis and biotransformation of ether lipids. *Lipids*. 22:789-799.
19. Hermetter, A., B. Rainer, E. Ivessa, E. Kalb, J. Loidl, A. Roscher, and F. Paltauf. 1989. Influence of plasmalogen deficiency on membrane fluidity of human skin fibroblasts: a fluorescence anisotropy study. *Biochim. Biophys. Acta*. 978:151-157.
20. Schrakamp, G., R. B. Schutgens, R. J. Wanders, H. S. Heymans, J. M. Tager, and H. Van den Bosch. 1985. The cerebrohepato renal (Zellweger) syndrome. Impaired de novo biosynthesis of plasmalogens in cultured skin fibroblasts. *Biochim. Biophys. Acta*. 833:170-174.
21. Ginsberg, L., S. Rafique, J. H. Xuereb, S. I. Rapoport, and N. L. Gershfeld. 1995. Disease and anatomic specificity of ethanolamine plasmalogen deficiency in Alzheimer's disease brain. *Brain Res.* 698:223-226.
22. Pentchev, P. G., M. E. Comly, H. S. Kruth, M. T. Vanier, D. A. Wenger, S. Patel, and R. O. Brady. 1985. A defect in cholesterol esterification in Niemann-Pick disease (type C) patients. *Proc. Natl. Acad. Sci., USA*. 82:8247-8251.
23. Roff, C. F., E. Goldin, M. E. Comly, J. Blanchette-Mackie, A. Cooney, R. O. Brady, and P. G. Pentchev. 1992. Niemann-Pick type-C disease: deficient intracellular transport of exogenously derived cholesterol. *Am. J. Med. Genet.* 42:593-598.
24. Murphy, E. J., M. B. Schapiro, S. I. Rapoport, and H. U. Shetty. 2000. Phospholipid composition and levels are altered in Down syndrome brain. *Brain Res.* 867:9-18.
25. Benveniste, J., P. M. Henson, and C. G. Cochrane. 1972. Leukocyte-dependent histamine release from rabbit platelets. The role of IgE, basophils, and a platelet-activating factor. *J. Exp. Med.* 136:1356-1377.
26. Benveniste, J. 1974. Platelet-activating factor, a new mediator of anaphylaxis and immune complex deposition from rabbit and human basophils. *Nature*. 249:581-582.
27. Schlame, M., D. Rua, and M. L. Greenberg. 2000. The biosynthesis and functional role of cardiolipin. *Prog. Lipid. Res.* 39:257-288.

28. Lecocq, J., and C. E. Ballou. 1964. On the Structure of Cardiolipin. *Biochemistry*. 3:976-980.
29. Chicco, A. J., and G. C. Sparagna. 2007. Role of cardiolipin alterations in mitochondrial dysfunction and disease. *Am. J. Physiol. Cell Physiol.* 292:C33-44.
30. Hatch, G. M. 1998. Cardiolipin: biosynthesis, remodeling and trafficking in the heart and mammalian cells (Review). *Int. J. Mol. Med.* 1:33-41.
31. Cable, M. B., J. Jacobus, and G. L. Powell. 1978. Cardiolipin: a stereospecifically spin-labeled analogue and its specific enzymic hydrolysis. *Proc. Natl. Acad. Sci., USA.* 75:1227-1231.
32. McMillen, D. A., J. J. Volwerk, J. Ohishi, M. Erion, J. F. Keana, P. C. Jost, and O. H. Griffith. 1986. Identifying regions of membrane proteins in contact with phospholipid head groups: covalent attachment of a new class of aldehyde lipid labels to cytochrome c oxidase. *Biochemistry*. 25:182-193.
33. Schlame, M., M. Ren, Y. Xu, M. L. Greenberg, and I. Haller. 2005. Molecular symmetry in mitochondrial cardiolipins. *Chem. Phys. Lipids* 138:38-49.
34. Hoch, F. L. 1992. Cardiolipins and biomembrane function. *Biochim. Biophys. Acta.* 1113:71-133.
35. Robinson, N. C. 1993. Functional binding of cardiolipin to cytochrome c oxidase. *J Bioenerg. Biomembr.* 25:153-163.
36. Mileykovskaya, E., M. Zhang, and W. Dowhan. 2005. Cardiolipin in energy transducing membranes. *Biochemistry (Mosc).* 70:154-158.
37. Lange, C., J. H. Nett, B. L. Trumpower, and C. Hunte. 2001. Specific roles of protein-phospholipid interactions in the yeast cytochrome bc1 complex structure. *EMBO J.* 20:6591-6600.
38. Koshkin, V., and M. L. Greenberg. 2002. Cardiolipin prevents rate-dependent uncoupling and provides osmotic stability in yeast mitochondria. *Biochem. J.* 364:317-322.
39. Ostrander, D. B., G. C. Sparagna, A. A. Amoscato, J. B. McMillin, and W. Dowhan. 2001. Decreased cardiolipin synthesis corresponds with cytochrome c release in palmitate-induced cardiomyocyte apoptosis. *J. Biol. Chem.* 276:38061-38067.
40. Ott, M., J. D. Robertson, V. Gogvadze, B. Zhivotovsky, and S. Orrenius. 2002. Cytochrome c release from mitochondria proceeds by a two-step process. *Proc. Natl. Acad. Sci., USA.* 99:1259-1263.
41. McMillin, J. B., and W. Dowhan. 2002. Cardiolipin and apoptosis. *Biochim. Biophys. Acta.* 1585:97-107.

42. Zhang, M., E. Mileykovskaya, and W. Dowhan. 2002. Gluing the respiratory chain together. Cardiolipin is required for supercomplex formation in the inner mitochondrial membrane. *J. Biol. Chem.* 277:43553-43556.
43. Pfeiffer, K., V. Gohil, R. A. Stuart, C. Hunte, U. Brandt, M. L. Greenberg, and H. Schagger. 2003. Cardiolipin stabilizes respiratory chain supercomplexes. *J. Biol. Chem.* 278:52873-52880.
44. Kobayashi, T., E. Stang, K. S. Fang, P. de Moerloose, R. G. Parton, and J. Gruenberg. 1998. A lipid associated with the antiphospholipid syndrome regulates endosome structure and function. *Nature.* 392:193-197.
45. Body, D. R., and G. M. Gray. 1967. The isolation and characterization of phosphatidylglycerol and a structural isomer from pig lung. *Chem. Phys. Lipids.* 1:254-263.
46. Kolter, T., and K. Sandhoff. 2005. Principles of lysosomal membrane digestion: stimulation of sphingolipid degradation by sphingolipid activator proteins and anionic lysosomal lipids. *Annu. Rev. Cell. Dev. Biol.* 21:81-103.
47. Brotherus, J., O. Renkonen, W. Fischer, and J. Herrmann. 1974. Novel stereoconfiguration in lyso-bis-phosphatidic acid of cultured BHK-cells. *Chem. Phys. Lipids.* 13:178-182.
48. Joutti, A. 1979. The stereoconfiguration of newly formed molecules of bis(monoacylglycero)phosphate in BHK cells. *Biochim. Biophys. Acta.* 575:10-15.
49. Joutti, A., J. Brotherus, O. Renkonen, R. Laine, and W. Fischer. 1976. The stereochemical configuration of lysobisphosphatidic acid from rat liver, rabbit lung and pig lung. *Biochim. Biophys. Acta.* 450:206-209.
50. Joutti, A., and O. Renkonen. 1979. The stereochemical configuration of lysosomal phosphatidylcholine and phosphatidylethanolamine: comparison with lysobisphosphatidic acid. *J. Lipid Res.* 20:230-233.
51. Garavito, R. M., and S. Ferguson-Miller. 2001. Detergents as tools in membrane biochemistry. *J Biol Chem* 276:32403-32406.
52. Epand, R. M. 1998. Lipid polymorphism and protein-lipid interactions. *Biochim. Biophys. Acta.* 1376:353-368.
53. Epand, R. M. 2007. Membrane lipid polymorphism: relationship to bilayer properties and protein function. *Methods. Mol. Biol.* 400:15-26.
54. Taylor, T. M., P. M. Davidson, B. D. Bruce, and J. Weiss. 2005. Liposomal nanocapsules in food science and agriculture. *Crit. Rev. Food Sci. Nutr.* 45:587-605.

55. Bangham, A. D., and R. W. Horne. 1964. Negative staining of phospholipids and their structural modification by surface-active agents as observed in the electron microscope. *J. Mol. Biol.* 8:660-668.
56. Hauser, H., I. Pascher, R. H. Pearson, and S. Sundell. 1981. Preferred conformation and molecular packing of phosphatidylethanolamine and phosphatidylcholine. *Biochim. Biophys. Acta.* 650:21-51.
57. Edwards, K. A., and A. J. Baeumner. 2006. Liposomes in analyses. *Talanta.* 68:1421-1431.
58. Edwards, K. A., and A. J. Baeumner. 2006. Optimization of DNA-tagged liposomes for use in microtiter plate analyses. *Anal Bioanal. Chem.* 386:1613-1623.
59. Cowan-Jacob, S. W., V. Guez, G. Fendrich, J. D. Griffin, D. Fabbro, P. Furet, J. Liebetanz, J. Mestan, and P. W. Manley. 2004. Imatinib (STI571) resistance in chronic myelogenous leukemia: molecular basis of the underlying mechanisms and potential strategies for treatment. *Mini Rev. Med. Chem.* 4:285-299.
60. Abdiche, Y. N., and D. G. Myszka. 2004. Probing the mechanism of drug/lipid membrane interactions using Biacore. *Analytical Biochemistry.* 328:233-243.
61. Beigi, F., Q. Yang, and P. Lundahl. 1995. Immobilized-liposome chromatographic analysis of drug partitioning into lipid bilayers. *Journal of Chromatography A.* 704:315-321.
62. Foldvari, M., A. Gesztes, and M. Mezei. 1990. Dermal drug delivery by liposome encapsulation: clinical and electron microscopic studies. *J. Microencapsul.* 7:479-489.
63. Schott, H., D. Von Cunow, and H. Langhals. 1992. Labelling of liposomes with intercalating perylene fluorescent dyes. *Biochim. Biophys. Acta.* 1110:151-157.
64. Jones, M. A., P. K. Kilpatrick, and R. G. Carbonell. 1994. Competitive immunosorbent assays for biotin using bifunctional unilamellar vesicles. *Biotechnology Progress.* 10:174-186.
65. Weissig, V., J. Lasch, A. L. Klivanov, and V. P. Torchilin. 1986. A new hydrophobic anchor for the attachment of proteins to liposomal membranes. *Febs Letters.* 202:86-90.
66. Kung, V. T., and C. T. Redemann. 1986. Synthesis of carboxyacyl derivatives of phosphatidylethanolamine and use as an efficient method for conjugation of protein to liposomes. *Biochimica. Et Biophysica. Acta.* 862:435-439.
67. Maruyama, K., S. J. Kennel, and L. Huang. 1990. Lipid composition is important for highly efficient target binding and retention of immunoliposomes. *Proc. Natl. Acad. Sci., USA.* 87:5744-5748.

68. Rule, G. S., R. A. Montagna, and R. A. Durst. 1997. Characteristics of DNA-tagged liposomes allowing their use in capillary-migration, sandwich-hybridization assays. *Analytical Biochemistry*. 244:260-269.
69. Carroll, T. R., A. Davison, and A. G. Jones. 1986. Functional cholesteryl binding-agents - synthesis, characterization, and evaluation of antibody-binding to modified phospholipid-vesicles. *Journal of Medicinal Chemistry*. 29:1821-1826.
70. Chambers, J. P., B. P. Arulanandam, L. L. Matta, A. Weis, and J. J. Valdes. 2008. Biosensor recognition elements. *Curr. Issues Mol. Biol.* 10:1-12.
71. Zhu, J. M., F. Yan, Z. W. Guo, and R. E. Marchant. 2005. Surface modification of liposomes by saccharides: Vesicle size and stability of lactosyl liposomes studied by photon correlation spectroscopy. *Journal of Colloid and Interface Science*. 289:542-550.
72. Torchilin, V. P. 2000. Drug targeting. *European Journal of Pharmaceutical Sciences*. 11:S81-S91.
73. Lestini, B. J., S. M. Sagnella, Z. Xu, M. S. Shive, N. J. Richter, J. Jayaseharan, A. J. Case, K. Kottke-Marchant, J. M. Anderson, and R. E. Marchant. 2002. Surface modification of liposomes for selective cell targeting in cardiovascular drug delivery. *Journal of Controlled Release*. 78:235-247.
74. Moreira, J. N., C. B. Hansen, R. Gaspar, and T. M. Allen. 2001. A growth factor antagonist as a targeting agent for sterically stabilized liposomes in human small cell lung cancer. *Biochimica Et Biophysica Acta-Biomembranes*. 1514:303-317.
75. Clark, M. A., H. Blair, L. Liang, R. N. Brey, D. Brayden, and B. H. Hirst. 2001. Targeting polymerised liposome vaccine carriers to intestinal M cells. *Vaccine*. 20:208-217.
76. Dharap, S. S., Y. Wang, P. Chandna, J. J. Khandare, B. Qiu, S. Gunaseelan, P. J. Sinko, S. Stein, A. Farmanfarmanian, and T. Minko. 2005. Tumor-specific targeting of an anticancer drug delivery system by LHRH peptide. *Proc. Natl. Acad. Sci., USA*. 102:12962-12967.
77. Moase, E. H., W. Qu, T. Ishida, Z. Gabos, B. M. Longenecker, G. L. Zimmermann, L. Ding, M. Krantz, and T. M. Allen. 2001. Anti-MUC-1 immunoliposomal doxorubicin in the treatment of murine models of metastatic breast cancer. *Biochimica Et Biophysica Acta-Biomembranes*. 1510:43-55.
78. Turk, M. J., D. J. Waters, and P. S. Low. 2004. Folate-conjugated liposomes preferentially target macrophages associated with ovarian carcinoma. *Cancer Letters*. 213:165-172.

79. Chaize, B., J. P. Colletier, M. Winterhalter, and D. Fournier. 2004. Encapsulation of enzymes in liposomes: high encapsulation efficiency and control of substrate permeability. *Artif. Cells Blood Substit. Immobil. Biotechnol.* 32:67-75.
80. Tsumoto, K., S. M. Nomura, Y. Nakatani, and K. Yoshikawa. 2001. Giant liposome as a biochemical reactor: Transcription of DNA and transportation by laser tweezers. *Langmuir.* 17:7225-7228.
81. Sakai, H., K. Sou, H. Horinouchi, K. Kobayashi, and E. Tsuchida. 2008. Haemoglobin-vesicles as artificial oxygen carriers: present situation and future visions. *Journal of Internal Medicine.* 263:4-15.
82. Vorauer-Uhl, K., A. Wagner, and H. Katinger. 2002. Long term stability of rh-Cu/Zn-superoxide dismutase (SOD)-liposomes prepared by the cross-flow injection technique following International Conference on Harmonisation (ICH)-guidelines. *European Journal of Pharmaceutics and Biopharmaceutics.* 54:83-87.
83. Sharma, A., and U. S. Sharma. 1997. Liposomes in drug delivery: progress and limitations. *International Journal of Pharmaceutics.* 154:123-140.
84. Ulrich, A. S. 2002. Biophysical aspects of using liposomes as delivery vehicles. *Bioscience Reports.* 22:129-150.
85. Allen, T. M., and P. R. Cullis. 2004. Drug delivery systems: Entering the mainstream. *Science.* 303:1818-1822.
86. Deo, N., T. Somasundaran, and P. Somasundaran. 2004. Solution properties of amitriptyline and its partitioning into lipid bilayers. *Colloids and Surfaces B-Biointerfaces.* 34:155-159.
87. Berg, E. S., and K. Skaug. 2003. Liposome encapsulation of the internal control for whole process quality assurance of nucleic acid amplification-based assays. *Journal of Microbiological Methods.* 55:303-309.
88. Oberholzer, T., M. Albrizio, and P. L. Luisi. 1995. Polymerase chain-reaction in liposomes. *Chemistry & Biology.* 2:677-682.
89. Arifin, D. R., and A. F. Palmer. 2003. Determination of size distribution and encapsulation efficiency of liposome-encapsulated hemoglobin blood substitutes using asymmetric flow field-flow fractionation coupled with multi-angle static light scattering. *Biotechnology Progress.* 19:1798-1811.
90. Somerharju, P., and O. Renkonen. 1980. Conversion of phosphatidylglycerol lipids to bis(monoacylglycero)phosphate in vivo. *Biochim. Biophys. Acta.* 618:407-419.

91. Luquain, C., R. Dolmazon, J. M. Enderlin, C. Laugier, M. Lagarde, and J. F. Pageaux. 2000. Bis(monoacylglycerol) phosphate in rat uterine stromal cells: structural characterization and specific esterification of docosahexaenoic acid. *Biochem. J.* 351 Pt 3:795-804.
92. Thornburg, T., C. Miller, T. Thuren, L. King, and M. Waite. 1991. Glycerol reorientation during the conversion of phosphatidylglycerol to bis(monoacylglycerol)phosphate in macrophage-like RAW 264.7 cells. *J. Biol. Chem.* 266:6834-6840.
93. Holopainen, J. M., T. Soderlund, J. M. Alakoskela, M. Saily, O. Eriksson, and P. K. Kinnunen. 2005. Intermolecular interactions of lysobisphosphatidic acid with phosphatidylcholine in mixed bilayers. *Chem. Phys. Lipids.* 133:51-67.
94. Kobayashi, T., M. H. Beuchat, J. Chevallier, A. Makino, N. Mayran, J. M. Escola, C. Lebrand, P. Cosson, and J. Gruenberg. 2002. Separation and characterization of late endosomal membrane domains. *J. Biol. Chem.* 277:32157-32164.
95. Kobayashi, T., K. Startchev, A. J. Whitney, and J. Gruenberg. 2001. Localization of lysobisphosphatidic acid-rich membrane domains in late endosomes. *Biol. Chem.* 382:483-485.
96. Kobayashi, T., and Y. Hirabayashi. 2000. Lipid membrane domains in cell surface and vacuolar systems. *Glycoconj. J.* 17:163-171.
97. Kobayashi, T., F. Gu, and J. Gruenberg. 1998. Lipids, lipid domains and lipid-protein interactions in endocytic membrane traffic. *Semin. Cell. Dev. Biol.* 9:517-526.
98. Matsuo, H., J. Chevallier, N. Mayran, I. Le Blanc, C. Ferguson, J. Faure, N. S. Blanc, S. Matile, J. Dubochet, R. Sadoul, R. G. Parton, F. Vilbois, and J. Gruenberg. 2004. Role of LBPA and Alix in multivesicular liposome formation and endosome organization. *Science.* 303:531-534.
99. Joutti, A., and O. Renkonen. 1979. The stereoconfiguration of bis(monoacylglycerol)phosphate synthesized in vitro in lysosomes of rat liver: comparison with the natural lipid. *J. Lipid Res.* 20:840-847.
100. Joutti, A., and O. Renkonen. 1976. The structure of phosphatidyl glycerol prepared by phospholipase D-catalyzed transphosphatidylation from egg lecithin and glycerol. *Chem. Phys. Lipids.* 17:264-266.
101. Hayakawa, T., A. Makino, M. Murate, I. Sugimoto, Y. Hashimoto, H. Takahashi, K. Ito, T. Fujisawa, H. Matsuo, and T. Kobayashi. 2007. pH-dependent formation of membranous cytoplasmic body-like structure of ganglioside G(M1)/bis(monoacylglycerol)phosphate mixed membranes. *Biophys. J.* 92:L13-16.

102. Luzio, J. P., B. A. Rous, N. A. Bright, P. R. Pryor, B. M. Mullock, and R. C. Piper. 2000. Lysosome-endosome fusion and lysosome biogenesis. *J. Cell Sci.* 113 (Pt 9):1515-1524.
103. Piper, R. C., and J. P. Luzio. 2001. Late endosomes: sorting and partitioning in multivesicular bodies. *Traffic.* 2:612-621.
104. Somsel Rodman, J., and A. Wandinger-Ness. 2000. Rab GTPases coordinate endocytosis. *J. Cell Sci.* 113 Pt 2:183-192.
105. Frederick, T. E., J. N. Chebukati, C. E. Mair, P. C. Goff, and G. E. Fanucci. 2009. Bis(monoacylglycero)phosphate forms stable small lamellar vesicle structures: insights into vesicular body formation in endosomes. *Biophys. J.* 96:1847-1855.
106. Hayakawa, T., Y. Hirano, A. Makino, S. Michaud, M. Lagarde, J. F. Pageaux, A. Doutheau, K. Ito, T. Fujisawa, H. Takahashi, and T. Kobayashi. 2006. Differential membrane packing of stereoisomers of bis(monoacylglycero)phosphate. *Biochemistry.* 45:9198-9209.
107. Amidon, B., A. Brown, and M. Waite. 1996. Transacylase and phospholipases in the synthesis of bis(monoacylglycero)phosphate. *Biochemistry.* 35:13995-14002.
108. Kobayashi, T., M. H. Beuchat, M. Lindsay, S. Frias, R. D. Palmiter, H. Sakuraba, R. G. Parton, and J. Gruenberg. 1999. Late endosomal membranes rich in lysobisphosphatidic acid regulate cholesterol transport. *Nat. Cell Biol.* 1:113-118.
109. Wilkening, G., T. Linke, G. Uhlhorn-Dierks, and K. Sandhoff. 2000. Degradation of membrane-bound ganglioside GM1. Stimulation by bis(monoacylglycero)phosphate and the activator proteins SAP-B and GM2-AP. *J. Biol. Chem.* 275:35814-35819.
110. Werth, N., C. G. Schuette, G. Wilkening, T. Lemm, and K. Sandhoff. 2001. Degradation of membrane-bound ganglioside GM2 by beta -hexosaminidase A. Stimulation by GM2 activator protein and lysosomal lipids. *J. Biol. Chem.* 276:12685-12690.
111. Linke, T., G. Wilkening, F. Sadeghlar, H. Mozcall, K. Bernardo, E. Schuchman, and K. Sandhoff. 2001. Interfacial regulation of acid ceramidase activity. Stimulation of ceramide degradation by lysosomal lipids and sphingolipid activator proteins. *J. Biol. Chem.* 276:5760-5768.
112. Makino, A., K. Ishii, M. Murate, T. Hayakawa, Y. Suzuki, M. Suzuki, K. Ito, T. Fujisawa, H. Matsuo, R. Ishitsuka, and T. Kobayashi. 2006. D-threo-1-phenyl-2-decanoylamino-3-morpholino-1-propanol alters cellular cholesterol homeostasis by modulating the endosome lipid domains. *Biochemistry.* 45:4530-4541.

113. Alessandri, C., M. Bombardieri, L. Di Prospero, P. Conigliaro, F. Conti, G. Labbadia, R. Misasi, M. Sorice, and G. Valesini. 2005. Anti-lysobisphosphatidic acid antibodies in patients with antiphospholipid syndrome and systemic lupus erythematosus. *Clin. Exp. Immunol.* 140:173-180.
114. Le Blanc, I., P. P. Luyet, V. Pons, C. Ferguson, N. Emans, A. Petiot, N. Mayran, N. Demaurex, J. Faure, R. Sadoul, R. G. Parton, and J. Gruenberg. 2005. Endosome-to-cytosol transport of viral nucleocapsids. *Nat. Cell Biol.* 7:653-664.
115. Lebrand, C., M. Corti, H. Goodson, P. Cosson, V. Cavalli, N. Mayran, J. Faure, and J. Gruenberg. 2002. Late endosome motility depends on lipids via the small GTPase Rab7. *EMBO J.* 21:1289-1300.
116. Mayran, N., R. G. Parton, and J. Gruenberg. 2003. Annexin II regulates multivesicular endosome biogenesis in the degradation pathway of animal cells. *EMBO J.* 22:3242-3253.
117. Burkhardt, J. K., S. Huttler, A. Klein, W. Mobius, A. Habermann, G. Griffiths, and K. Sandhoff. 1997. Accumulation of sphingolipids in SAP-precursor (prosaposin)-deficient fibroblasts occurs as intralysosomal membrane structures and can be completely reversed by treatment with human SAP-precursor. *Eur. J. Cell Biol.* 73:10-18.
118. Schnabel, D., M. Schroder, and K. Sandhoff. 1991. Mutation in the sphingolipid activator protein 2 in a patient with a variant of Gaucher disease. *FEBS Lett.* 284:57-59.
119. (www.malvern.co.uk). Dynamic Light Scattering: An Introduction in 30 Minutes.
120. Tscharnuter, W. Photon Correlation Spectroscopy in Particle Sizing In Encyclopedia of Analytical Chemistry. R.A. Meyers (Editor.) John Wiley & Sons Ltd., Holtsville, NY.
121. Lee, S.P., and B. Chu. 1972. Calibration of an optical self-beating spectrometer by polystyrene latex spheres, and confirmation of the stokes-einstein formula. *Polym. Sci.* 10.
122. Tyndall, J. 1869. On the blue color of the sky, the polarization of the skylight and on the polarization of light by cloudy matter generally. *Phil. Mag.*, 37.
123. Kerker, M. 1969. The Scattering of Light and Other Electromagnetic Radiation. Academic Press, New York, NY.
124. Nobbmann, U., M. Connah, B. Fish, P. Varley, C. Gee, S. Mulot, J. Chen, L. Zhou, Y. Lu, F. Shen, J. Yi, and S. E. Harding. 2007. Dynamic light scattering as a relative tool for assessing the molecular integrity and stability of monoclonal antibodies. *Biotechnol. Genet. Eng. Rev.* 24:117-128.

125. Pecora, R., 1964. Doppler shifts in light scattering from pure liquids and polymer solutions. *J. Chem. Phys.* 40:1604-1614.
126. Bertero, M., and E.R. Pike. 1982. On the recovery and resolution of exponential relaxation rates from experimental data: a singular-value analysis of the Laplace Transform Inversion in the presence of noise. *Proc. Royal Soc. London.* A383:15-29.
127. Bertero, M., and E.R. Pike. 1984. On the recovery and resolution of exponential relaxation rates from experimental data. II. The optimum choice of the sampling points. *Proc. Royal Soc. London.* A393. 51-65 A393:51-65.
128. Lawrie, A. S., A. Albanyan, R. A. Cardigan, I. J. Mackie, and P. Harrison. 2009. Microparticle sizing by dynamic light scattering in fresh-frozen plasma. *Vox. Sang.* 96:206-212.
129. (ISO), I. O. f. S. 1996. Methods for Determination of Particle Size Distribution Part 8: Photon Correlation Spectroscopy. *In International Standard ISO13321.*
130. Dahneke, B. E., (editor). 1983. Measurement of Suspended Particles by Quasielastic Light Scattering. Wiley, Holtsville, NY.
131. O'Neal, D., P. Harrip, G. Dragicevic, D. Rae, and J. D. Best. 1998. A comparison of LDL size determination using gradient gel electrophoresis and light-scattering methods. *J. Lipid Res.* 39:2086-2090.
132. Pecora, R. 1985. Dynamic Light Scattering: Applications of Photon Correlation Spectroscopy. Plenum Press, New York, NY.
133. Cantu, L., M. Musolino, and P. Salina. 1991. Spontaneous vesicle formation from a one-component solution of a biological surfactant. *Progr. Colloid. Polym. Sci.* 84:21-23.
134. Dhadwal, H.S., R.R. Ansari, and W.V. Meyer. 1993. Dynamic Light Scattering Studies of BSA and Lysozyme Using a Backscatter Fiber Optic System In Proceedings Static and Dynamic Scattering in Medicine and Biology, *Society of Photo-optical Instrumentation Engineers.* Bellingham, WA 98227.
135. Mikol, V., and R. Giege. 1989. Monitoring protein crystallization by dynamic light scattering. *FEBS Lett.* 258:63-66.
136. Herb, C.A., K. Chang, I.D. Morrison and E.F. Grabowski. 1987. Using Quasi-elastic Light Scattering to Study Particle Size Distributions in Submicrometer Emulsion Systems *In ACS Symposium Series.*

137. Weiner, B., and A. Banerjee. 1996. Developing Fiber Optic Probes for Noninvasive Particle Size Measurements in Concentrated Suspensions using DLS. Or How to Make a Zero Shear Rheometer without Really Trying. *Brookhaven Corp. Internal Memorandum*.
138. Neuman, R. D., and N. Zhou. 1990. Photon correlation spectroscopy applied to hydro metallurgical solvent extraction systems. *Coll. Surf.* 46:45-64.
139. Caldwell, K.D. 1989. Emulsion characterization by the combined sedimentation field-flow fractionation-photon correlation spectroscopy methods. *J. Coll. Interf. Sci.* 132:256-268.
140. Ludwig, R. 1993. *Transmission Electron Microscopy: Physics of Image Formation and Microanalysis*. Springer-Verlag, New York, NY.
141. Fultz, B., and J.M. Howe. 2002. *Transmission Electron Microscopy and Diffractometry of Materials*. Springer, New York, NY.
142. Hawkes, P., (editor). 1985. *The Beginnings of Electron Microscopy*. Academic Press, New York, NY.
143. Champness, P. E. 2001. *Electron Diffraction in the Transmission Electron Microscope*. Garland Science, London, UK.
144. Hubbard, A. 1995. *The Handbook of Surface Imaging and Visualization*. CRC Press, New York, NY.
145. Rose, H. H. 2008. Optics of high-performance electron microscopes. *Science and Technology of Advanced Materials*. 9.
146. Reimer, L. 2008. *Transmission Electron Microscopy: Physics of Image Formation*. Springer, New York, NY.
147. Williams, D. 1996. *Transmission Electron Microscopy. 1 - Basics*. Plenum Press, New York, NY.
148. Dykstra, M. J., and L. E. Reuss. 2003. *Biological Electron Microscopy: Theory, Techniques and Troubleshooting*. Springer, New York, NY.
149. Chapman, S. K. 1986. *Maintaining and Monitoring the Transmission Electron Microscope*. Oxford University Press, New York, NY.
150. Slayter, E. M., and H.S. Slayter. 1992. *Light and Electron Microscopy*. Cambridge University Press, New York, NY.
151. Amos, L. A., R. Henderson, and P. N. Unwin. 1982. Three-dimensional structure determination by electron microscopy of two-dimensional crystals. *Prog. Biophys. Mol. Biol.* 39:183-231.

152. Dubochet, J., M. Adrian, J. J. Chang, J. C. Homo, J. Lepault, A. W. McDowell, and P. Schultz. 1988. Cryo-electron microscopy of vitrified specimens. *Q. Rev. Biophys.* 21:129-228.
153. Amzallag, A., C. Vaillant, M. Jacob, M. Unser, J. Bednar, J. D. Kahn, J. Dubochet, A. Stasiak, and J. H. Maddocks. 2006. 3D reconstruction and comparison of shapes of DNA minicircles observed by cryo-electron microscopy. *Nucleic Acids Research.* 34.
154. Kiselev, N. A., M. B. Sherman, and V. L. Tsuprun. 1990. Negative staining of proteins. *Electron Microscopy Reviews.* 3:43-72.
155. Hoenger, A., and U. Aebi. 1996. 3-D reconstructions from ice-embedded and negatively stained biomacromolecular assemblies: A critical comparison. *Journal of Structural Biology.* 117:99-116.
156. Ruprecht, J., and J. Nield. 2001. Determining the structure of biological macromolecules by transmission electron microscopy, single particle analysis and 3D reconstruction. *Prog. Biophys. Mol. Biol.* 75:121-164.
157. Stark, H., F. Mueller, E. V. Orlova, M. Schatz, P. Dube, T. Erdemir, F. Zemlin, R. Brimacombe, and M. van Heel. 1995. The 70S Escherichia coli ribosome at 23 Å resolution: fitting the ribosomal RNA. *Structure.* 3:815-821.
158. Biel, S. S., and H. R. Gelderblom. 1999. Diagnostic electron microscopy is still a timely and rewarding method. *J. Clin. Virol.* 13:105-119.
159. Horne, R. W. 1978. Special specimen preparation methods for image processing in transmission electron microscopy: a review. *J. Microsc.* 113:241-256.
160. Brenner, S., and R. W. Horne. 1959. A negative staining method for high resolution electron microscopy of viruses. *Biochim. Biophys. Acta.* 34:103-110.
161. Horne, R. W., and V. P. Whittaker. 1962. The use of the negative staining method for the electron-microscopic study of subcellular particles from animal tissues. *Z. Zellforsch Mikrosk. Anat.* 58:1-16.
162. Dourmashkin, R. R., R. M. Dougherty, and R. J. Harris. 1962. Electron microscopic observations on Rous sarcoma virus and cell membranes. *Nature.* 194:1116-1119.
163. Bangham, A. D., R. W. Horne, A. M. Glauert, J. T. Dingle, and J. A. Lucy. 1962. Action of saponin on biological cell membranes. *Nature.* 196:952-955.
164. Trantum-Jensen, J. 1988. Electron microscopy: assays involving negative staining. *Methods Enzymol.* 165:357-374.

165. Kulkarni, V. S., W. H. Anderson, and R. E. Brown. 1995. Bilayer nanotubes and helical ribbons formed by hydrated galactosylceramides: acyl chain and headgroup effects. *Biophys. J.* 69:1976-1986.
166. De la Maza, A., and J. L. Parra. 1994. Vesicle-micelle structural transition of phosphatidylcholine bilayers and Triton X-100. *Biochem. J.* 303 (Pt 3):907-914.
167. Polozova, A., and F. M. Winnik. 1997. Mechanism of the interaction of hydrophobically-modified poly-(N-isopropylacrylamides) with liposomes. *Biochim. Biophys. Acta.* 1326:213-224.
168. Polozova, A. I., G. E. Dubachev, T. N. Simonova, and L. I. Barsukov. 1995. Temperature-induced micellar-lamellar transformation in binary mixtures of saturated phosphatidylcholines with sodium cholate. *FEBS Lett.* 358:17-22.
169. Berney, C., and G. Danuser. 2003. FRET or no FRET: a quantitative comparison. *Biophys. J.* 84:3992-4010.
170. Bastiaens, P. I. 1998. Fluorescence Resonance Energy Transfer Microscopy in Cell Biology: A Laboratory Handbook. Academic Press, New York, NY.
171. Lakowicz, J. R. 1999. Principles of Fluorescence Spectroscopy. Plenum Publishing Corp., New York, NY.
172. Sekar, R. B., and A. Periasamy. 2003. Fluorescence resonance energy transfer (FRET) microscopy imaging of live cell protein localizations. *J. Cell. Biol.* 160:629-633.
173. Rao, M., and S. Mayor. 2005. Use of Forster's resonance energy transfer microscopy to study lipid rafts. *Biochim. Biophys. Acta.* 1746:221-233.
174. Gryczynski, Z., I. Gryczynski, and J.R. Lakowicz. 2005. Basics of Fluorescence and FRET in Molecular Imaging: FRET Microscopy and Spectroscopy. Oxford University Press, New York, NY.
175. Jares-Erijman, E. A., and T. M. Jovin. 2003. FRET imaging. *Nat. Biotechnol.* 21:1387-1395.
176. Vogel, S. S., C. Thaler, and S. V. Koushik. 2006. Fanciful FRET. *Sci. STKE* 2006:re2.
177. Lakowicz, J. R., H. Szmajcinski, K. Nowaczyk, K. W. Berndt, and M. Johnson. 1992. Fluorescence lifetime imaging. *Anal. Biochem.* 202:316-330.
178. Gadella, T. W., Jr., and T. M. Jovin. 1995. Oligomerization of epidermal growth factor receptors on A431 cells studied by time-resolved fluorescence imaging microscopy. A stereochemical model for tyrosine kinase receptor activation. *J. Cell. Biol.* 129:1543-1558.

179. Bastiaens, P. I., and A. Squire. 1999. Fluorescence lifetime imaging microscopy: spatial resolution of biochemical processes in the cell. *Trends Cell Biol.* 9:48-52.
180. Jovin, T. M., and D. J. Arndt-Jovin. 1989. Luminescence digital imaging microscopy. *Annu. Rev. Biophys. Chem.* 18:271-308.
181. Kenworthy, A. K., and M. Edidin. 1998. Distribution of a glycosylphosphatidylinositol-anchored protein at the apical surface of MDCK cells examined at a resolution of <100 Å using imaging fluorescence resonance energy transfer. *J. Cell. Biol.* 142:69-84.
182. Wouters, F. S., P. I. Bastiaens, K. W. Wirtz, and T. M. Jovin. 1998. FRET microscopy demonstrates molecular association of non-specific lipid transfer protein (nsL-TP) with fatty acid oxidation enzymes in peroxisomes. *EMBO J.* 17:7179-7189.
183. Gordon, G. W., G. Berry, X. H. Liang, B. Levine, and B. Herman. 1998. Quantitative fluorescence resonance energy transfer measurements using fluorescence microscopy. *Biophys. J.* 74:2702-2713.
184. Pires, P., S. Simoes, S. Nir, R. Gaspar, N. Duzgunes, and M. C. Pedroso de Lima. 1999. Interaction of cationic liposomes and their DNA complexes with monocytic leukemia cells. *Biochim. Biophys. Acta.* 1418:71-84.
185. Meers, P., J. D. Ernst, N. Duzgunes, K. L. Hong, J. Fedor, I. M. Goldstein, and D. Papahadjopoulos. 1987. Synexin-like proteins from human polymorphonuclear leukocytes. Identification and characterization of granule-aggregating and membrane-fusing activities. *J. Biol. Chem.* 262:7850-7858.
186. Stegmann, T., S. Nir, and J. Wilschut. 1989. Membrane fusion activity of influenza virus. Effects of gangliosides and negatively charged phospholipids in target liposomes. *Biochemistry.* 28:1698-1704.
187. Ramalho-Santos, J., M. C. Lima, and S. Nir. 1996. Partial fusion activity of influenza virus toward liposomes and erythrocyte ghosts is distinct from viral inactivation. *J. Biol. Chem.* 271:23902-23906.
188. Kenworthy, A. 2002. Peering inside lipid rafts and caveolae. *Trends Biochem. Sci.* 27:435-437.
189. Lommerse, P. H., G. A. Blab, L. Cognet, G. S. Harms, B. E. Snaar-Jagalska, H. P. Spaank, and T. Schmidt. 2004. Single-molecule imaging of the H-ras membrane-anchor reveals domains in the cytoplasmic leaflet of the cell membrane. *Biophys. J.* 86:609-616.
190. Lagerholm, B. C., G. E. Weinreb, K. Jacobson, and N. L. Thompson. 2005. Detecting microdomains in intact cell membranes. *Annu. Rev. Phys. Chem.* 56:309-336.

191. Silvius, J. R., and I. R. Nabi. 2006. Fluorescence-quenching and resonance energy transfer studies of lipid microdomains in model and biological membranes. *Mol. Membr. Biol.* 23:5-16.
192. Kenworthy, A. K. 2007. Fluorescence recovery after photobleaching studies of lipid rafts. *Methods Mol. Biol.* 398:179-192.
193. Kenworthy, A. K., N. Petranova, and M. Edidin. 2000. High-resolution FRET microscopy of cholera toxin B-subunit and GPI-anchored proteins in cell plasma membranes. *Mol. Biol. Cell.* 11:1645-1655.
194. Varma, R., and S. Mayor. 1998. GPI-anchored proteins are organized in submicron domains at the cell surface. *Nature.* 394:798-801.
195. Zacharias, D. A., J. D. Violin, A. C. Newton, and R. Y. Tsien. 2002. Partitioning of lipid-modified monomeric GFPs into membrane microdomains of live cells. *Science.* 296:913-916.
196. Nichols, B. 2003. Caveosomes and endocytosis of lipid rafts. *J. Cell Sci.* 116:4707-4714.
197. Sohn, H. W., P. Tolar, T. Jin, and S. K. Pierce. 2006. Fluorescence resonance energy transfer in living cells reveals dynamic membrane changes in the initiation of B cell signaling. *Proc. Natl. Acad. Sci. USA.* 103:8143-8148.
198. Wilschut, J., N. Duzgunes, R. Fraley, and D. Papahadjopoulos. 1980. Studies on the mechanism of membrane fusion: kinetics of calcium ion induced fusion of phosphatidylserine vesicles followed by a new assay for mixing of aqueous vesicle contents. *Biochemistry.* 19:6011-6021.
199. Duzgunes, N., S. Nir, J. Wilschut, J. Bentz, C. Newton, A. Portis, and D. Papahadjopoulos. 1981. Calcium- and magnesium-induced fusion of mixed phosphatidylserine/phosphatidylcholine vesicles: effect of ion binding. *J. Membr. Biol.* 59:115-125.
200. Duzgunes, N., J. Wilschut, R. Fraley, and D. Papahadjopoulos. 1981. Studies on the mechanism of membrane fusion. Role of head-group composition in calcium- and magnesium-induced fusion of mixed phospholipid vesicles. *Biochim. Biophys. Acta.* 642:182-195.
201. Duzgunes, N., and S. Ohki. 1981. Fusion of small unilamellar liposomes with phospholipid planar bilayer membranes and large single-bilayer vesicles. *Biochim. Biophys. Acta.* 640:734-747.
202. Weinstein, J. N., S. Yoshikami, P. Henkart, R. Blumenthal, and W. A. Hagins. 1977. Liposome-cell interaction: transfer and intracellular release of a trapped fluorescent marker. *Science.* 195:489-492.

203. Straubinger, R. M., K. Hong, D. S. Friend, and D. Papahadjopoulos. 1983. Endocytosis of liposomes and intracellular fate of encapsulated molecules: encounter with a low pH compartment after internalization in coated vesicles. *Cell*. 32:1069-1079.
204. Straubinger, R. M., and D. Papahadjopoulos. 1983. Liposomes as carriers for intracellular delivery of nucleic acids. *Methods. Enzymol.* 101:512-527.
205. Allen, T. M., A. Y. Romans, H. Kercret, and J. P. Segrest. 1980. Detergent removal during membrane reconstitution. *Biochim. Biophys. Acta.* 601:328-342.
206. Allen, T. M., and L. G. Cleland. 1980. Serum-induced leakage of liposome contents. *Biochim. Biophys. Acta.* 597:418-426.
207. Straubinger, R. M., N. Duzgunes, and D. Papahadjopoulos. 1985. pH-sensitive liposomes mediate cytoplasmic delivery of encapsulated macromolecules. *FEBS Lett.* 179:148-154.
208. Slepishkin, V. A., S. Simoes, P. Dazin, M. S. Newman, L. S. Guo, M. C. Pedroso de Lima, and N. Duzgunes. 1997. Sterically stabilized pH-sensitive liposomes. Intracellular delivery of aqueous contents and prolonged circulation in vivo. *J. Biol. Chem.* 272:2382-2388.
209. Kayalar, C., and N. Duzgunes. 1986. Membrane action of colicin E1: detection by the release of carboxyfluorescein and calcein from liposomes. *Biochim Biophys Acta* 860:51-56.
210. Rapaport, E., A. Levina, V. Metelev, and P. C. Zamecnik. 1996. Antimycobacterial activities of antisense oligodeoxynucleotide phosphorothioates in drug-resistant strains. *Proc. Natl. Acad. Sci. USA.* 93:709-713.
211. Tian, P., J. M. Ball, C. Q. Zeng, and M. K. Estes. 1996. The rotavirus nonstructural glycoprotein NSP4 possesses membrane destabilization activity. *J. Virol.* 70:6973-6981.
212. Babbitt, B., L. Burtis, P. Dentinger, P. Constantinides, L. Hillis, B. McGirl, and L. Huang. 1993. Contact-dependent, immunocomplex-mediated lysis of hapten-sensitized liposomes. *Bioconjug. Chem.* 4:199-205.
213. Fan, Q., A. Relini, D. Cassinadri, A. Gambacorta, and A. Gliozzi. 1995. Stability against temperature and external agents of vesicles composed of archaeal bolaform lipids and egg PC. *Biochim. Biophys. Acta.* 1240:83-88.
214. Ellens, H., J. Bentz, and F. C. Szoka. 1984. pH-induced destabilization of phosphatidylethanolamine-containing liposomes: role of bilayer contact. *Biochemistry.* 23:1532-1538.

215. Shiffer, K., S. Hawgood, N. Duzgunes, and J. Goerke. 1988. Interactions of the low molecular weight group of surfactant-associated proteins (SP 5-18) with pulmonary surfactant lipids. *Biochemistry*. 27:2689-2695.
216. Duzgunes, N., and F. Gambale. 1988. Membrane action of synthetic N-terminal peptides of influenza virus hemagglutinin and its mutants. *FEBS Lett.* 227:110-114.
217. Duzgunes, N., and S. A. Shavnin. 1992. Membrane destabilization by N-terminal peptides of viral envelope proteins. *J. Membr. Biol.* 128:71-80.
218. Duzgunes, N., M. C. Pedroso de Lima, L. Stamatatos, D. Flasher, D. Alford, D. S. Friend, and S. Nir. 1992. Fusion activity and inactivation of influenza virus: kinetics of low pH-induced fusion with cultured cells. *J. Gen. Virol.* 73 (Pt 1):27-37.
219. Harwood, L.M. *Experimental Organic Chemistry: Principles and Practice*. Wiley Blackwell, Indianapolis, IN.
220. Vogel, A.I., B.S. Furnis, A.J. Hannaford, and P.W.G. Smith. 1996. *Vogel's Textbook of Practical Organic Chemistry*. Prentice Hall, Upper Saddle River, NJ.
221. Nyiredy, S., and G. Szepesi. 1992. Planar chromatography: current status and future perspectives in pharmaceutical analysis (short review)--II. Special techniques and future perspectives in planar chromatography. *J. Pharm. Biomed. Anal.* 10:1017-1024.
222. Poole, C. F. 1999. Planar chromatography at the turn of the century. *J. Chromatogr. A.* 856:399-427.
223. Poole, S. K., and C. F. Poole. 1999. Chromatographic models for the sorption of neutral organic compounds by soil from water and air. *J. Chromatogr. A.* 845:381-400.
224. Stoddard, J. M., L. Nguyen, H. Mata-Chavez, and K. Nguyen. 2007. TLC plates as a convenient platform for solvent-free reactions. *Chem. Commun. (Camb)*. 1240-1241.
225. Szepesi, G., and S. Nyiredy. 1992. Planar chromatography: current status and future perspectives in pharmaceutical analysis--I. Applicability, quantitation and validation. *J. Pharm. Biomed. Anal.* 10:1007-1015.
226. Mriziq, K. S., and G. Guiochon. 2008. Column properties and flow profiles of a flat, wide column for high-pressure liquid chromatography. *J. Chromatogr. A.* 1187:180-187.
227. Mriziq, K. S., J. A. Abia, Y. Lee, and G. Guiochon. 2008. Structural radial heterogeneity of a silica-based wide-bore monolithic column. *J. Chromatogr. A.* 1193:97-103.

228. Clarkstill, W., and A. Mitra. 1978. Rapid chromatographic technique for preparative separations with moderate resolution. *J. Org. Chem.* 43.
229. Vandemter, J. J., F. J. Zuiderweg, and A. Klinkenberg. 1956. Longitudinal diffusion and resistance to mass transfer as causes of nonideality in chromatography. *Chemical Engineering Science.* 5:271-289.
230. Mullock, B. M., R. H. Hinton, J. V. Peppard, J. W. Slot, and J. P. Luzio. 1987. The preparative isolation of endosome fractions: a review. *Cell Biochem. Funct.* 5:235-243.
231. Matsuzawa, Y., and K. Y. Hostetler. 1979. Degradation of bis(monoacylglycero)phosphate by an acid phosphodiesterase in rat liver lysosomes. *J. Biol. Chem.* 254:5997-6001.
232. Duzgunes, N. 2003. Fluorescence assays for liposome fusion. *Methods Enzymol.* 372:260-274.
233. Hullin-Matsuda, F., K. Kawasaki, I. Delton-Vandenbroucke, Y. Xu, M. Nishijima, M. Lagarde, M. Schlame, and T. Kobayashi. 2007. De novo biosynthesis of the late endosome lipid, bis(monoacylglycero)phosphate. *J. Lipid Res.* 48:1997-2008.
234. Bassi, R., and S. Sonnino. 1992. The role of the ganglioside lipid moiety in the process of ganglioside-cell interactions. *Chem. Phys. Lipids.* 62:1-9.
235. Furst, W., and K. Sandhoff. 1992. Activator proteins and topology of lysosomal sphingolipid catabolism. *Biochim. Biophys. Acta.* 1126:1-16.
236. Jeyakumar, M., R. A. Dwek, T. D. Butters, and F. M. Platt. 2005. Storage solutions: treating lysosomal disorders of the brain. *Nat. Rev. Neurosci.* 6:713-725.
237. Simons, K., and J. Gruenberg. 2000. Jamming the endosomal system: lipid rafts and lysosomal storage diseases. *Trends Cell Biol.* 10:459-462.
238. Demaurex, N. 2002. pH Homeostasis of cellular organelles. *News Physiol. Sci.* 17:1-5.
239. Frey, S. L., E. Y. Chi, C. Arratia, J. Majewski, K. Kjaer, and K. Y. Lee. 2008. Condensing and fluidizing effects of ganglioside GM1 on phospholipid films. *Biophys. J.* 94:3047-3064.
240. Bach, D., and E. Wachtel. 2003. Phospholipid/cholesterol model membranes: formation of cholesterol crystallites. *Biochim. Biophys. Acta.* 1610:187-197.
241. Sobo, K., I. Le Blanc, P. P. Luyet, M. Fivaz, C. Ferguson, R. G. Parton, J. Gruenberg, and F. G. van der Goot. 2007. Late endosomal cholesterol accumulation leads to impaired intra-endosomal trafficking. *PLoS ONE.* 2:e851.

242. Aniento, F., and J. Gruenberg. 1995. Membrane transport from early to late endosomes. *Cold Spring Harb. Symp. Quant. Biol.* 60:205-209.
243. Gruenberg, J., and F. R. Maxfield. 1995. Membrane transport in the endocytic pathway. *Curr. Opin. Cell Biol.* 7:552-563.
244. Ikonen, E., and M. Holtta-Vuori. 2004. Cellular pathology of Niemann-Pick type C disease. *Semin. Cell Dev. Biol.* 15:445-454.
245. Maxfield, F. R., and I. Tabas. 2005. Role of cholesterol and lipid organization in disease. *Nature.* 438:612-621.
246. Vanier, M. T., and G. Millat. 2003. Niemann-Pick disease type C. *Clin. Genet.* 64:269-281.
247. Puri, V., R. Watanabe, M. Dominguez, X. Sun, C. L. Wheatley, D. L. Marks, and R. E. Pagano. 1999. Cholesterol modulates membrane traffic along the endocytic pathway in sphingolipid-storage diseases. *Nat. Cell Biol.* 1:386-388.
248. Leventhal, A. R., W. Chen, A. R. Tall, and I. Tabas. 2001. Acid sphingomyelinase-deficient macrophages have defective cholesterol trafficking and efflux. *J Biol Chem* 276:44976-44983.
249. Desnick, R. J., and E. H. Schuchman. 2002. Enzyme replacement and enhancement therapies: lessons from lysosomal disorders. *Nat. Rev. Genet.* 3:954-966.
250. Sturley, S. L., M. C. Patterson, W. Balch, and L. Liscum. 2004. The pathophysiology and mechanisms of NP-C disease. *Biochim. Biophys. Acta.* 1685:83-87.
251. Mobius, W., E. van Donselaar, Y. Ohno-Iwashita, Y. Shimada, H. F. Heijnen, J. W. Slot, and H. J. Geuze. 2003. Recycling compartments and the internal vesicles of multivesicular bodies harbor most of the cholesterol found in the endocytic pathway. *Traffic.* 4:222-231.
252. Mobius, W., V. Herzog, K. Sandhoff, and G. Schwarzmann. 1999. Gangliosides are transported from the plasma membrane to intralysosomal membranes as revealed by immuno-electron microscopy. *Biosci. Rep.* 19:307-316.
253. Mobius, W., V. Herzog, K. Sandhoff, and G. Schwarzmann. 1999. Intracellular distribution of a biotin-labeled ganglioside, GM1, by immunoelectron microscopy after endocytosis in fibroblasts. *J. Histochem. Cytochem.* 47:1005-1014.
254. McQuaw, C. M., L. Zheng, A. G. Ewing, and N. Winograd. 2007. Localization of sphingomyelin in cholesterol domains by imaging mass spectrometry. *Langmuir.* 23:5645-5650.

255. Veatch, S. L., and S. L. Keller. 2005. Miscibility phase diagrams of giant vesicles containing sphingomyelin. *Phys. Rev. Lett.* 94:148101.
256. Simons, K., and W. L. Vaz. 2004. Model systems, lipid rafts, and cell membranes. *Annu. Rev. Biophys. Biomol. Struct.* 33:269-295.
257. Sobo, K., J. Chevallier, R. G. Parton, J. Gruenberg, and F. G. van der Goot. 2007. Diversity of raft-like domains in late endosomes. *PLoS ONE.* 2:e391.
258. Lasic, D. D. 1998. Novel applications of liposomes. *Trends Biotechnol.* 16:307-321.

BIOGRAPHICAL SKETCH

Janetricks Nanjala Chebukati (Rhodah) was born on July 30th 1976, in the Western province of Kenya, in a small rural township called Bungoma that is situated close to the foothills of Mt. Elgon. She is the fourth born of ten children to Mr. Gerishom Muchungi Chebukati, a retired primary school teacher, and Mrs. Ritah Nekesa Muchungi, a housewife. From an early age, Janetricks quickly learnt the value of an education through her parents' guidance and direction. She started high school in 1991, and graduated in the top 5 % of her class from the prestigious Lugulu Girls' High School in 1994. Janetricks joined Jomo Kenyatta University of Agriculture and Technology (JKUAT) in Nairobi, Kenya in March 1997 and graduated in April 2001 with *honors* in BSc (Chemistry).

In August 2001, Janetricks started work as a pharmaceutical sales representative for Ranbaxy Laboratories Ltd, and relocated to the lakeside city of Kisumu, Kenya. She remained in this position for two years, before enrolling for graduate school in the Department of Chemistry at the University of Florida (UF) in fall 2003.

At UF, she briefly worked on Laser Ablation-Inductively Coupled Plasma Mass Spectrometry (LA-ICPMS) in Jim Winefordner's group, before eventually joining the Fanucci research group in the summer of 2006. Janetricks spent the next three and half years in the Fanucci group working on the characterization of the physico-chemical properties of lipids using analytical techniques such as electron microscopy (EM) and dynamic light scattering (DLS). She also earned a dual Masters degree in Forensic Drug Chemistry from the UF School of Pharmacy in December 2008.

Janetricks recently accepted a postdoctoral research associate position in Dr. Dale Benos' lab in the Department of Biophysics and Physiology, in the School of Medicine at

the University of Alabama, Birmingham, to commence in January, 2010. Janetricks is married to Dr. George Odhiambo Okeyo, and they are blessed with two daughters, Lavender (13 years old) and Subi (2 years old).